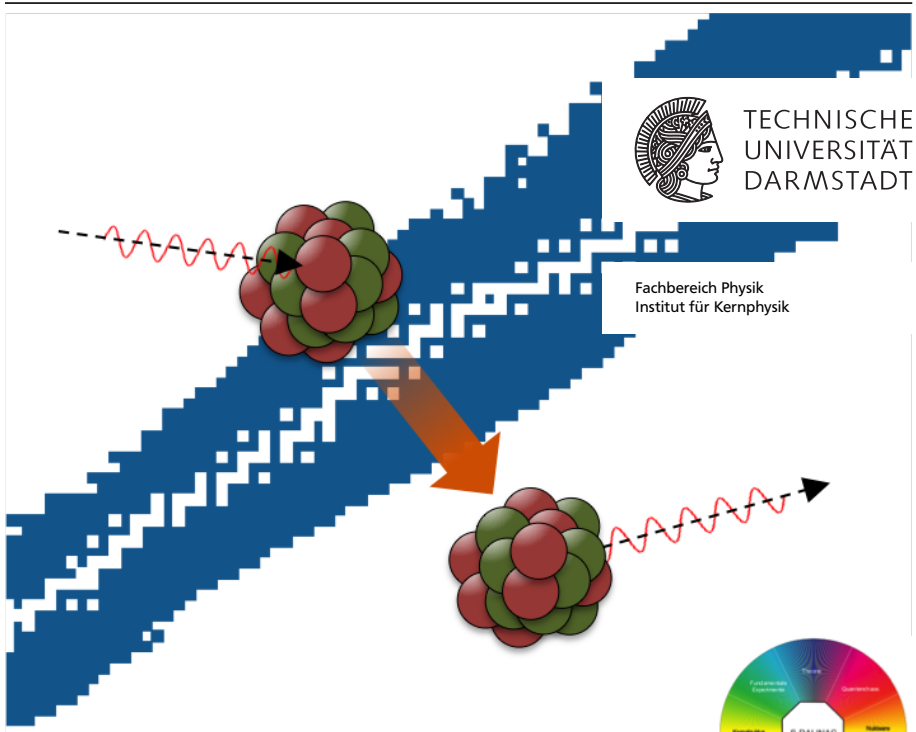


Investigation of Nuclear Structure with Relative Self-Absorption Measurements

Kernstrukturuntersuchungen mit relativen Selbstabsorptionsmessungen

Vom Fachbereich Physik der Technischen Universität Darmstadt zur Erlangung
des akademischen Grades eines Doktors der Naturwissenschaften (Dr. rer. nat.)
genehmigte Dissertation von Christopher Romig, M.Sc. aus Darmstadt
2015 – Darmstadt – D 17



Supported by the DFG under contract No. SFB 634

**Investigation of Nuclear Structure with Relative Self-Absorption Measurements
Kernstrukturuntersuchungen mit relativen Selbstabsorptionsmessungen**

Vom Fachbereich Physik der Technischen Universität Darmstadt zur Erlangung
des akademischen Grades eines Doktors der Naturwissenschaften (Dr. rer. nat.)
genehmigte Dissertation von Christopher Romig, M.Sc. aus Darmstadt

1. Gutachten: Prof. Dr. Dr. h.c. Norbert Pietralla

2. Gutachten: Prof. Dr. Joachim Enders

Tag der Einreichung: 14.10.2014

Tag der Prüfung: 24.11.2014

Erscheinungsjahr: 2015

Darmstadt – D 17

Abstract

In this work, a special application of the nuclear resonance fluorescence technique has been used and further advanced to study nuclear structure effects: so-called relative self-absorption experiments. They allow for the direct determination of ground-state transition widths of excited states, an important quantity for comparisons to model calculations, as well as the level width and the branching ratio to the ground state of individual states in a model-independent way. Two self-absorption measurements have been performed. On the one hand, the absolute excitation widths and the decay pattern of low-lying excited dipole states in the energy regime of the pygmy dipole resonance have been investigated in the nucleus ^{140}Ce . The results of the nuclear resonance fluorescence measurement, which is part of a self-absorption experiment, as well as of the actual self-absorption measurement are presented for 117 and 104 excited states of ^{140}Ce , respectively. They are compared to previous measurements and discussed with respect to the statistical model. On the other hand, a high-precision measurement of the self absorption of the $T = 1$, $J^\pi = 0^+$ level at an excitation energy of 3563 keV in ^6Li has been conducted. A precisely measured level width of this state can serve as a benchmark for modern ab-initio calculations.

Zusammenfassung

Im Rahmen der vorliegenden Arbeit wurde die Methode der relativen Selbstabsorption, die auf Kernresonanzfluoreszenzmessungen basiert, weiterentwickelt und zur Untersuchung von Kernstruktureffekten eingesetzt. Sie erlaubt es, Grundzustandsübergangsbreiten, eine essentielle Größe für den Vergleich mit Modellrechnungen, sowie natürliche Linienbreiten und Verzweigungsverhältnisse in den Grundzustand modellunabhängig für individuelle Zustände zu bestimmen. Insgesamt wurden zwei Selbstabsorptionsexperimente durchgeführt. Zum Einen wurden absolute Anregungsstärken und das Zerfallsverhalten

tiefliegender Dipolzustände im Anregungsbereich der Pygmy-Dipolresonanz im Kern ^{140}Ce untersucht. Die Ergebnisse der Kernresonanzfluoreszenzmessung, die ein Teil eines Selbstabsorptionsexperimentes ist, sowie jene der eigentlichen Selbstabsorptionsmessung werden für 117 bzw. 104 angeregte Zustände von ^{140}Ce vorgestellt. Sie werden mit früheren Messungen verglichen und im Rahmen des statistischen Modells diskutiert. Zum Anderen wurde eine Hochpräzisionsmessung der Selbstabsorption des $T = 1, J^\pi = 0_1^+$ Zustands von ^6Li bei einer Anregungsenergie von 3563 keV durchgeführt. Eine präzise Bestimmung der natürlichen Linienbreite dieses Zustands kann als Referenzwert für aktuelle ab-initio Rechnungen herangezogen werden.

Contents

1. Introduction	1
2. Motivation	7
2.1. Self-Absorption Method	7
2.2. Decay Pattern of ^{140}Ce	11
2.3. Lifetime Measurement in ^6Li	14
3. Low-Lying Electric Dipole Strength	19
4. Nuclear Resonance Fluorescence	25
4.1. Basic Principle	25
4.2. Measured Observables and Extracted Quantities	27
5. Relative Self Absorption	41
5.1. Basic Principle	41
5.2. Absorption and Attenuation Effects	43
5.3. Normalisation and Atomic Attenuation Correction - A new Approach	48
5.4. Determination of Self Absorption	50
5.4.1. Experimental Self Absorption	50
5.4.2. Calculation of Self Absorption	52
6. Experimental Setup	59
6.1. S-DALINAC	59
6.2. DHIPS	61
7. Direct Determination of Transition Widths of ^{140}Ce	65
7.1. The Measurements	65
7.2. The Classical NRF Measurement - Analysis	68
7.3. The Classical NRF Measurement - Results and Discussion	75

7.4. The RSA Measurement - Analysis	88
7.4.1. Determination of R_{exp}	88
7.4.2. Determination of Resulting Quantities	95
7.5. The RSA Measurement - Results	103
7.6. The Statistical Model	126
7.7. Conclusions	135
8. High-Precision Self-Absorption Measurement on ${}^6\text{Li}$	137
8.1. The Measurement	137
8.2. Self Absorption	139
8.3. Determination of the Level Width	147
8.4. Conclusions	153
9. Aspects of Relative Self-Absorption Measurements - A Conclusion	157
A. Spectra	163
B. Results of the NRF Measurement on ${}^{140}\text{Ce}$	171
C. Results of the RSA Measurement on ${}^{140}\text{Ce}$	187
Bibliography	199
List of Publications	209
List of Figures	211
List of Tables	215
Danksagung	217
Lebenslauf	221

1 Introduction

All along, mankind is driven by its curiosity and exploratory urge. From early human civilisations to the modern world, from childhood to old age, we strive after exploring our surroundings. One of the central questions plaguing mankind aims at the fundamental nature of matter. What is the world, what are we composed of?

The first surviving attempts to answer this question date back to Greek philosophers in the fourth century B.C. At this time, people had not much more than their own senses at their disposal to study the composition of matter. The philosophers were aiming to explain the complexity of different materials with fundamental building blocks. Empedocles, a pre-Socratic philosopher (~ 494 to 434 B.C.) was the very first one postulating that everything can be ascribed to the composition and interaction of only four “roots”, namely air, earth, fire, and water: *“But these (elements) are the same; and penetrating through each other they become one thing in one place and another in another, while ever they remain alike (i.e. the same).”*¹ These classical elements (Fig. 1.1) are conserved and changeless hinting already to modern concepts. At the same time, Leucippus and particularly his student Democritus (both ~ 460 to 370 B.C.), also Greek philosophers, followed a different approach: *“...by convention sweet and by convention bitter, by convention hot, by convention cold, by convention color; but in reality atoms and void”*.² They postulated that no material can be endlessly subdivided into smaller parts. At some point a limit is reached, a smallest particle that cannot further be assembled: the atom (from ἄτομος, atomos, ancient Greek for indivisible). In this context, different properties of materials, such as taste or colour, were ascribed to different forms and shapes of the corresponding atoms.

¹ Empedocles, from A. Fairbanks, *The first Philosophers of Greece* (London: K. Paul, Trench, Trübner & CO. Ltd., 1898)

² Democritus, from H. Diels and W. Kranz, *Die Fragmente der Vorsokratiker*, 6th edition, Berlin: Weidmann, 1951, trans. C.C.W. Taylor, *The Atomists: Leucippus and Democritus. Fragments, A Text and Translation with Commentary*, Toronto: University of Toronto Press, 1999

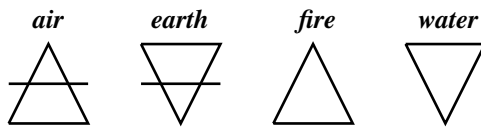


Figure 1.1.: Alchemical symbols of the four classical elements air, earth, fire, and water that were used until the 18th century.

It took many centuries before this theory, called atomism, was further studied and experimental scientists discovered chemical elements which, indeed, have different properties. In 1869, Mendelejew classified the by then known elements according to their properties in a periodic system of elements [Men69] which basically endures till nowadays (Fig. 1.2). From then on, scientists, exploiting more and more advanced technologies, tried to investigate atoms and, thus, the nature of matter, increasingly closer and the field of atomic physics was born even before Einstein finally proved the existence of atoms in 1905 with the explanation of Brownian motion [Ein05a]. However, at his time, new observations already indicated that atoms are not at all indivisible.

In 1896, Becquerel discovered radioactivity in Uranium [Bec96], a phenomenon that Marie and Pierre Curie further studied, identifying more radioactive substances in 1898 [Cur98]. One year earlier, in 1897, Thomson had discovered the electron [Tho97] - the first sub-atomic particle. Based on his discovery, he proposed that the neutral atom consists of a homogenous positively charged sphere in which negatively charged electrons are distributed (see Fig. 1.3) [Tho04]. This model was disproved in 1911 when Rutherford interpreted the famous α -scattering experiments on gold foils that Geiger and Marsden [Gei09] conducted under his leadership at the Physical Laboratories of the University of Manchester. From their observations he concluded that "*the atom consists of a central charge supposed concentrated at a point,...*" [Rut11]. This conclusion lead to Rutherford's atomic model: the positive charge as well as the main part of the atomic mass is concentrated in a, compared to the atom, very small nucleus (Fig. 1.3). Only a few years later, he discovered one of the building blocks of nuclei, showing that also nuclei can be divided into smaller parts. Irradiating nitrogen with α particles, he generated oxygen and a new kind of particle radiation which he called *proton* [Rut19]. However, the nucleus seemed to consist out of further constituents. Atomic

1	1 H	2 He
2	3 Li	4 Be
3	11 Na	12 Mg
4	19 K	20 Ca
5	37 Rb	38 Sr
6	55 Cs	56 Ba
7	87 Fr	88 Ra
	21 Sc	22 Ti
	39 Y	40 Zr
	72 Hf	73 Ta
	104 Rf	105 Db
	58 Ce	59 Pr
	89 Ac	90 Th
	23 V	41 Nb
	74 W	42 Mo
	106 Sg	107 Bh
	91 Pa	92 U
	25 Cr	43 Tc
	75 Re	44 Ru
	93 Np	94 Pu
	26 Mn	45 Rh
	76 Os	46 Pd
	95 Am	96 Cm
	27 Fe	47 Ag
	77 Ir	48 Cd
	97 Bk	98 Cf
	109 Pt	99 Es
	110 Hs	100 Fm
	111 Ds	101 Md
	112 Rg	102 No
	113 Ut	103 Lr
	114 Cn	115 Fl
	116 Lv	117 Uus
	118 Uuo	119 Lu
	50 Sn	51 Sb
	81 Tl	82 Pb
	83 Bi	84 Po
	115 Uup	116 Lv
	67 Ho	68 Er
	69 Tm	70 Yb
	71 Lu	
	half-metals	metalloids
	alkaline metals	non-metals
	alkaline earth metals	halogens
	lanthanides	nobel gases
	actinides	
	transition metals	

Figure 1.2.: The periodic system of elements. The elements are ordered according to their atomic number and divided into 18 groups corresponding to the columns and seven periods corresponding to the rows.

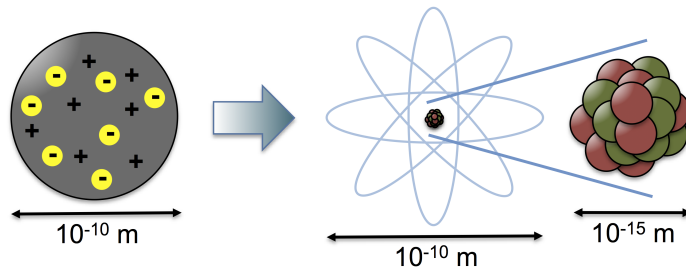


Figure 1.3.: In the Thomson model the atom is given by a homogenous positively charged sphere in which the electrons are distributed (left-hand side). Rutherford disproved this model and showed that the main part of the atomic mass as well as the positive charge is concentrated in the atomic nucleus (right-hand side). Being five orders of magnitude smaller as the actual atom, the nucleus is composed out of neutrons and protons and orbited by the electrons.

nuclei were found to have only half the charge number as was expected if they were completely composed out of positively charged protons [Bar11]. Thus, in 1920, Rutherford postulated the existence of a neutrally charged building block of nuclei which may explain this discrepancy [Rut20]. Indeed, in 1930, Bothe and Becker found a new strongly penetrating radiation when they irradiated light elements, such as lithium or boron, with α particles [Bot30]. However, they misinterpreted the radiation as a kind of γ radiation. Eventually, in 1932, Chadwick, one of Rutherford's students, disproved this interpretation and showed that the observed radiation consists of uncharged particles with a mass comparable to that of the proton [Cha32]. He named the new particle *neutron*.

Nowadays, we know that the two constituents of nuclei, protons and neutrons, are no fundamental particles either. They consist out of even smaller particles, the *quarks*, that do not only form nucleons but also many other particles subsumed as mesons and baryons. Nevertheless, with their discoveries and conclusions, the physicists in the early 20th century and in particular Ernest Rutherford shaped our nowadays view of atomic nuclei and laid the foundation for nuclear physics which is till today an important field of physics.

Nuclear structure physics treats the weak, strong, and electromagnetic interaction of nuclear systems. It aims at a consistent description of all nuclei throughout the nuclear chart - 254 stable and about 6000 unstable ones (see Fig. 1.4) - based on the just mentioned three of four fundamental forces. However, the interactions within nuclei are difficult to describe. On the one hand, nuclei are often too complex to model the complex interactions exactly. On the other hand, the number of nucleons that nuclei consist of (e.g., 208 for the heaviest stable nucleus ^{208}Pb) is much too small for a statistical approach. Thus, nowadays nuclear structure physics relies on many different models that often describe only selected characteristics of nuclei. Furthermore, they are often valid only in limited mass regions. However, within their range of applicability many models are already in very good agreement with experimental observations. The area of experimental nuclear structure physics provides observations and results that serve as foundation and benchmark of such models. Systematic studies of the properties of nuclei are used to test and improve models which on the other hand provide important input for the analysis of many experiments such that experiment and theory are driven by each other.

Beyond the fundamental understanding of nuclei and their characteristics, nuclear structure physics also have a strong impact on further research fields such as particle physics, radiation therapy or astrophysics. For instance, nuclear

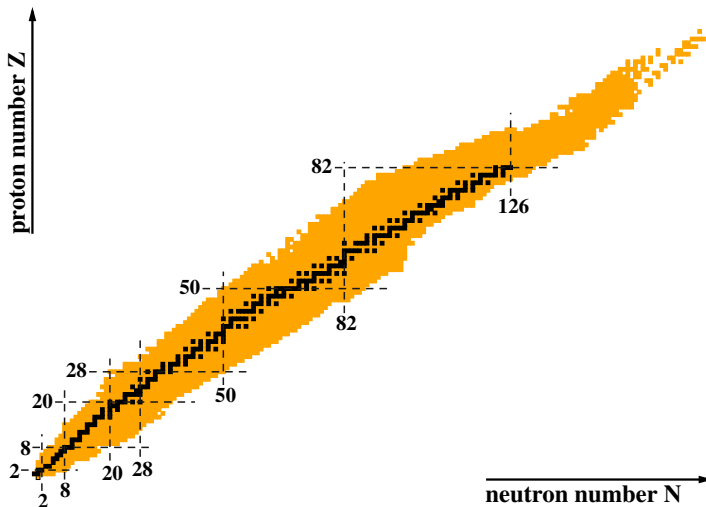


Figure 1.4.: Chart of nuclides containing the known isotopes. Stable nuclei are coloured in black. The numbers mark classical shell closures where nuclei are particularly well bound.

structure physics provides fundamental input for astrophysical calculations that aim to determine reaction rates during the nucleosynthesis and, thus, to answer another central question of mankind: where do we come from?

An ideally suited technique to study nuclei and their properties are scattering reactions in the tradition of Rutherford's α -scattering experiment. Objects of interest are irradiated with certain particles or they are themselves scattered off fixed targets. Observables like scattering intensities, the spatial distribution after and the energy loss during the scattering reaction allow for conclusions on the interaction and on the structure of the involved objects. Depending on the choice of the scattering particles or target and their characteristics, different properties of nuclear structure can be addressed with scattering experiments.

A well established method to study nuclear structure at low excitation energies is photon scattering which is also referred to as nuclear resonance fluorescence (NRF) [Met59, Kne96, Kne06]. The idea of nuclear resonance fluorescence experiments was already proposed in the late twenties by Kuhn: “*The*

question was put forward some time ago whether, corresponding to an emission of monochromatic γ -rays by atomic nuclei, there should also exist a selective absorption of these rays.” [Kuh29]. Supported by Rutherford and Chadwick, he conducted the first NRF experiment on the nucleus ^{208}Pb at Cavendish Laboratory. However, like other NRF measurements in the following years, he did not succeed since he did not consider the recoil energy of the nucleus. During the absorption and emission of a photon with energy E_γ , the nucleus experiences a recoil of $E_\gamma^2/2Mc^2$ (with M being the mass of the nucleus) in the opposite direction to account for conservation of energy and momentum. Thus, the energy of the emitted photon is lowered by that amount with respect to the resonance energy of the excited state and cannot be re-absorbed.

In 1951, Moon solved this problem by accelerating a radioactive gold foil (^{198}Au β decays to the 2_1^+ level of ^{198}Hg) on a centrifuge to such high velocities that the associated Doppler shift of the energy of the emitted photons compensates for the recoil loss. With this method, he determined the half-life of the 2_1^+ level of ^{198}Hg with astonishing precision to about 10^{-11} s [Moo51]. The current literature value amounts to $2.3 \cdot 10^{-11}$ s [CHU02].

With the advent of modern particle accelerators it became possible to perform NRF measurements exploiting continuous bremsstrahlung to avoid the recoil problem as it was proposed by Schiff in 1946 [Sch46]. The first successfull NRF experiment with bremsstrahlung was conducted by Hayward and Fuller in 1957 [Hay57]. They measured the self absorption of the $J^\pi = 1^+$, $T = 1$ level in ^{12}C at 15.1 MeV exploiting a 19 MeV bremsstrahlung beam from a betatron accelerator. However, it shall take another twenty years before NRF started to establish. The development of high-resolution γ -ray detectors in the late 1970s and not least the interest in the new scissors mode, which Richter discovered with an (e, e') measurement in 1983 [Ric83, Boh84], helped NRF to a breakthrough. Nowadays, also other phenomena of nuclear structure, such as the pygmy dipole resonance (PDR) [Sav13], which has been firstly observed via a NRF measurement by Herzberg and collaborators in ^{140}Ce [Her97], are typically studied by means of NRF making this measuring technique to a standard approach for nuclear structure investigations below the neutron-separation threshold.

2 Motivation

In the framework of this thesis, nuclear structure has been investigated exploiting the method of self absorption. In particular, experiments on the nuclei ${}^6\text{Li}$ and ${}^{140}\text{Ce}$ have been performed. For the isotope ${}^{140}\text{Ce}$, ground-state transition widths Γ_0 and branching ratios Γ_0/Γ to the ground state have been investigated for individual excited states particularly in the energy range of the pygmy dipole resonance. Furthermore, a high-precision self-absorption measurement has been performed on ${}^6\text{Li}$ aiming at the investigation of the level width of the strongly excited $J^\pi = 0^+$ state at an excitation energy of $E_i = 3563\text{ keV}$.

In this chapter, the choice of the method of self absorption will be discussed. Following this, the measurements on ${}^6\text{Li}$ and ${}^{140}\text{Ce}$ will be motivated.

2.1 Self-Absorption Method

Excited states of nuclei are characterised by only a small number of basic quantities. The resonance energy E_x describes how much energy has to be irradiated to the nucleus in its ground state to excite a particular higher-lying state. A nuclear state is further classified by its spin and parity quantum numbers J^π . Eventually, its lifetime τ indicates how long it takes before the nucleus decays from an excited state to lower-lying ones or back to the ground state. For isolated resonances the lifetime is related to the natural line width Γ via the expression $\Gamma \cdot \tau = \hbar$, with $\Gamma = \sum_i \Gamma_i$ being the sum of the partial transition widths Γ_i to lower-lying levels i . The ground-state transition width Γ_0 is of particular importance. It is a measure for the probability to excite a state from the ground state and is often expressed in terms of the reduced transition strength $B(\lambda L)$, with λ being the radiation character and L being the order of the multipole radiation. Reduced transition strengths can, *e.g.*, be extracted from microscopic model calculations. Hence, they are, next to E_x and J^π , ideally suited to compare theory and experiment.

This work addresses the investigation of low-lying nuclear states up to the neutron-separation threshold that can be excited by dipole transitions. Nuclear resonance fluorescence (NRF) measurements use high-energy photons

to probe nuclear structure. Due to the low momentum transfer of photons NRF is a standard approach to study low-lying dipole excited states. In NRF experiments the target of interest is irradiated with a γ -ray beam. The photons emitted during the decay of resonantly excited states are investigated by means of γ -ray spectroscopy. Exploiting the excellent energy resolution of semiconductor detectors of a few keV, NRF can even be applied at comparatively high level densities to investigate individual states. However, NRF is sensitive to the product of the ground-state transition width Γ_0 , accounting for the excitation, and the branching ratio Γ_0/Γ to the ground state which takes the decay into account. As a consequence, Γ_0 can only be determined provided that the branching ratio to the ground state is known. However, Γ_0/Γ is often not measured. In this case, appropriate assumptions of the size of the decay branch to the ground state have to be made. For example, $\Gamma_0/\Gamma \approx 1$ is usually assumed for excited states where no decay to other states than the ground state has been observed in the NRF measurement. Nevertheless, even though individual decay branches Γ_i to lower-lying excited states i may be small, this must not be true for their sum $\sum_{i \neq 0} \Gamma_i$. It is this sum which determines the size of the ground-state branching ratio:

$$\frac{\Gamma_0}{\Gamma} = \frac{\Gamma_0}{\Gamma_0 + \sum_{i \neq 0} \Gamma_i}. \quad (2.1)$$

An alternative approach to access Γ_0/Γ is represented by simulations of γ -ray cascades within the statistical model (see, e.g., Refs. [Sch08, Mas12, Sch13c]). However, with this statistical approach only averaged properties for certain energy bins can be extracted. It cannot be applied to isolated, individual states which actually is one of the advantages of NRF measurements. Furthermore, the results become model dependent since this analysing technique has to rely not only on the validity of the statistical model at excitation energies below the neutron-separation threshold, but also on a reasonable description of level density (LD) and photon-strength functions (PSFs).

A promising alternative opportunity to study reduced transition strengths is provided by inelastic proton scattering reactions [Tam09, Pol11, Tam11]. At extreme forward scattering angles, *i.e.*, angles close to and including zero degree, the cross section is dominated by Coulomb excitation resulting in $E1$ transitions and by nuclear $M1$ spin-flip transitions. To a lesser extent also higher multipole orders can occur. Applying background corrections and multipole-decomposition methods to the measured spectra, the contribution of electric

dipole excitations can be extracted. Eventually, the photon-absorption cross section and the $B(E1)$ -strength distribution for the excitation-energy range can be determined. In contrast to NRF measurements, inelastic proton scattering is not constrained by the neutron-separation threshold and can provide a complete measurement of the $B(E1)$ distribution up to excitation energies above the giant dipole resonance (GDR). However, the absolute extraction of reduced transition strengths is model dependent. Furthermore, the energy resolution of (p, p') measurements is about one order of magnitude worse than in NRF measurements. Consequently, (p, p') experiments can be applied to well separated individual states or to energy bins of about 30 keV only. An investigation of individual excited states in energy regions with rather high level density like it often occurs, *e.g.*, for the PDR, is not feasible by means of (p, p') reactions.

In contrast to (p, p') measurements, the technique of self absorption [Met56, Met59] allows for the investigation of reduced transition strengths in a model-independent way. Self-absorption experiments combine two measurements. The first one investigates the absorption process, the second one is a classical NRF measurement investigating the excitation process as well as the subsequent decay. Combining both measurements, the ground-state transition width Γ_0 , the total width Γ and also the branching ratio to the ground state Γ_0/Γ can be determined. Since two measurements have to be performed for one self-absorption experiment, self absorption is comparatively time consuming. However, this goes hand in hand with important advantages.

Being based on photon-scattering measurements, self absorption profits of advantages like the excellent energy resolution of semiconductor detectors as NRF does. Thus, it can be applied to study individual states. Furthermore, the knowledge of the actual photon-flux distribution is not required as long as it is identical in both measurements. Eventually, self-absorption experiments do not have to rely on calibration standards nor to suffer from their uncertainties. This fact allows for high-precision measurements exploiting self absorption. It is, *e.g.*, perfectly suited to improve the accuracy of calibration standards used in NRF experiments such as ^{11}B and ^{27}Al [Pie95]. Due to increasing statistics in the self-absorption signal, self-absorption measurements become more precise for excited states with large Γ_0 and Γ which are related to short lifetimes. Therefore, self absorption is also perfectly suited for indirect lifetime measurements in the range of 10^{-15} s and below. There, direct measurements like the Doppler shift attenuation method (DSAM), which works in the range

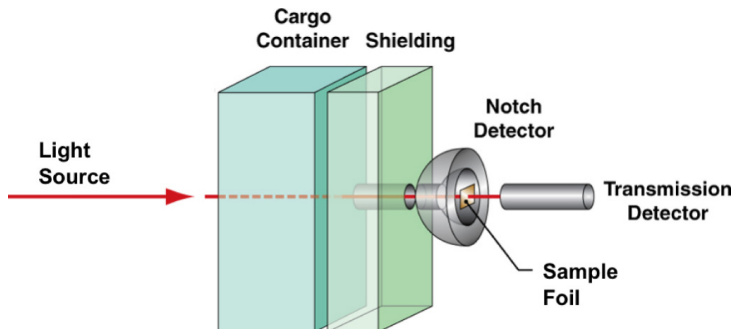


Figure 2.1.: The diagram shows a potential detection system to scan cargo containers for weapons or other hazardous substances. The container is irradiated with a γ -ray beam. A scattering target (here denoted as “notch detector”) made of the material that is looked for is used to analyse the transmitted beam. The transmission detector serves for normalisation.

Reprinted with permission from Ref. [Pru06]. Copyright 2006, AIP Publishing LLC.

of ~ 10 fs to 1 ps, are not feasible anymore. Details of lifetime measurements are reviewed in Ref. [Nol79].

In short, self absorption represents a powerful method to investigate reduced transition strengths, lifetimes and also decay properties of individual dipole excited states at the same time. However, the method of self absorption is not only of interest for nuclear structure investigations. As of recently, it also draws attention as a potential opportunity to scan cargo containers for weapons of mass destruction containing certain isotopes such as ^{235}U and ^{239}Pu , as well as for explosive and toxic substances in an efficient way [Ber05, Pru06]. Figure 2.1 shows a schematic detection system for such a scanning device. A container is irradiated with a γ -ray beam and the transmitted γ rays are analysed with a scattering target, here referred to as “notch detector”. It consists of the material the container is scanned for. Should the container enclose this material the beam intensity at typical resonance energies of corresponding isotopes will be reduced and so-called “notches” are generated in the transmission spectrum. Therefore, the number of photons scattered in the scatterer decreases with respect to the total transmitted intensity recorded via the transmission

detector. Such intensity differences will immediately be detected. In form of this application, self absorption provides a possibility to rapidly scan for hazardous materials with high precision, large throughput and low susceptibility to errors as needed for commercial institutions like sea- and airports.

2.2 Decay Pattern of ^{140}Ce

Exploiting the photon-scattering reaction to study nuclear structure, this work deals with the investigation of low-lying dipole-excited states. Here, low-lying means excited states up to the neutron-separation threshold S_N and, in particular, the energy region in the vicinity of S_N . In this region, multiple lower-lying levels open multiple decay channels for excited states. However, the decay cannot yet fully be described by statistical properties. Thus, complex decay patterns occur.

The pygmy dipole resonance (PDR) [Sav13] is an important phenomenon of nuclear structure which is typically observed in this energy range. It is a resonance-like concentration of states that can be excited by electric dipole transitions. Having strong impact on nuclear astrophysics (see, e.g., [Gor98]) and being related to properties of nuclear matter (see, e.g., [Bro00]), the PDR attracted a lot of attention in the last decade. However, neither its detailed structure nor its decay pattern is fully investigated, much less understood, yet.

Recently, Tonchev *et al.* [Ton10] demonstrated that measurements at the High Intensity $\vec{\gamma}$ -ray Source (HI $\vec{\gamma}$ S) [Wel09] offer an opportunity to study average decay properties of low-lying dipole states. They allow for the determination of the “elastic” cross section $\sigma_{\gamma\gamma}$ which accounts for direct decays of excited states back to the ground state. Additionally, also the “inelastic” cross section $\sigma_{\gamma\gamma'}$ can be determined. It takes the decay via intermediate states into account. The sum of both cross sections yields the absorption cross section $\sigma_\gamma = \sigma_{\gamma\gamma} + \sigma_{\gamma\gamma'}$. Hereupon, similar measurements have been performed on ^{142}Nd [Ang12], ^{60}Ni [Sch13a, Sch13b], ^{94}Mo [Rom13], and ^{130}Te [Isa13]. These experiments as well as the pioneering one of Tonchev *et al.* demonstrate that on average the decay via intermediate states cannot be neglected. In contrast, $\sigma_{\gamma\gamma'}$ makes up a significant part of the total absorption cross section $\sigma_\gamma = \sigma_{\gamma\gamma} + \sigma_{\gamma\gamma'}$. Figure 2.2 exemplarily shows the findings for the cross sections of ^{94}Mo from Ref. [Rom13]. They have been determined for five different energy settings at HI $\vec{\gamma}$ S. The inelastic cross section $\sigma_{\gamma\gamma'}$ (blue triangles) is of comparable order to $\sigma_{\gamma\gamma}$ (green circles). At about 7 MeV excitation energy

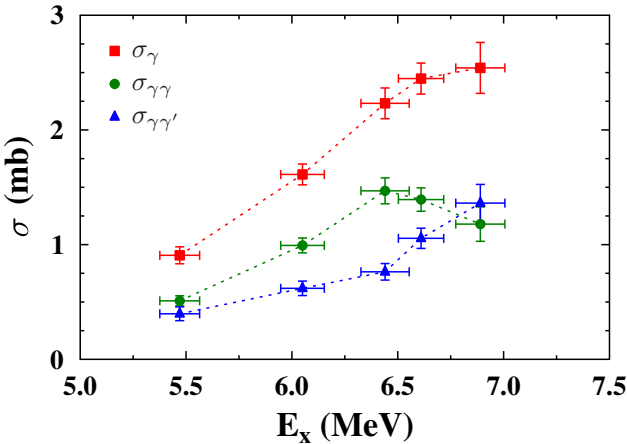


Figure 2.2.: Cross sections of ^{94}Mo from the measurements at HI γ S with five energy settings. The total cross section is marked with red squares, the elastic and inelastic ones with green circles and blue triangles, respectively. The figure has been taken from Ref. [Rom13].

$\sigma_{\gamma\gamma'}$ even exceeds $\sigma_{\gamma\gamma}$. This demonstrates the increasing influence of decays via intermediate states with increasing energy.

In combination of both quantities, the elastic and the inelastic cross section, also conclusions on the average decay pattern can be drawn. The average branching ratio $\langle b_0 \rangle$ to the ground state is defined via

$$\langle b_0 \rangle = \frac{\sigma_{\gamma\gamma}}{\sigma_{\gamma\gamma} + \sigma_{\gamma\gamma'}}. \quad (2.2)$$

Being independent from absolute numbers of the cross sections, this quantity is well suited for comparisons to simulations within the statistical model (see also Sec. 7.6). In Fig. 2.3 such a comparison is shown for ^{94}Mo [Rom13]. The red circles represent the experimentally determined results for $\langle b_0 \rangle$. The blue band and squares show the results of simulations of γ -ray cascades within the statistical model. They have been determined exploiting the DICEBOX code [Beč98] which was adapted to simulate NRF experiments (Sec. 7.6). The squares represent simulations with the real photon-flux distributions from the experiment. In contrast, the band shows results that were obtained with 200 keV wide bins

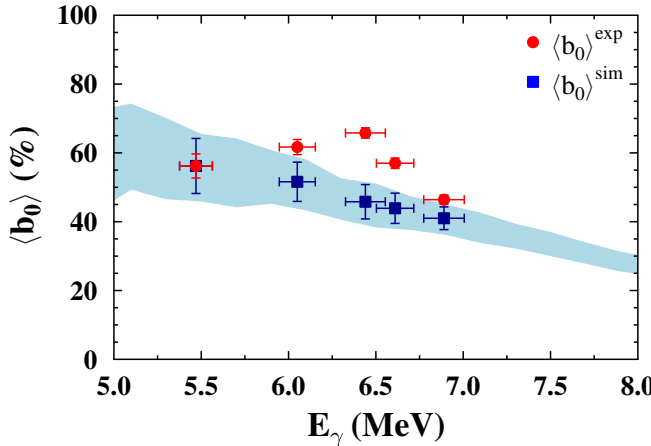


Figure 2.3.: Average branching ratio $\langle b_0 \rangle$ to the ground state of ^{94}Mo . The experimentally deduced data (red circles) stem from measurements at the HI7S facility. The blue coloured area as well as the blue squares depict results that have been extracted from simulations of γ -ray cascades.

of constant photon flux to demonstrate trends as a function of the energy. Details of the simulations and the used parametrisation of the photon-strength functions and the level density that are required to perform the simulations are given in Ref. [Rom13]. Figure 2.3 emphasises that the decay via intermediate states cannot be neglected. In the case of ^{94}Mo , the average branching ratio $\langle b_0 \rangle$ to the ground state accounts to values between 45 % and 65 %. As a consequence, up to 55 % of the decays occur via intermediate states. Moreover, it is demonstrated that the experimental findings cannot completely be described with simulations of γ -ray cascades. At least not, exploiting a simple, structureless Lorentz parametrisation for the photon-strength functions as has been done in the case of ^{94}Mo . Thus, the decay does not fully obey statistical properties. Further difficulties in reproducing the experimental findings for $\langle b_0 \rangle$ by means of the statistical model are reported in Refs. [Ang12, Isa13].

The observations of the measurements that have been performed at the HI7S facility illustrate the complexity of the decay pattern of dipole excited states particularly in the energy range in the vicinity of the neutron-separation

threshold. However, only averaged quantities are considered leaving open how individual excited states behave. Do strongly excited states contribute preferentially to $\sigma_{\gamma\gamma}$, $\sigma_{\gamma\gamma'}$ or in equal parts? How do weakly excited states contribute? And is there a dependence of the excitation strength or the excitation energy at all? These open questions demonstrate the importance of and the urgent need for model-independent experimental results for both, the ground-state transition width Γ_0 and the branching ratio Γ_0/Γ to the ground state, for individual states.

As has been pointed out in the previous section, self absorption is ideally suited to achieve these results. Therefore, in the framework of this thesis, the decay pattern of individual excited states in the energy region of the PDR is investigated for the first time applying the method of self absorption. The nuclide ^{140}Ce is a well-suited candidate to perform such a pioneering “proof of principle” measurement. It has already been investigated exploiting the method of nuclear resonance fluorescence [Vol06] and also via the $(\alpha, \alpha'\gamma)$ reaction [Sav06a]. These measurements showed that ^{140}Ce exhibits an accumulation of $B(E1)$ strength in the energy range between 5.5 MeV and 7.5 MeV. It has a resonance-like structure and is associated with the PDR. Being located at the major $N = 82$ shell closure, the level density of ^{140}Ce in this energy range is still small enough to make the analysis of individual states feasible. Furthermore, from a practical point of view, a lot of target material is required particularly for the thick absorbing target which is needed for self-absorption measurements. Due to the high natural abundance of ^{140}Ce of 88.48 %, this requirement can economically be covered with natural cerium.

2.3 Lifetime Measurement in ^6Li

Nowadays, properties of light nuclei can be calculated to a high precision within the framework of *ab-initio* methods. For stringent tests and for the definition of limits of the predicting power of these models precisely measured quantities for observables in light nuclei are mandatory. This need for high-precision measurements faces experimental nuclear structure physics with new challenges.

For example, Quantum Monte Carlo (QMC) calculations made rapid progress in the description of light nuclei and their properties during the last decade. The QMC approach is based on a combination of Variational Monte Carlo (VMC) and Green’s Function Monte Carlo (GFMC) calculations.

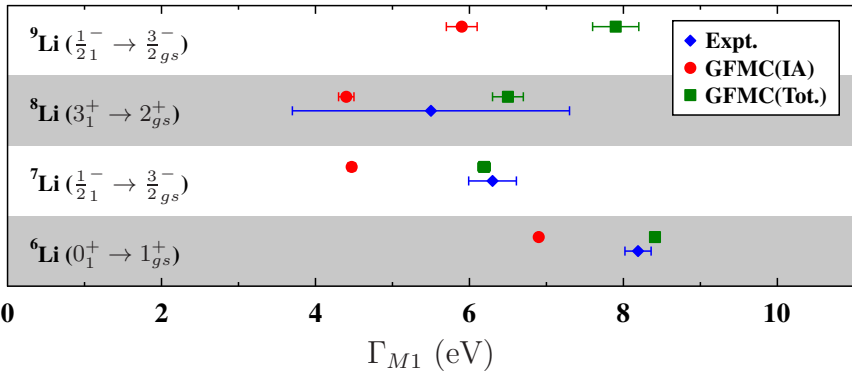


Figure 2.4.: Comparison of experimentally determined values for the lowest-lying $M1$ transition of the isotopes ${}^{6-9}\text{Li}$ with widths calculated in the QMC framework with (green squares) and without (red circles) taking two-body MECs into account. The experimental results are reported in Refs. [Til02, Til04]. The $M1$ transition width of ${}^9\text{Li}$ has not yet been measured. The QMC results were taken from Ref. [Pas13].

First, a trial wave function is determined using the VMC method. Afterwards, this wave function is further improved within a GFMC calculation. The QMC method has already been successfully applied to reproduce ground- and excited-state energies of light $A \leq 10$ nuclei for many years (see, e.g., Refs. [Pud95, Pie04]). Recently, the approach has been advanced to study also electromagnetic transitions. This new aim requires to calculate also off-diagonal matrix elements. Pervin and co-workers [Per07] performed such a calculation for the first time in the framework of GFMC. However, in particular the $M1$ transition strengths were underestimated. Only when the electromagnetic current operator included two-body meson-exchange currents (MEC) in addition to the standard one-body terms the agreement with experimental results was significantly improved [Mar08, Pas13].

Figure 2.4 shows a comparison of QMC and experimental results for the lowest-lying $M1$ transition of the lithium isotopes ${}^{6-9}\text{Li}$. The QMC values are reported in Ref. [Pas13]. On the one hand, they have been calculated

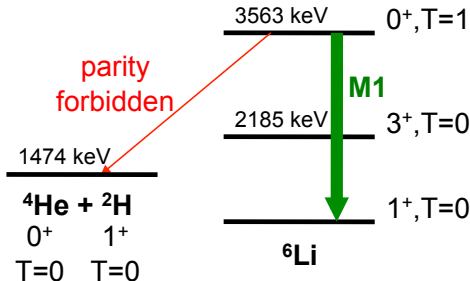


Figure 2.5.: Decay scheme of the first excited 0^+ level of ${}^6\text{Li}$. The decay via the α channel is parity forbidden and the excited state exhibits a strong $M1$ transition to the ground state.

including only the one-body component, which is also called impulse approximation (IA) operator. The corresponding results are represented by the red circles [GFMC(IA)]. On the other hand, two-body MEC terms have been added to the EM current operator. Those results are shown by the green squares [GFMC(Tot.)]. The two-body operator was constructed in the framework of chiral effective field theory. Further information can be found in Ref. [Pas13]. Statistical uncertainties in the calculations are indicated by the error bars. The experimental values are given by blue diamonds. They are taken from Refs. [Til02, Til04] whereby the lowest-lying $M1$ transition width in ${}^9\text{Li}$ is not yet measured. The two-body MECs contribute significantly to the $M1$ transition widths and improve the agreement with the measured values particularly for ${}^6\text{Li}$ and ${}^7\text{Li}$. For further, highly sensitive tests of the contribution of chiral currents to the $M1$ strength the experimentally determined transition widths have to be improved.

Therefore, the second aim of this work is a high-precision measurement of the lifetime or the level width of the $J^\pi = 0^+_1$ state of ${}^6\text{Li}$, respectively. This state with isospin $T = 1$ at an excitation energy of $E_i = 3563\text{ keV}$ is of particular interest. It decays predominantly via γ -ray emission, whereas all excited states in lighter nuclei with $A \leq 5$ are particle unbound. Figure 2.5 shows the corresponding part of the decay scheme of ${}^6\text{Li}$. In principle, also the 3563 keV level of ${}^6\text{Li}$ is particle unbound. However, its decay to an α particle and a deuteron is parity forbidden. According to the expression

$$|J_i - J_f| \leq L \leq J_i + J_f, \quad (2.3)$$

the α decay of the $J_i^\pi = 0^+$ level of ${}^6\text{Li}$ into the $J_f^\pi = 1^+$ ground state of the deuteron requires that the α particle with $J_\alpha^\pi = 0^+$ carries an angular momentum of $L = 1$. In this case, the α particles parity quantum number is $\pi_\alpha \cdot (-1)^L = +1 \cdot (-1) = -1$. Thus, the parity quantum number of the initial state would not be conserved; the α decay is parity forbidden. An upper limit of the α decay width was determined to $\Gamma_\alpha \leq 6.5 \cdot 10^{-7}$ eV [Rob84]. In contrast, the 3563 keV level exhibits a strong $M1$ transition to the $J^\pi = 1^+$ ground state with $\Gamma_{M1} = (8.19 \pm 0.17)$ eV [Til02] corresponding to a lifetime of $\tau = (80.4 \pm 1.6) \cdot 10^{-18}$ s. Such a short lifetime can only be measured indirectly via the absolute transition width according to $\tau = \hbar/\Gamma$.

The $M1$ transition width of the 0_1^+ level was already studied in various experiments, mainly inelastic electron-scattering and self-absorption measurements. Figure 2.6 summarises the previous measurements. The corresponding references are listed in the caption. Although the three most recent measurements are in good agreement, earlier measurements found significantly different values for the $M1$ transition width. Nevertheless, the literature value $\Gamma_{M1} = (8.19 \pm 0.17)$ eV, which is represented by the grey line, was determined as mean value of the three most recent measurements (two (e, e') [Eig69, Ber75] and one self-absorption [Ras69] measurement) resulting in a small relative uncertainty of about 2.1 % [Til02]. The most precise individual measurement is an (e, e') experiment from 1975 reported in Ref. [Ber75] yielding $\Gamma_{M1} = (8.16 \pm 0.19)$ eV with a relative uncertainty of 2.3 %. However, transition widths extracted from inelastic electron-scattering experiments are model dependent. They are determined by calculating the corresponding form factor and extrapolating it to the photon point. In contrast, self-absorption measurements do not depend on input from models. In 1969 Rasmussen and Swann [Ras69] performed the most precise self-absorption measurement on ${}^6\text{Li}$ up to now. It results in $\Gamma_{M1} = (8.1 \pm 0.5)$ eV with 6.2 % relative uncertainty. Within the framework of this thesis, the self-absorption technique has further been advanced. Exploiting the improvements of the method as well as modern semiconductor γ -ray detectors, the intention of this work is to push the relative uncertainty to less than 1 %.

In the following, an overview of low-lying electric dipole strength will be given. Furthermore, the methods of nuclear resonance fluorescence as well as self absorption will be explained and discussed in detail. In a further chapter, the bremsstrahlung measuring site at TU Darmstadt will be presented.

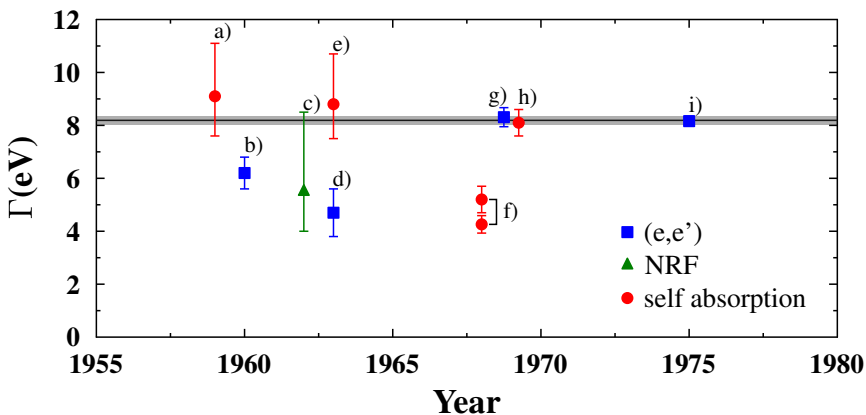


Figure 2.6.: Overview of previous results for the $M1$ transition width of the 0_1^+ level of ${}^6\text{Li}$. Data are taken from a) Ref. [Coh59], b) Ref. [Bar60], c) Ref. [Boo62], d) Ref. [Bar63], e) Ref. [Sko63], f) Ref. [Cre68], g) Ref. [Eig69], h) Ref. [Ras69], and i) Ref. [Ber75]. In Ref. [Cre68] (f) two self-absorption measurements with different targets are reported. Therefore, two results are shown. The grey bar represents the current literature value [Til02], the average of the three most recent measurements which are g, h, and i.

Subsequently, the analysis and the results of both measurements as well as difficulties, tripping hazards, and improvements of self-absorption measurements and the analysis procedure will be discussed. Eventually, this work will conclude with a brief summary and an outlook to future measurements and projects.

3 Low-Lying Electric Dipole Strength

This thesis deals with the investigation of low-lying dipole-excitation strength in atomic nuclei. In the case of the measurement on ^{140}Ce , mainly dipole states excited via electric dipole transitions are investigated. Such excited states can occur due to different phenomena of nuclear structure. Typically, the electric dipole-strength distribution of spherical even-even nuclei up to about 25 MeV is composed of three phenomena: the two-phonon state below 5 MeV excitation energy, the pygmy dipole resonance in the vicinity of the neutron separation threshold S_N , and the giant dipole resonance above S_N . Figure 3.1 shows an overview of a generic $E1$ -strength distribution.

At low excitation energies a strong, isolated electric dipole excitation is observed in many nuclei. It is attributed to the coupling of a quadrupole and an octupole phonon ($2_1^+ \otimes 3_1^-$) resulting in a quintuplet of states (see, e.g., Refs. [Lip66, Vog71, Her95b, Kne06]). The two-phonon 1^- member of this quintuplet occurs typically at the sum of the excitation energies of the 2_1^+ and 3_1^- levels below ~ 5 MeV [And01].

Above the neutron separation threshold the isovector giant dipole resonance (IVGDR) [Har01] is situated which dominates the electric part of the nuclear dipole response. It exhausts about 100 % of the Thomas-Reiche-Kuhn (TRK) sum rule for isovector electric dipole transitions [Gre96]. First observations of enhanced photo-dissociation cross sections have already been made in 1937 [Bot37] by Bothe and Gentner. In 1944, Migdal associated these observations with a dipole oscillation of the neutrons against the protons in the nuclei [Mig44]. This approach has further been advanced in a hydrodynamical picture where the IVGDR is attributed to an out-of-phase oscillation of the neutron against the proton fluid [Gol48, Ste50], which still is the common macroscopic description of the phenomenon of the IVGDR. From the experimental point of view, the IVGDR has been well studied in various measurements, especially with the (γ, n) reaction since the early 1970's. Hence, nowadays macroscopic properties like the mean excitation energy or the width of the resonance are well known [Har01].

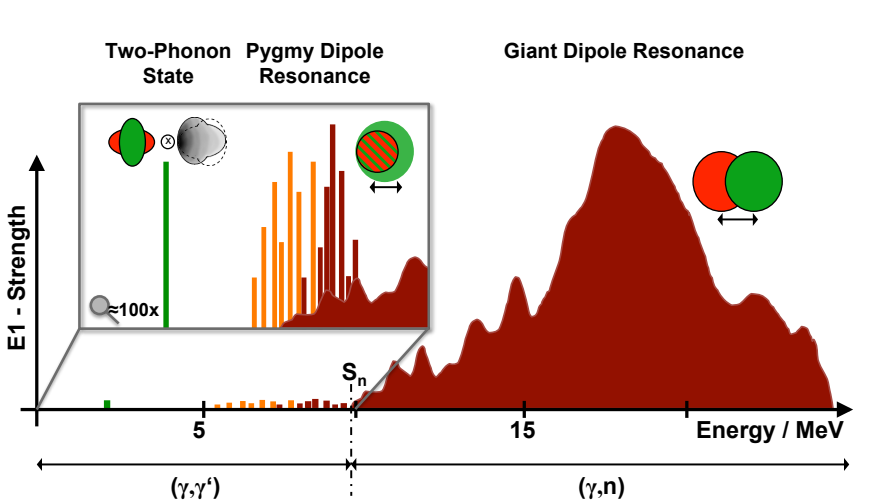


Figure 3.1.: Schematic illustration of the generic $E1$ -strength distribution of spherical even-even nuclei. It is dominated by the giant dipole resonance exhausting up to 100 % of the Thomas-Reiche-Kuhn sum rule. The pygmy dipole resonance is located in the vicinity of S_N . It splits up into two components, one being associated with the low-energy tail of the giant dipole resonance and the other one with a neutron-skin oscillation. Below ~ 5 MeV excitation energy, the two-phonon state is observed. More details can be found in the text.

In-between these two phenomena, a concentrated enhancement of electric dipole strength is reported for many nuclei, in particular for nuclei close to and at major shell closures. This low-lying dipole strength often exhibits a resonance-like structure and, thus, is commonly referred to as pygmy dipole resonance (PDR) [Sav13]. An enhancement of γ -ray strength in the vicinity of S_N was already observed about five decades ago when Bartholomew and co-workers studied the γ decay of nuclei with low ground-state spin following thermal neutron capture [Bar61]. A few years later, the enhanced strength was denoted as “*pigmy resonance*” [Brz69, Bar73] emphasising that its strength is only in the order of 1 % of the IVGDR. The nature of the PDR is still highly debated. Nevertheless, it is often described in the geometrical picture of an out-of-phase oscillation of the isospin saturated $N = Z$ core against a neutron

skin generated by the excess neutrons. Although the PDR makes up a rather small part of the electric dipole response, it exhibits fundamental character.

On the one hand, it has an impact on nuclear astrophysics and particularly on the nucleosynthesis. About 50 % of all elements heavier than iron, which occur in nature, originate from the rapid neutron-capture process. This so-called r-process is believed to take place in astrophysical scenarios with comparatively high neutron densities. Thus, very neutron rich nuclei can be formed. The capture rates of those nuclei can affect the abundances of nuclei synthesised via the r-process [Gor98]. In turn, the capture rates themselves are sensitive to low-lying dipole strength in the vicinity of S_N . In particular, an enhancement of neutron-capture rates due to the PDR has been observed [Gor98, Gor04]. Since extremely neutron-rich nuclei far off the valley of stability cannot be studied experimentally, the capture rates have to be modelled. For reliable model calculations, systematic experimental input on low-lying dipole strength and a deep understanding of its nature is required.

On the other hand, only recently the PDR's sensitivity to properties of nuclear matter has been shown. Being associated with a neutron-skin oscillation, the PDR should depend on the neutron-skin thickness $R_n - R_p$ [Fur02]. Here, R_n and R_p are the mean radii of the nuclear neutron and proton bodies, respectively. Indeed, a theoretical study of tin isotopes exploiting the relativistic random-phase approximation approach revealed a correlation between $R_n - R_p$ and the PDR for the $A \leq 120$ Sn isotopes [Pie06]. Furthermore, the neutron-skin thicknesses of ^{68}Ni , ^{132}Sn , and ^{208}Pb have been determined applying experimental results for the PDR [Kli07, Tam11, Ros13]. The neutron-skin thickness is sensitive to fundamental quantities such as the equation of state (EOS) of neutron matter [Bro00]. An improved knowledge of the neutron EOS will provide new insight to properties of neutron stars such as their solid crusts, their radii, and their cooling mechanisms [Hor01a, Hor01b, Hor02].

These examples demonstrate that a deep understanding of the PDR and its nature is mandatory. Therefore, a lot of effort from both, theoretical and experimental side, has been made to study this phenomenon.

In the last two decades, the PDR was mainly investigated exploiting NRF which is ideally suited to study low-lying dipole strength (see Sec. 2.1 and Ch. 4). Throughout the nuclear chart, systematic studies found an enhancement of dipole strength in the vicinity of S_N in many nuclei, particularly in those located at major shell closures. It was observed, *e.g.*, in the stable Ca isotopes [Har04, Isa11], for ^{52}Cr [Pai13] as well as for the stable

Ni [Bau00, Sch13a, Sch13b], Ge [Jun95], Mo [Rus09, Erh10, Rom13], Sn [Gov98, Öze07], and Pb isotopes [Rye02, End03]. Furthermore, enhanced strength was reported for the $N = 50$ isotones ^{86}Kr [Sch13c], ^{88}Sr [Sch07], ^{89}Y [Ben09], and ^{90}Zr [Sch08], for the open shell nucleus ^{136}Ba [Mas12] and the stable $N = 82$ isotones [Zil02, Vol06, Sav08, Sav11]. A complete overview can be found in Ref. [Sav13]. These investigations indicate that, in general, the integrated strength increases with increasing mass number exhausting up to about 1 % of the TRK sum rule.

More recently, also other methods have been applied to study the PDR. The investigation of very neutron-rich unstable nuclei became feasible with Coulomb excitation experiments in inverse kinematics. With this method, low-lying dipole strength was studied in the medium mass isotopes $^{129-132}\text{Sn}$ and $^{133,134}\text{Sb}$ [Adr05, Kli07], as well as in the lower mass region in ^{68}Ni [Wie09, Ros13]. The results yield up to one order of magnitude more strength in the vicinity of S_N than in less neutron-rich nuclei. This fact supports the interpretation of the PDR as a neutron-skin oscillation.

Besides investigations exploiting photons to probe nuclear structure also complementary probes can be used. As an isoscalar, hadronic probe, the α particle mainly interacts via the strong interaction with nuclei. In principle, states with different multipolarity can be excited. However, exploiting the $(\alpha, \alpha'\gamma)$ reaction mainly electric dipole transitions are selected [Sav06b]. The $(\alpha, \alpha'\gamma)$ reaction was applied to different nuclei in the past revealing a splitting of the PDR [Sav06a, End09, Der13]. The first part is located at lower energies. It is excited in both, $(\alpha, \alpha'\gamma)$ and NRF reactions. The second part at higher energies is only excited by photons. Although the splitting is not yet fully understood, calculations showed that both components have a different underlying structure. The low-energy component has isoscalar character and can be attributed to neutron-skin oscillations. In contrast, the component at higher energies exhibits isovector character. It may be attributed to the IVGDR [End10, Lan14].

Very recently, first studies with the (p, p') reaction [Tam09] have been performed with respect to the PDR. In contrast to other approaches like NRF, the (p, p') reaction allows for studies of the full strength. It is not constrained by particle-separation thresholds. A pioneering measurement on ^{208}Pb [Tam11, Pol11] demonstrated the potential of this new approach. The measurement of the complete dipole response of ^{208}Pb allowed for the determination of the dipole polarisability and the related neutron-skin thickness [Tam11].

A more complete and detailed review on the different experimental approaches to study the PDR was published by Savran *et al.* [Sav13]. Theoretical approaches to describe and investigate the PDR were recently reviewed by Paar *et al.* [Paa07].



4 Nuclear Resonance Fluorescence

In the past decades, the method of nuclear resonance fluorescence (NRF) [Met59, Kne96, Kne06] has been established as a standard approach to study low-lying dipole strength distributions up to the particle-separation threshold. NRF measurements yield information on various characteristic quantities describing properties of excited nuclear states. Basically, they allow for the determination of excitation and γ -ray energies, spin and parity quantum numbers, decay branches, and integrated cross sections.

In this chapter, the basic principle of nuclear resonance fluorescence experiments will be presented. Furthermore, the access to the just mentioned observables will be elucidated.

4.1 Basic Principle

In nuclear resonance fluorescence measurements the material of interest is irradiated with γ quanta. These high-energetic photons hit the target nuclei and, depending on the corresponding cross section, which describes the probability for resonant absorption, may be absorbed (see also Sec. 4.2). With the absorption of a photon the nucleus is excited from the ground state to a higher-lying state. After a short period of time, which is typically in the order of a few femtoseconds, the excited state decays back to the ground state accompanied by the emission of one or more photons. The radiated photons are detected and analysed with respect to their energy, intensity and angular distribution to determine the above mentioned quantities. Due to the recoil during the absorption and emission processes the emitted photons are shifted by twice the recoil energy of the nucleus and, thus, cannot be re-absorbed by other nuclei.

The NRF process, *i.e.*, the resonant absorption and subsequent emission of a photon (Fig. 4.1), is often denoted as *photon scattering*, although the photons are not scattered in the classical sense. Analogous to classical scattering experiments, the direct decay to the ground state is denoted as *elastic* photon scattering, whereas *inelastic* scattering represents the decay via intermediate lower-lying excited states. In general, NRF measurements are constrained to

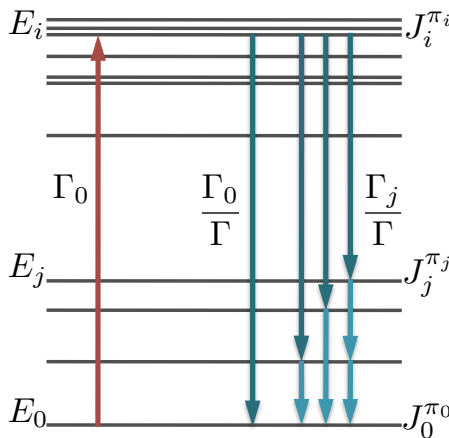


Figure 4.1.: Schematic diagram of the NRF process. A nucleus is excited from its ground state to a higher-lying state and subsequently decays either directly or via intermediate states back to the ground state. The absorption is related to the ground-state transition width Γ_0 , whereas the decay is related to the branching ratio of the corresponding decay channel.

the energy region below the neutron separation threshold. At higher energies the γ decay is strongly suppressed in favour of the emission of a neutron.

Electromagnetic radiation occurring during the transitions between nuclear states can be characterised in terms of two quantities. These are the order L of multipole radiation and the radiation character λ . The order of multipole radiation depends on the spin quantum numbers J_i and J_f of the initial and final states, respectively. It cannot exceed the limits of the following inequality:

$$|J_i - J_f| \leq L \leq (J_i + J_f). \quad (4.1)$$

The radiation character distinguishes *electric* (E) and *magnetic* (M) radiation depending on the multipole order of the radiation and the parity quantum numbers π_i and π_f of the involved states. The relation

$$\pi_i = (-1)^L \cdot \pi_f \quad (4.2)$$

corresponds to electric radiation, that is usually shortly denoted as *EL* radiation, whereas magnetic radiation (*ML*) occurs when the expression

$$\pi_i = (-1)^{L+1} \cdot \pi_f \quad (4.3)$$

holds. Being massless particles, photons typically transfer negligible momenta. Thus, with NRF mainly *E1* and *M1* transitions and to a lesser extent *E2* transitions are induced.

If a transition exhibits only one particular order of multipole radiation, it is denoted as pure transition. Typically, this is the case for ground-state transitions in even-even nuclei (ground-state spin $J_0^\pi = 0^+$). During mixed transitions, *e.g.*, to other states or to a ground-state with $J_0^\pi \neq 0^+$, various multipole radiation orders occur. The fractions of particular multipole orders to a transition are described with the mixing ratio

$$\delta_{i \rightarrow j} = \frac{\langle J_i | M(L+1) | J_j \rangle}{\langle J_i | M(L) | J_j \rangle}, \quad (4.4)$$

which is defined via the transition matrix elements *M*.

4.2 Measured Observables and Extracted Quantities

The photons emitted during the de-excitation of excited states are detected via γ -ray detectors. Registered events are recorded in spectra and often occurring energies sum up as peaks. In NRF measurements basically two quantities are measured - the position of the peaks in the recorded spectra and the corresponding peak area. The peak position is related to the energy of the detected photon and, thus, to the transition energy. The peak area is a measure for the number of photons registered at a particular transition energy and, therefore, for the probability that such a transition occurs. Additional information can be gained from the angular distribution of the scattered photons. Usually, for this purpose, it is sufficient to measure at least at two different, subtle chosen angles.

These pieces of information, implying also knowledge of the detector efficiencies, as well as the photon-flux distribution, allow for the determination of various quantities describing excited states of nuclei. These quantities, as well as the corresponding relations to the measured observables are discussed in the following paragraphs.

Level and Transition Energies

For the determination of transition and level energies, which are extracted from the recorded spectra, those have to be calibrated. An energy calibration can be done exploiting known transitions either of a calibration standard which is measured together with the actual target or of a radioactive source which was measured directly before or after the actual measurement. In the case of a calibration standard which is measured together with the actual target, the Doppler shift due to the recoil of the nucleus during the absorption and emission of a photon has to be taken into account. After the excitation of a level with energy E_i from the ground state, the photon emitted during the subsequent ground-state decay carries an energy of

$$E_\gamma = \frac{Mc^2}{1 - 2 \cos \vartheta} \cdot \left(\sqrt{1 + \frac{2E_i}{Mc^2} \cdot (1 - 2 \cos \vartheta)} - 1 \right), \quad (4.5)$$

where M is the mass of the nucleus and ϑ is the angle between the incident and outgoing photon. These ground-state transition energies are then used to calibrate a spectrum. With this calibration, the peak positions corresponding to previously unknown transitions can be translated into transition energies. For the case that such a transition is unambiguously identified as a ground-state transition, the level energy of the excited state can be determined by rewriting Eq. (4.5) as

$$E_i = E_\gamma \cdot \left(1 + \frac{E_\gamma}{2Mc^2} \cdot (1 - 2 \cos \vartheta) \right). \quad (4.6)$$

Spin Quantum Numbers

The emission of a photon during the decay of an excited state follows an angular distribution $W_{i \rightarrow j \rightarrow k}$. It depends on the spin quantum numbers of the initial state i , the excited state j , and the final state k . Following the definition by Krane and Steffen [Kra70], it is given by

$$W_{i \rightarrow j \rightarrow k}(\vartheta) = \sum_{\nu=\text{even}} A_\nu^-(\gamma_{i \rightarrow j}) A_\nu^+(\gamma_{j \rightarrow k}) P_\nu(\cos \vartheta), \quad (4.7)$$

with P_ν being a Legendre polynomial and ϑ the angle between incident and outgoing photon. In NRF measurements, ϑ is measured with respect to the beam axis. With no axis settled, *i.e.*, with no fixed reference frame, like it is the case for radioactive sources, the angular distributions appear to be isotropic.

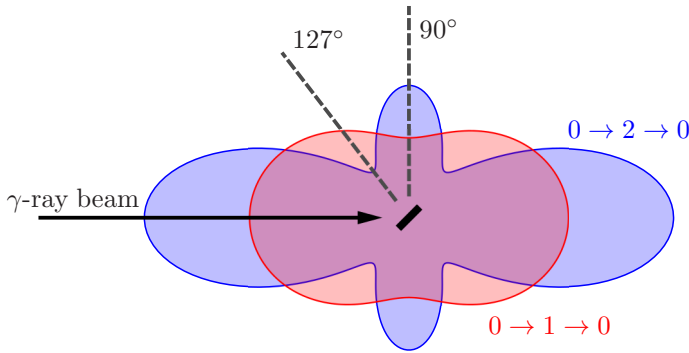


Figure 4.2.: Angular distributions corresponding to $0 \rightarrow 1 \rightarrow 0$ and $0 \rightarrow 2 \rightarrow 0$ spin sequences. Simultaneous measurements at both, 90° and 127° , allow to decide whether a level with $J = 1$ or with $J = 2$ was excited.

The coefficients A_v^- and A_v^+ are related to so-called F_v coefficients and the mixing ratio $\delta_{x \rightarrow y}$ from Eq. (4.4) [Kra70]:

$$A_v^\pm(\gamma_{x \rightarrow y}) = \left[1 + \delta_{x \rightarrow y}^2 \right]^{-1} \cdot \left[F_v(L_{x \rightarrow y} L_{x \rightarrow y} J_x J_y) \right. \\ \left. \pm 2\delta_{x \rightarrow y} \cdot F_v(L_{x \rightarrow y} L'_{x \rightarrow y} J_x J_y) + \delta_{x \rightarrow y}^2 \cdot F_v(L'_{x \rightarrow y} L'_{x \rightarrow y} J_x J_y) \right]. \quad (4.8)$$

A compilation of F_v coefficients for different combinations of L , L' , J_x , and J_y can, *e.g.*, be found in Ref. [Fra65]. The angular distributions for a $0 \rightarrow 1 \rightarrow 0$ and a $0 \rightarrow 2 \rightarrow 0$ spin sequence, as they occur in NRF measurements on even-even nuclei, are exemplarily shown in Fig. 4.2. To distinguish between these two angular distributions, it is sufficient to measure at two different angles ϑ_1 and ϑ_2 that are chosen such that the ratio

$$w = \frac{W(\vartheta_1)}{W(\vartheta_2)} \quad (4.9)$$

differs significantly for both cases. In the case of the $0 \rightarrow 1 \rightarrow 0$ and $0 \rightarrow 2 \rightarrow 0$ spin sequences, typically angles of $\vartheta_1 = 90^\circ$ and $\vartheta_2 = 127^\circ$ are chosen

resulting in $w_{0 \rightarrow 1 \rightarrow 0} = 0.71$ and $w_{0 \rightarrow 2 \rightarrow 0} = 2.26$. These numbers are compared to experimental values that can be determined via

$$w_{\text{exp}} = \frac{A_{\vartheta_1}/\varepsilon_{\vartheta_1}}{A_{\vartheta_2}/\varepsilon_{\vartheta_2}} \quad (4.10)$$

with the peak area A_{ϑ} measured at a specific angle ϑ and the absolute detector efficiency ε_{ϑ} at this angle.

In the case of odd-mass nuclei, the angular distributions are far less pronounced and differ only slightly from isotropic distributions. Thus, the ratio w is close to one and unambiguous assignments of spin quantum numbers are only feasible with high statistics resulting in small uncertainties of w_{exp} .

Parity Quantum Numbers

The measurement of parity quantum numbers with NRF requires information on the polarisation of either the incident or the outgoing (scattered) photon. The polarisation of the scattered photon can be determined exploiting Compton polarimetry. However, this method suffers from the low analysing power of Compton polarimeters. The analysing power Σ is a measure for the sensitivity of a quantity to the polarisation. In the case of Compton polarimetry, it is determined exploiting the Compton scattering cross section $\frac{d\sigma}{d\Omega}$ for polarised photons via

$$\Sigma = \frac{\frac{d\sigma}{d\Omega}(\vartheta, \varphi = 0^\circ) - \frac{d\sigma}{d\Omega}(\vartheta, \varphi = 90^\circ)}{\frac{d\sigma}{d\Omega}(\vartheta, \varphi = 0^\circ) + \frac{d\sigma}{d\Omega}(\vartheta, \varphi = 90^\circ)}. \quad (4.11)$$

At energies above ~ 4 MeV, the Compton scattering cross section significantly decreases in favour of the pair production cross section which starts to dominate the photon interaction requiring longer measuring times at these energies. Furthermore, the analysing power becomes less distinct at these energies making Compton polarimetry increasingly unfeasible. Nevertheless, only recently, modern polarimeters with high photo-peak efficiency and high granularity together with long measuring times made Compton polarimetry applicable at energies well above 4 MeV [Hut02, Büs08, Ali12].

Exploiting polarised γ -ray beams in the entrance channel is a much simpler yet more subtle way to determine parity quantum numbers. Doing so, they can be obtained in comparatively simple intensity measurements [Pie01]. For polarised γ radiation in the entrance channel, the analysing power is determined

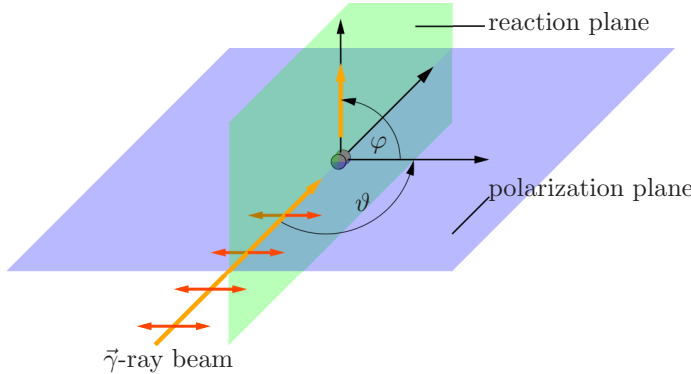


Figure 4.3.: The polarisation plane (blue) is formed by the beam propagation vector and the electric field vector, which defines the polarisation of the beam. In this plane, the scattering angle between incident and scattered photon is given by the polar angle ϑ , whereas φ is the azimuthal angle between the polarisation and the reaction plane (green). The latter is spanned by the incident and the scattered photon.

with respect to the angular distribution W of the scattered photons. Hence, it is given by

$$\Sigma = \frac{W(\vartheta, 0^\circ) - W(\vartheta, 90^\circ)}{W(\vartheta, 0^\circ) + W(\vartheta, 90^\circ)}. \quad (4.12)$$

Regarding an even-even nucleus, the angular distribution $W(\vartheta, \varphi)$ describing the electromagnetic decay following the excitation of a state with $J^\pi = 1^\pm$ via the absorption of a linearly polarised photon $\vec{\gamma}$ according to a $0^+ \xrightarrow{\vec{\gamma}} 1^\pm \xrightarrow{\gamma} 0^+$ spin sequence is represented by [Fag59]

$$W(\vartheta, \varphi) = 1 + \frac{1}{4} \left[(3 \cdot \cos^2 \vartheta - 1) + \pi \cdot 3 \cdot \cos 2\varphi (1 - \cos^2 \vartheta) \right]. \quad (4.13)$$

Here, π represents the sign of the excited state's parity quantum number. The quantity ϑ denotes the polar scattering angle with respect to the incident photons, whereas φ describes the azimuthal angle between the reaction plane and the polarisation plane of the incident photons. The relations between these angles and planes are illustrated in Fig. 4.3. The angular distribution exhibits

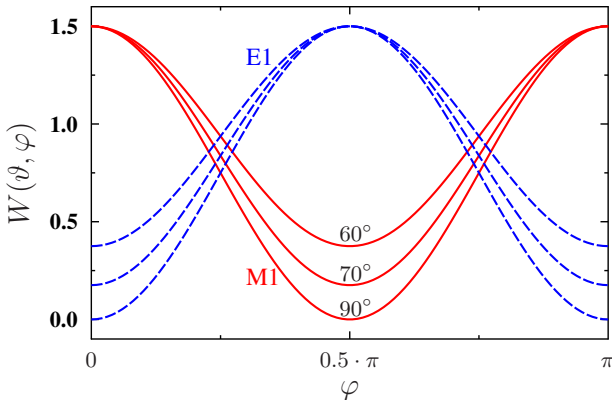


Figure 4.4.: Azimuthal angular distributions for electromagnetic decay radiation after excitation of a dipole state via the absorption of polarised photons according to Eq. (4.13) for different polar angles ϑ . At $\vartheta = \pi/2$, the distributions for electric and magnetic radiation differ the most.

maxima at $\varphi = m \cdot \pi$ and minima at $\varphi = m \cdot \pi/2$ in the case of electric ($E1$, $\pi = -1$) radiation and vice versa minima at $\varphi = m \cdot \pi$ and maxima at $\varphi = m \cdot \pi/2$ in the case of magnetic radiation ($M1$, $\pi = +1$) with $m \in \mathbb{Z}$ (see Fig. 4.4). The difference between the angular distributions for electric and magnetic radiation and, thus, also the analysing power become maximal at $\vartheta = \pi/2$ [Pie01]. At this angle, the analysing power Σ is given by $\Sigma = -1$ for electric and $\Sigma = +1$ for magnetic transitions, respectively. Therefore, the measurement of Σ allows for an unambiguous assignment of the parity quantum number to dipole excited states. However, Σ is defined for point-like scattering targets and detectors. In the experiment, it is diminished by the experimental sensitivity q . Taking a value between zero and one, the experimental sensitivity accounts for the finite size of the scattering target and the finite solid angles of the detectors. The product of the analysing power and the experimental sensitivity, the so-called experimental asymmetry

$$\epsilon = q \cdot \Sigma = \frac{N_{\parallel} - N_{\perp}}{N_{\parallel} + N_{\perp}} \quad (4.14)$$

is experimentally accessible. It can be obtained by simple intensity measurements at two different angles. In this equation, N_{\parallel} and N_{\perp} denote the efficiency-corrected peak areas recorded in and perpendicular to the polarisation plane, respectively. Since, basically, only positive and negative asymmetries have to be distinguished, even comparatively small statistics are sufficient for unambiguous parity assignments. Hence, rather short measurements or experiments with small amounts of target material are still feasible.

Decay Branches

Figure 4.1 emphasises that an excited state can decay either directly back to the ground state or via intermediate states. NRF measurements allow for the determination of the corresponding decay branches to lower-lying excited states. Taking possible different angular distributions into account, it is solely related to the efficiency-corrected intensity of photons corresponding to the decay to the ground state and an intermediate state j , respectively, and can be obtained via

$$\frac{\Gamma_j}{\Gamma_0} = \frac{A_{0 \rightarrow i \rightarrow j}}{A_{0 \rightarrow i \rightarrow 0}} \cdot \frac{\varepsilon(E_i) \cdot W_{0 \rightarrow i \rightarrow 0}}{\varepsilon(E_i - E_j) \cdot W_{0 \rightarrow i \rightarrow j}}. \quad (4.15)$$

However, in NRF measurements, especially with continuous bremsstrahlung, various states are excited simultaneously. Therefore, it becomes difficult to distinguish ground-state transitions from decays to intermediate states. Furthermore, decays to intermediate states are often rather weak such that the corresponding peaks in the spectra cannot be observed within the experimental sensitivity. In particular, the low-energy background appearing in experiments exploiting bremsstrahlung leads to a rather low sensitivity to decay branches to more highly excited states.

These problems may be circumvented by exploiting quasi-monochromatic γ -ray beams as they are provided, *e.g.*, by the High Intensity $\vec{\gamma}$ -Ray Source (HI $\vec{\gamma}$ S) [Wel09]. There, the spectral γ -ray distribution has a nearly Gaussian shape with a width of about 3 % of the chosen mean beam energy. Consequently, states are excited only in a narrow energy range. Usually, in particular for even-even nuclei, the excitation energy of the first excited state of the investigated isotope is large compared to the spread of the beam of about 200 keV to 300 keV. In this case, peaks appearing within the narrow excitation-energy range can be unambiguously ascribed to ground-state transitions. In turn, peaks below the excitation range can be ascribed to transitions from higher to lower-lying levels if they do not correspond to natu-

ral background radiation. This selectivity allows for the investigation of the average decay pattern of excited states as it has been performed, *e.g.*, in Refs. [Ton10, Ang12, Isa13, Rom13, Sch13a, Sch13b]. If, as an example, the decay of the first excited 2^+ level is observed although it was not excited by the incident photon beam, it must be populated by higher-lying levels. Assuming, that all states which do not decay directly back to the ground state, decay either directly or via intermediate states to the 2_1^+ level, the decay intensity of the 2_1^+ state can be exploited to estimate the “inelastic” cross section $\sigma_{\gamma\gamma'}$. This cross section describes the average probability for decays to lower-lying excited states for the levels within the energy range covered by the incident beam. Since the peak intensities observed within the excitation range can be attributed to ground-state transitions, they can be used to extract also the “elastic” cross section $\sigma_{\gamma\gamma}$. However, it should be noted that this cross section does not account for unresolved strength due to too high level density. Both cross sections taken together provide access to an average branching ratio

$$\langle b_0 \rangle = \frac{\sigma_{\gamma\gamma}}{\sigma_{\gamma\gamma} + \sigma_{\gamma\gamma'}} \quad (4.16)$$

to the ground state.

Furthermore, in measurements with quasi-monochromatic photon beams, the background radiation is significantly reduced with respect to measurements with bremsstrahlung. Therefore, the experimental sensitivity is larger and also smaller individual branching ratios to lower-lying states can be determined. Nevertheless, non-resonant background stemming from atomic processes occurring in the scattering target remains a problem. This problem can be solved by performing $\gamma - \gamma$ coincidence experiments. By measuring two photons of a γ cascade in coincidence, non-resonant background is suppressed to a minimum. This procedure allows for the determination of very small branching ratios. Recently, the high-efficiency γ -ray spectroscopy γ^3 setup [Löh13, Löh14] has been established at HI γ S for this purpose.

Cross Section

In general, cross sections describe the probability that two particles interact with each other in a particular way. For NRF measurements, the absorption cross section $\sigma_{0 \rightarrow i}(E)$ plays a central role. It describes the probability that a photon with energy E is resonantly absorbed from a nucleus in its ground state corresponding to the excitation of a higher-lying state i with resonance energy

E_i . The absorption cross section of an isolated resonance can be expressed in terms of a Breit-Wigner distribution [Bre36]:

$$\sigma_{0 \rightarrow i}(E) = \frac{\pi}{2} \cdot \left(\frac{\hbar c}{E_i} \right)^2 \cdot \underbrace{\frac{2J_i + 1}{2J_0 + 1}}_g \cdot \frac{\Gamma_0 \Gamma}{(E - E_i)^2 + \Gamma^2/4} = \frac{\sigma_{\max}}{1 + \left(\frac{E - E_i}{\Gamma/2} \right)^2}. \quad (4.17)$$

Here, Γ_0 and Γ denote the ground-state transition width and the total level width, respectively. The spin factor g takes the number of magnetic substates of the excited and the ground state into account and depends on the spin quantum numbers J_0 and J_i of the ground and the excited state. At the resonance energy E_i , the cross section

$$\sigma_{0 \rightarrow i}(E_i) = 2\pi \cdot g \cdot \left(\frac{\hbar c}{E_i} \right)^2 \cdot \frac{\Gamma_0}{\Gamma} \equiv \sigma_{\max} \quad (4.18)$$

becomes maximal.

Equation (4.17) holds for nuclei in rest only. Due to the thermal motion of the target nuclei and quantum-mechanical lattice vibrations the cross section becomes wider in the laboratory frame. The resulting broadened resonance can be described with the Doppler broadened absorption cross section $\sigma_{0 \rightarrow i}^D$, which will be deduced in the following. The depiction follows that in Refs. [Met59, Pie93].

The velocities of the nuclei corresponding to thermal motion are assumed in an ideal gas-approximation to be Maxwellian distributed. Thus, the probability $w(v_{\parallel})$ for a velocity component v_{\parallel} in or against the photon's direction of motion is given by

$$w(v_{\parallel}) d v_{\parallel} = \sqrt{\frac{M}{2\pi k_B T}} \cdot e^{-\frac{M v_{\parallel}^2}{2k_B T}} d v_{\parallel}, \quad (4.19)$$

with the mass M of the nucleus, the Boltzmann constant k_B , and the absolute temperature T of the investigated target. For a nucleus moving with a particular velocity v_{\parallel} in the laboratory frame towards an incident photon with energy E_{γ}^{lab} , the photon's energy is shifted to

$$E_{\gamma}^{\text{nucl}} = \frac{1 + v_{\parallel}/c}{\sqrt{1 - (v_{\parallel}/c)^2}} \cdot E_{\gamma}^{\text{lab}} \stackrel{v_{\parallel} \ll c}{\approx} \left(1 + \frac{v_{\parallel}}{c} \right) \cdot E_{\gamma}^{\text{lab}} \quad (4.20)$$

in the nucleus' rest frame. Conversely, for the laboratory frame the shifted resonance energy E_i^{lab} can be obtained via retransformation of the last relation:

$$E_i^{\text{lab}} \approx \left(1 - \frac{v_{\parallel}}{c}\right) E_i^{\text{nucl}}. \quad (4.21)$$

This shift of the resonance energy has to be taken into account when, for the determination of the Doppler broadened absorption cross section $\sigma_{0 \rightarrow i}^D(E)$, the Breit-Wigner distribution is averaged over all possible velocities of the nuclei:

$$\sigma_{0 \rightarrow i}^D(E) = \int_{-\infty}^{\infty} \sigma_{0 \rightarrow i}(E, E_i^{\text{nucl}} \rightarrow E_i^{\text{lab}}(v_{\parallel})) \cdot w(v_{\parallel}) d v_{\parallel}. \quad (4.22)$$

Introducing the so-called Doppler width

$$\Delta = \sqrt{\frac{2k_B T}{Mc^2}} \cdot E_i \quad (4.23)$$

and three further abbreviating quantities

$$x = \frac{E - E_i^{\text{nucl}}}{\Gamma/2}, \quad y = \frac{E - E_i^{\text{lab}}}{\Gamma/2}, \quad t = \left(\frac{\Delta}{\Gamma}\right)^2, \quad (4.24)$$

the integral can compactly be rewritten as

$$\sigma_{0 \rightarrow i}^D(E) = \frac{\sigma_{\text{max}}}{2\sqrt{t \cdot \pi}} \cdot \int_{-\infty}^{\infty} \frac{e^{-\frac{(y-x)^2}{4t}}}{1+y^2} dy. \quad (4.25)$$

This integral can, in general, not be solved analytically. Only in the limiting case of very small transition widths Γ with respect to the Doppler width Δ , *i.e.*, $\Gamma \ll \Delta$, an analytical solution can be determined, which results in the Doppler cross section

$$\tilde{\sigma}_{0 \rightarrow i}^D(E) \equiv \frac{\sigma_{\text{max}} \cdot \sqrt{\pi}}{2\sqrt{t}} \cdot e^{-\left(\frac{E-E_i}{\Delta}\right)^2} \underset{\Gamma/\Delta \ll 1}{\approx} \sigma_{0 \rightarrow i}^D(E). \quad (4.26)$$

Eventually, for solid targets, the temperature T in the Doppler width Δ has to be replaced with an effective temperature T_{eff} which accounts for vibrational

degrees of freedom in the lattice of the target material. It is related to the Debye temperature T_D via

$$T_{\text{eff}} = 3T \cdot \left(\frac{T}{T_D} \right)^3 \int_0^{T_D/T} t^3 \cdot \left(\frac{1}{e^t + 1} + \frac{1}{2} \right) dt. \quad (4.27)$$

The effective temperature T_{eff} is always higher than the thermodynamical temperature T and approaches it asymptotically at high T .

Figure 4.5 illustrates the discussed absorption cross sections for a generic state at $E_i = 5$ MeV of ^{140}Ce . On the left-hand side, they have been calculated with $\Gamma = \Gamma_0 = 0.5$ eV, on the right-hand side with $\Gamma = \Gamma_0 = 1.5$ eV. The Doppler width accounted to $\Delta = 3.3$ eV in both cases. The Breit-Wigner cross section is sharp and pronounced. Its full width at half maximum (FWHM) is given by the total level width Γ . As has been pointed out in this section, the Doppler broadened and the Doppler cross section are significantly wider as the Breit-Wigner cross section. For $\Gamma = 0.5$ eV both, $\sigma_{0 \rightarrow i}^D(E)$ and $\tilde{\sigma}_{0 \rightarrow i}^D(E)$, agree well with each other. However, with the larger $\Gamma = 1.5$ eV the condition $\Gamma \ll \Delta$ is not fulfilled anymore. The Doppler cross section significantly deviates from the Doppler broadened cross section in the vicinity of E_i .

Although the shape of the three discussed cross sections is different, the integrated cross section for the absorption of a photon and the corresponding excitation of a particular state does not change. It is expressed in terms of the integrated cross section

$$\begin{aligned} I_{0 \rightarrow i} &= \int_{-\infty}^{\infty} \sigma_{0 \rightarrow i}(E) dE = \int_{-\infty}^{\infty} \sigma_{0 \rightarrow i}^D(E) dE = \int_{-\infty}^{\infty} \tilde{\sigma}_{0 \rightarrow i}^D(E) dE \\ &= \pi^2 \cdot \left(\frac{\hbar c}{E_i} \right)^2 \cdot g \cdot \Gamma_0 \end{aligned} \quad (4.28)$$

for photo absorption and depends on the excitation energy E_i , the spin factor g and the ground-state transition width Γ_0 , only.

Up to now, solely, the absorption cross section was discussed. However, in NRF the resonant *absorption* of a photon, as well as the subsequent electromagnetic *decay* have to be considered. Commonly, several decay channels are available for the de-excitation of an excited state. The probability for the decay via one of these channels can be expressed by the branching ratio Γ_j/Γ , where

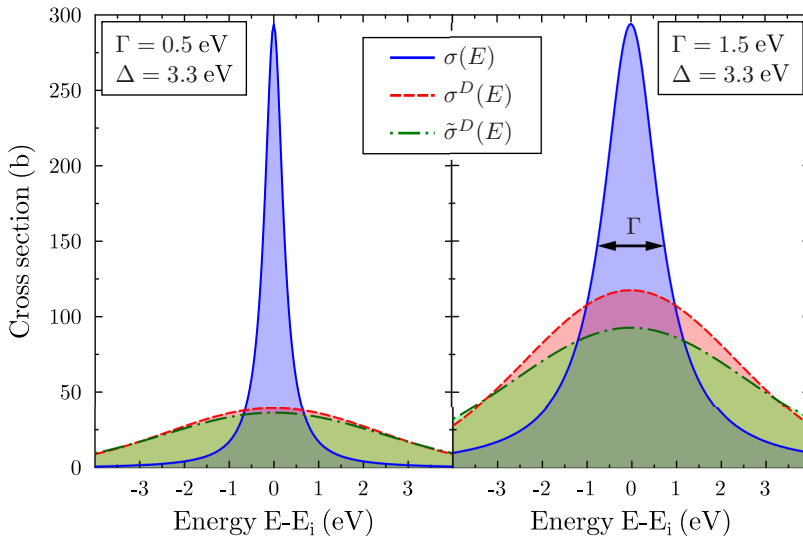


Figure 4.5.: Comparison of absorption cross sections for a generic excited state of ^{140}Ce at $E_j = 5 \text{ MeV}$. The ground-state and total transition widths were set to $\Gamma = \Gamma_0 = 0.5 \text{ eV}$ (left-hand side) and $\Gamma = \Gamma_0 = 1.5 \text{ eV}$ (right-hand side), respectively. The Breit-Wigner cross section $\sigma(E)$ (blue) is pronounced and sharp, whereas the cross sections which take Doppler broadening into account are significantly wider. The Doppler cross section $\tilde{\sigma}^D(E)$ (green) is a good description of the exact solution $\sigma^D(E)$ (red) for $\Gamma \ll \Delta$. In the case of $\Gamma = 1.5 \text{ eV}$ ($\Gamma/\Delta = 0.68$) the agreement is already rather bad.

Γ_j denotes the transition width to a final state j . The NRF cross section is obtained by multiplying the absorption cross section with the corresponding branching ratio. Thus, the NRF cross section is always smaller than or equal to the absorption cross section. The integrated cross section for the NRF process corresponding to the excitation of a state i from the ground state and the subsequent decay to a state j is given by

$$I_{0 \rightarrow i \rightarrow j} = \pi^2 \cdot \left(\frac{\hbar c}{E_i} \right)^2 \cdot g \cdot \Gamma_0 \cdot \frac{\Gamma_j}{\Gamma}. \quad (4.29)$$

Summing up the integrated cross section over all possible decay channels again gives the absorption cross section from Eq. (4.28).

The integrated cross section $I_{0 \rightarrow i \rightarrow j}$ can directly be determined from NRF measurements. In general, the corresponding measured peak area $A_{0 \rightarrow i \rightarrow j}$ can be written as

$$A_{0 \rightarrow i \rightarrow j} = N_T \cdot \varepsilon(E_i - E_j) \cdot W_{0 \rightarrow i \rightarrow j}^{\text{eff}}(\vartheta) \cdot \int dE \cdot N_\gamma(E) \cdot \sigma_{0 \rightarrow i}^D(E) \cdot \frac{\Gamma_j}{\Gamma}. \quad (4.30)$$

Here, N_T denotes the number of target nuclei, $\varepsilon(E_i - E_j)$ describes the absolute efficiency of the γ -ray detector to register a photon with energy $E_i - E_j$, $W_{0 \rightarrow i \rightarrow j}^{\text{eff}}(\vartheta)$ is the effective angular distribution accounting for the finite opening angle of the detector, and Γ_j/Γ accounts for the branching ratio to the final state j . The product of the photon-flux distribution $N_\gamma(E)$ and the Doppler broadened cross section $\sigma_{0 \rightarrow i}^D(E)$ has to be integrated over the energy. However, the cross section deviates only in a narrow energy range of a few eV from zero. Within this narrow region, the photon-flux can be assumed to be constant if the photon-flux distribution is sufficiently broad. This is usually the case for photons stemming from bremsstrahlung or Compton-backscattering processes. In this case,

$$\int dE \cdot N_\gamma(E) \cdot \sigma_{0 \rightarrow i}^D(E) \cdot \frac{\Gamma_j}{\Gamma} = N_\gamma(E_i) \cdot \int dE \cdot \sigma_{0 \rightarrow i}^D(E) \cdot \frac{\Gamma_j}{\Gamma} = N_\gamma(E_i) \cdot I_{0 \rightarrow i \rightarrow j} \quad (4.31)$$

holds and the peak area

$$A_{0 \rightarrow i \rightarrow j} = I_{0 \rightarrow i \rightarrow j} \cdot N_T \cdot \varepsilon(E_i - E_j) \cdot N_\gamma(E_i) \cdot W_{0 \rightarrow i \rightarrow j}^{\text{eff}}(\vartheta). \quad (4.32)$$

becomes directly related to the integrated cross section $I_{0 \rightarrow i \rightarrow j}$. As will be discussed in the next chapter, the above made assumption of the photon flux being constant in the vicinity of the resonance energy does not hold in the case of self-absorption measurements. In that case, the integral must be evaluated for the product of the photon flux and the cross section.

In short, with knowledge of the efficiency, the photon flux and the number of target nuclei, the measured peak areas and the corresponding intensities of photons scattered in the target allows for the determination of the integrated NRF cross section $I_{0 \rightarrow i \rightarrow j}$. Eventually, the NRF cross section is related to transition widths and strengths that will be discussed in the following.

Lifetime, Transition Width, and Transition Strength

The total transition or level width Γ has already been mentioned in the previous sections. For an isolated excited state, it is directly related to its lifetime τ via

$$\tau \cdot \Gamma = \hbar. \quad (4.33)$$

The lifetime indicates the average time which a nucleus in a particular excited state needs to decay to a lower-lying state. Typically, a number of decay channels is available and the level width

$$\Gamma = \sum_j \Gamma_j \quad (4.34)$$

is given by the sum of the corresponding partial widths Γ_j to lower-lying states j .

In general, the ground-state transition width Γ_0 is of particular interest. It is proportional to the reduced transition probability which is often also simply called transition strength $B(\lambda L)$:

$$\Gamma_0 = 8\pi \sum_{\lambda L} \left(\frac{E_\gamma}{\hbar c} \right)^{2L+1} \frac{(L+1)}{L [(2L+1)!!]} \cdot \frac{1}{g} \cdot B(\lambda L)^\uparrow. \quad (4.35)$$

The determination of transition strengths allows not only for easy comparisons between different nuclei. They are also often calculated in modern microscopic calculations such as within the quasi-particle phonon model (QPM) [Sol92] and, thus, also allow for direct comparisons to those models. For the absorption and decay process the corresponding transition strengths $B(\lambda L)^\uparrow$ and $B(\lambda L)^\downarrow$ differ by the spin factor g via

$$B(\lambda L)^\uparrow = g \cdot B(\lambda L)^\downarrow. \quad (4.36)$$

However, as has been depicted in the previous section, NRF measurements are sensitive to the integrated cross section which is, in turn, proportional to the product of the ground-state transition width Γ_0 and the branching ratio Γ_j/Γ to an arbitrary final state j [see Eq. (4.29)]. Consequently, Γ_0 and, hence, the reduced transition probability can only be determined in the case that this particular branching ratio is known or, equivalent to this condition, that all decay branches to other states are observed or already known.

Alternatively, a more sophisticated approach to determine Γ_0 directly is provided by the method of self absorption. This method will be discussed in the next chapter.

5 Relative Self Absorption

The central aspect of this thesis is the method of self absorption. First reports on this previously well-established approach backdate to the 1950's (see, e.g., Refs. [Met56, Met59]). Originally, self-absorption measurements were developed with regard to the, at that time, often unknown shape of the photon-flux distributions used for photon-scattering experiments. Without information on the photon-flux distribution, it is not possible to determine level widths of excited states. In contrast, self absorption allows for the determination of level widths without knowing the shape of the incident photon spectrum. However, when bremsstrahlung started to establish as photon source for photon-scattering experiments, NRF measurements relative to calibration standards became available which are less time consuming and require less effort as self-absorption measurements. Thus, nowadays self absorption is rather seldom used, mostly for calibration of photon-flux standards [Pie95].

In the scope of this work, the method of *relative* self absorption (RSA) has been developed. A new normalisation technique is applied which reduces the experimental effort and systematic uncertainties of self-absorption measurements. Thus, investigations of the decay pattern of low-lying dipole strength and high-precision lifetime measurements exploiting the method of self absorption become feasible.

In this chapter, the idea behind and the basic principle of RSA will be elucidated. The newly developed approach and the determination of the self absorption from experiments as well as from calculations exploiting the well-known absorption cross section will be discussed. Both, the experimental and the calculated self absorption are required to eventually determine quantities such as the ground-state transition width Γ_0 or the total width Γ .

5.1 Basic Principle

Although the methods of NRF and RSA are very similar - RSA is even based on NRF measurements - they approach the photo-absorption process from different sides. As has been pointed out in the previous chapter, in NRF measure-

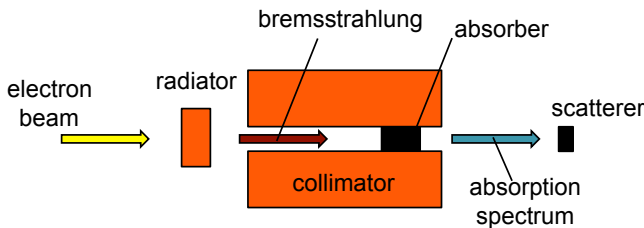


Figure 5.1.: An absorption target is irradiated with bremsstrahlung photons that were produced by stopping an electron beam in a radiator target. The resulting absorption spectrum is analysed in self-absorption measurements exploiting a scatterer made of the same material as the absorber.

ments the electromagnetic decay after the absorption of a photon via a nucleus is investigated. Usually, for the de-excitation of an excited state, except for the first excited state, various decay channels are available (see also Fig. 4.1). As a consequence, NRF measurements on the decay to the ground state are sensitive to the product $\Gamma_0 \cdot \Gamma_0/\Gamma$ of the ground-state transition width and the branching ratio to the ground state.

In contrast, the basic idea of self-absorption measurements is the investigation of the absorption process which is unambiguous and independent of the decay behaviour. For this purpose, γ radiation is transmitted through an absorption target composed of the material to be investigated. Figure 5.1 shows a corresponding principle scheme of a self-absorption setup where bremsstrahlung is used as source for γ rays. In the absorber, nuclei are resonantly excited to higher-lying states. When they decay back to the ground state, the decay radiation is distributed in all directions according to the particular angular distribution. Furthermore, the energy of the photons is slightly shifted due to the recoil of the nucleus. As a result, an absorption spectrum occurs which has absorption lines at exactly the resonance energies of the absorption target material. The distinctness of those absorption lines varies with the ground-state transition width Γ_0 , with the level width Γ , and with the absorber thickness. Thus, it allows for the determination of Γ_0 and Γ . However, being at maximum only a few eV wide, the absorption lines are very narrow and cannot be measured directly exploiting, e.g., a γ -ray detector. Instead, a scattering target, which is made of the same material as the absorber, is used

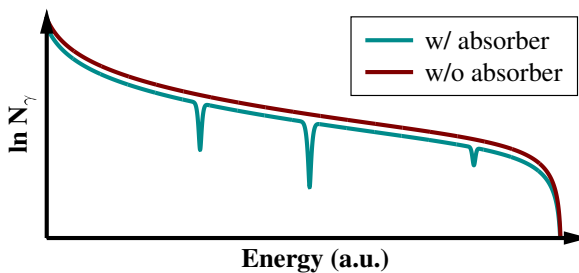


Figure 5.2.: Schematic illustration of spectral bremsstrahlung distributions before and after transmission through an absorption target.

as *high-resolution detector* for the absorption lines. The number of NRF reactions in the scatterer decreases for more pronounced absorption lines since less photon flux is available for absorption processes at the resonance energies. Consequently, the self absorption is defined as the decrease of NRF reactions in the scattering target due to resonant absorption. For the determination of the decrease of NRF reactions, a second measurement is required which serves as a reference for the self-absorption measurement. It defines how many NRF reactions occur when no absorption target is put into the beam line. Eventually, the decrease of NRF reactions in the scatterer for the measurement with absorber is determined with respect to the reference measurement without absorber.

5.2 Absorption and Attenuation Effects

Figure 5.2 schematically illustrates a typical absorption spectrum (turquoise) when bremsstrahlung (red) has passed through an absorber. The changes in the absorption spectrum with respect to the former bremsstrahlung distribution can be ascribed to two basic attenuation processes. On the one hand, *resonant absorption* produces pronounced absorption lines in the photon-flux distribution only at the resonance energies. On the other hand, *atomic attenuation* results in a smooth decrease of the photon flux over the entire energy range. The attenuation processes are discussed in the following.

Resonant Absorption

Resonant absorption, *i.e.*, the absorption of a photon by a nucleus corresponding to the excitation of an excited state, can be described with the

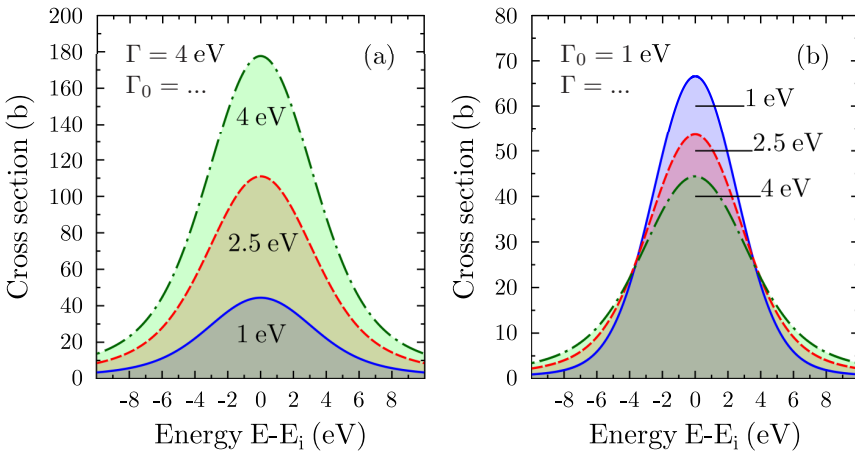


Figure 5.3.: The Doppler broadened cross section (Eq. (4.25)) for different combinations of Γ_0 and Γ . On the left-hand side (a), the total width Γ is fixed, on the right-hand side (b), Γ_0 has a constant value. The ground-state transition width Γ_0 influences the amplitude of the cross section, whereas different values of Γ result in different widths of the cross section curve.

Doppler broadened cross section $\sigma_{0 \rightarrow i}^D(E)$ from Eq. (4.25). As has been demonstrated in Fig. 4.5, it significantly differs from zero only in a narrow energy region of a few eV in the vicinity of the resonance energy E_i of the excited state. Beside the energy, the absorption cross section depends on the ground-state transition width Γ_0 , as well as on the total width Γ . Figure 5.3 illustrates these dependencies. On the left-hand side, in Fig. 5.3 (a), the total width is fixed to $\Gamma = 4$ eV, whereas Γ_0 takes values of 1 eV, 2.5 eV, and 4 eV. Since Γ_0 enters solely the prefactor in the Doppler broadened cross section, it changes the cross section's scale, only. In contrast, different total widths Γ result also in different shapes of the cross section as is demonstrated in Fig. 5.3 (b). There, Γ_0 is fixed. Larger values for Γ implicate wider cross section curves with smaller maxima, *i.e.*, the cross section becomes less distinct.

The electromagnetic decay following the absorption of a photon happens according to an angular distribution which depends on the spin quantum numbers of the ground state, as well as the excited and the final state (see also

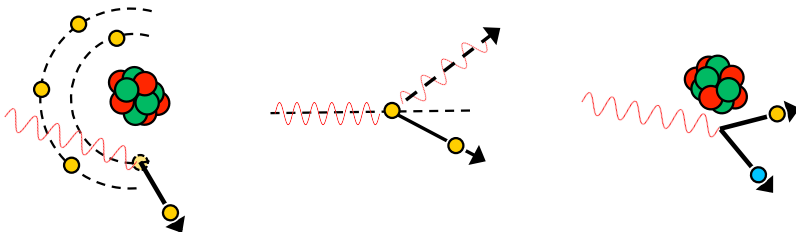


Figure 5.4.: Schematic representation of the most important contributions to the atomic attenuation. The photoelectric effect (left) corresponds to the absorption of a photon via an electron in the near-core area which is subsequently revealed from the atomic bond. In the case of Compton scattering (middle), a photon is scattered from a quasi-free electron, whereas in the pair production process (right) a photon converts into an electron-positron pair in the vicinity of a nucleus.

Sec. 4.2). In particular, the emission does *not* exclusively occur in the former direction of motion of the incident photon and, thus, results in an absorption line in the photon-flux distribution at the resonance energy of the excited state. As the cross section depends on Γ_0 and Γ , also the absorption line depends on these quantities. Therefore, the investigation of the absorption line allows for the determination of the ground-state transition width Γ_0 and the total width Γ . In particular, in the case of small widths $\Gamma \ll \Delta$ the cross section simplifies to the Doppler cross section $\tilde{\sigma}_{0-i}^D(E)$ [see Eq. (4.26)] which depends exclusively on Γ_0 . Hence, the investigation of the absorption line provides direct access to this quantity alone.

Atomic attenuation

Next to resonant absorption, various further processes involve an attenuation of the beam intensity behind the absorption target. In the following, these effects are subsumed under the term *atomic attenuation*. They include, e.g., Compton scattering [Com23], the pair production process [Mot69], and the photoelectric effect [Her87, Ein05b], that are schematically illustrated in Fig. 5.4. The effective attenuation cross section κ_{at} is given by

$$\kappa_{\text{at}} = \kappa_C + \kappa_{\text{pp}} + \kappa_{\text{rest}}. \quad (5.1)$$

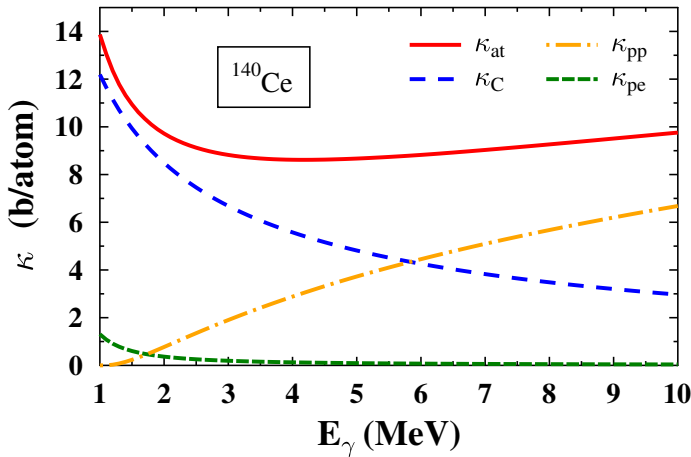


Figure 5.5.: The atomic attenuation cross section (κ_{at} , red) is composed of contributions from Compton scattering (κ_C , blue, dashed), pair production (κ_{pp} , orange, dash-dotted) and other processes with smaller cross sections like the photoelectric effect (κ_{pe} , green, dashed). Data are taken from Ref. [Ber98].

Here, κ_C , κ_{pp} , and κ_{rest} denote the cross sections for Compton scattering, for pair production, and for further contributions, respectively. As demonstrated in Fig. 5.5 for the example of ^{140}Ce , κ_C and κ_{pp} have the strongest contributions to the atomic attenuation in the energy region up to $\sim 10\text{ MeV}$ where NRF is usually applied in. The contribution of the photoelectric effect κ_{pe} is already small at energies above $\sim 1\text{ MeV}$ and, together with other effects, summarised in κ_{rest} .

In contrast to resonant absorption, the atomic attenuation occurs over the entire energy range and varies only weakly with energy. In particular, for energies above 4 MeV , κ_{at} is almost constant and, thus, the atomic attenuation almost constantly reduces the photon flux for all energies above 4 MeV . Furthermore, all effects contributing to the atomic attenuation depend neither on the ground-state transition width Γ_0 nor on the total width Γ . Nevertheless, reducing the overall photon-flux intensity, the atomic attenuation affects the investigation of the absorption lines and has to be corrected for during the analysis of self-absorption measurements.

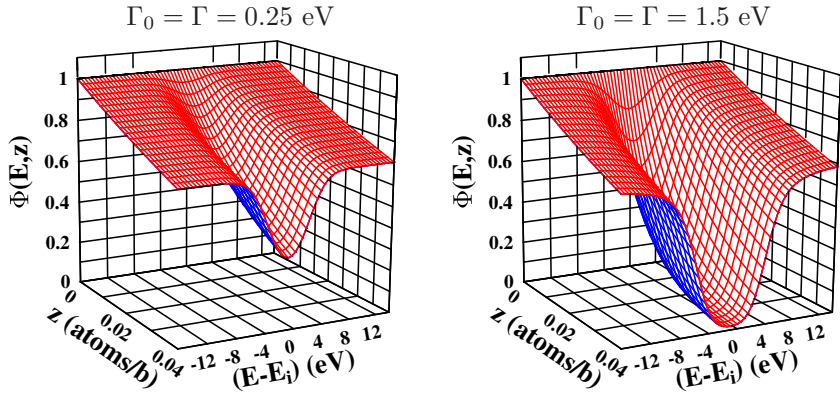


Figure 5.6.: Photon-flux densities for two generic states of ^{140}Ce at 5 MeV excitation energy. Resonant absorption contributes in a narrow energy region around the excitation energy E_i only. However, within this region it dominates over the atomic attenuation.

Knowing the influences of resonant absorption and atomic attenuation on the photon-flux distribution, the photon flux can be determined as a function of the photon energy E and the penetration depth z into a target:

$$N_\gamma(E, z) = N_\gamma(E) \cdot e^{-(\kappa_{\text{at}}(E) + \sigma_{0 \rightarrow i}^D(E)) \cdot z}. \quad (5.2)$$

In this equation, $N_\gamma(E)$ denotes the incident photon spectrum irradiating the target. By normalising to the initial spectrum, the so-called *photon-flux density* [Pie93]

$$\Phi(E, z) = e^{-(\kappa_{\text{at}}(E) + \sigma_{0 \rightarrow i}^D(E)) \cdot z} \quad (5.3)$$

is obtained. It describes the photon-flux distribution with respect to the original spectrum as a function of the distance passed in the target. In Fig. 5.6, two examples for the photon-flux density are shown. They were calculated for the case of a generic excited state of ^{140}Ce at 5 MeV excitation energy. Resonant absorption contributes only in a narrow energy region to the attenuation. Within the narrow resonance, the atomic attenuation cross section κ_{at} can be assumed to be constant. It accounts to $\kappa_{\text{at}} = 8.67 \text{ b/atom}$ at 5 MeV [Ber98]. The

example with $\Gamma_0 = \Gamma = 1.5$ eV shows that, if the absorber is chosen too thick, the photon flux can drop down to zero in the resonance. In this case, only limits for the self absorption can be determined since no photons are available for NRF reactions in the scattering target. As a consequence, for self-absorption measurements, the absorber thickness has to be optimised with respect to the values of Γ_0 the measurement shall be sensitive to.

5.3 Normalisation and Atomic Attenuation Correction - A new Approach

Self-absorption experiments are usually composed out of two measurements, a reference measurement and the actual self-absorption measurement. These measurements have to be compared during the analysis. The decrease of NRF reactions in the scattering target in the self-absorption measurement is determined with respect to the reference measurement. Thus, the initial beam conditions, *i.e.*, the shape and the intensity of the photon-flux distribution, have to be identical in both measurements. For the case, that such conditions can not be provided, a normalisation of both measurements to each other is mandatory. Furthermore, as has been pointed out in the previous section, atomic attenuation occurs over the entire range of excitation energy. In particular, it also occurs at the resonance energies of the investigated material and influences the decrease of NRF reactions in the scatterer. Thus, the correct determination of the self absorption requires a reliable correction for atomic attenuation effects as well as a normalisation of the two measurements with respect to each other.

In this section, earlier methods and a new approach, developed in the scope of this work, to normalise the measurements and to correct for atomic attenuation are introduced.

Earlier Approaches

Up to now, the usual approach to account for atomic attenuation was to conduct measurements with a resonant and an atomic absorption target, respectively (see, *e.g.*, Refs. [Pie93, Pie95, Vod84]). Ideally, the atomic absorber has the same atomic attenuation cross section κ_{at} as the resonant absorber, whereas it has no excited states at the resonance energies of the resonant absorber, in other words material with the same proton number Z but not including the investigated isotope. Then, the relative decrease of NRF reactions in the scatterer in the measurement with resonant absorber compared to

the measurement with atomic absorber can completely be attributed to resonant absorption. However, an ideal atomic absorber can often not be realised. Therefore, an energy-dependent correction factor has to be introduced which accounts for different atomic attenuation cross sections.

In an alternative approach, a ‘standard’ NRF measurement where the γ -ray beam does not pass an absorption target is performed next to the measurement with the resonant absorber. In the following, it will also be denoted as *classical* NRF measurement. In this case, the atomic attenuation in the resonant absorption target has again to be corrected for with an energy-dependent factor which is determined theoretically exploiting known beam attenuation coefficients. With this approach, also the product of $\Gamma_0 \cdot \Gamma_0/\Gamma$ can be obtained from the NRF measurement which is needed to determine Γ_0 in those cases where the absorption cross section cannot be approximated via Eq. (4.26), *i.e.*, when $\Gamma \ll \Delta$ does not hold (see Sec. 5.4). Furthermore, in combination with Γ_0 obtained in self absorption, it allows for the determination of the total width Γ and the branching ratio Γ_0/Γ to the ground state.

Both approaches require that the measurements are normalisable to each other. Therefore, the measuring conditions have to be identical during both measurements such that a normalisation of the measured spectra to the photon-flux intensity is possible. This can be realised, *e.g.*, for measurements with bremsstrahlung, by counting the number of electrons that were stopped in the radiator target where the bremsstrahlung is produced. However, for this approach, very stable beam conditions, in particular a stable end-point energy, as well as a reliable current measurement are mandatory. Nevertheless, it is prone to systematic errors. Therefore, a new reliable approach is of major importance, particularly with respect to high-precision measurements.

New Approach

In the present work, a new approach was chosen to correct for atomic attenuation. As in the second approach discussed in the last paragraph, two measurements are performed, one with and one without absorption target. However, a second scatterer of a different element is added to the actual scattering target to serve as a target monitoring the photon flux. Ideally, this beam monitor should have only a few excited states that do not coincide with the ones of the scatterer and that are well distributed over the entire energy region of interest. Then, the decrease of NRF reactions in the beam monitor is solely related to atomic attenuation. Thus, the intensities of scattered photons at the resonance energies of the beam monitoring target can be used to correct for

the influence of atomic attenuation. At the same time, they can be exploited to normalise both measurements to each other. To realise this, no information on the excited states of the monitor except for their resonance energies is needed. Therefore, beside statistical errors no further uncertainties, *e.g.*, of the excitation strengths of the beam monitoring target, enter the analysis. One of the advantages of self absorption is its independence of the spectral photon-flux distribution. With the measurement relative to such a flux monitor, it also becomes independent of the photon-flux intensity as well as further parameters like measuring times, dead times or any other global normalisation effect.

In summary, the new approach, the method of *relative* self absorption, *i.e.*, the measurement relative to a beam monitor, allows for the correction for atomic attenuation and for the normalisation of the measurements to each other in a reliable and potentially accurate way. Additionally, systematic uncertainties are reduced in comparison to the usual approaches that were discussed before. As a bonus, also NRF results on $\Gamma_0 \cdot \Gamma_0/\Gamma$ are obtained that, as will be discussed in the next section, allow for a general determination of Γ_0 , Γ and Γ_0/Γ even in the case of $\Gamma \approx \Delta$ where the absorption cross section depends not solely on Γ_0 .

5.4 Determination of Self Absorption

The self absorption R is defined as the decrease of NRF reactions in the scattering target due to the resonant absorption of photons in the absorber. In this section, the determination of the self absorption R_{exp} from the experiment, *i.e.*, from spectra as they are schematically shown in Fig. 5.7 is described. Furthermore, the calculation of the self absorption $R_{\Gamma_0, \Gamma}$ as a function of the ground-state transition width Γ_0 and of the total width Γ is explained. It is required to extract Γ_0 and Γ from the experimental result R_{exp} .

5.4.1 Experimental Self Absorption

As has been described before, in this work the self absorption is obtained exploiting two NRF measurements, a classical one and one with the beam passing an absorption target before reaching the scatterer and the beam monitor. Generic spectra of such measurements are schematically shown in Fig. 5.7.

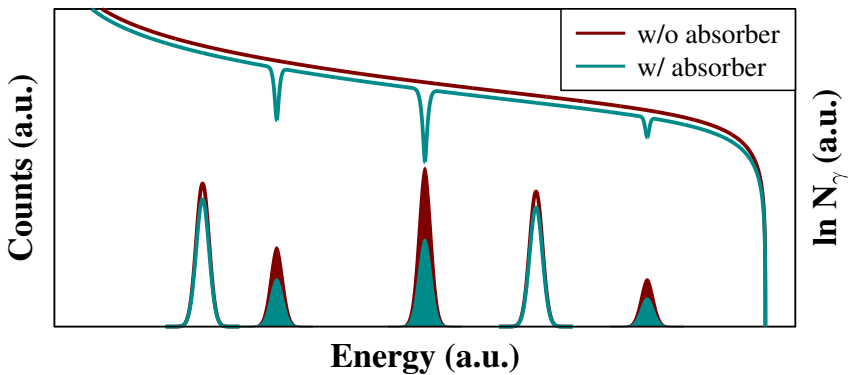


Figure 5.7.: Schematic spectra recorded with bremsstrahlung passing (blue) and without passing (red) an absorption target before reaching the scatterer. Filled peaks correspond to resonances of the scatterer, unfilled ones to resonances of the monitoring target.

There, the filled peaks correspond to transitions in the scattering target of interest, whereas the open peaks stem from transitions in the beam monitor. The measured intensities are reduced in the measurement with absorber (blue) with respect to the one without absorber (red) either exclusively due to atomic attenuation in the case of the beam monitor or due to resonant absorption as well as atomic attenuation in the case of the actual scatterer.

The experimental self absorption is given as

$$R_{\text{exp}} = \frac{N_{\text{NRF}} - N_{\text{RSA}}/f_{\text{RSA,NRF}}(E_i)}{N_{\text{NRF}}} = 1 - \frac{1}{f_{\text{RSA,NRF}}(E_i)} \frac{N_{\text{RSA}}}{N_{\text{NRF}}} = 1 - \frac{1}{f_{\text{RSA,NRF}}(E_i)} \frac{A_{\text{RSA}}}{A_{\text{NRF}}}. \quad (5.4)$$

Here, N_{RSA} denotes the number of NRF reactions in the measurement with absorber. The corresponding number for the classical NRF measurement is abbreviated with N_{NRF} . The number of scattered photons in a target is proportional to the measured yields, *i.e.*, the peak areas. Assuming identical settings in both measurements, the constant of proportionality, which is mainly given by the absolute detection efficiency, is also identical. Therefore, the number of NRF reactions can be replaced by the corresponding peak intensities A_{NRF} and A_{RSA} in Eq. (5.4). The energy-dependent factor $f_{\text{RSA,NRF}}(E)$ serves, in general, for normalisation between both measurements of a RSA experiment. In par-

ticular, it accounts for atomic attenuation. At the resonance energies E_i^{mon} of excited states of the beam monitoring target, it can be obtained via

$$f_{\text{RSA},\text{NRF}}(E = E_i^{\text{mon}}) = \frac{N_{\text{RSA}}^{\text{mon}}}{N_{\text{NRF}}^{\text{mon}}} = \frac{A_{\text{RSA}}^{\text{mon}}}{A_{\text{NRF}}^{\text{mon}}}, \quad (5.5)$$

where N^{mon} and A^{mon} are the number of NRF reactions in the beam monitor and the corresponding peak intensities. The general energy dependence of $f_{\text{RSA},\text{NRF}}(E)$ can be deduced either exploiting known and interpolated attenuation cross sections, *e.g.*, from Ref. [Ber98], or simulating beam attenuation effects in the absorber with **GEANT4** [Ago03] (compare Secs. 7.4 and 8.2). The resulting curve has to be scaled to the experimental results for $f_{\text{RSA},\text{NRF}}(E = E_i^{\text{mon}})$.

5.4.2 Calculation of Self Absorption

The next step requires to calculate the self absorption

$$R_{\Gamma_0,\Gamma} = \frac{N_{\Gamma_0,\Gamma}^{\text{NRF}} - N_{\Gamma_0,\Gamma}^{\text{RSA}}}{N_{\Gamma_0,\Gamma}^{\text{NRF}}} = 1 - \frac{N_{\Gamma_0,\Gamma}^{\text{RSA}}}{N_{\Gamma_0,\Gamma}^{\text{NRF}}}, \quad (5.6)$$

i.e., the relative decrease of the scattering yield with absorption target, as a function of Γ_0 and Γ . Thus, also the number of NRF reactions in the scatterer $N_{\Gamma_0,\Gamma}^{\text{RSA}}$ and $N_{\Gamma_0,\Gamma}^{\text{NRF}}$ have to be determined as a function of these quantities. To realise this, the so-called *resonance-absorption density* [Pie93]

$$\alpha(E, z) = \sigma_{0 \rightarrow i}^D(E) \cdot \Phi(E, z) = \sigma_{0 \rightarrow i}^D(E) \cdot e^{-(\kappa_{\text{at}}(E) + \sigma_{0 \rightarrow i}^D(E)) \cdot z} \quad (5.7)$$

is needed. It is given as the product of the photon-flux density with the absorption cross section. The resonance-absorption density describes the probability for resonant absorption of a photon with energy E at a particular penetration depth z into a target. In Fig. 5.8, two examples for $\alpha(E, z)$ are shown for generic states of ^{140}Ce at an excitation energy of 5 MeV. Outside the resonance, the probability to resonantly absorb a photon rapidly drops to zero. In analogy to the photon-flux density, the absolute resonance-absorption density and its decrease with the penetration depth z depend mainly on Γ_0 . For large values of Γ_0 and large penetration depths into the absorber, it can form a double-hump structure as it is demonstrated on the right-hand side of Fig. 5.8. At the

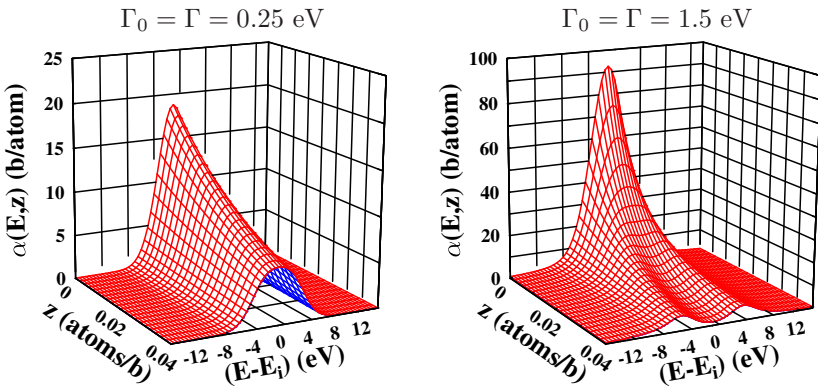


Figure 5.8.: Resonance-absorption densities for two generic states of ^{140}Ce at $E_i = 5\text{ MeV}$. The probability for resonant absorption of photons decreases with the penetration depth z . For large values of Γ_0 and Γ , it even drops to zero right at the resonance resulting in a minimum enclosed by two maxima: only photons with energies $\neq E_i$ are still available for resonant absorption.

resonance energy E_i , the probability for resonant absorption initially is maximal. As a consequence, photons with this energy are most frequently absorbed. Eventually, the photon flux at the resonance energy E_i is reduced in such a way that the probability to absorb further photons is smaller as in the vicinity of E_i . There, photons are still available for resonant absorption.

In the following, the atomic attenuation cross section will be set to $\kappa_{\text{at}}(E) = 0$ since, in this work, the experimentally deduced result R_{exp} for the self absorption is already corrected for contributions of atomic attenuation processes. As a consequence, the resonance-absorption density

$$\alpha(E, z) = \sigma_{0 \rightarrow i}^D(E) \cdot e^{-\sigma_{0 \rightarrow i}^D(E) \cdot z} \quad (5.8)$$

depends only on the Doppler broadened absorption cross section of the individual resonances.

Eventually, the self absorption can be calculated as a function of Γ_0 and Γ according to Eq. (5.6). Exploiting the resonance-absorption density, the num-

ber of photons scattered resonantly via a channel j in the scatterer can be determined via

$$N_{\Gamma_0, \Gamma}^{\text{NRF}} = N_\gamma(E_i, 0) \cdot \frac{\Gamma_j}{\Gamma} \cdot \int_0^{d_s} dz \int_{-\infty}^{\infty} dE \alpha(E, z). \quad (5.9)$$

In this equation, $N_\gamma(E_i, 0)$ represents the number of photons at the resonance energy initially available for scattering reactions. Here, it is assumed that the initial photon-flux distribution is constant in the vicinity of E_i (compare Sec. 4.2). The branching ratio to the channel j is taken into account via Γ_j/Γ . Eventually, d_s denotes the areal particle density or the thickness of the scatterer, respectively. For the self-absorption measurement, the number of resonantly scattered photons can be calculated in an identical way. However, the shape of the photon-flux distribution has changed after having passed an absorber with thickness d_a . The initial distribution cannot be assumed anymore to be constant with energy. This is accounted for by multiplying the resonance-absorption density with the photon-flux density $\Phi(E, d_a)$:

$$N_{\Gamma_0, \Gamma}^{\text{RSA}} = N_\gamma(E_i, 0) \cdot \frac{\Gamma_j}{\Gamma} \cdot \int_0^{d_s} dz \int_{-\infty}^{\infty} dE \Phi(E, d_a) \cdot \alpha(E, z). \quad (5.10)$$

With a transformation of the coordinate $z \rightarrow z + d_a$ this integral can be written as

$$N_{\Gamma_0, \Gamma}^{\text{RSA}} = N_\gamma(E_i, 0) \cdot \frac{\Gamma_j}{\Gamma} \cdot \int_{d_a}^{d_a + d_s} dz \int_{-\infty}^{\infty} dE \alpha(E, z). \quad (5.11)$$

Thus, the RSA measurement can be interpreted as an NRF measurement on a target with thickness $d_a + d_s$, whereby only photons scattered in the region between d_a and $d_a + d_s$ are registered with the detectors. Eventually, the self absorption is calculated via

$$R_{\Gamma_0, \Gamma} = 1 - \frac{\int_{d_a}^{d_a + d_s} dz \int_{-\infty}^{\infty} dE \alpha(z, E)}{\int_0^{d_s} dz \int_{-\infty}^{\infty} dE \alpha(z, E)}, \quad (5.12)$$

presupposing a normalisation of the photon-flux intensities in both measurements with respect to each other.

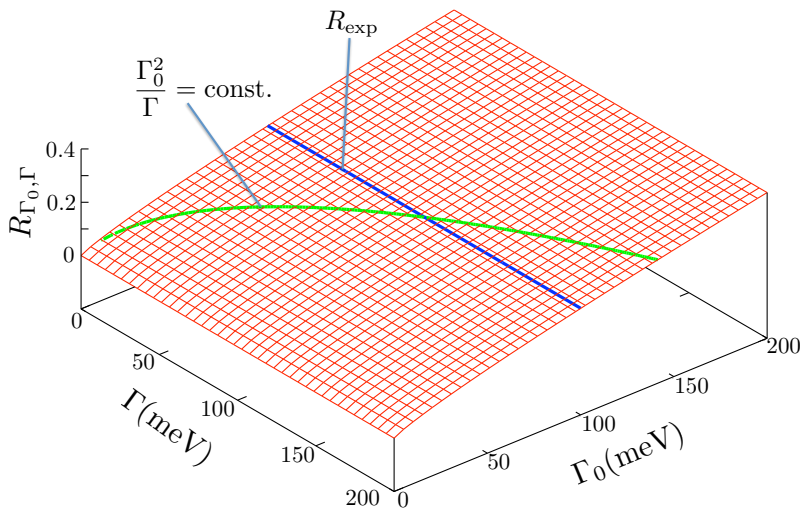


Figure 5.9.: Schematic three-dimensional plot of the self absorption $R_{\Gamma_0, \Gamma}$ (red) as function of Γ_0 and Γ . The blue line represents an experimentally deduced value R_{exp} . The green line shows the relation between Γ_0 and Γ . The intersection point of the curves on the plane corresponds to the transition widths Γ_0 and Γ of the excited state.

Basically, this equation depends through the resonance-absorption density $\alpha(E, z)$ and, thus, through the Doppler broadened absorption cross section $\sigma_{0 \rightarrow i}^D$ on the ground-state transition width Γ_0 as well as on the total width Γ . Consequently, in general, these quantities cannot be unambiguously determined with a self-absorption measurement alone. Figure 5.9 emphasises this point. It shows a schematic three-dimensional plot of the self absorption $R_{\Gamma_0, \Gamma}$ as a function of Γ_0 and Γ . An experimental result R_{exp} is represented by the blue line. All combinations of Γ_0 and Γ at this intersection line with the red plane result in a self absorption identical to the experimental one. Thus, additional information is required to determine a unique solution. Since a classical NRF measurement is always part of a self-absorption experiment, the result for Γ_0^2/Γ can be used to describe the relation between both, Γ_0 and Γ . The green line in Fig. 5.9 represents this relation and a solution for Γ_0 and Γ is given by the interaction point of the blue and the green lines on the $R_{\Gamma_0, \Gamma}$ plane. However, also this solution is not unambiguous.

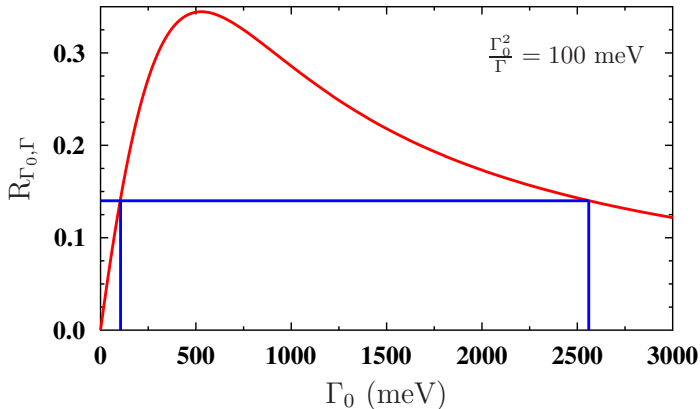


Figure 5.10.: Self absorption $R_{\Gamma_0, \Gamma}$ as function of Γ_0 for a generic excited state of ^{140}Ce at an excitation energy of 5 MeV. The red curve is calculated with the condition that Γ_0^2/Γ is fixed to 100 meV. An experimentally determined result for R is indicated by the blue line. It corresponds to two different solutions for Γ_0 and, thus, also for Γ .

In Fig. 5.10 the self absorption $R_{\Gamma_0, \Gamma}$ of a generic $E_i = 5$ MeV state is plotted against Γ_0 . It was calculated with the condition that Γ_0^2/Γ is fixed to an arbitrary value of 100 meV representing the result of an NRF measurement. The curve rises steeply, exhibits a maximum at $\Gamma_0 \sim 500$ meV, and, finally, slowly decreases. This dependence on Γ_0 can be ascribed to the fact, that, while Γ_0 increases linearly, Γ has to increase quadratically in order to keep Γ_0^2/Γ constant. As has been demonstrated in Fig. 5.3, for large values of Γ the Doppler broadened cross section becomes broad and flat. The corresponding absorption lines become less distinct. Therefore, also $R_{\Gamma_0, \Gamma}$ decreases resulting in the typical dependence on Γ_0 that is shown in Fig. 5.10. As a consequence, two solutions for Γ_0 and Γ can be found for a given experimental result R_{exp} . In this example, with $\Gamma_0^2/\Gamma = 100$ meV, Γ_0 yields 105 meV, whereas Γ accounts to 110 meV for the first solution. The second one yields $\Gamma_0 = 2560$ meV and $\Gamma = 65540$ meV, respectively. The second solution corresponds to an unlikely large value for the total transition width Γ and may be excluded. However, in cases where the experimental value R_{exp} is located close to the maximum of the $R_{\Gamma_0, \Gamma}$ curve, this may not be feasible anymore.

Solely in the limiting case of $\Gamma \ll \Delta$, *i.e.*, when the simplified Doppler cross section [see Eq. (4.26)] can be used, the self absorption R depends on Γ_0 alone. Therefore, Γ_0 can directly be determined. A first-order correction factor k [Pie95] defined via

$$k = \frac{\int_{E_i-\Delta}^{E_i+\Delta} \tilde{\sigma}_{0 \rightarrow i}^D(E) dE}{\int_{E_i-\Delta}^{E_i+\Delta} \sigma_{0 \rightarrow i}^D(E) dE} \quad (5.13)$$

takes small differences between the Doppler broadened $\sigma_{0 \rightarrow i}^D(E)$ and the Doppler cross section $\tilde{\sigma}_{0 \rightarrow i}^D(E)$ in a narrow energy range around the resonance energy E_i into account and can be applied to correct Γ_0 for those differences via

$$\Gamma'_0 = \Gamma_0/k. \quad (5.14)$$



6 Experimental Setup

The self-absorption measurements on ^{140}Ce and ^6Li have been performed at the Darmstadt High Intensity Photon Setup (DHIPS) which is located at the Superconducting DArmstadt electron LINear ACcelerator (S-DALINAC) at TU Darmstadt. At the NRF measuring site DHIPS, bremsstrahlung is used as photon source. In this chapter, a short overview over the S-DALINAC and its characteristics will be given. Following this, the experimental setup will be presented in detail.

6.1 S-DALINAC

A schematic overview of the superconducting Darmstadt electron linear accelerator S-DALINAC [Ric96, Bru00, Hug11] is given in Fig. 6.1. At the S-DALINAC, electrons are provided either by a thermionic gun or by a polarised source generating spin-polarised electrons [Fri11]. The electrons with kinetic energies of up to 250 keV initially pass the normal-conducting part of the S-DALINAC. In this part, a chopper-prebuncher system imprints a 3 GHz time structure to the electrons, preparing them for further acceleration. Subsequently, they enter the superconducting injector module and are accelerated in cavities made of niobium. In the new injector module, that was installed in 2014, the electrons can be accelerated up to 14 MeV with currents up to $250\,\mu\text{A}$. The previous injector module, which was used for the experiments in the framework of this thesis, provided electrons with kinetic energies up to 10 MeV and currents up to $60\,\mu\text{A}$.

Directly behind the injector module, the electrons can either be provided to the DHIPS measuring site for NRF and photo-fission experiments or they are extracted to the main linac. It consists out of eight superconducting cavities. Each time, the beam passes the main linac, the electrons can gain up to 40 MeV energy. Up to now, two recirculations can be used, such that the beam can pass the main linac three times. This results in a maximum electron energy of 130 MeV. However, typically only $\sim 90\,\text{MeV}$ can be reached as the cavities do not reach their design values. A third recirculation is planned to be installed

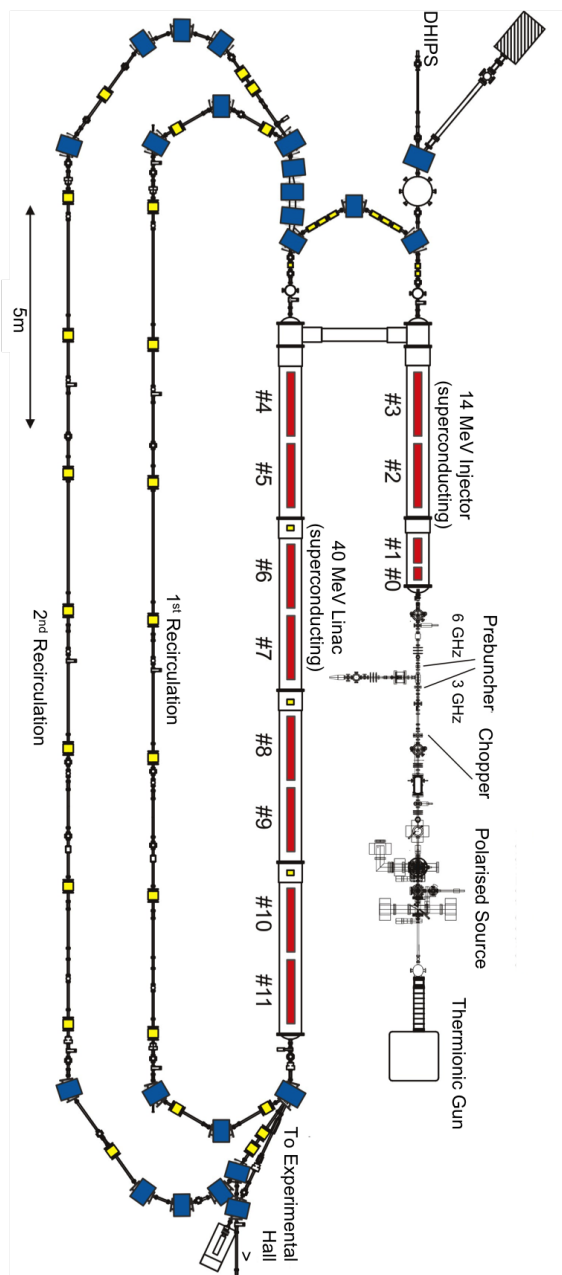


Figure 6.1.: Schematic overview of the superconducting Darmstadt electron linear accelerator S-DALINAC. Electrons are provided either by the thermionic gun or the polarised source. In the normal conducting part of the accelerator, the electrons are prepared and eventually accelerated up to 14 MeV in the injector module. The NRF measuring site DHIPS is located directly behind the injector. The electrons can either be extracted towards DHIPS or further be accelerated in the main linac. Figure adapted from Ref. [Hug11].

in 2015 which allows for passing the main linac a fourth time giving $E_{\max} \sim 130$ MeV. Behind the main linac, the electrons can be extracted to the so-called experimental hall where they are used for electron scattering experiments at the QCLAM [Kni91] and Lintott [Sch78] spectrometer, respectively. On the other hand, they can be provided to the photon-tagger NEPTUN [Sav10].

6.2 DHIPS

The Darmstadt High Intensity Photon Setup DHIPS [Son11], the measuring site for real photon scattering at the S-DALINAC, is located subsequently to the injector module of the S-DALINAC. A schematic drawing of DHIPS is shown in Fig. 6.2. At DHIPS, bremsstrahlung is used as source for high-energy photons. It is produced by irradiating a thick radiator target with the electron beam of the S-DALINAC. The radiator is two-fold segmented with the segments being isolated against each other. Thus, the electrons first hit a thinner segment before reaching the thicker second one where they are completely stopped. The ratio of the current deposited on each segment provides a sensitive measure for the energy of the electrons. For higher electron energies, more electrons can pass the first segment and reach the second one resulting in a larger current ratio. The material of the segment can be individually adapted to different beam conditions. In general, materials with large proton number Z are preferred since the bremsstrahlung yield increases with Z . However, beside thermal and electric conductivity, also the neutron separation threshold has to be taken into account to avoid the production of neutrons that, in turn, produce background radiation and may damage the detectors.

The produced bremsstrahlung passes a copper collimator which cuts out a spatially well-defined beam reaching two experimental sites behind the collimator. The beam-spot sizes are 25 mm and 30 mm in diameter at the first (S1) and second (S2) target position, respectively, where scattering targets can be mounted. The main experimental site, S1, is surrounded by three high-purity Germanium (HPGe) detectors, where detectors DET2 and DET3 are located at 127° and 90° with respect to the incoming beam. The position of the third detector (DET1) can be varied between about 90° and 130° . At position S1, classical NRF as well as RSA measurements can be performed. Since the main part of the γ -ray beam passes the target at S1 without being influenced, the second experimental site S2 allows for measurements in parallel to measurements at S1. A segmented HPGe detector (DET4) can, e.g., be installed in such

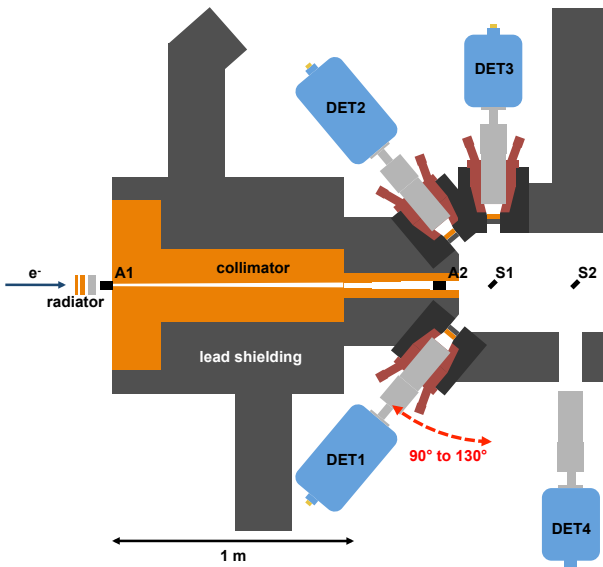


Figure 6.2.: Schematic drawing of the Darmstadt High Intensity Photon Setup DHIPS. Electrons provided by the S-DALINAC are stopped in the two-fold segmented radiator. Bremsstrahlung is produced and passes a beam hardener and a copper collimator before reaching the target positions S1 and S2. High-purity germanium detectors that are shielded with lead, active BGO shields and filters surround S1 and S2. At positions A1 and A2, absorption targets can be placed for RSA measurements.

a way that the polarisation of the scattered photons can be measured. This allows for the determination of the parity quantum number of dipole excited states [Büs08] (compare Sec. 4.2).

Detectors DET1 to DET3 are equipped with bismuth germanate (BGO) shields for active Compton suppression and additionally mounted in lead collimators. The BGO shielding significantly reduces single (SE) and double (DE) escape peaks and improves the overall peak-to-total ratio. Next to the lead collimators, the detectors are further massively shielded with thick lead walls against the bremsstrahlung background stemming from the radiator and the accelerator itself. In addition, low-energy background is reduced exploiting an

aluminium beam hardener which is located between the radiator and the collimator. Finally, low-energy background produced by Compton scattering in the scattering target at S1 and/or S2 is reduced with the help of “filters” made of copper and lead that are placed in front of the detectors.

Relative Self Absorption at DHIPS

For relative self-absorption measurements at DHIPS, the scattering and the monitoring target are positioned at S1. Additionally, the absorber target has to be placed in the setup. For this purpose, two main requirements have to be fulfilled. In the first place, the detectors have to be sufficiently shielded against scattered photons from the absorption target. If the detectors register events stemming from the absorber, the self-absorption measurement becomes distorted. In this case, the number of NRF reactions measured with absorber target would be too high resulting in a self absorption R which is too small. Secondly, the exact knowledge of the number of absorber nuclei irradiated by the γ -ray beam is mandatory. It is needed during the analysis of the RSA measurement. In the scope of this work, two different positions for the absorber have been tested. The first position A1 is located in front of the collimator. Alternatively, it can be placed into the last part of the collimator. However, for absorbers at position A1, the absorption lines in the absorption spectrum are affected by scattering at small angles in the collimator. Photons with energies higher than a particular excitation energy E_i of the absorber can lose energy by being Compton scattered in the collimator and thereby be shifted to E_i and, thus, “fill up” the absorption lines again. For absorbers at position A2, photons scattered in the absorber have been detected despite the shielding via the copper collimator and the lead collimator of the detectors. The treatment of these shortcomings is discussed in the corresponding chapters dealing with the specifications of the individual experiments.



7 Direct Determination of Transition Widths of ^{140}Ce

In the first experiment discussed in this thesis, the method of self absorption has been applied pioneering to study ground-state transition widths, level widths, and branching ratios to the ground state for excited dipole states of ^{140}Ce . A particular focus will be on the energy region the PDR is located in since information on the decay pattern of individual states attributed to the PDR do only scarcely exist.

In this chapter, the experiment on ^{140}Ce is described. Beside information on the measuring parameters, the analysis and results of the classic NRF measurement are presented. Subsequently, a detailed description of the analysis method of the RSA measurement is given, which has been applied to obtain results for R , Γ_0 , Γ , as well as Γ_0/Γ . The crucial aspects and difficulties of the analysis of self-absorption measurements will be pointed out. Afterwards, the results of the RSA measurement are presented and discussed with respect to simulations within the statistical model which is also introduced. Eventually, conclusions from this “proof of principle” measurement on ^{140}Ce are drawn and discussed.

7.1 The Measurements

For the RSA measurement on ^{140}Ce , three different targets have been used. The absorption target has been made of natural CeO_2 , the scattering target of CeO_2 highly enriched (99.5 %) in the isotope of interest, and, eventually, the monitoring target consisted of boron enriched to 99.52 % in ^{11}B . Information on the targets are summarised in Tab. 7.1.

In total, three measurements have been performed with different measuring times and combinations of the targets. The electron energy and, thus, the highest possible photon energy was set to 8.0(2) MeV in all measurements. In the first place, a measurement with the absorber and the monitoring target alone has been done to check whether photons scattered in the absorption target are

Table 7.1.: Information on the targets used during the RSA experiment on ^{140}Ce . The natural abundance of the isotope ^{140}Ce accounts to 88.5 %, the one of ^{11}B to 80.1 %.

target	chem. compound	mass (g)	enrichment
absorber	CeO_2	59.28	99.99 % in nat. CeO_2
scatterer	CeO_2	2.4115	99.5 % in ^{140}Ce
monitor	B	0.312	99.52 % in ^{11}B

Table 7.2.: Information on the measurements performed during the self-absorption experiment on ^{140}Ce . The positions of the targets correspond to the nomenclature introduced in Fig. 6.2.

	E_0 (MeV)	absorber pos.	scatterer pos.	monitor pos.	t_{meas}
ABS	8.0(2)	A2	X	S1	70 h
NRF	8.0(2)	X	S1	S1	97 h
RSA	8.0(2)	A2	S1	S1	98 h

observed with the detectors. In the following, this measurement will be referred to as absorption (ABS) measurement. The absorber has been placed at position A2 at the end of the collimator (see also Fig. 6.2), the monitoring target at position S1. Afterwards, the actual self-absorption measurements were conducted. For both measurements, the scatterer has been located at position S1 together with the monitoring target, whereas one measurement was performed with the absorber (RSA measurement) at A2 and one without absorber at all (NRF measurement). An overview of the performed measurements is provided in Tab. 7.2.

Figure 7.1 shows a part of the summed-up spectra of all three detectors between 5.5 MeV and 6 MeV that have been recorded during the experiment. The peaks correspond to transitions in ^{140}Ce . Although both, the NRF (red spectrum) and RSA (turquoise) measurement, lasted for about four days (see Tab. 7.2) a clear discrepancy is observed in the total yield of the corresponding spectra. Firstly, the entire yield of detected photons is reduced due to atomic attenuation in the absorber. Secondly, the peak areas are reduced in the measurement with absorption target due to resonant absorption. As demonstrated by Fig. 7.1, the decrease of NRF reactions scales with the former height of

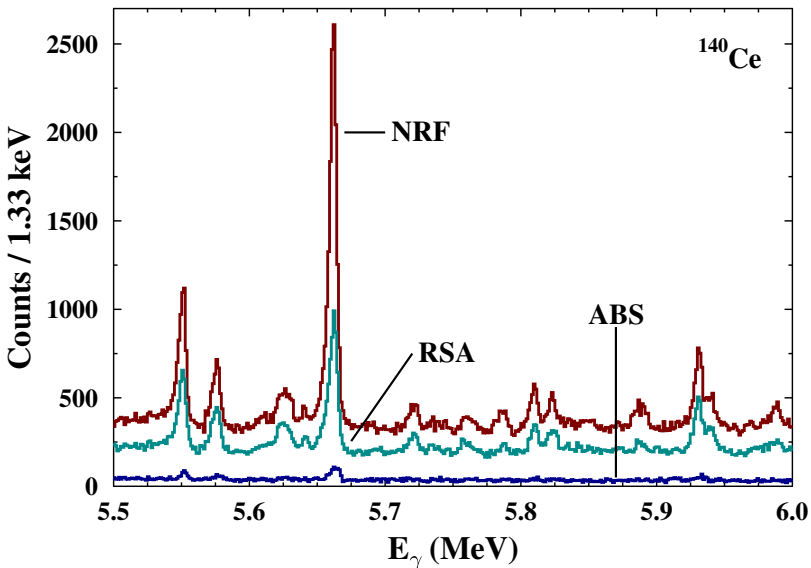


Figure 7.1.: Spectra recorded during the self-absorption experiment on ^{140}Ce . The upper (red) spectrum was recorded without using an absorber. It represents the classical NRF measurement. The middle spectrum (turquoise) was taken with absorption target. The yield is lowered due to atomic attenuation and resonant absorption. Eventually, the spectrum at the bottom (blue) was recorded solely with absorption and monitoring target. Peaks appearing in this spectrum represent photons that were scattered in the absorber.

the peaks, *i.e.*, with the transition widths of the corresponding transitions. The largest peak at about 5660 keV is suppressed by a factor of about 50 %, whereas the reduction of the initially smaller peaks is substantially lower. The spectrum plotted in blue at the bottom of Fig. 7.1 corresponds to the absorption measurement. It demonstrates that a small part of photons scattered in the absorption target can reach the detectors and is registered providing strong evidence that this effect must be taken into account (see Sec. 7.4.1).

A complete overview of the spectra taken during the self-absorption experiment on ^{140}Ce is given in the Appendix A of this work.

7.2 The Classical NRF Measurement - Analysis

As a first step, the classical NRF measurement is analysed. In particular, the results for Γ_0^2/Γ , that can be extracted from this measurement, are an essential part of the following analysis of the actual RSA measurement. In this chapter, important steps of the analysis of NRF measurements are summarised.

The integrated NRF cross section $I_{0 \rightarrow i \rightarrow j}$ [Eq. (4.29)] has to be extracted from the NRF measurements in order to determine Γ_0^2/Γ . According to Eq. (4.32), it can be obtained via

$$I_{0 \rightarrow i \rightarrow j} = \frac{A_{0 \rightarrow i \rightarrow j}}{N_T \cdot \epsilon(E_i - E_j) \cdot N_\gamma(E_i) \cdot W_{0 \rightarrow i \rightarrow j}^{\text{eff}}(\vartheta)}. \quad (7.1)$$

In this equation, $A_{0 \rightarrow i \rightarrow j}$ denotes the peak area, N_T the number of target nuclei, $\epsilon(E_i - E_j)$ the absolute efficiency, $N_\gamma(E_i)$ the photon-flux intensity, and the angular distribution is abbreviated via $W_{0 \rightarrow i \rightarrow j}^{\text{eff}}(\vartheta)$. While the number of target nuclei can directly be determined via the target mass, more effort is required for the remaining quantities.

Energy Calibration

The procedure for the energy calibration of the measured spectra has already been discussed in Sec. 4.2. In the case of the measurements on ^{140}Ce , the energy is calibrated exploiting both, the well-known transitions of a ^{56}Co source as well as of the ^{11}B monitoring target. After the energy calibration, the spectra are systematically analysed. In particular, peak positions, *i.e.*, transition energies E_γ , and peak intensities $A_{i \rightarrow j}$ are determined for all observed peaks. The observed transition energies E_γ of ^{140}Ce for each detector in the NRF and the RSA measurements, respectively, have been corrected for the recoil of the nucleus via Eq. (4.6). Eventually, the resulting excitation energies have been averaged for each observed level. In the following, if not marked differently, these excitation energies E_i will be presented.

Feeding and Single-Escape Calibration

For the determination of the NRF cross section $I_{0 \rightarrow i \rightarrow j}$, the knowledge of the corresponding peak intensity $A_{0 \rightarrow i \rightarrow j}$ describing the decay of a level i to a level j after excitation from the ground state is required [see Eq. (7.1)]. From the spectra, the peak intensity $A_{i \rightarrow j}$ is extracted. However, the level i must not exclusively be excited by the incident γ -ray beam. It may also be populated

by higher-lying levels, *i.e.*, it may be fed. Without correcting for feeding from higher-lying states, the integrated cross sections would be overestimated. Assuming, that an excited state i is fed by a higher-lying level f , the correction of the measured peak intensity can be conducted via

$$A_{0 \rightarrow i \rightarrow j} = A_{i \rightarrow j} - \frac{\Gamma_i}{\Gamma_0} \cdot \frac{\epsilon(E_i - E_j)}{\epsilon(E_f)} \cdot \frac{W_{0 \rightarrow f \rightarrow i \rightarrow j}^{\text{eff}}(\vartheta)}{W_{0 \rightarrow f \rightarrow 0}^{\text{eff}}(\vartheta)} \cdot A_{f \rightarrow 0}. \quad (7.2)$$

Here, Γ_i/Γ_0 denotes the branching ratio of level f to level i and $A_{0 \rightarrow f \rightarrow 0}$ represents the peak intensity corresponding to the direct ground-state decay of level f . The angular distribution $W_{0 \rightarrow f \rightarrow 0}^{\text{eff}}(\vartheta)$ depends on the spin quantum number of the excited state f (see also Sec. 4.2), whereas $W_{0 \rightarrow f \rightarrow i \rightarrow j}^{\text{eff}}(\vartheta)$ can be assumed to be one. For the determination of the ratio of the detector efficiencies at the energies E_i and E_f , respectively, the energy dependence of the efficiency has to be known. It can be extracted from simulations as will be discussed in the next paragraph concerning the *Efficiency and Photon-Flux Calibration*.

To decide whether an excited state may be fed at all, the Ritz variation principle can be applied. For the case, that three peaks A , B , and C appear in a spectrum at energies E_A , E_B , and E_C with $E_A < E_B < E_C$ and $E_A = E_C - E_B$, one of the corresponding possible levels a and b may be fed from level c . However, the energies may also coincide by chance. Assuming that a and c correspond to levels and level a is fed by level c , peak B can either completely or partly be attributed to the decay of c to a . In the second case, also b is an excited state. However, although not being fed, the intensity of the corresponding peak would increase due to the decay of c to a . Further evidence, whether a level is fed from a higher-lying one or not, can be provided by the angular distribution of the photons emitted during the decay of this level. For an excited state, which is fed, the angular distributions $W_{0 \rightarrow i \rightarrow 0}$ corresponding to the excitation via the incident γ -ray beam and $W_{f \rightarrow i \rightarrow 0}$ corresponding to the population from a higher-lying level f overlap resulting in a rather isotropic distribution. However, finally, only additional measurements, in which only the level supposed to be fed or, in turn, the feeding level is excited, can give a clear answer, whether a level is fed or not.

Besides feeding, another possible case leading to overestimated peak intensities and, thus, overestimated cross sections in NRF measurements are contaminations with single-escape events. Despite the active Compton suppression via

BGO shields, which has been introduced in Sec. 6.2, single-escape peaks are not fully suppressed in the measured spectra. Thus, a single-escape calibration has to be performed. Well separated single-escape peaks corresponding to strong transitions of ^{140}Ce and to those of ^{11}B are used to calibrate the energy dependence of the ratio

$$r_{\text{SE}}(E) = \frac{A_{\text{SE}}}{A_{\text{P}}}. \quad (7.3)$$

It describes the single-escape peak intensity A_{SE} as a fraction of the yield A_{P} of the peak corresponding to a particular transition. The calibration is conducted for each detector separately. With these calibrations, the spectra are searched for peaks (with intensity B) that are located (511 ± 2) keV below another peak (with intensity B_{P}), *i.e.*, they are searched for possible single escape peaks. For such candidates, the single-escape contribution is determined exploiting $r_{\text{SE}}(E)$ and the corresponding peak intensity B_{P} . This contribution is subtracted from the peak at the single-escape energy. Eventually, the corrected peak intensity B_{cor} is given as

$$B_{\text{cor}} = B - r_{\text{SE}}(E) \cdot B_{\text{P}}. \quad (7.4)$$

For the case, that B_{cor} agrees with zero within its uncertainties, the corresponding peak is treated as pure single-escape peak and is not taken into account for the further analysis.

The same procedure can be applied to treat double-escape events. However, in the present measurements no double-escape peaks have been observed above the experimental sensitivity limit for the strongest full-energy peaks. Consequently, contributions of double-escape events are neglected.

Efficiency and Photon-Flux Calibration

An important step during the analysis of an NRF measurement is the calibration of the detector efficiency as well as of the photon-flux distribution. Both quantities enter into the equation for the NRF cross section $I_{0 \rightarrow i \rightarrow j}$ [see Eq. (7.1)]. They can either be treated separately or the product is directly calibrated for the case that only ground-state transitions are investigated. In the present work, the second procedure has been chosen. However, in particular the energy dependence of the detector efficiency has been determined separately since it is required for the correction of feeding effects.

Table 7.3.: Information on the excited states of ^{11}B that are of relevance for this work. The level energy, the ground-state transition width Γ_0 , the NRF cross section for direct decay back to the ground-state $I_{0 \rightarrow i \rightarrow 0}$, as well as the corresponding angular distribution $W_{0 \rightarrow i \rightarrow 0}^{\text{eff}}$ evaluated at an scattering angle of 90° and 130° , respectively, are listed. Data are taken from Ref. [Ajz90].

E_{Level} (keV)	Γ_0 (eV)	$I_{0 \rightarrow i \rightarrow 0}$ (keV · fm 2)	$W_{0 \rightarrow i \rightarrow 0}^{\text{eff}}(90^\circ)$	$W_{0 \rightarrow i \rightarrow 0}^{\text{eff}}(130^\circ)$
2124.69	0.120(9)	5.11(38)	1.000	1.000
4444.89	0.54(2)	15.76(58)	1.000	1.000
5020.31	1.68(6)	22.0(14)	0.938	1.014
7285.51	1.00(8)	9.5(13)	0.931	1.016

From the experimental side, the product of photon flux and efficiency, in the following referred to as $N_\gamma \varepsilon$, is determined exploiting the well-known ground-state transitions of the ^{11}B monitoring target by writing Eq. (7.1) as

$$N_\gamma \varepsilon(E_\gamma) = \frac{A_{0 \rightarrow i \rightarrow 0}}{N_T \cdot W_{0 \rightarrow i \rightarrow 0}^{\text{eff}} \cdot I_{0 \rightarrow i \rightarrow 0}}. \quad (7.5)$$

This equation is evaluated at the ground-state transition energies of ^{11}B . The corresponding excited states of ^{11}B are well investigated. Thus, the right-hand side of this equation contains only known quantities. The relevant data for the observed transitions [Ajz90] are summarised in Table 7.3. The excited levels at $E_i = 5020.31$ keV and $E_i = 7285.51$ keV do not decay exclusively to the ground state. The first one decays with $\Gamma_{2124} = 0.28(1)$ eV to the first excited state at 2124.69 keV. The second one decays with $\Gamma_{4444} = 0.063(12)$ eV to the 4444.89 keV level and has a partial decay width of $\Gamma_{5020} = 0.080(12)$ eV to the excited state at 5020.31 keV excitation energy. Thus, before $N_\gamma \varepsilon$ can be deduced, the peaks corresponding to the ground-state decay of the levels at 2124.69 keV, 4444.89 keV, and 5020.31 keV have to be corrected for feeding according to Eq. (7.2).

In a further step, the energy dependence of $N_\gamma \varepsilon$ is determined. For this purpose, in the first place, the energy dependence of the photon flux and the efficiency is separately deduced. Although being developed for thin radiator targets, where electrons interact, if at all, only once with the radiator material,

the Schiff formula [Sch51] represents a good description of bremsstrahlung distributions also in the case of thicker radiators. Therefore, it has been applied to parametrise the photon-flux distribution in the present work. For the absolute detector efficiency no such formula exists. Its energy dependence has been deduced exploiting GEANT4 (GEometry AND Tracking) [Ago03]. The Monte-Carlo simulation tool GEANT4 has been developed at CERN, the European Organization for Nuclear Research, to study physical processes during the transmission of particles and γ radiation through material. For the determination of the detector efficiency, an isotropically radiating, mono-energetic photon source has been generated and placed in front of the detectors corresponding to the real setup. The detectors have been implemented in the simulation according to the corresponding data sheets. As in the experiment, they were shielded with filters reducing the efficiency particularly at low energies. Within the relevant energy range of 500 keV to 9000 keV, simulations in steps of 100 keV with $100 \cdot 10^6$ photons each have been performed resulting in simulated energy spectra for each detector. These spectra have been analysed with respect to the full energy peak, *i.e.*, corresponding to photons that deposit their full energy in the detector crystal. Those are relevant for the detector efficiency. The intensity in the full energy peak has been divided by the number of simulated photons yielding the detector efficiency. The resulting data have been described via the empirically found expression [Kno10]

$$\ln \varepsilon(E) = \sum_{k=1}^5 a_k \cdot \left(\ln \frac{E}{E_{\text{const}}} \right)^{k-1}, \quad (7.6)$$

where the constant E_{const} was arbitrarily set to 1000 keV.

The parametrisation of the photon-flux distribution and the detector efficiency are multiplied leaving two fitting parameters free. On the one hand, the endpoint energy of the Schiff parametrisation and, on the other hand, a normalisation factor are used to fit the parametrisation for $N_\gamma \varepsilon$ to the experimentally deduced data points. The fit is performed separately for each detector and measurement. Eventually, for each measurement the results are averaged. With this method, endpoint energies of $E_0(\text{ABS}) = 7.99(15)$ MeV, $E_0(\text{NRF}) = 8.38(28)$ MeV, and $E_0(\text{RSA}) = 8.07(12)$ MeV are found for the absorption, nuclear resonance fluorescence and relative self-absorption measurements, respectively. Figure 7.2 exemplarily illustrates the parametrisations for the photon flux, the efficiency and the resulting product for the case of DET2 in the NRF measurement. Panel (d) depicts the residuum δ between the

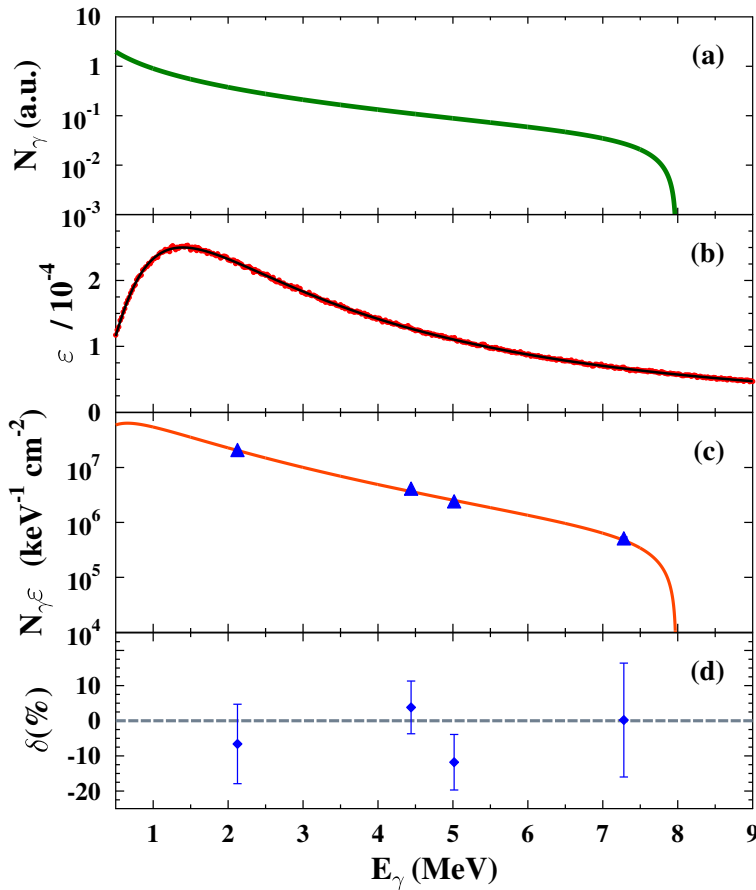


Figure 7.2.: (a) The photon-flux distribution parametrised exploiting the Schiff formula [Sch51]. The parameter describing the endpoint energy is set to 8380 keV. **(b)** The energy dependence of the detector efficiency of DET2. The red points are results from simulations performed with GEANT4. The black curve has been fitted to these points. **(c)** The blue triangles represent the experimentally deduced results for $N_\gamma \epsilon$ which have been evaluated at the transitions energies of ^{11}B for DET2. The orange parametrisation is the product of the green photon-flux curve and the black efficiency curve. It is normalised to the experimental points. **(d)** The residuum between the experimentally determined results and the fitted curve.

experimentally deduced results for $N_\gamma \epsilon$ and the fitted curve. For DET2, it varies between -11% and 6% . Those numbers are also typical residua of $N_\gamma \epsilon$ for the other detectors and measurements.

The Angular Distribution

Having calibrated the photon-flux distribution and the detector efficiency, it is possible to determine the spin quantum number J_i of states excited in the NRF measurement. The spin quantum number is required to deduce the angular distribution of the emitted photons which, in turn, is the last missing quantity in Eq. (7.1) to deduce the NRF cross section $I_{0 \rightarrow i \rightarrow j}$. As has been pointed out in Sec. 4.2, with the ratio

$$w = \frac{A_{i \rightarrow j}(90^\circ)}{A_{i \rightarrow j}(130^\circ)} \cdot \frac{\epsilon(130^\circ)}{\epsilon(90^\circ)} \quad (7.7)$$

of the measured peak intensities in the detectors at 90° and 130° and the corresponding detector efficiencies, the spin quantum number can be determined. The results of the spin assignments are presented and discussed in Sec. 7.3.

After having determined the spin quantum numbers of the excited states, they can be used to evaluate the angular distribution $W_{i \rightarrow j \rightarrow k}(\vartheta)$ from Eq. (4.7) at $\vartheta = 130^\circ$ for DET1 and DET2 as well as at $\vartheta = 90^\circ$ for DET3. For the spin sequences occurring in the present case, $0 \rightarrow 1 \rightarrow 0$ and $0 \rightarrow 2 \rightarrow 0$, respectively, $W_{i \rightarrow j \rightarrow k}(\vartheta)$ specialises to

$$\begin{aligned} W_{0 \rightarrow 1 \rightarrow 0}(\vartheta) &= \frac{3}{4} (1 + \cos^2 \vartheta), \\ W_{0 \rightarrow 2 \rightarrow 0}(\vartheta) &= \frac{5}{4} (1 - 3 \cos^2 \vartheta + 4 \cos \vartheta^4). \end{aligned} \quad (7.8)$$

Γ_0^2/Γ and Reduced Transition Probability

At last, when all quantities are prepared and determined as described above, the integrated NRF cross section $I_{0 \rightarrow i \rightarrow 0}$ for ground-state transitions is determined via Eq. (7.1). Further, rewriting Eq. (4.29), the quantity

$$\frac{\Gamma_0^2}{\Gamma} = \frac{I_{0 \rightarrow i \rightarrow 0}}{\pi^2 \cdot \left(\frac{\hbar c}{E_i}\right)^2 \cdot g} \quad (7.9)$$

is deduced, too. It is required as input for the analysis of the RSA measurement as has been discussed in Sec. 5.4.2. Eventually, by specialising Eq. (4.35), the reduced transition probabilities

$$\frac{B(E1)\uparrow}{[e^2 \text{fm}^2]} = 9.554 \cdot 10^{-4} \cdot g \cdot \frac{\Gamma_0}{[\text{meV}]} \cdot \left(\frac{[\text{MeV}]}{E_\gamma} \right)^3 \quad (7.10)$$

and

$$\frac{B(M1)\uparrow}{[\mu_N^2]} = 8.641 \cdot 10^{-2} \cdot g \cdot \frac{\Gamma_0}{[\text{meV}]} \cdot \left(\frac{[\text{MeV}]}{E_\gamma} \right)^3 \quad (7.11)$$

for electric and magnetic dipole transitions can be determined, respectively.

7.3 The Classical NRF Measurement - Results and Discussion

In the previous section, all quantities required to determine the integrated cross section $I_{0 \rightarrow i \rightarrow 0}$ have been discussed and the analysis procedure has been described. The recorded spectra have been analysed in this way exploiting the analysing and fitting program `Tv` [The92]. In this section, the obtained results will be presented and discussed with respect to four other NRF measurements on ^{140}Ce . Herzberg and collaborators performed two NRF measurements on this nuclide. At the bremsstrahlung facility of the Stuttgart Dynamitron, the endpoint energy accounted to $E_0 = 4.1 \text{ MeV}$ [Her95a, Her95b]. Thus, it is well suited for a comparison of the half-lives of low-lying excited states such as 2^+ levels. The second measurement has been conducted at the S-DALINAC in Darmstadt with an endpoint energy of $E_0 = 6.7 \text{ MeV}$ [Her95a, Her97]. Another NRF experiment on ^{140}Ce by Volz and co-workers has also been performed in Darmstadt [Vol06]. They extended the endpoint energy to $E_0 = 9.9 \text{ MeV}$, which is slightly higher as the neutron separation energy of ^{140}Ce at $S_N = 9.2 \text{ MeV}$. Recently, Löher and collaborators performed NRF measurements at the High Intensity γ -ray Source scanning the energy range between 5.2 MeV and 8.3 MeV in steps of about 250 keV where the width of the quasi-monochromatic photon spectra accounted also to $\sim 250 \text{ keV}$ [Löh14]. These measurements were performed with the γ^3 setup [Löh13] which allows for $\gamma - \gamma$ coincidence measurements.

In total, 117 peaks have been assigned to transitions in ^{140}Ce of which 45 have also been observed in Ref. [Her95a, Her97] and 41 have also been re-

Table 7.4.: Possible inelastic transitions to the first excited 2^+ level. Two transition energies $E_{\gamma,1}$ and $E_{\gamma,2}$ are listed if their difference is in accordance with the energy $E_{2_1^+} = 1596.5(4)$ keV of the 2_1^+ state within the uncertainties. Those are given by the sum of the individual uncertainties of $E_{\gamma,1}$ and $E_{\gamma,2}$.

$E_{\gamma,1}$ (keV)	$E_{\gamma,2}$ (keV)	$E_{\gamma,1} - E_{\gamma,2}$ (keV)
5620.4(4)	4025.2(4)	1595.2(8)
6923.8(3)	5327.9(3)	1595.9(6)
6934.2(3)	5337.1(2)	1597.1(5)
7216.3(5)	5620.4(4)	1595.9(9)
7714.7(6)	6118.9(1)	1595.8(8)

ported by Volz *et al.* [Vol06]. All despite of six transitions have also been observed by Löher [Löh14]. The results for the 117 transitions observed in this work are summarised in Tables B.1 to B.4 in Appendix B. In the following, they are discussed with respect to different aspects.

Ground-State and Inelastic Transitions

The Ritz variation principle, that has been explained in the previous section, has been applied to all transition energies that have been assigned to ^{140}Ce to search for possible transitions to lower-lying excited states, *i.e.*, for so-called *inelastic* transitions. The list, which includes 117 energies, has further been extended by nine previously known levels up to 3 MeV excitation energy with spin quantum numbers of 0^+ , 1^\pm , 2^+ , and 3^\pm which were not observed in the present measurement. They still may be fed by higher-lying levels, but not be observed due to the rather high background at small energies. A comparison of all combinations of the transition energies with this list yielded 20 combinations of energies $E_{\gamma,1}$ and $E_{\gamma,2}$ whose difference $E_{\gamma,1} - E_{\gamma,2}$ is in accordance with a transition energy within the uncertainties. In this case, the uncertainties were determined by adding the individual errors of the transition energies. For instance, five peaks may correspond to inelastic transitions to the first excited 2^+ level. They are summarised in Table 7.4. However, the energy criterion is not sufficient to distinguish between ground-state and inelastic transitions. This is emphasised by the following test. Instead of the real ground-state transition energy of the 2_1^+ level, the Ritz variation principle has been applied to two randomly chosen energies, namely “ $E_{2_1^+}$ ” = 1644.5(5) keV

and “ $E_{2_1^+}$ ” = 1505.7(3) keV. Interestingly, four and three combinations, respectively, have been found suggesting inelastic decays via these made up levels. For another test, all transition energies below 3 MeV excitation energy have been replaced by randomly chosen numbers which resulted in about 20 combinations of transition energies coinciding with a transition energy, too.

With the $\gamma - \gamma$ coincidence measurement reported in Ref. [Löh14], $b_{2_1^+}$ branching ratios to the 2_1^+ level for individual states have been investigated. In total, inelastic transitions to the 2_1^+ state have been observed for 25 excited states between 5.5 MeV and 6.8 MeV. The corresponding branchings to the 2_1^+ level range from about 1 % up to 60 %. These results can be exploited to check if the found candidates for inelastic transitions to the 2_1^+ level from Table 7.4 can be confirmed. Indeed, only the excited level at 5620.4 keV was found in Ref. [Löh14] to decay via the 2_1^+ level with a decay branch of $b_{2_1^+} = 11(4)\%$. The remaining 24 excited states, that exhibit a decay branch to the first excited 2^+ level according to Ref. [Löh14], either have not been observed at all in the present measurement or their branching ratio to the 2_1^+ level is such small that the corresponding transition to the 2_1^+ level has not been observed. In particular, the excited states that are reported to have strong $b_{2_1^+}$ branching ratios larger than 5 % are comparatively weakly excited. In general, they do not exceed $\Gamma_0^2/\Gamma \sim 50$ meV and, hence, are not observed in the present measurement. In turn, those states being stronger excited exhibit only small values for $b_{2_1^+}$.

Assuming, that the peak at an energy of 4025.2 keV can purely be ascribed to the inelastic decay of the excited state at 5620.4 keV, the branching ratio to the 2_1^+ determined in this work would yield 63(15) %. This branching ratio is significantly larger as the one from Ref. [Löh14] indicating that there is also an excited state at 4025.2 keV. The peak intensity at 4025.2 keV has been corrected for the feeding from the level at 5620.4 keV excitation energy exploiting the branching ratio $b_{2_1^+}$ from [Löh14].

For the remaining combinations of transition energies that match the energy of the 2_1^+ level or any other transition energy from the list, no unambiguous assignment as inelastic transition can be made. However, in nine out of the 20 combinations, peaks at the transition energies $E_{\gamma,2}$ have also been observed at $\text{HI}^{\gamma}\text{S}$ within the narrow excitation-energy regions [Löh14]. In these measurements, inelastic decays from higher-lying levels can be ruled out and, consequently, a complete inelastic character of those peaks can be ruled out, as well. Nevertheless, a reliable decision whether these peaks may correspond at least partly to inelastic decays is not feasible. Therefore, all observed transitions are

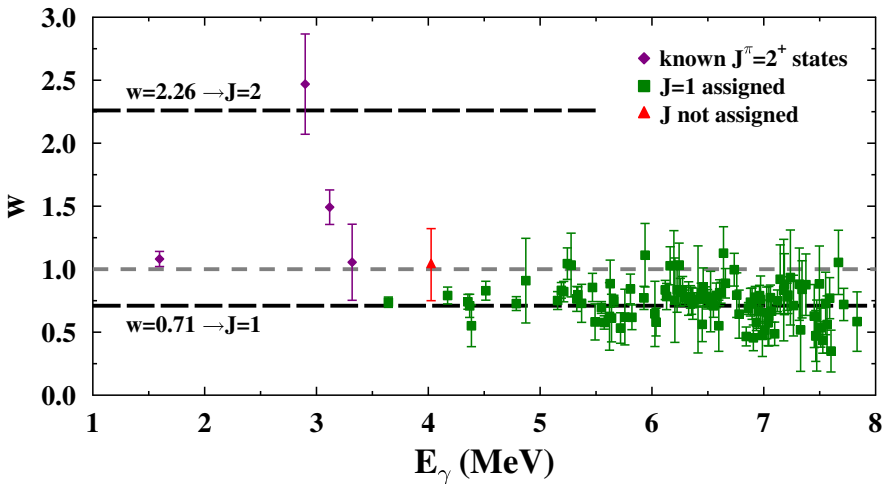


Figure 7.3.: Results for the intensity ratio w and the corresponding spin assignments. The first four observed excited states are already known as $J^\pi = 2^+$ states (purple diamonds). The green squares represent excited states that have been identified as $J = 1$ states. No spin quantum number can be assigned to the excited state shown with a red triangle.

treated as ground-state transitions in the following.

Spin Quantum Numbers

For the spin assignment to the observed excited states, the intensity ratio w has been determined according to Eq. (7.7) exploiting the detector combinations of DET3 with DET1 as well as of DET3 with DET2. A detailed overview of the results for w and the corresponding peak intensities in the NRF measurement, that have been corrected for single escape contributions, is given in the Appendix in Tables B.1 and B.2. Figure 7.3 shows the averaged results for w of both detector combinations. In the case, that the ratio yields $w = 2.26$ the corresponding excited state can be identified as $J = 2$ level. The first four observed excited states at excitation energies of 1596.5 keV, 2899.2 keV, 3117.9 keV, and 3319.0 keV are already known as $J^\pi = 2^+$ levels [Nic07]. They are illustrated via purple diamonds. In the present work, $J = 2$ can

only be assigned to the level at $E_i = 2899.2\text{keV}$. For the other three states, the intensity ratio is significantly shifted towards unity. This shift can be attributed to a feeding of these levels. Although only in one case a decay to the 2^+_1 level has been observed, many states may have only weak branchings to low-lying levels which, in sum, also lead to a strong feeding of these low-lying levels. Thereby, the angular distribution for photon emission becomes diluted on average leading to a more isotropic distribution. A spin quantum number of $J = 1$ can be assigned to those states where the intensity ratio calculates to $w = 0.71$. In the present work, the ratio w agrees with $w = 0.71$ for 108 excited states within a 2σ interval. They are marked by green squares in Fig. 7.3. The assignment as $J = 1$ states confirms the results of the previous experiments [Her95a, Vol06, Löh14]. However, four of these states have not been observed in the other measurements. They exhibit an intensity ratio being smaller than $w = 1$ within a 2σ interval and, thus, can be reliably assigned as $J = 1$ states. In contrast, the intensity ratio of another state at 4025.2keV excitation energy (marked with a red triangle) accounts to $w = 1.04(29)$. This is in agreement with $w = 0.71$ within a 2σ interval, as well. However, it may also be a strongly fed 2^+ level. Indeed, it is fed by the level at an excitation energy of 5620.4keV . Since it has not been observed in any of the other measurements, a spin assignment to this level is not possible.

Eventually, for four other excited states at 6065.3keV , 6581.8keV , 7159.5keV , and 7659.5keV , the intensity ratio cannot be determined from this work since the corresponding ground-state transition has not been observed in the detector at a scattering angle of 90° (DET3). However, the detection limit for $E2$ transitions is smaller for DET3 as for DET1 and DET2 since the angular distribution of the decay photons after a $0 \rightarrow 2 \rightarrow 0$ spin sequence exhibits a maximum at $\vartheta = 90^\circ$ (see also Fig. 4.2). The detection limits for $E1$ and $E2$ transitions are shown in Fig. B.1 of Appendix B. Being not observed in DET3 hints at a dipole character of the decay radiation. Thus, $J = 1$ is assumed for those states. The levels at excitation energies of 6065.3keV , 6581.8keV , and 7159.5keV have also been reported by Löher *et al.* and, indeed, have been identified as dipole states. The excited state at 7659.5keV has not been observed in Ref. [Löh14].

Integrated Cross Sections and Related Quantities

In this paragraph, the results of the integrated cross sections and related quantities will be presented and compared to the literature values of Refs. [Her95a, Her95b, Her97, Vol06, Nic07]. At first, the four 2^+ lev-

Table 7.5.: Comparison of level energies E_{level} and half-lives $T_{1/2}$ of the four $J^\pi = 2^+$ levels that have been observed in this work. The level energies are taken from Ref. [Nic07], the half-lives from Ref. [Her95b].

E_{level} (keV)	$E_{\text{level}}^{\text{lit}}$ (keV)	Γ_0^2/Γ (meV)	$T_{1/2}$ (fs)	$T_{1/2}^{\text{lit}}$ (fs)
1596.5(4)	1596.237(25)	32(8)*	14(4)*	91(7)
2899.2(3)	2899.66(15)	12(1)	14(1)**	67(16)
3117.9(1)	3118.55(16)	24(4)	19(3)	36(3)
3319.0(2)	3320.4(6)	10(3)	46(14)	154(38)

* corrected for feeding from the level at 2899 keV acc. to Ref. [Nic07]

** determined with $\Gamma_0/\Gamma = 0.61(4)$ from Ref. [Nic07]

els observed in this work will be discussed. Subsequent, the 1_1^- level at $E_i = 3642.9$ keV will be treated. Eventually, the $B(E1)\uparrow$ -strength distribution is discussed and compared to previous measurements. An overview of the results for the integrated cross section, for Γ_0^2/Γ , as well as for the reduced transition strengths is furthermore given by Tables B.3 and B.4 in Appendix B.

i) Quadrupole-excited Levels

Table 7.5 gives an overview of the four 2^+ states that have been observed in the present measurement. The level energies deduced in this work and those of the *Nuclear Data Sheets* [Nic07] are listed as well as the results for Γ_0^2/Γ and the half-lives deduced in this work in comparison to those of Ref. [Her95b]. The measured level energies E_{level} are in good agreement with the literature values. However, the level energies of the 2^+ states at $E_{\text{level}} = 3117.9$ keV and $E_{\text{level}} = 3319.0$ keV exhibit a small deviation to smaller values compared to those reported in the *Nuclear Data Sheets* [Nic07]. In contrast, the half-lives of the 2^+ levels determined in the framework of this thesis strongly deviate from the results of Herzberg and co-workers [Her95b]. They are significantly smaller. This deviation can be ascribed to a feeding of the low-lying 2^+ levels. The NRF measurement of Herzberg has been conducted at an endpoint energy of $E_0 = 4.1$ MeV [Her95b]. Therefore, feeding of the 2^+ levels from higher-lying levels can be excluded, while inelastic transitions in-between the 2^+ levels have been taken into account. The half-lives being too small in the present experiment is tantamount to the cross section being overestimated. This, in turn, means that the low-lying states are not exclusively populated by

the incident photon beam. They must be fed from higher-lying excited states. Further evidence for a strong feeding has already been discussed in the previous paragraph. The intensity ratios of the observed 2^+ states are shifted to values close to one. This also hints at a strong feeding of these states.

For the excited state at 2899.2 keV excitation energy, a branching ratio of $\Gamma_{2_1^+}/\Gamma = 0.39(4)\%$ is reported in Ref. [Nic07]. This ratio has been taken into account for the determination of the half-life of the excited level. The feeding of the 2_1^+ state coupled to this inelastic transition has been accounted for as well.

ii) 1_1^- State at $E_i = 3643$ keV

The lowest-lying excited dipole state, which has been observed in the present work, is the 1_1^- level. It has been identified as the 1^- member of the two-phonon $(2_1^+ \otimes 3_1^-)$ quintuplet [Her97]. The measured level energy of $E_i = 3642.9(1)$ keV is in good agreement with the literature value which accounts to $3643.1(10)$ keV [Nic07]. The current literature value for the transition width is reported to be $\Gamma = 289(18)$ meV [Nic07]. This value is the weighted average of the NRF results of Herzberg and collaborators that have been obtained at bremsstrahlung-endpoint energies of 4.1 MeV and 6.7 MeV, respectively. The individual results yielded $\Gamma_0^2/\Gamma = 281(20)$ meV at $E_0 = 4.1$ MeV [Her95b] and $\Gamma_0^2/\Gamma = 307(39)$ meV at $E_0 = 6.7$ MeV [Her95b]. A branching to lower-lying states has not been observed. In contrast, for the decay to the 2_1^+ level an upper limit for the branching ratio of $\Gamma_{2_1^+}/\Gamma < 4\%$ has been found. Eventually, the NRF measurement by Volz with an endpoint energy of 9.9 MeV resulted in a higher value of $\Gamma_0^2/\Gamma = 367(56)$ meV. The trend of an increasing value for Γ_0^2/Γ with increasing endpoint energy exploited in the corresponding NRF measurements may hint at a feeding of the two-phonon state. However, in the present work, the product of ground-state transition width and branching ratio to the ground state has been determined to $\Gamma_0^2/\Gamma = 265(9)$ meV which is in agreement with the results of the NRF measurements with the lower endpoint energies. At the same time, the intensity ratio w doesn't show any evidence for the two-phonon state being fed. Yielding $w = 0.74(4)$, it is not shifted to one and is in good agreement with the theoretically expected value of $w = 0.71$ for a $0 \rightarrow 1 \rightarrow 0$ spin sequence. Although it exhibits a rather large uncertainty, the result from Ref. [Vol06] significantly differs from the other measurements. It is questionable whether this deviation can be ascribed to feeding effects. Actually, a systematic deviation between the transition widths of the present measure-

ment with those of Ref. [Vol06] but also with the ones from Ref. [Her95a] is observed as will be discussed in the next paragraph.

iii) $B(E1)\uparrow$ -Strength Distribution

The results for the integrated cross section, the product Γ_0^2/Γ and the reduced transition strengths are shown in detail in Table B.3 in the Appendix. All transition strengths have been deduced from the NRF results for Γ_0^2/Γ assuming that the branching ratio to the ground state amounts to one. The $B(E1)\uparrow$ and $B(M1)\uparrow$ values are determined according to the parity assignments of [Löh14]. Where no parity quantum number is known, both values are listed. Starting at 5.1 MeV, a positive parity has only been assigned to one of the dipole states observed in the present work. For 29 states either no parity quantum number has been assigned or they have not been observed in Ref. [Löh14]. Further nine levels are located below the energy range which has been investigated by Löher. To these states no spin has been assigned either. Only the two-phonon state at 3643 keV is known to have negative parity [Nic07]. In total, 117 excited states have been observed in the present measurement. The four lowest-lying states are quadrupole excited 2^+ levels. The majority of 79 states have a spin quantum number of $J^\pi = 1^-$. Furthermore, one 1^+ level has been observed at 6131.0 keV excitation energy. No parity quantum number has been assigned to the remaining 37 levels.

Figure 7.4 summarises the results in form of a $B(E1)\uparrow$ -strength distribution. It is generated assuming negative parity also for those states, where no parity quantum number has been determined so far. The blue line at the bottom represents the sensitivity limit of DET2. Excited states with $B(E1)\uparrow$ strengths smaller than this limit cannot be resolved from the background in the spectra. The strong transition strength at 3.6 MeV corresponds to the two-phonon state which has been discussed before. The strongest excited state has an excitation energy of $E_i = 5659.6$ keV. Its reduced transition strength accounts to $B(E1)\uparrow = 18.7(6) \cdot 10^{-3} \text{ e}^2 \text{fm}^2$. In the excitation-energy range between ~ 5 MeV and 7.5 MeV an accumulation of strongly excited electric dipole states is observed which may be interpreted as the pygmy dipole resonance. In an $(\alpha, \alpha'\gamma)$ measurement [Sav06a], a splitting of this group of levels into two parts with different nuclear structure has been observed. The excited states between ~ 5 MeV and 6 MeV are excited with the (γ, γ') as well as the $(\alpha, \alpha'\gamma)$ reaction, whereas the levels between ~ 6 MeV and 7.5 MeV are exclusively excited via the NRF reaction. This phenomenon has later been attributed to a

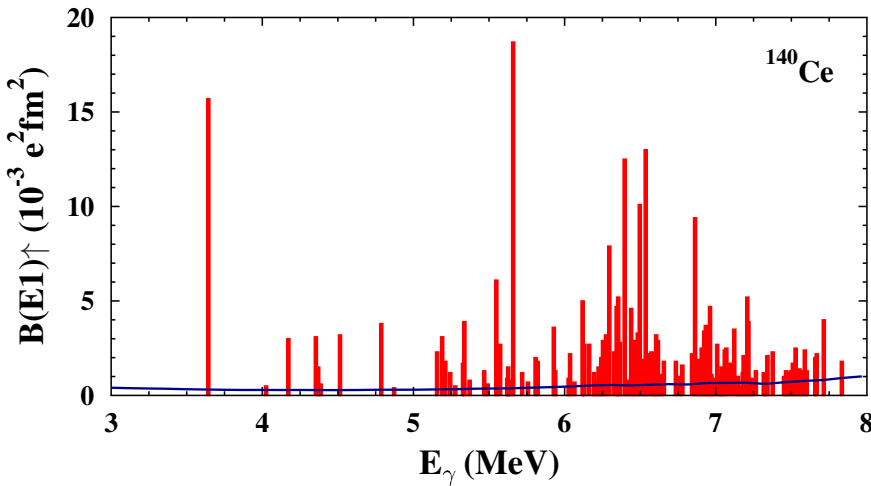


Figure 7.4.: The $B(E1)\uparrow$ -strength distribution of ^{140}Ce has been determined from the results for Γ_0^2/Γ assuming that $\Gamma_0/\Gamma = 1$ for all states. Furthermore, also excited states with no parity assignment have been treated as electric dipole states. The sensitivity limit of DET2 is given via the blue line.

splitting into an isoscalar and an isovector part, where the first is more related to a neutron-skin oscillation (the “real” PDR) and the second one to the tail of the giant dipole resonance [End10, Lan14].

A comparison of the transition strengths determined in the framework of this thesis to the results of Herzberg and Volz is shown in Figs. 7.5 and 7.6. Additionally, the detailed $B(E1)\uparrow$ values deduced in this thesis, as well as in the works of Herzberg and Volz are listed in Table B.4 in the Appendix of this thesis.

Herzberg observed 45 dipole excited states in the NRF measurement with an endpoint energy of 6.7 MeV [Her95a, Her97]. The corresponding $B(E1)\uparrow$ strengths are illustrated in Figure 7.5 via the green circles. The results of the present analysis are shown with red diamonds. When available, also the results of the NRF measurement with bremsstrahlung up to an energy of 9.9 MeV [Vol06] are included. They are represented via blue squares. For clarity, the results are shown in a row and are not plotted as function of the energy. As is

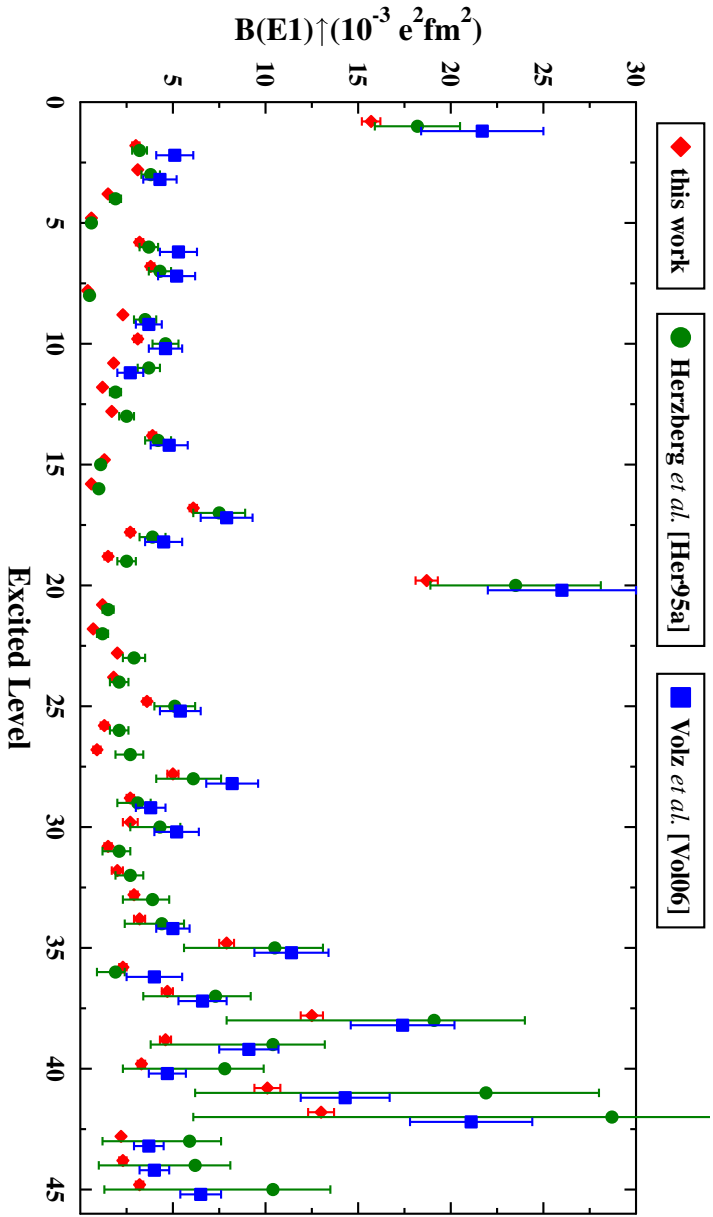


Figure 7.5.: Results for $B(E1)\uparrow$ -transition strengths as obtained in the present work compared to results of Herzberg [Her95a, Her97] and Volz [Vol06]. For the clarity of the figure, the excited states are listed in a row and not as function of the energy.

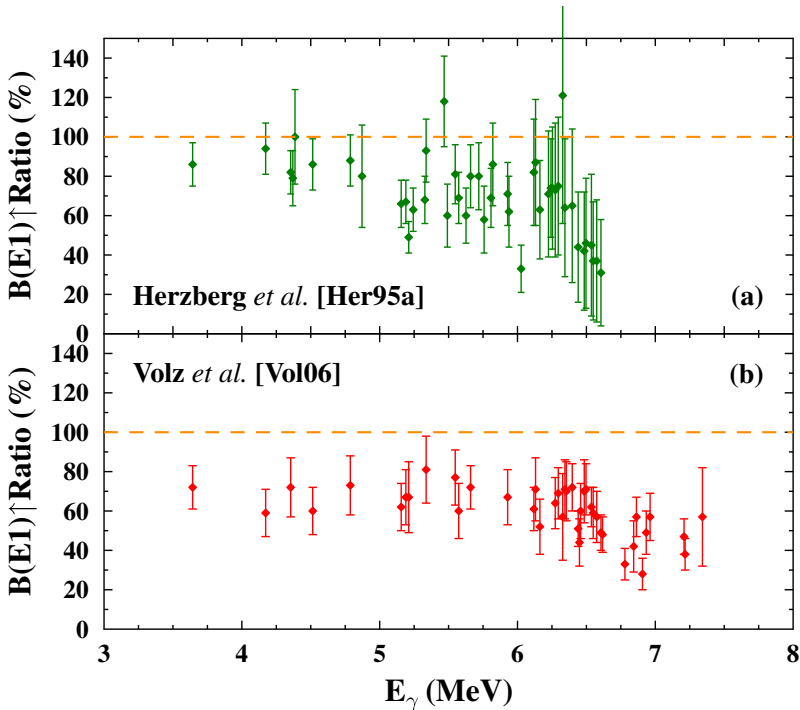


Figure 7.6.: Ratios of the $B(E1)\uparrow$ -transition strengths that have been determined in this thesis with the ones obtained (a) by Herzberg [Her95a, Her97] and (b) by Volz [Vol06]. The present results are substantially smaller as the results of the previous measurements.

apparent from the figure, the results of the present work deviate significantly from those of Herzberg and in particular from the results of Volz. This difference has already been observed during the discussion of the two-phonon state. It even becomes more evident in Fig. 7.6. There, the ratio of the $B(E1)\uparrow$ strengths determined in this work to the ones from Herzberg [Fig. 7.6 (a), upper panel] and from Volz [Fig. 7.6 (b), bottom panel] are shown as function of the energy for the 45 and 41 dipole states observed by Herzberg and Volz, respectively. Besides a few exceptions, the results of Herzberg are larger as the ones determined in this work. The $B(E1)\uparrow$ ratios differ between 40 and 90 %. However, especially the ratios close to the endpoint energy at 6.7 MeV exhibit

large uncertainties. The $B(E1)\uparrow$ strengths determined by Volz *et al.* are considerably larger than those from this thesis, too. Apart from the energy region above ~ 6.5 MeV, these ratios seem to be nearly constant. Fitting a constant parameter to the data yields a deviation of 56(3) % with a reduced chisquare of $\chi^2 = 1.3$. Also the fit of a linear slope $m \cdot x + b$ results in a chisquare close to one. It yields $m = -0.009$ and $b = 113.05$ with $\chi^2 = 0.9$. However, the gradient is close to zero. This systematic deviation hints at a missing constant number during the calculation of the integrated cross section in the analysis of either the data of Volz or those of this thesis. The fact, that also the results of Herzberg deviate from the ones obtained in the present work suggests a problem in the present analysis. However, a reanalysis of the current spectra and the ones recorded during the measurement of Volz, that are still available, confirmed the corresponding results and yielded the same deviation.

Therefore, an independent NRF measurement on ^{140}Ce from 2007 at the S-DALINAC in Darmstadt with an endpoint energy of 9.3 MeV has been analysed. It has been performed for a very first test of the self-absorption method at the DHIPS measuring site. A different target as in the current measurement has been used. It consisted out of 2.3 g of natural CeO_2 . The corresponding results for Γ_0^2/Γ are shown in Fig. 7.7 via yellow triangles (denoted as *NRF II*) for the two-phonon state and the nine strongest excited states that have been observed in the present measurement as well as the one of Volz. The uncertainties of *NRF II* include only the statistical uncertainties of the measured intensities and do not take uncertainties of the detector efficiency and the photon flux into account. As in Fig. 7.5, the red diamonds represent the results of this thesis, whereas the blue squares illustrate the Γ_0^2/Γ values of Volz. The results of *NRF II* rather confirm the ones of this work as the ones of Volz and co-workers.

Eventually, a final check of the transition widths has been performed exploiting the self-absorption measurement, *i.e.*, the measurement with an upstream absorption target, too. As has been pointed out in Sec. 5.4.2, the NRF results for Γ_0^2/Γ are actually required to determine a relation between the ground-state transition width Γ_0 and the level width Γ which, in turn, allows for the analytical calculation of the self absorption as a function of Γ_0 . However, assuming $\Gamma_0 = \Gamma$, the self-absorption measurement can also be evaluated yielding results for Γ_0 and with the assumption $\Gamma_0/\Gamma = 1$ also for Γ_0^2/Γ . The self absorption describes the relative decrease of the number of NRF reactions in the scattering target in the measurement with absorber with respect to the classic NRF measurement without absorption target. Therefore, this quantity does not depend on the target mass of the scatterer. During the evaluation of the self absorption

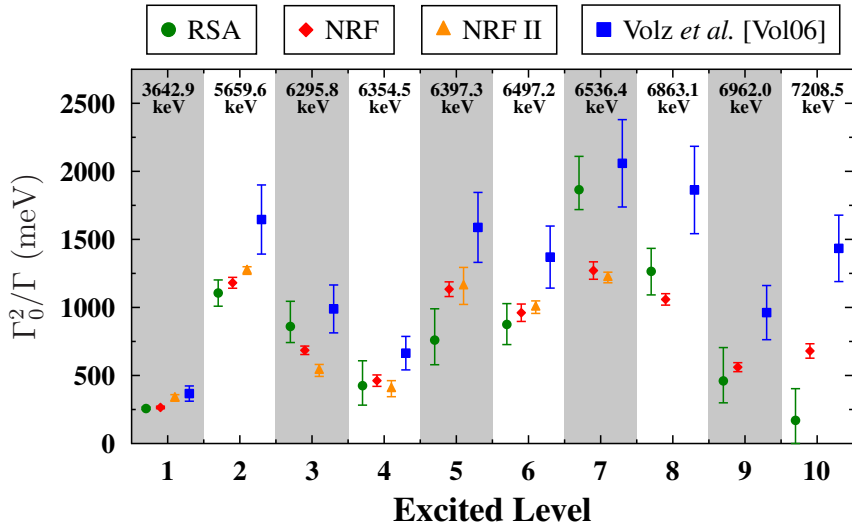


Figure 7.7.: The results for Γ_0^2/Γ of the two-phonon state at 3642.9 keV excitation energy and the nine strongest excited states are compared for different measurements. The red diamonds correspond to the present NRF measurement, whereas the results of Volz [Vol06] are shown via blue squares. The results shown via yellow triangles stem from an independent, unpublished NRF measurement at DHIPS in Darmstadt. Eventually, the green circles illustrate results of the self-absorption measurement that have been determined with the condition $\Gamma_0 = \Gamma$. Details are discussed in the text.

the scatterer mass appears as an integration limit [see Eq. (5.12)]. However, a change of the target mass by 30 % affected the results for Γ_0 only on a sub-% level.

Such an analysis of the self absorption R has been performed for the excited states shown in Fig. 7.7. Since strongly excited states are expected to decay predominantly directly to the ground state which will be confirmed with the results of the actual self-absorption measurement in Sec. 7.5, the above made assumption is justified for these states. Besides the assumption $\Gamma_0 = \Gamma$, the analysis procedure is analogous to the one described in Sec. 7.4. The results of this analysis are given via the green circles in Fig. 7.7. Apart of the excited

states at $E_i = 6295.8\text{ keV}$ and $E_i = 6536.4\text{ keV}$, the RSA results support the present NRF measurement. However, as will be discussed in Sec. 7.5, for the level at $E_i = 6536.4\text{ keV}$, a non-physically large self absorption has been measured. The corresponding large value for Γ_0 should not be relied on.

In conclusion, a significant deviation between the cross sections determined in the framework of this thesis and earlier measurements by Herzberg [Her95a, Her97] and Volz [Vol06] has been observed. Despite a reanalysis of the present data and those of Volz *et al.*, no explanation for this deviation has been found. However, with the reanalysis of the data sets, a mistake during the analysis like a factor not taken into account can be ruled out fairly confidently. Consequently, the last remaining considerable element of uncertainty are the target masses. One of them may have been determined wrongly or may have been affected by intercalation of hydrogen, water or any other contaminant.

The results of the current measurement agree with an independently, unpublished NRF measurement in Darmstadt. Furthermore, an analysis of the self absorption R for strongly excited states assuming $\Gamma_0 = \Gamma$ also confirms the present results. This approach has only a very weak dependence on the target mass and, thus, would only be little affected by a wrongly determined target mass. Consequently, the following analysis of the self-absorption measurement will be based and will rely on the results for Γ_0^2/Γ obtained in this work.

7.4 The RSA Measurement - Analysis

After the analysis of the NRF measurement, the RSA measurement can be evaluated. In a first step, the self absorption R_{exp} is determined. Then, exploiting the results of the NRF experiment for Γ_0^2/Γ , results for the ground-state transition width Γ_0 , for the level width Γ , and, as a consequence, for the branching ratio to the ground state can be extracted. In this chapter, the mandatory steps of the analysis are presented and discussed.

7.4.1 Determination of R_{exp}

The experimental results for the self absorption R_{exp} are determined according to Eq. (5.4). Before this equation can be applied, preparatory steps have to be performed such as a correction for single-escape events and inelastic transitions

as it has already been discussed in the analysis chapter of the NRF measurement (see, Sec. 7.2). In particular, for the analysis of the RSA experiment on ^{140}Ce , two corrections had to be applied to the RSA spectrum. The first one corrects for photons scattered from the absorber into the detectors, whereas the second one corrects for atomic attenuation. Both corrections require a normalisation of the RSA spectrum to the ABS and NRF spectrum, respectively. This is realised exploiting the peaks corresponding to transitions in the monitoring target. The exact procedure is discussed in the following paragraph.

Corrections and Normalisation Factors

As depicted in Fig. 7.1 the absorption measurement revealed that photons are partly directly scattered from the absorber into the detectors. Those events must be subtracted from the RSA spectrum. Before doing so, both, the RSA and the ABS spectrum, have to be normalised to each other exploiting the peak areas A^{mon} from the ^{11}B monitoring target. At the ^{11}B transition energies E_γ , the normalisation factor is determined via

$$f_{\text{RSA,ABS}}(E_\gamma) = \frac{A_{\text{RSA}}^{\text{mon}}}{A_{\text{ABS}}^{\text{mon}}} = \frac{N_{\gamma,\text{RSA}}(E_\gamma) \cdot \varepsilon(E_\gamma) \cdot N_T^{\text{mon}} \cdot W_{0 \rightarrow i \rightarrow 0} \cdot I_{0 \rightarrow i \rightarrow 0}}{N_{\gamma,\text{ABS}}(E_\gamma) \cdot \varepsilon(E_\gamma) \cdot N_T^{\text{mon}} \cdot W_{0 \rightarrow i \rightarrow 0} \cdot I_{0 \rightarrow i \rightarrow 0}}, \quad (7.12)$$

where the second part of the equation corresponds to Eq. (4.32). The detector efficiency $\varepsilon(E_\gamma)$, the number of target nuclei N_T^{mon} , the angular distribution $W_{0 \rightarrow i \rightarrow 0}$, as well as the integrated cross section $I_{0 \rightarrow i \rightarrow 0}$ are identical for both measurements and, hence, cancel out. Therefore, $f_{\text{RSA,ABS}}$ depends on the ratio of the photon flux at E_γ , only. With identical endpoint energies, the spectral photon-flux distribution is the same in both measurements. Consequently, the normalisation factor $f_{\text{RSA,ABS}}(E)$ is expected to be constant with energy. However, as it is demonstrated in Fig. 7.8 and in Table 7.6, the experimentally deduced results for $f_{\text{RSA,ABS}}$ exhibit a weak energy dependence. In Table 7.6, the factor $f_{\text{RSA,ABS}}$ is listed for all three detectors, as well as the uncertainty-weighted average of these values. Figure 7.8 (a) illustrates the averaged values.

The energy dependence may be explained with the endpoint energies of the RSA and the ABS measurement not being perfectly identical. Indeed, an investigation of the endpoint energies in both measurements resulted in slightly different values. The analysis yields 7990 keV for the absorption measurement and 8070 keV for the self-absorption measurement. The determination of these endpoint energies has been described in the discussion of the efficiency and

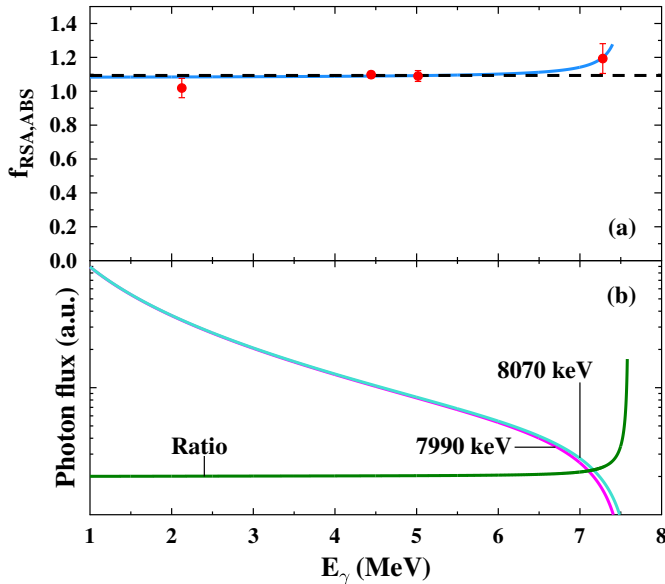


Figure 7.8.: In the upper panel (a) the normalisation factor $f_{RSA,ABS}$ is shown. The red points represent experimental results that have been obtained at the ^{11}B transition energies. While the dotted line corresponds to the fit of a constant to the experimental data, the blue fitting curve has been extracted from the ratio of two bremsstrahlung distributions with endpoint energies of 7990 keV and 8070 keV, respectively. They are shown in the lower panel (b) together with their ratio (green).

Table 7.6.: Normalisation factors $f_{RSA,ABS}$ that were determined for each detector individually at the ^{11}B transition energies. For further analysing steps, the error-weighted average is taken. It is shown in the last column.

E_γ (keV)	DET1	DET2	DET3	$\bar{f}_{RSA,ABS}$
2124.5	1.29(13)	1.01(7)	0.99(4)	1.02(6)
4443.9	1.09(3)	1.13(2)	1.07(2)	1.10(2)
5019.1	1.17(3)	1.09(2)	1.05(2)	1.09(3)
7282.9	1.15(19)	1.37(6)	1.11(13)	1.19(9)

photon-flux calibration in Sec. 7.2. The ratio of two Schiff parametrisations with endpoint energies of 7990 keV and 8070 keV [see Fig. 7.8 (b), blue and magenta curves], respectively, yields an almost constant curve which has a strong upbend at ~ 7590 keV (green curve). It can be described using the following parametrisation

$$\frac{p_1}{E - 7590 \text{ keV}} + p_2. \quad (7.13)$$

This parametrisation has been exploited to describe $f_{\text{RSA,ABS}}(E)$. It accounts for the different endpoint energies and the resulting energy dependence of $f_{\text{RSA,ABS}}$. Thus, particularly the description of the point at 7282.9 keV is improved [see Fig. 7.8 (a), blue curve] in comparison to a fit with a constant parameter, which is shown via the dotted line.

Events stemming from NRF reactions in the absorption target are subtracted from the measured peak areas via

$$A'_{\text{RSA}} = A_{\text{RSA}} - f_{\text{RSA,ABS}}(E_{\gamma}) \cdot A_{\text{ABS}}, \quad (7.14)$$

exploiting the normalisation factor $f_{\text{RSA,ABS}}(E)$ obtained in this way. Corrected peak areas are calculated for the corresponding transition energies E_{γ} of ^{140}Ce . As has been illustrated with Fig. 7.1, this correction is comparatively small. Only few photons passed through the shielding. However, for the strongest transitions, the correction can amount to up to 12 %.

Furthermore, a correction for atomic attenuation processes has to be applied during the analysis of self-absorption experiments. In analogy to the correction for scattered photons in the absorber, a normalisation factor has to be determined for a proper comparison of the RSA and the NRF spectrum. It is defined via

$$f_{\text{RSA,NRF}}(E_{\gamma}) = \frac{A_{\text{RSA}}^{\text{mon}}}{A_{\text{NRF}}^{\text{mon}}} = \frac{N_{\gamma,\text{RSA}}(E_{\gamma}) \cdot \varepsilon(E_{\gamma}) \cdot N_T^{\text{mon}} \cdot W_{0 \rightarrow i \rightarrow 0} \cdot I_{0 \rightarrow i \rightarrow 0}}{N_{\gamma,\text{NRF}}(E_{\gamma}) \cdot \varepsilon(E_{\gamma}) \cdot N_T^{\text{mon}} \cdot W_{0 \rightarrow i \rightarrow 0} \cdot I_{0 \rightarrow i \rightarrow 0}}. \quad (7.15)$$

Again, $\varepsilon(E_{\gamma})$, N_T^{mon} , $W_{0 \rightarrow i \rightarrow 0}$, and $I_{0 \rightarrow i \rightarrow 0}$ cancel out since they are identical for both measurements. However, in this case, the spectral photon-flux distributions at the scattering-target position in the RSA and the NRF measurement differ as in the RSA measurement the photon flux is modified by the upstream absorber which has not been used in the NRF measurement. The atomic attenuation processes are energy dependent (Sec. 5.2) and, consequently, also

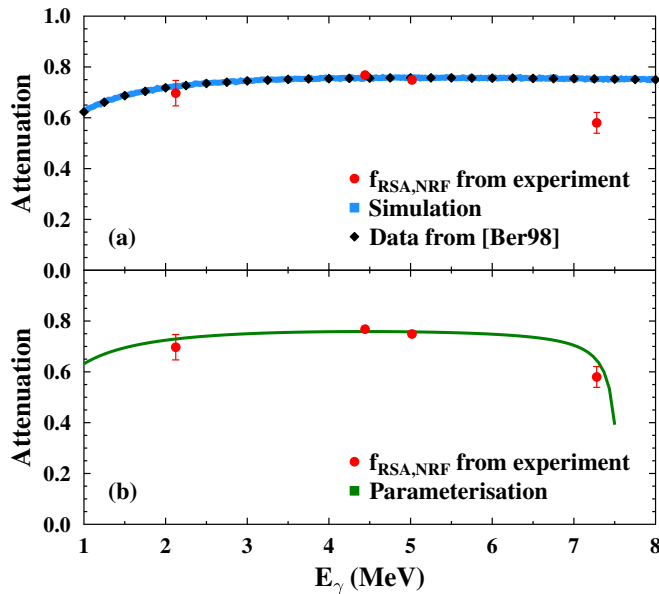


Figure 7.9.: (a) Atomic attenuation simulated with GEANT4 (blue line) and deduced from the atomic attenuation cross section (black diamonds) [Ber98]. The red circles represent the experimentally determined results. (b) The parametrisation of the atomic attenuation takes different endpoint energies of the RSA and NRF measurements into account. It has been scaled to the experimental results.

$f_{RSA,NRF}(E)$ is expected to depend on the energy. In Fig. 7.9 (a) the atomic attenuation is illustrated. The blue line corresponds to simulations with GEANT4 of the absorption target being irradiated with γ -ray beams of varying energies. The black diamonds have been determined exploiting the data for the atomic attenuation cross section κ_{at} taken from Ref. [Ber98] via

$$e^{-\kappa_{at} \cdot d_a}, \quad (7.16)$$

where d_a is the thickness of the absorption target. Both data sets are in good agreement. The experimental results for the normalisation factor $f_{RSA,NRF}$ at the excitation energies of ^{11}B have been deduced separately for each detector and afterwards been averaged. Detailed numbers are listed in Table 7.7. Fig-

Table 7.7.: Normalisation factors $f_{\text{RSA,NRF}}$ that were determined for each detector individually at the ^{11}B transition energies. The error-weighted average given in the last column is taken for further analysing steps.

E_γ (keV)	DET1	DET2	DET3	$\bar{f}_{\text{RSA,NRF}}$
2124.5	0.85(8)	0.63(4)	0.72(4)	0.70(5)
4443.9	0.77(2)	0.77(1)	0.76(2)	0.77(1)
5019.1	0.77(2)	0.73(1)	0.75(2)	0.75(1)
7282.9	0.57(9)	0.59(6)	0.57(7)	0.58(4)

ure 7.9 illustrates the average numbers via the red points. They take atomic attenuation effects as well as different measuring times and absolute photon-flux intensities into account, whereas the simulation and the calculation solely account for atomic attenuation effects. Therefore, they have to be scaled to the experimental values. However, the point at 7282.9 keV shows a significant deviation from the simulated and calculated energy dependence. As in the previous case, this deviation can be ascribed to different endpoint energies of both measurements. With the method described in Sec. 7.2, an endpoint energy of 8380 keV has been determined for the NRF measurement. With $E_0 = 8070$ keV, the endpoint energy in the RSA measurement was clearly smaller. Therefore, the ratio of two Schiff parametrisations with according endpoint energies has been determined as before. It accounts to one in the energy region between 1 and 7 MeV and steeply increases at 7670 keV. Thus, it can be parametrised via

$$\frac{p_1}{E - 7670} + p_2. \quad (7.17)$$

This expression multiplied with the simulated curve, which describes the energy dependence of the atomic attenuation processes, has been scaled to the experimentally deduced values of the normalisation factor $f_{\text{RSA,NRF}}$. The result is shown in Fig.7.9 (b) by the green curve. In the following, when the self absorption for excited states of ^{140}Ce is determined, this parametrisation is exploited to deduce $f_{\text{RSA,NRF}}$ at the corresponding transition energies.

Figure 7.10 demonstrates the normalisation of the RSA to the NRF spectrum. It exemplarily shows the summed spectra of all three detectors for the NRF and the RSA measurement in the energy range between 4 MeV and 6 MeV. The RSA spectrum is shifted by 30 keV such that the spectra can better be compared. The upper panel shows the original spectra, whereas in the lower panel the

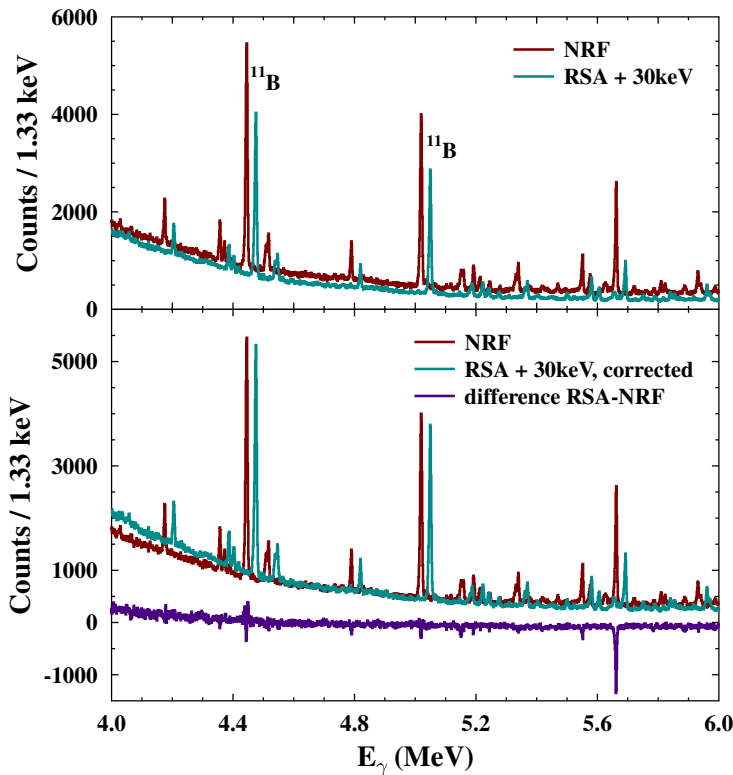


Figure 7.10.: Cutout of the summed NRF and RSA spectra of all three detectors in the energy range between 4 MeV and 6 MeV. The RSA spectrum is shifted by 30 keV. In the lower panel, the normalisation factor $f_{\text{RSA},\text{NRF}}(E)$ has been applied to the RSA spectrum. Furthermore, the purple spectrum represents the difference of the corrected RSA and the NRF spectrum. The negative peaks exemplify the self absorption signal. The self absorption of the excited state at 5.6 MeV is comparatively strong.

normalisation factor $f_{\text{RSA},\text{NRF}}(E)$ has been applied to the RSA spectrum. While in the upper panel a substantial deviation in the yield of the ^{11}B peaks can be observed, it is almost identical after the normalisation has been applied. Owed to slightly different peak shapes, the peaks in the RSA spectrum still

seem to be smaller than in the NRF spectrum. However, the intensities account to 26715(218) and 21052(177) counts in the NRF spectrum for the peaks at 4443.9 keV and 5019.1 keV, respectively, and to 27337(255) and 21140(203) counts in the case of the normalised RSA spectrum. Interestingly, the background is identical only above ~ 4.5 MeV. This may be ascribed to different background radiation, *i.e.*, to photons that are detected without being scattered in the scattering target. On the one hand, atomic scattering of photons from the absorber into the detectors can occur which results in an additional background compared to the NRF measurement. On the other hand, a larger electron current has been chosen in the RSA as in the NRF measurement to balance out the loss of photon-flux intensity due to atomic attenuation in the absorber. Thus, the bremsstrahlung background is higher, as well. Applying the normalisation factor to the RSA spectrum with enhanced statistics in the background, it exceeds the one of the NRF measurement.

Besides the corrected RSA and the NRF spectrum, also their difference is shown in the lower panel of Fig. 7.10. It exemplifies the self-absorption signal with the negative peaks that can completely be attributed to resonant absorption. The excited state at 5.6 MeV exhibits a comparatively strong self absorption, whereas the self-absorption effect is smaller for the weaker excited states.

Determination of $R_{\Gamma_0, \Gamma}$

As a final preparatory step, the Γ_0 dependence of the self absorption has to be analytically calculated. The procedure to determine $R_{\Gamma_0, \Gamma}$ is outlined in detail in Sec. 5.4.2. Since the self absorption depends also on the total level width Γ , the result of the NRF measurement, Γ_0^2/Γ , has been used to define a relation between Γ_0 and Γ . Further input entering the evaluation of $R_{\Gamma_0, \Gamma}$ is represented by the Debye temperature of ^{140}Ce . It is required to deduce the Doppler width Δ (see Sec. 4.2). In the case of CeO_2 it accounts to 480 K [His06]. The calculation of $R_{\Gamma_0, \Gamma}$ for the individual excited states has been performed exploiting the program MATHEMATICA.

7.4.2 Determination of Resulting Quantities

The results for the self absorption R_{exp} allow for the determination of related quantities by comparing this experimentally deduced value with the self-absorption curve $R_{\Gamma_0, \Gamma}$. This curve is determined with the condition that the

relation between Γ_0 and Γ is fixed by the NRF result for Γ_0^2/Γ . It has been discussed in Sec. 5.4.2 that, in this case, a particular value of R_{exp} generally corresponds to two solutions for Γ_0 . However, in the following discussion of the practical determination of Γ_0 , Γ , as well as Γ_0/Γ only the first solution at smaller Γ_0 will be taken into account since the second one is usually related to unlikely large values for Γ . The determination of Γ_0 and further quantities will be depicted in detail in the following paragraphs. Thereby, two different approaches to the analysis have been followed.

Conventional Approach

Figure 7.11 shows the conventional approach used to determine the ground-state transition width Γ_0 from the measured self absorption. The curve of $R_{\Gamma_0, \Gamma}$ has been determined exploiting the relation Γ_0^2/Γ between Γ_0 and Γ from the NRF measurement and, thus, depends only on Γ_0 . Consequently, the direct comparison of R_{exp} with this curve, where R_{exp} is projected to the Γ_0 axis, provides the corresponding result for this quantity. In the same way, the uncertainty barriers $R_{\text{exp}} - \Delta R_{\text{exp}}$ and $R_{\text{exp}} + \Delta R_{\text{exp}}$ can be treated and be projected to the Γ_0 axis. In turn, the resulting values of Γ_0 may be used as uncertainty barriers for the result of Γ_0 . However, these uncertainties are asymmetric and do not obey to a Gaussian distribution. As a consequence, Gaussian error propagation cannot be applied to quantities related to Γ_0 such as the branching ratio to the ground state via $\Gamma_0/\Gamma = (\Gamma_0^2/\Gamma)/\Gamma_0$. An appropriate error calculation is not feasible. To remedy this problem, probability density functions of the investigated quantities will be exploited for the remaining analysis. In particular, a Bayesian data analysis [Wei99, Wei06] and the principle of maximum information entropy [Jay57, Jay89] has been applied to the present data. The general concept of such an analysis procedure is introduced in the following paragraph.

Principle of Maximum Information Entropy

The Bayesian concept of probability [Wei99, Wei06] differs from the conventional one which is usually used. The conventional (frequentist) approach assumes that there is exactly one true value η for a measurand Y . When Y is investigated with a measurement, the probability distribution $p(y|\eta)$ describes the distribution of measured values y given the condition that η is the true value. In contrast, the Bayesian concept aims in the determination of a probability density function (PDF) $p(\eta|y, \sigma_y)$ of the true value η considering that

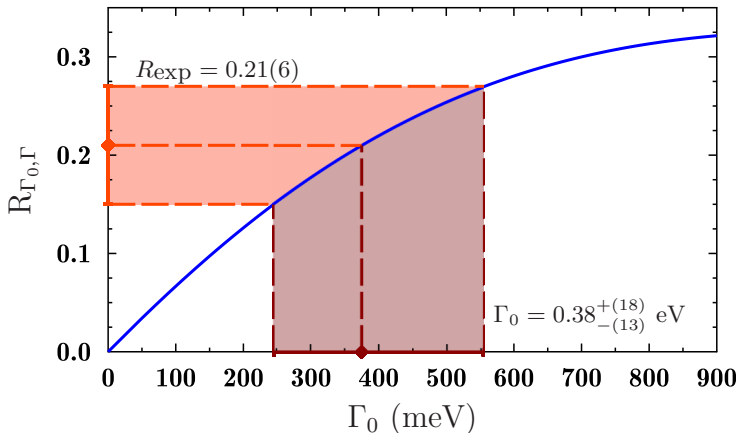


Figure 7.11.: This figure illustrates the conventional approach used to determine the ground-state transition width Γ_0 from the self-absorption measurement for the excited state at 6484.4 keV of ^{140}Ce . The experimentally deduced value of $R_{\text{exp}} = 0.21(6)$ together with the corresponding uncertainty barriers is projected to the Γ_0 axis. However, this results in $\Gamma_0 = 0.38^{+(18)}_{-(13)} \text{ eV}$ with asymmetric uncertainties. These are difficult to treat for further calculations exploiting the results for Γ_0 .

the measurand Y has been measured to y with an uncertainty of σ_y . This means, the Bayesian approach doesn't assume that there is a particular true value but a probability distribution of true values. This distribution, denoted also as *posterior*, follows from the so-called principle of maximum information entropy (PME) [Jay57, Jay89] and is given as

$$p(\eta|y, \sigma_y) = C \cdot p_0(\eta|y, \sigma_y) \cdot p(\eta). \quad (7.18)$$

Here, $p_0(\eta|y, \sigma_y)$ is a likelihood function which describes the probability distribution of the true value η with the condition that the measurement yielded y with an uncertainty of σ_y neglecting any other information. *A-priori* information on the experiment, that are available before the measurement starts, are represented by $p(\eta)$ which is called *prior*. Eventually, C denotes a normalisation constant.

A typical application for the Bayesian approach are activity measurements of radioactive samples. In this case, the likelihood function for the true value η of the activity assuming that the measured activity yields y with an uncertainty of σ_y would be a Gaussian distribution:

$$p_0(\eta|y, \sigma_y) = C \cdot \exp\left(-\frac{1}{2} \left(\frac{\eta - y}{\sigma_y}\right)^2\right) \quad (7.19)$$

Furthermore, an activity cannot be negative. Thus, the non-physical region $\eta < 0$ of the true value is excluded by this a-priori constraint via

$$p(\eta) = \begin{cases} 1 & (\eta \geq 0) \\ 0 & (\eta < 0) \end{cases}. \quad (7.20)$$

Eventually, this results in

$$p(\eta|y, \sigma_y) = \begin{cases} C \cdot \exp\left(-\frac{1}{2} \left(\frac{\eta - y}{\sigma_y}\right)^2\right) & (\eta \geq 0) \\ 0 & (\eta < 0) \end{cases}. \quad (7.21)$$

describing the probability distribution of true values for the activity taking the measured value y with its uncertainty σ_y into account. The probability density functions for this example are illustrated in Fig. 7.12.

Analogous analysis procedures will be applied to determine probability density functions of Γ_0 , Γ , and Γ_0/Γ in the following. To allow for an easier comparison of the obtained results, the most probable value of the distributions will be extracted. Furthermore, the 68.3 %-confidence interval will be determined for each distribution in analogy to the $1-\sigma$ uncertainty interval of Gaussian distributions. The confidence-interval barriers $\eta^<$ and $\eta^>$ are determined via

$$P = \int_{\eta^<}^{\eta^>} p(\eta|y, \sigma_y) d\eta \equiv 0.683 \quad (7.22)$$

with the condition

$$p(\eta^<|y, \sigma_y) = p(\eta^>|y, \sigma_y). \quad (7.23)$$

If $\partial p / \partial y = 0$ has only one solution in $]-\infty, \infty[$, than the confidence interval is well defined by Eqs. (7.22) and (7.23).

The detailed, individual proceeding for the quantities Γ_0 , Γ , and Γ_0/Γ will be elucidated in the following paragraphs.

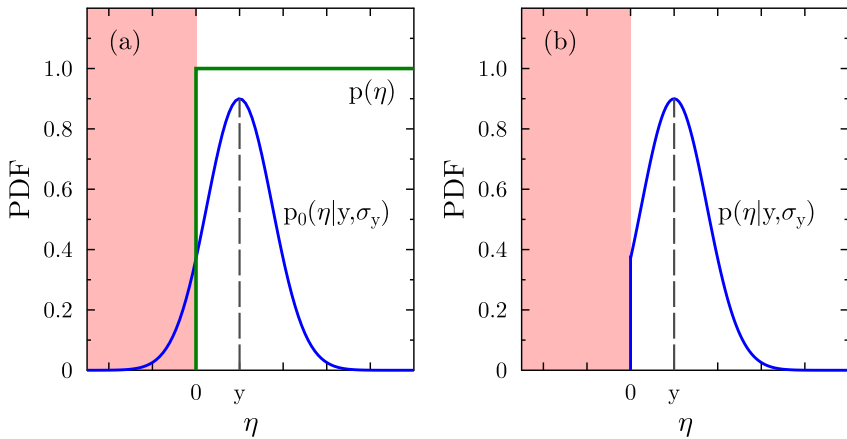


Figure 7.12.: Illustration of the principle of maximum information entropy. (a) The blue curve represents the likelihood function after the measurement yielded y with an uncertainty of σ_y . The red coloured region corresponds to non-physical values. It is excluded via the a-priori distribution $p(\eta)$ which describes information that is known before the experiment is conducted (green). (b) The posterior $p(\eta|y, \sigma_y)$ is obtained by applying the prior to the likelihood distribution.

Determination of Γ_0

For the determination of Γ_0 , a Gaussian distribution has been taken to describe the experimentally deduced self absorption R_{exp} . Furthermore, two a-priori constraints are taken into account. First of all, R_{exp} cannot take values smaller than zero. A negative self absorption would correspond to an increase of NRF reactions in the scattering target in the measurement with absorber with respect to the one without absorption target. This, however, is not possible as the absorber reduces the photon-flux intensity available for NRF reactions in the scatterer. Nevertheless, the measurement may result in a negative self absorption especially for weakly excited states where the yield in both measurements, with and without absorption target, differs slightly only. The partly large uncertainties of R_{exp} may also reach into the negative region. Moreover, values for the self absorption R_{exp} exceeding the maximum R_{max} in the $R_{\Gamma_0, \text{r}}$

curve do not correspond to a result of Γ_0 and, thus, are also non-physical. These a-priori information on the experiment can be expressed via the step function

$$p(R_{\text{exp}}) = \begin{cases} 1 & (0 \leq R_{\text{exp}} \leq R_{\text{max}}) \\ 0 & (R_{\text{exp}} < 0, R_{\text{exp}} > R_{\text{max}}) \end{cases}. \quad (7.24)$$

This *prior* distribution is applied on the Gaussian distribution of R_{exp} such that non-physical regions are excluded. The remaining distribution is renormalised and projected to the Γ_0 axis via the $R_{\Gamma_0, \Gamma}$ curve. In praxis, 10^6 values of R_{exp} are randomly chosen according to its probability density function. For each of these values, the corresponding Γ_0 is determined, in turn leading to a distribution of Γ_0 values. This distribution is normalised and, finally, the most probable value and the 68.3 %-confidence interval are deduced from the resulting probability density function. These numbers are discussed in the chapter about the results of the RSA measurement (Ch. 7.5). An example for this analysing procedure is given with Fig. 7.13. It regards the same excited level at 6484.4 keV of ^{140}Ce as has already been investigated in Fig. 7.11. The Gaussian distribution of R_{exp} is cut off at R_{max} of the curve $R_{\Gamma_0, \Gamma}$. The projection of the remaining distribution to the Γ_0 axis yields the distribution of Γ_0 which is shown in red. The most probable value is given as $\Gamma_0 = 0.34^{+(16)}_{-(13)} \text{ eV}$. This result differs only little from the first approach which yielded $\Gamma_0 = 0.38^{+(18)}_{-(13)} \text{ eV}$. However, it should be emphasised that the result from the present analysis is a probability distribution for Γ_0 . In particular, the confidence interval that is given as “uncertainty” does not correspond to a classical Gaussian uncertainty. For the determination of further quantities, which are related to Γ_0 , the probability distribution has to be exploited and not the extracted numbers as will be pointed out in the following paragraphs. Two further examples, giving an example for a cut at $R = 0$ and a case where the a-priori constraints do not influence the distribution of R_{exp} , are shown in Figs. C.1 and C.2 in the Appendix C of this work.

Determination of Γ

In analogy to Γ_0 , the total level width Γ is determined exploiting probability density functions. The level width can be expressed as a function of the ground-state transition width Γ_0 and of the NRF result Γ_0^2/Γ via

$$\Gamma = \frac{(\Gamma_0)^2}{\left(\Gamma_0^2/\Gamma\right)}. \quad (7.25)$$

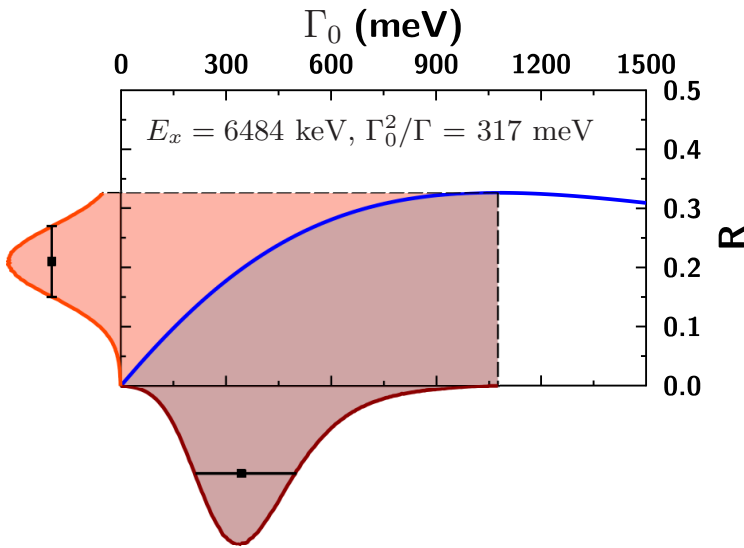


Figure 7.13.: Determination of Γ_0 exploiting probability distributions for the excited state of ^{140}Ce at 6484 keV excitation energy. The orange curve on the left-hand side corresponds to a Gaussian distribution of R_{exp} that has been cut off at $R_{\text{max}} = 0.326$ of the blue $R_{\Gamma_0, \Gamma}$ curve. The projection of this distribution to Γ_0 yields the red distribution whose most probable value and the corresponding 68.3 %-confidence interval account to $\Gamma_0 = 0.34^{+(16)}_{-(13)}$ eV.

The determination of the probability distribution of Γ_0 has been outlined in the previous paragraph. For the distribution of Γ_0^2/Γ , a Gaussian distribution is taken with the mean value given by the result of the NRF measurement and the full width at half maximum by its uncertainty. This Gaussian is cut off at $\Gamma_0^2/\Gamma = 0$ since this quantity cannot take negative values. From these distributions 10^6 random combinations of Γ_0 and Γ_0^2/Γ are chosen. For each combination, Eq. (7.25) is evaluated yielding a distribution of 10^6 values of Γ . Eventually, this distribution can be translated into a probability density function for Γ and, again, the most probable value and the 68.3 %-confidence interval around this value are extracted. The corresponding results are presented and discussed in Ch. 7.5.

During the determination of Γ , no a-priori constraints are taken into account. Since the branching ratio to the ground state cannot be larger than one, the condition $\Gamma_0 \leq \Gamma$ must hold. This could be realised when each combination of randomly chosen numbers for Γ_0 and Γ_0^2/Γ has to fulfil the requirement $(\Gamma_0^2/\Gamma) \leq \Gamma_0$. However, both quantities are mutually dependent. Thus, the analysis procedure could also be turned around and Γ could be deduced from the comparison to $R_{\Gamma_0, \Gamma}$. In this case, Γ_0 would be constrained by the distribution of Γ . Furthermore, the results should be determined as independently from each other as possible. Besides, the above mentioned condition would only hold for individual combinations of Γ_0 and Γ . Nevertheless, the final distribution of Γ would still partly overlap with the one of Γ_0 . This means there would still be a part of the distribution of Γ which does not fulfil the condition $\Gamma_0^2/\Gamma \leq \Gamma_0$. Therefore, during the determination of Γ this constraint is not applied to the probability distributions.

Determination of Γ_0/Γ

The branching ratio Γ_0/Γ to the ground state can be deduced from the probability distributions for Γ_0 and Γ_0^2/Γ , as well. The according relation is given via

$$\frac{\Gamma_0}{\Gamma} = \frac{\left(\Gamma_0^2/\Gamma\right)}{\Gamma_0}. \quad (7.26)$$

Again, a pair of values for Γ_0 and Γ_0^2/Γ is randomly chosen from the corresponding distributions. Equation (7.26) is evaluated and yields a value for the branching ratio. This procedure is repeated 10^6 times and, eventually, results in a distribution describing the branching ratio to the ground state. Branching ratios which are smaller than $\Gamma_0/\Gamma = 0$ or larger than $\Gamma_0/\Gamma = 1$ are non-physical. They are excluded by applying the step function

$$p\left(\frac{\Gamma_0}{\Gamma}\right) = \begin{cases} 1 & (0 \leq \frac{\Gamma_0}{\Gamma} \leq 1) \\ 0 & (\frac{\Gamma_0}{\Gamma} < 0, \frac{\Gamma_0}{\Gamma} > 1) \end{cases}. \quad (7.27)$$

to the probability distribution of the branching ratio. Afterwards, as for the previously discussed quantities, the most probable value and the corresponding 68.3 %-confidence interval are deduced which are presented and discussed in Ch. 7.5.

Determination of b_0

The results for the branching ratio to the ground state will be compared to calculations within the statistical model in Ch. 7.6. To do so, the b_0 value is extracted from both, the experiment and the calculation. It is defined as

$$b_0 = \frac{\sum_i \left(\frac{\Gamma_0^2}{\Gamma} \right)_i}{\sum_i (\Gamma_0)_i} \quad (7.28)$$

and, hence, expresses a weighted, averaged branching ratio to the ground state. The b_0 value is determined for certain bins of individual excited states i , *e.g.*, with respect to the excitation energy or to the transition strength. The determination of b_0 is carried out analogously to the above discussed cases. For all states i within a certain bin of excited states, values for Γ_0^2/Γ and Γ_0 are randomly chosen from the corresponding probability density functions. With these numbers, b_0 is evaluated. After 10^6 repetitions of this step, a probability distribution is generated for b_0 . As b_0 describes an averaged branching ratio, it can neither be smaller than zero nor exceed one. Therefore, the step function

$$p(b_0) = \begin{cases} 1 & (0 \leq b_0 \leq 1) \\ 0 & (b_0 < 0, b_0 > 1) \end{cases} \quad (7.29)$$

is applied to the PDF describing b_0 before the most probable value and the 68.3 %-confidence interval can be deduced.

All results that have been obtained in this way will be presented and discussed in the following chapter. In particular, issues of the just discussed analysing approach will be closer elucidated.

7.5 The RSA Measurement - Results

In total, the self absorption R_{exp} has been determined for 104 excited states out of 117 levels that have been observed in the NRF measurement. The four lowest-lying excited states observed in this work, namely four 2^+ states, have not further been investigated since they are strongly fed (see Sec. 7.3). Furthermore, the endpoint energies of the NRF and the RSA measurement slightly differed. As a consequence, the correction factor for atomic attenuation

steeply drops above ~ 7 MeV (see Fig. 7.9) and even becomes negative above ~ 7.5 MeV. Therefore, the excited state at $E_i = 7509.9$ keV is the highest-lying level, that has been taken into account during the analysis of the RSA measurement. Nine further states above 7.5 MeV have not been investigated with respect to the self absorption.

In this chapter, the results of the RSA measurement on ^{140}Ce for the self absorption R_{exp} , for the ground-state transition width Γ_0 , for the total level width Γ , and for the branching ratio Γ_0/Γ to the ground state will be presented and discussed in detail for the remaining 104 levels. But before the results are shown, it shall be investigated whether and to what extent the above described analysis procedure affects the results.

Influence of the Analysing Method on the Results

As has been discussed in the previous Section (Sec. 7.4), the results for Γ_0 , Γ_0/Γ , and b_0 have been obtained exploiting the Bayesian concept of probability and the principle of maximum information entropy. This approach also includes the exclusion of non-physical regions such as branching ratios that are larger than one. This analysing approach and its possible influence on the results of this work are investigated in the following in order to better assess the results determined in this way. For this purpose, generic excited states of ^{140}Ce have been investigated. Parameters, such as the absorber and scatterer masses, have been taken from the experiment. At first, Γ_0^2/Γ has been fixed to 100 meV and the self absorption of this state has been determined with the branching ratio to the ground state being fixed to $\Gamma_0/\Gamma = 0.5$ and to $\Gamma_0/\Gamma = 1$. This yields $R_{\text{exp}} = 0.15$ and $R_{\text{exp}} = 0.08$, respectively. These numbers for the self absorption as well as $\Gamma_0^2/\Gamma = 100$ meV have been used as input for the analysing approach and Γ_0 , Γ and Γ_0/Γ have been determined. If the analysis works properly, it should reproduce the input. For the self absorption $R_{\text{exp}} = 0.08$, the analysis should yield $\Gamma_0 = 100$ meV, $\Gamma = 100$ meV, and $\Gamma_0/\Gamma = 1$. For the self absorption $R_{\text{exp}} = 0.15$, the analysis should result in $\Gamma_0 = 200$ meV, $\Gamma = 400$ meV, and $\Gamma_0/\Gamma = 0.5$. Figure 7.14 shows the results of the analysis for these three quantities as a function of the relative uncertainty of R_{exp} which has been increased step by step. For small relative uncertainties $\Delta R_{\text{exp}}/R_{\text{exp}} \sim 20\%$ of the experimentally deduced self absorption, the input is well reproduced. The branching ratio does not become larger than one even within the uncertainties since this region has been excluded before. Large uncertainties of R_{exp} are also reflected in corresponding large uncertainties of Γ_0 and Γ . However,

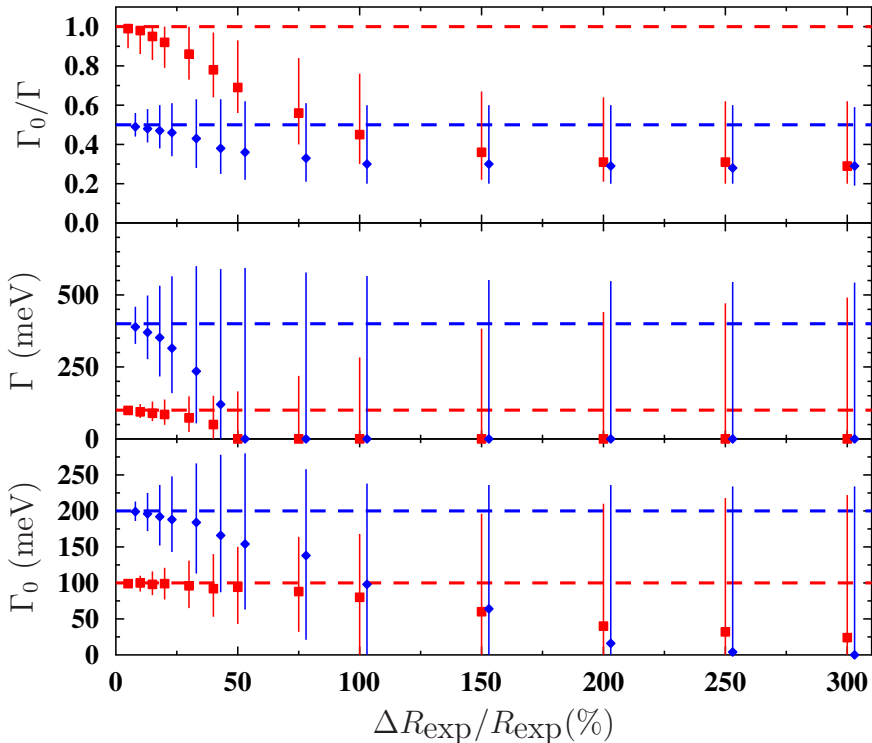


Figure 7.14.: Results for Γ_0 , Γ , and Γ_0/Γ of two generic states with Γ_0^2/Γ fixed to 100 meV as a function of the relative uncertainty of R_{exp} . The red squares represent data that have been deduced with $R_{\text{exp}} = 0.08$ corresponding to $\Gamma_0/\Gamma = 1$ and, consequently, $\Gamma_0 = \Gamma = 100$ meV. In contrast, the blue diamonds have been determined with $R_{\text{exp}} = 0.15$ corresponding to $\Gamma_0/\Gamma = 0.5$ and, thus, $\Gamma_0 = 200$ meV and $\Gamma = 400$ meV. With increasing relative uncertainty of R_{exp} , the results obtained with the Bayesian analysis exhibit an increasing deviation from the expected values (dotted lines). They saturate above $\Delta R_{\text{exp}}/R_{\text{exp}} \sim 150\%$.

the most probable values differ significantly from the expected ones and approach zero. The branching ratios to the ground state move to smaller values, as well. However, in this case, large uncertainties of R_{exp} are not properly reflected. Although the determined results for Γ_0/Γ deviate significantly from the expected values, the 68.3 %-confidence intervals stay comparatively small. All quantities saturate above $\Delta R_{\text{exp}}/R_{\text{exp}} \sim 150\%$, *i.e.*, at this point a lowest level of information about R_{exp} is reached. If R_{exp} becomes even more uncertain, this doesn't further affect the relevant region between zero and R_{max} .

For a further investigation of these observations, Fig. 7.15 illustrates the probability density functions of R_{exp} , Γ_0 , Γ , and Γ_0/Γ as obtained during the analysis of the just discussed level with $\Gamma_0^2/\Gamma = 100 \text{ meV}$ and $\Gamma_0/\Gamma = 1$, *i.e.*, $R_{\text{exp}} = 0.08$. They are depicted for the uncertainties $\Delta R_{\text{exp}} = 0.01$, 0.025, 0.05, and 0.15 of the self absorption. The larger the uncertainty becomes, the flatter becomes the distribution of R_{exp} . With increasing degree of uncertainty, the level of information about the self absorption decreases. This is reflected in the distributions of Γ_0 and Γ . They also become broader and, hence, the result becomes more uncertain. The distribution of Γ_0 is obtained by projecting R_{exp} via the curve $R_{\Gamma_0, \Gamma}$ to Γ_0 . Since the $R_{\Gamma_0, \Gamma}$ curve becomes flat in the vicinity of its maximum R_{max} , the distribution of Γ_0 exhibits a long tail towards large transition widths. Being determined via

$$\Gamma = \frac{(\Gamma_0)^2}{\Gamma_0^2/\Gamma}, \quad (7.30)$$

the distribution of Γ exhibits an even more distinct tail. This tail results in the larger 1- σ confidence intervals of Γ with respect to those of Γ_0 . Eventually, Γ_0/Γ is determined via

$$\frac{\Gamma_0}{\Gamma} = \frac{\Gamma_0^2/\Gamma}{\Gamma_0}. \quad (7.31)$$

As a consequence, the long tail of the Γ_0 distribution results in a high probability for small branching ratios to the ground state. Smaller values of Γ_0 generate the according tail of the Γ_0/Γ distribution. However, this tail is cut off at Γ_0/Γ before the corresponding 1- σ confidence interval is determined. Therefore, the confidence interval becomes comparatively narrow and, at the same time, the branching ratio is shifted towards smaller values as it is the case for Γ_0 and Γ . The saturation value $(\Gamma_0/\Gamma)_{\text{sat}}$, which is obtained with $\Delta R_{\text{exp}}/R_{\text{exp}} = 300\%$ as a function of $\Gamma_0^2/\Gamma = \Gamma = \Gamma_0$, is shown in Fig. 7.16. In particular for the weaker

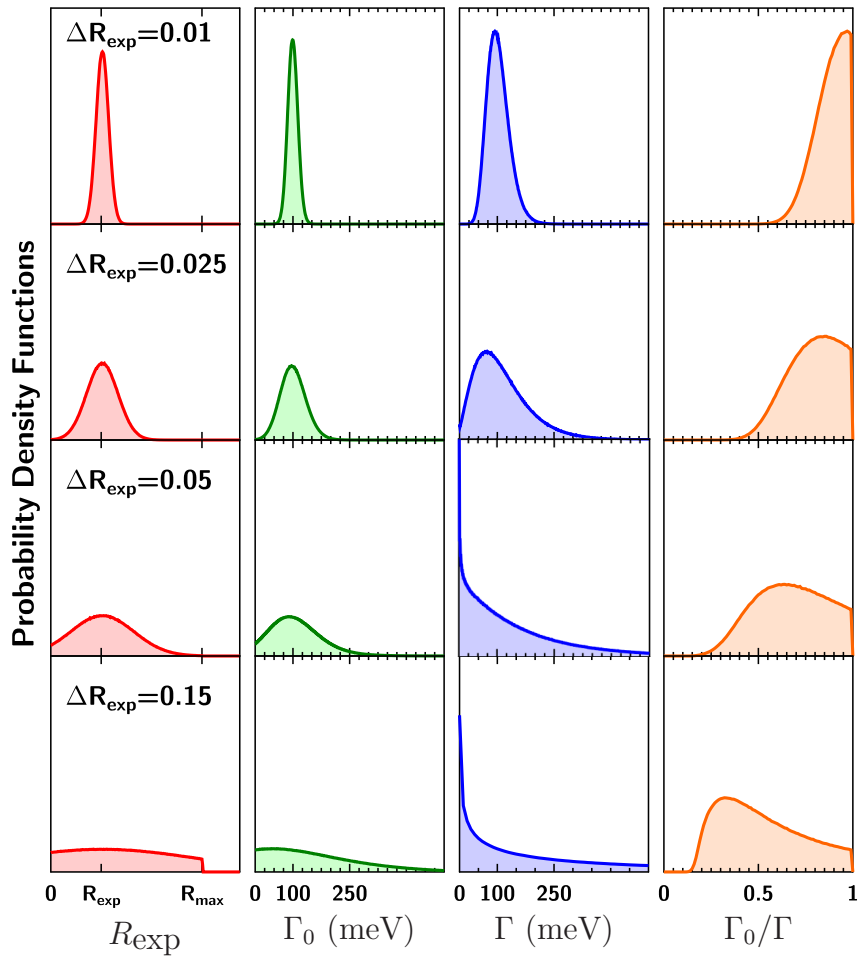


Figure 7.15.: Probability density functions of R_{exp} , Γ_0 , Γ , and Γ_0/Γ as they have been exploited and generated during the analysis for four different values of the uncertainty of $R_{\text{exp}} = 0.08$.

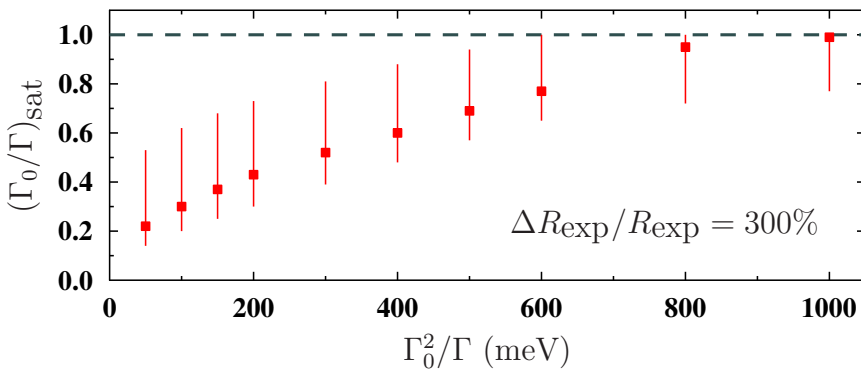


Figure 7.16.: The saturation value $(\Gamma_0/\Gamma)_{\text{sat}}$ of the branching ratio to the ground state for generic states of ^{140}Ce with varying Γ_0^2/Γ . It has been determined with $\Delta R_{\text{exp}}/R_{\text{exp}} = 300\%$, where R_{exp} has been chosen such that $\Gamma_0 = \Gamma$.

excited states, the branching ratio is significantly shifted towards small values. For stronger excited states, it agrees with the original value $\Gamma_0/\Gamma = 1$.

In conclusion of this investigation it should be noted that the analysis procedure that has been chosen to determine Γ_0 , Γ , Γ_0/Γ , as well as b_0 may affect the results especially in the case of large uncertainties of R_{exp} . In the following, the results for all 104 states that have been investigated will be presented. However, to avoid a misinterpretation of the results, those corresponding to “small” uncertainties of R_{exp} will be highlighted. As criteria for “small” uncertainties, the conditions

$$R_{\text{exp}} - \Delta R_{\text{exp}} \geq 0 \quad (7.32)$$

$$R_{\text{exp}} + \Delta R_{\text{exp}} \leq R_{\text{max}} \quad (7.33)$$

have been chosen. In total, 29 out of 104 states fulfil these criteria as will be discussed in the following paragraph.

Self Absorption R_{exp}

The self absorption R_{exp} has been determined separately for each detector. The corresponding error-weighted average of these results is summarised in

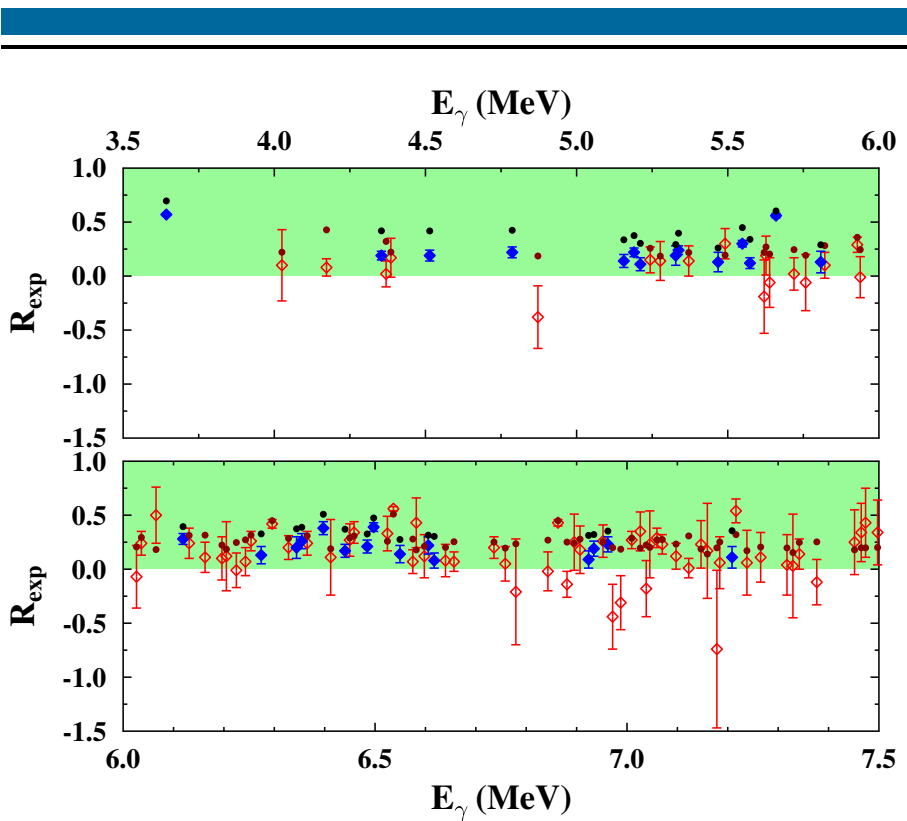


Figure 7.17.: The experimentally deduced self absorption R_{exp} as a function of the energy. Filled (blue) symbols represent levels for which $R_{\text{exp}} - \Delta R_{\text{exp}} \geq 0$ and $R_{\text{exp}} + \Delta R_{\text{exp}} \leq R_{\text{max}}$ hold. The results of the remaining excited states violate at least one of these conditions. They are shown as open, red diamonds. The circles represent the corresponding values of R_{max} .

Fig. 7.17. It shows the self absorption as a function of the energy for the energy ranges between 3.5 MeV and 6.0 MeV as well as between 6.0 MeV and 7.5 MeV. The self absorption is represented via open (red) and filled (blue) diamonds. Furthermore, the red and black dots, respectively, indicate the corresponding maximum value R_{max} of the self-absorption curve $R_{\Gamma_0, \Gamma}$. It is calculated for each excited level for the determination of Γ_0 and related quantities (see Secs. 5.4.2 and 7.4). The open and filled symbols distinguish between excited states where

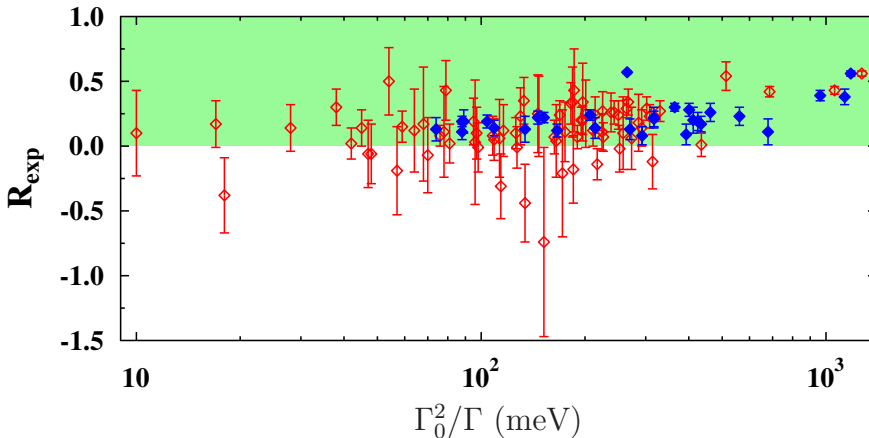


Figure 7.18.: The experimentally determined self absorption R_{exp} as a function of Γ_0^2/Γ . The best sensitivity is given for levels with $\Gamma_0^2/\Gamma \gtrsim 400.$

the self absorption R_{exp} is larger than zero and smaller than R_{max} within its $1-\sigma$ range. In sum, 29 excited states marked by filled, blue diamonds fulfil this condition, whereas the remaining 75 levels shown as red, open diamonds violate it.

The self absorption is expected to range between zero and one. The corresponding region is visualised via the green coloured area in Fig. 7.17. Moreover, R_{exp} is further be expected to be smaller than R_{max} . Nevertheless, the experiment yields also negative values and such being larger than R_{max} . In particular, such cases occur for comparatively weak excited states and consequently poor statistics. For those levels, the self absorption effect is small and, hence, the peak intensity in the RSA measurement differs only slightly from the one in the NRF measurement after the correction for atomic attenuation has been applied. Therefore, small changes of the fitting parameters during the analysis of the peak intensities in the recorded spectra such as a little differently chosen background description may already strongly affect the result. In such situations, *e.g.*, the intensity in the RSA measurement may become larger than the one in the NRF measurement. Figure 7.18 emphasises this fact. It shows the experimental results of the self absorption as a function of the NRF results Γ_0^2/Γ . Excited states with $\Gamma_0^2/\Gamma \lesssim 400 exhibit large uncertainties of R_{exp} becoming also negative or extending into the negative region. By the$

Table 7.8.: Four excited states with R_{exp} being larger than R_{max} within the uncertainties.

E_i (keV)	Γ_0^2/Γ (meV)	R_{exp}	R_{max}
6065.3	54 (13)	0.50 (26)	0.18
6536.4	1270 (64)	0.56 (2)	0.51
6581.8	79 (30)	0.43 (23)	0.18
7216.3	513 (65)	0.54 (11)	0.32

same token, the measurement was sensitive especially to excited states with $\Gamma_0^2/\Gamma \gtrsim 400$ meV.

However, as is apparent from Fig. 7.18, there are also strongly excited states for which R_{exp} does not fulfil the above mentioned conditions. They do not reach into the negative region but exceed R_{max} . Four states with R_{exp} being significantly larger than R_{max} even within the uncertainties have been observed. They are summarised in Table 7.8. The excited states at excitation energies of 6065.3 keV and 6581.8 keV are comparatively weakly excited resulting in a large uncertainty of R_{exp} .

More remarkable are the excited states at $E_i = 6536.4$ keV and $E_i = 7216.3$ keV which are strongly excited. The level at 6536.4 keV has a relative uncertainty of 3.6 % with $R_{\text{exp}} = 0.56(2)$ and exceeds $R_{\text{max}} = 0.51$ within a 2σ range. The same holds for the excited state at 7216.3 keV although it exhibits a larger uncertainty with $R_{\text{exp}} = 0.54(11)$. In this case, R_{max} accounts to 0.32. In both cases, the deviation into the non-physical region can hardly be attributed to statistical fluctuations raising the question about the nature of these deviations.

On the one hand, R_{exp} could be too large. In this case, either the intensity in the RSA measurement would be too small or, in turn, the intensity in the NRF measurement would be too large. Additional events in the NRF measurement may stem from background events that coincide with the transition energy of the excited states of ^{140}Ce . However, such background peaks have not been observed in the ABS measurement. This measurement is particularly sensitive to background events since, if at all, only few photons scattered in the absorption target are detected. Besides, background events would also affect the intensity measured in the RSA part of the experiment. On the other side, R_{max} may be too small. Figure 7.19 shows R_{max} (red diamonds) as a function of Γ_0^2/Γ for a generic $J = 1$ state of ^{140}Ce at an excitation energy of

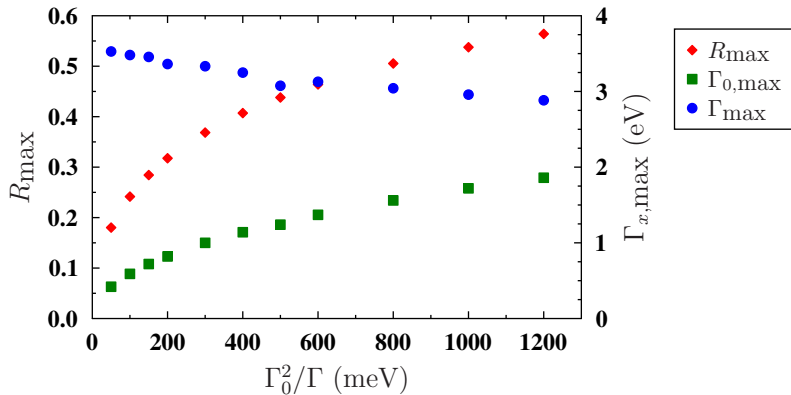


Figure 7.19.: The maximum R_{\max} (red diamonds) of the self-absorption curve $R_{\Gamma_0,\Gamma}$ as a function of Γ_0^2/Γ . It has been determined for generic states of ^{140}Ce . Next to R_{\max} , the corresponding values of $\Gamma_{0,\max}$ (green squares) and Γ_{\max} (blue circles) are shown with the right-hand ordinate.

$E_i = 6000$ keV. Besides R_{\max} , also the corresponding ground-state transition widths $\Gamma_{0,\max}$ (green squares) and the total level widths Γ_{\max} (blue circles) are presented. With increasing Γ_0^2/Γ , also the value of R_{\max} increases since the self-absorption curve $R_{\Gamma_0,\Gamma}$ reaches its maximum later. As a consequence, a too small value of R_{\max} could also hint at a value of Γ_0^2/Γ which is too small. This would be equivalent to the intensities in the NRF measurement being too small. And this would lead, indeed, to a smaller result for R_{\exp} , eventually ensuring $R_{\exp} < R_{\max}$.

All results for R_{\exp} and R_{\max} are also summarised in Table C.1 in the Appendix of this work. Furthermore, Table C.2 gives an overview of all results extracted from the RSA measurement. A shorter version of this table for the 29 excited states where R_{\exp} is larger than zero and smaller than R_{\max} within its $1-\sigma$ interval is provided in Table 7.9.

Ground-State Transition Width Γ_0 - Conventional Approach

Before the results for the ground-state transition width Γ_0 determined with the Bayesian approach are presented, results from the conventional approach

Table 7.9.: Overview of the results for the self absorption R_{exp} , the ground-state transition width Γ_0 , the total level width Γ , and the branching ratio Γ_0/Γ to the ground state from the RSA measurement. For comparison, the result of the NRF measurement, Γ_0^2/Γ , is listed, as well. The given uncertainties of Γ_0 , Γ , and Γ_0/Γ correspond to the 68.3 %-confidence interval around the most probable value of the corresponding probability density functions and should not be misinterpreted as classical Gaussian uncertainties.

E_i (keV)	R_{exp}	Γ_0^2/Γ (meV)	Γ_0 (eV)	Γ (eV)	Γ_0/Γ
3642.9	0.57 (1)	265 (9)	$0.26^{+0.01}_{-0.01}$	$0.25^{+0.02}_{-0.02}$	$0.99^{+0.01}_{-0.03}$
4354.3	0.19 (4)	88 (4)	$0.09^{+0.03}_{-0.02}$	$0.09^{+0.06}_{-0.04}$	$0.84^{+0.14}_{-0.12}$
4514.1	0.19 (5)	104 (6)	$0.10^{+0.04}_{-0.03}$	$0.08^{+0.08}_{-0.05}$	$0.87^{+0.13}_{-0.15}$
4787.0	0.22 (5)	146 (6)	$0.14^{+0.05}_{-0.04}$	$0.12^{+0.11}_{-0.07}$	$0.85^{+0.15}_{-0.11}$
5156.2	0.14 (6)	109 (6)	$0.11^{+0.06}_{-0.06}$	$0.04^{+0.15}_{-0.04}$	$0.74^{+0.20}_{-0.17}$
5190.0	0.22 (4)	152 (9)	$0.19^{+0.05}_{-0.05}$	$0.21^{+0.14}_{-0.10}$	$0.70^{+0.18}_{-0.12}$
5210.8	0.11 (6)	88 (6)	$0.08^{+0.06}_{-0.04}$	$0^{+0.16}_{-0}$	$0.69^{+0.21}_{-0.19}$
5327.9	0.19 (9)	89 (6)	$0.14^{+0.11}_{-0.08}$	$0^{+0.55}_{-0}$	$0.36^{+0.25}_{-0.13}$
5337.1	0.24 (4)	207 (9)	$0.23^{+0.06}_{-0.05}$	$0.22^{+0.16}_{-0.08}$	$0.80^{+0.16}_{-0.13}$
5468.0	0.13 (9)	74 (5)	$0.10^{+0.09}_{-0.07}$	$0^{+0.40}_{-0}$	$0.35^{+0.28}_{-0.14}$
5548.3	0.30 (3)	364 (14)	$0.35^{+0.05}_{-0.05}$	$0.34^{+0.10}_{-0.10}$	$0.97^{+0.03}_{-0.11}$
5573.5	0.12 (5)	166 (11)	$0.11^{+0.06}_{-0.06}$	$0.04^{+0.09}_{-0.04}$	$0.99^{+0.01}_{-0.22}$
5659.6	0.56 (2)	1180 (41)	$1.05^{+0.14}_{-0.11}$	$0.90^{+0.28}_{-0.17}$	$0.99^{+0.01}_{-0.10}$
5807.7	0.13 (10)	134 (10)	$0.11^{+0.12}_{-0.10}$	$0^{+0.36}_{-0}$	$0.54^{+0.23}_{-0.22}$
6118.9	0.28 (5)	401 (22)	$0.43^{+0.12}_{-0.12}$	$0.40^{+0.31}_{-0.20}$	$0.81^{+0.17}_{-0.12}$
6274.0	0.13 (8)	270 (24)	$0.16^{+0.14}_{-0.11}$	$0^{+0.25}_{-0}$	$0.91^{+0.09}_{-0.25}$
6344.2	0.20 (10)	412 (26)	$0.27^{+0.20}_{-0.17}$	$0^{+0.42}_{-0}$	$0.94^{+0.06}_{-0.28}$
6354.5	0.26 (7)	462 (42)	$0.42^{+0.17}_{-0.17}$	$0.30^{+0.35}_{-0.23}$	$0.89^{+0.11}_{-0.20}$
6397.3	0.38 (6)	1133 (54)	$0.70^{+0.23}_{-0.17}$	$0.39^{+0.32}_{-0.18}$	$0.99^{+0.01}_{-0.15}$
6440.4	0.17 (6)	434 (23)	$0.25^{+0.13}_{-0.11}$	$0.10^{+0.17}_{-0.09}$	$0.98^{+0.02}_{-0.17}$
6484.4	0.21 (6)	317 (17)	$0.34^{+0.16}_{-0.13}$	$0.24^{+0.42}_{-0.18}$	$0.73^{+0.20}_{-0.17}$

continued on next page

continued from previous page

E_i (keV)	R_{exp}	Γ_0^2/Γ (meV)	Γ_0 (eV)	Γ (eV)	Γ_0/Γ
6497.2	0.39 (4)	962 (64)	$0.81^{+0.20}_{-0.14}$	$0.66^{+0.38}_{-0.23}$	$0.99^{+0.01}_{-0.16}$
6549.4	0.14 (8)	214 (15)	$0.19^{+0.17}_{-0.12}$	$0^{+0.46}_{-0}$	$0.58^{+0.27}_{-0.16}$
6605.6	0.22 (8)	317 (23)	$0.36^{+0.20}_{-0.17}$	$0.23^{+0.55}_{-0}$	$0.59^{+0.25}_{-0.15}$
6617.4	0.08 (7)	293 (18)	$0.13^{+0.10}_{-0.11}$	$0^{+0.14}_{-0}$	$0.98^{+0.02}_{-0.24}$
6923.8	0.09 (8)	393 (24)	$0.14^{+0.15}_{-0.13}$	$0^{+0.18}_{-0}$	$0.99^{+0.01}_{-0.26}$
6934.2	0.19 (7)	425 (27)	$0.38^{+0.17}_{-0.20}$	$0.17^{+0.39}_{-0.17}$	$0.87^{+0.13}_{-0.21}$
6962.0	0.23 (7)	561 (32)	$0.44^{+0.25}_{-0.17}$	$0.24^{+0.46}_{-0.20}$	$0.88^{+0.12}_{-0.18}$
7208.5	0.11 (10)	679 (54)	$0.17^{+0.23}_{-0.17}$	$0^{+0.22}_{-0}$	$0.98^{+0.02}_{-0.23}$

will shortly be discussed in this paragraph. In Sec. 5.4.2, it has been shown, that the self-absorption $R_{\Gamma_0, \Gamma}$ exhibits a maximum R_{max} when it is calculated with Γ_0^2/Γ fixed by the NRF result (compare Fig. 5.10). Therefore, two solutions for Γ_0 can be extracted. With the conventional approach, both solutions have been determined for those cases where the self absorption yielded a value above zero and below R_{max} . In other cases, the determination of Γ_0 is not feasible with the conventional approach. In this paragraph, these solutions for Γ_0 are compared to each other.

Results have been obtained for 71 excited states. They are shown in Fig. 7.20 as a function of the excitation energy of the corresponding levels. As is apparent from this figure, the second solution for Γ_0 (green triangles) in most cases significantly exceeds the corresponding first solution (red squares). It often corresponds to non-physically large values of several eV for the ground-state transition width. In four cases, which are not included in Fig. 7.20, the second solution is even larger as 10 eV. These large transition widths to the ground state result in even larger results for the total level width. It can be determined via

$$\Gamma = \frac{(\Gamma_0)^2}{\left(\Gamma_0^2/\Gamma\right)}. \quad (7.34)$$

For none of the investigated excited states, a level width smaller than $\Gamma = 6.9$ eV has been found in this way. Typically, Γ would have been calculated to be even substantially higher.

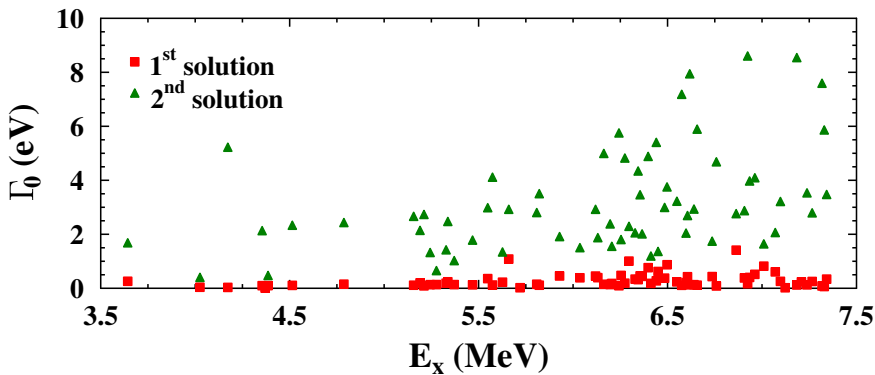


Figure 7.20.: The first (red squares) and second (green triangles) solution for Γ_0 has been determined via the conventional approach. The second solution substantially exceeds the first one and corresponds often to non-physically large values for Γ_0 .

In general, both solutions for the ground-state transition width differ at least by a factor of two. This is the case for four excited states at 6295.8 keV, 6449.7 keV, 6863.1 keV, and 7009.4 keV excitation energy, respectively. These states exhibit the smallest total level widths lying between 6.9 eV and 7.8 eV. Nevertheless, this is still rather large. Excited states being such strong are not expected to be found in the present case.

In conclusion, the comparison of both solutions of the ground-state transition width that can be extracted from the self absorption $R_{\Gamma_0, \Gamma}$ demonstrates that the second, higher-lying solution is generally related to non-physical large values for Γ_0 and, consequently, also for Γ . Therefore, the second solution will not further be regarded in the following discussion of the results of the RSA measurement.

Ground-State Transition Width Γ_0 - Bayesian Approach

The first quantity that has been extracted from the self-absorption results exploiting the Bayesian approach is the ground-state transition width Γ_0 . It is illustrated in Fig. 7.21 (a) as a function of the energy and in Fig. 7.21 (b) as a function of Γ_0^2/Γ . In both cases, the uncertainty bars do not represent classical Gaussian uncertainties but the range of the 68.3 %-confidence interval that has

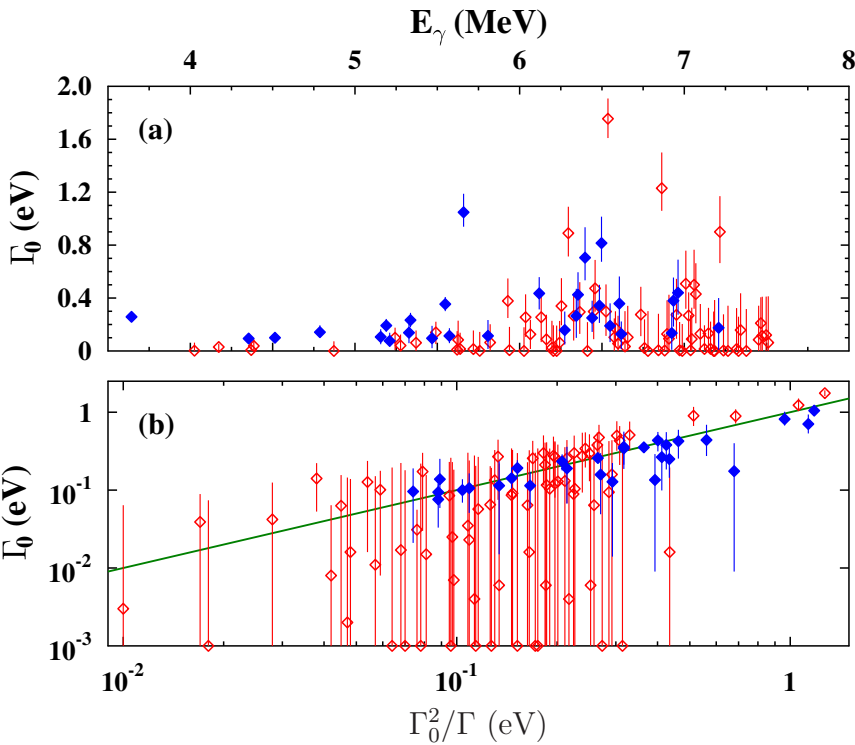


Figure 7.21.: Results of the RSA measurement for the ground-state transition width Γ_0 as a function of (a) the energy and (b) Γ_0^2/Γ . The blue, filled diamonds correspond to excited states where R_{exp} is completely located in the physically allowed region. The region below the green line in panel (b) marking $\Gamma_0/\Gamma = 1$ corresponds to branching ratios to the ground state that are larger than one and, hence, non-physical.

been discussed in Sec. 7.4. For clarity, the results in Fig. 7.21 (b) are shown on a double-logarithmic scale. Again, open and filled symbols distinguish between excited states with comparatively large and small uncertainties in R_{exp} .

As has been discussed before, the uncertainties of R_{exp} are reflected in those of the ground-state transition width. Therefore, in particular the states marked by filled (blue) diamonds exhibit small uncertainties. As an example for an

excited state which exhibits a small uncertainty in the self absorption and consequently in the ground-state transition width as well, the two-phonon state at $E_i = 3642.9$ keV will be discussed. Its self absorption accounts to $R_{\text{exp}} = 0.57(1)$ and the ground-state transition width yields $\Gamma_0 = 258_{-10}^{+11}$ meV. The NRF measurement resulted in $\Gamma_0^2/\Gamma = 265(9)$ meV, *i.e.*, the two-phonon state decays almost exclusively directly to the ground state. Indeed, no branching ratio to lower-lying states is reported in the literature for this level so far. In the work of Herzberg and collaborators [Her95b], an upper limit of 4 % is reported for the decay branch to the first excited 2^+ level. Assuming an exclusive decay directly back to the ground state, $\Gamma_0 = 281(20)$ meV has been found in Ref. [Her95b]. The results of the present work are in good agreement with these observations demonstrating the reliability of the RSA method.

In contrast, the states illustrated via open symbols have comparatively large uncertainties. This is especially emphasised via the logarithmic scale in Fig. 7.21 (b). Furthermore, the most probable value for Γ_0 often accounts to zero in these cases. As has been demonstrated in the discussion of the analysis procedure and its influence on the results this means that the experimentally deduced value of the self absorption is not precise enough to extract Γ_0 . The 68.3 %-confidence interval, that can be extracted for Γ_0 , at least indicates in which range the actual value of Γ_0 can be expected. However, this interval is less related to the measured self absorption but rather to Γ_0^2/Γ from the NRF measurement. The maximum R_{max} of the self-absorption curve increases with increasing Γ_0^2/Γ (Fig. 7.19) and, hence, also the physically allowed region of the self absorption between zero and R_{max} grows. For uncertain values of R_{exp} the distribution of R_{exp} approaches an equal distribution and, eventually, the confidence interval describing Γ_0 grows, as well.

Figure 7.21 (b) shows the ground-state decay widths Γ_0 resulting from self absorption as a function of the NRF result Γ_0^2/Γ . The green line corresponds to a branching ratio to the ground state which accounts to one. The region below the green line corresponds to non-physical branching ratios to the ground state that are larger than one. Most of the excited levels with small uncertainties in R_{exp} , *i.e.*, those marked via filled diamonds, exhibit ground-state transition widths that are in good agreement with the green line and, hence, with a branching ratio corresponding to a preferred decay directly to the ground state. In contrast, levels with large uncertainties in the self absorption often appear below the green line in the non-physical region. This may be attributed to the fact, that for large uncertainties of R_{exp} , Γ_0 is systematically shifted to too

Table 7.10.: Candidates for close lying levels of ^{140}Ce . For the listed levels, Γ_0 is significantly smaller than Γ_0^2/Γ . Therefore, $\Gamma_{0,\text{DP}}$ has been determined, assuming two close lying, equally strong excited states with $(\Gamma_0^2/\Gamma)_{\text{DP}}$.

E_i (keV)	R_{exp}	Γ_0^2/Γ (meV)	Γ_0 (eV)	$(\Gamma_0^2/\Gamma)_{\text{DP}}$ (meV)	$\Gamma_{0,\text{DP}}$ (eV)
6397.3	0.38 (6)	1133 (54)	$0.71^{+0.23}_{-0.17}$	550	$0.74^{+0.23}_{-0.19}$
6440.4	0.17 (6)	434 (23)	$0.25^{+0.13}_{-0.11}$	217	$0.26^{+0.14}_{-0.12}$
6617.4	0.08 (7)	293 (18)	$0.13^{+0.10}_{-0.11}$	146	$0.10^{+0.12}_{-0.09}$
6923.8	0.09 (8)	393 (24)	$0.14^{+0.16}_{-0.13}$	196	$0.15^{+0.12}_{-0.15}$
7208.5	0.11 (10)	679 (54)	$0.18^{+0.23}_{-0.17}$	339	$0.21^{+0.18}_{-0.20}$

smaller values by the analysis method used here. However, with their uncertainties they still reach into the region above the green line. In contrast, there are also five strongly excited states where the ground-state transition width is significantly smaller as the NRF value for Γ_0^2/Γ . They are listed in Tab. 7.10. For instance, this situation occurs for the excited state at $E_i = 6397.3$ keV. For this level, the NRF measurement yielded $\Gamma_0^2/\Gamma = 1133(54)$ meV, whereas the ground-state transition width from the RSA measurement accounts only to $\Gamma_0 = 0.71^{+0.23}_{-0.17}$ eV. This may be attributed to the self absorption effect being too weak, *i.e.*, less photons are absorbed in the absorption target as it is expected from the NRF result. Such a case occurs when two excited states lie very close to each other such that they cannot be resolved in the recorded spectra which is demonstrated with the following example.

First of all, an excited state with $\Gamma_0^2/\Gamma = \Gamma_0 = 1000$ meV shall be regarded. Its excitation strength shall correspond to a self absorption of 50 %. In this case, the yield in the RSA measurement is reduced by 50 % with respect to the NRF measurement yielding in the analysis as expected $\Gamma_0 = 1000$ meV. In contrast, two excited states with $\Gamma_0^2/\Gamma = \Gamma_0 = 500$ meV shall lie very close in energy to each other. They shall not be resolvable in the measurements. In this case, only *one* peak is observed in the NRF spectrum corresponding to the ground-state transitions of *both* states. As a consequence, it is attributed to a *single* state with $\Gamma_0^2/\Gamma = 1000$ meV from the measurement and cannot be distinguished from the above made example of a single state. However, the

self-absorption effect resolves excited states down to the eV level. The self absorption of the levels with $\Gamma_0^2/\Gamma = \Gamma_0 = 500$ meV is smaller than the self absorption of an level with $\Gamma_0^2/\Gamma = \Gamma_0 = 1000$ meV and shall amount to 30 %. As in the NRF spectrum, the levels cannot be resolved in the RSA spectrum. Thus, one single peak is measured with a yield reduced by 30 % with respect to the NRF measurement. This self absorption appears to be too small for a level with $\Gamma_0^2/\Gamma = \Gamma_0 = 1000$ meV resulting in the analysis in an unexpected ground-state transition width being too small with respect to $\Gamma_0^2/\Gamma = \Gamma_0 = 1000$ meV.

This situation may also be applicable to the five cases where Γ_0 is considerably smaller than Γ_0^2/Γ . For instance, the peak at an transition energy of 6397 keV may be attributed to two states with $\Gamma_0^2/\Gamma \sim 550$ meV each instead of one state with $\Gamma_0^2/\Gamma = 1133$ meV. In this case, the analysis would yield $\Gamma_0 = 0.74^{+0.23}_{-0.19}$ eV, $\Gamma = 0.74^{+0.80}_{-0.32}$ eV, and $\Gamma_0/\Gamma = 0.64^{+0.18}_{-0.14}$ for both levels. These results would be in the physically allowed region. The self absorption $R_{\text{exp}} = 0.38$ does not change since the intensities of the NRF and RSA measurement, respectively, are just halved. However, the two states must not be equally strongly excited. Nevertheless, the self absorption stays constant, independently of the ratio of the parts the strongly excited state is distributed to. As a consequence, the two states cannot have an NRF cross section corresponding to a value smaller than $\Gamma_0^2/\Gamma \sim 300$ meV. There, R_{max} drops below 0.38 and R_{exp} becomes non-physical.

For the remaining four cases, an analysis assuming two equally strong excited states instead of one has been performed, as well. The results are given in Table 7.10. However, in the spectra no evidence for double peaks has been found. The peaks corresponding to candidates for “double states” do not exhibit particular large widths. Therefore, possible “double states” must lie very close to each other.

Eventually, the $B(E1)\uparrow$ -strength distribution has been determined exploiting the results for the ground-state transition width from the RSA measurement. It is illustrated in Fig. 7.22 (a). The $B(E1)\uparrow$ -transition strengths have been determined using the most probable value of the probability density function which describes the ground-state transition width. Bars marked in blue correspond to ground-state transitions of excited states for which the self absorption accounts to a value between zero and R_{max} within the uncertainties. For the red bars, the self absorption of the corresponding levels is comparatively uncertain. For comparison, also the strength distribution that has been extracted from the NRF experiment is given in Fig. 7.22 (b). It has been obtained from the NRF results for Γ_0^2/Γ with the assumption that the states decay exclusively directly back

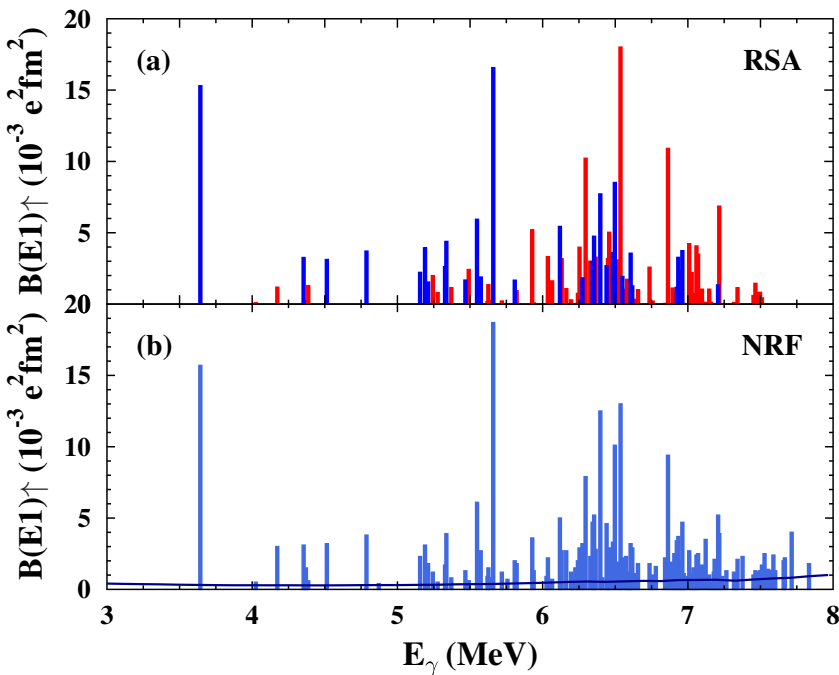


Figure 7.22.: Comparison of the $B(E1)^\uparrow$ -strength distributions which have been obtained via the RSA and NRF measurements, respectively. In the case of the NRF measurement, the reduced transition strengths have been determined from Γ_0^2/Γ assuming $\Gamma_0 = \Gamma$.

to the ground state, *i.e.*, with $\Gamma_0/\Gamma = 1$. As it becomes obvious from the figure, the distributions are similar. If at all, only small changes in the $B(E1)^\uparrow$ strength can be observed. For instance, the strength of the strongly excited state at ~ 5.6 MeV decreased a little in the RSA measurement, whereas the transition strength of the excited state at ~ 6.54 MeV increased such that this transition became the strongest one that has been observed. However, it should be noted that the self absorption of this particular level significantly exceeded R_{\max} as has been discussed in the paragraph concerning the self-absorption results R_{\exp} . In general, the enhancement of strength in the energy range between ~ 6 and 7 MeV is observed in the distribution obtained from the RSA measurement, as well. There, it is even a little more distinct. The general agreement of the

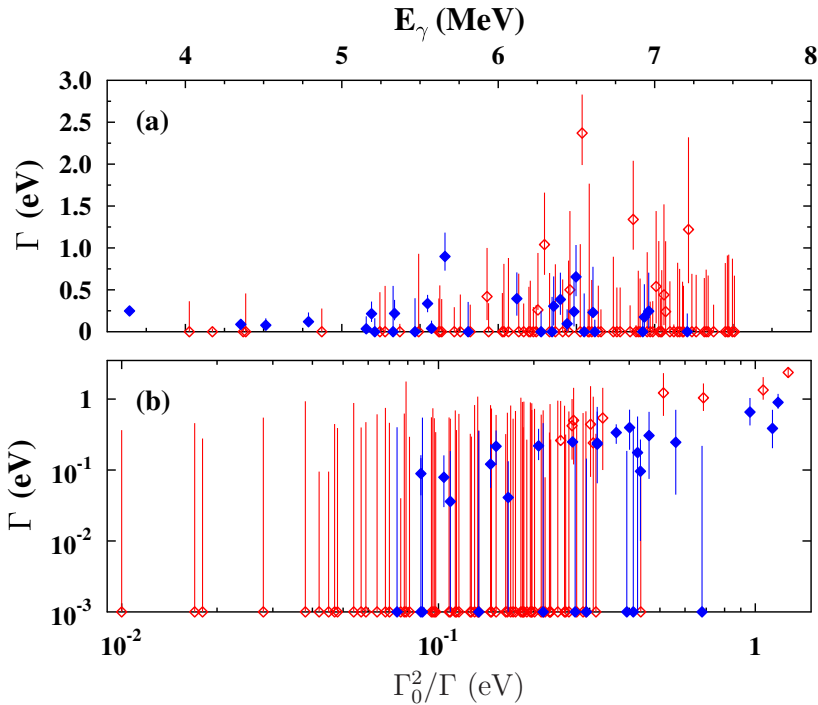


Figure 7.23.: The results for the total level width Γ as they have been extracted from the RSA measurement. Blue, filled diamonds correspond to excited states that exhibit a self absorption larger than zero and smaller than R_{\max} within their uncertainties.

distributions indicates that most of the observed states prefer the direct decay back to the ground state. This will further be elucidated during the discussion of the branching ratio to the ground state. However, before that, the results for the total level width Γ will be presented.

Level Width Γ

Next to the ground-state transition width, the total transition width or level width Γ has been determined, as well. It results from the distribution of Γ_0 in combination with the one of the NRF result for Γ_0^2/Γ as has been discussed in the previous chapter. The results are summarised in Fig. 7.23. The upper

panel shows the level width as a function of the energy and the lower one as a function of Γ_0^2/Γ . The nomenclature corresponds to the ones introduced in the previous paragraphs. Detailed numbers are provided via the Tables 7.9 and C.1.

As can be seen in the figure, the results for the level width Γ entail larger uncertainties compared to the ones of the ground-state transition width. This can be attributed to the fact, that the probability distribution of Γ results from the probability density functions of Γ_0 . As has been pointed out in the discussion of the analysis method and its influence on the results, this leads to a further increasing of the 68.3 %-confidence interval of Γ with respect to those of Γ_0 . Furthermore, the most probable value of the distributions describing Γ accounts more often to zero. This situation occurs even in the case of comparatively precisely determined values of the self absorption R_{exp} .

Branching Ratio Γ_0/Γ to the Ground-State

As the next quantity that has been extracted from the RSA measurement, the branching ratio to the ground state will be discussed. Like for the previously presented quantities, the results are shown in Fig. 7.24 (a) as a function of the energy and in Fig. 7.24 (b) as a function of Γ_0^2/Γ . Furthermore, they are listed in Tables 7.9 and C.1. The nomenclature is adopted, as well.

In contrast to Γ_0 and Γ , the results for the branching ratio to the ground state have to be carefully interpreted with respect to the influences of the analysing approach. As has been shown in Figs. 7.14 and 7.16, the results for the branching ratio Γ_0/Γ to the ground state of excited states are strongly affected by the analysis. With increasing uncertainty of the experimentally deduced self absorption, they are systematically pushed to too small values of Γ_0/Γ by the analysis procedure. If the self absorption is determined with such an uncertainty that the corresponding probability distribution approaches an equal distribution, the result for Γ_0/Γ saturates at a smallest value $(\Gamma_0/\Gamma)_{\text{sat}}$ which depends on Γ_0^2/Γ . The correlation between $(\Gamma_0/\Gamma)_{\text{sat}}$ and Γ_0^2/Γ can be observed in Fig. 7.24 (b). Between $\Gamma_0^2/\Gamma = 0$ and 300 meV, the red, open symbols corresponding to excited states with large ΔR_{exp} exhibit a clear linear correlation between Γ_0/Γ and Γ_0^2/Γ . It is emphasised via the green line which stems from a fit to $(\Gamma_0/\Gamma)_{\text{sat}}$ from Fig. 7.16. The red data points are not further discussed in the following since it is not possible to decide whether the corresponding states indeed exhibit strong decay branches to lower-lying excited states. The small

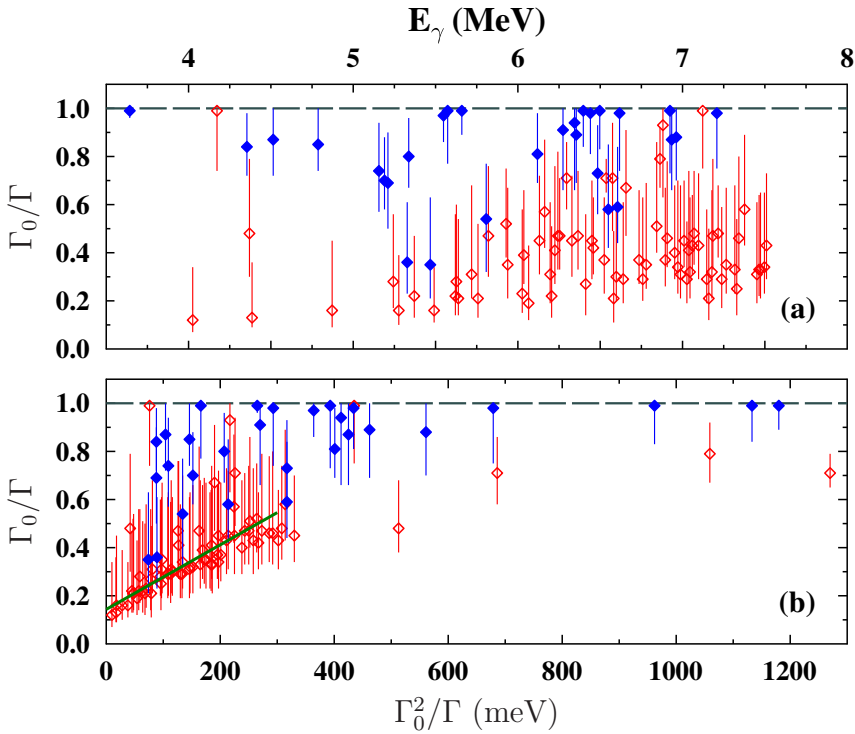


Figure 7.24.: Results for the branching ratio Γ_0/Γ to the ground state from the RSA measurement as a function of (a) the excitation energy of the corresponding excited states and (b) Γ_0^2/Γ . If R_{exp} of a level has been determined to be larger than zero and smaller than R_{max} within the uncertainties, it is marked with blue filled diamonds. In the contrary case, they are represented via red open symbols.

values for the branching ratio to the ground state may also be attributed to the analysing technique.

The remaining 29 levels with comparatively small uncertainties ΔR_{exp} , shown with blue filled diamonds, exhibit branching ratios to the ground state that vary between 30 % and 100 %. They are also illustrated in Fig. 7.25 together with results from the conventional analysis which did not include the Bayesian approach. In this case, R_{exp} has directly been projected to the Γ_0 axis

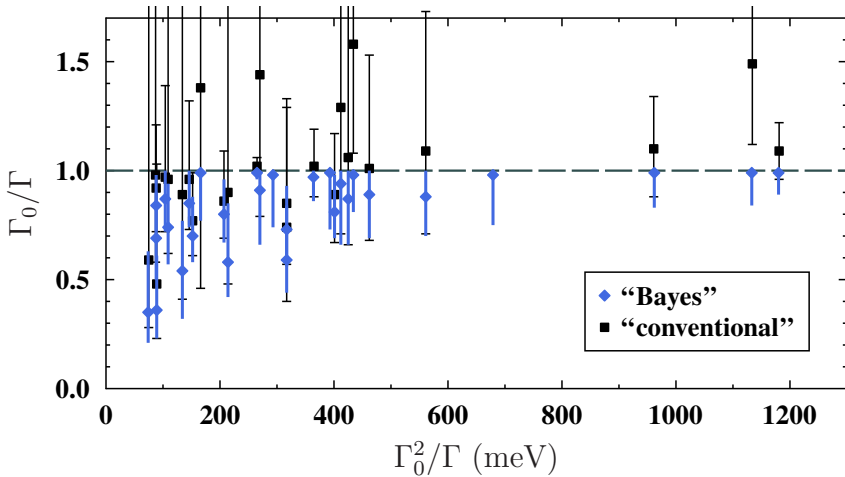


Figure 7.25.: Comparison of the branching ratios to the ground state obtained with the Bayesian (diamonds) and the conventional (squares) approach. Only states for which the self absorption accounts to values between zero and R_{\max} within the uncertainties are taken into account.

resulting in a single value for Γ_0 . The ground-state transition width together with Γ_0^2/Γ has been exploited to deduce the branching ratio to the ground state. The conventionally deduced results are represented via black squares. Maximum uncertainties are given. With the Bayesian approach the non-physical region above $\Gamma_0/\Gamma = 1$ is excluded and the results are restricted to the range between $\Gamma_0/\Gamma = 0$ and $\Gamma_0/\Gamma = 1$. Therefore, the results of this analysis approach, given as blue diamonds, are systematically shifted to lower values with respect to the conventionally determined results. Nevertheless, they still agree with the conventionally determined results within the uncertainties demonstrating that the Bayesian analysis yields reliable results for the case, that the self absorption has been determined with sufficient precision. The trend of small branching ratios to the ground state of the weakest excited states for which the self absorption fulfils the criteria to be larger than zero and smaller than R_{\max} is supported via the conventional analysis.

To close the discussion of the branching ratios, the obtained results will be compared to previous measurements. The two-phonon state at 3642.9 keV excitation energy has already been discussed with respect to the ground-state transition width. Its branching ratio to the ground state has been determined with a high accuracy to $0.99^{+0.01}_{-0.03}$ which is in good agreement with nowadays knowledge of this state. Up to now, no decay to lower-lying excited states has been observed for this state. On the contrary, an upper limit of 4% for the branching ratio to the 2_1^+ level has been reported by Herzberg [Her95b]. Besides, Herzberg observed a decay of the excited state at $E_i = 6536.4$ keV to the 2_1^+ level with a branching ratio of $\Gamma_{2_1^+}/\Gamma = 0.20(6)$ [Her95a]. If no further decay to lower-lying excited states occurs, the branching ratio to the ground state follows to $\Gamma_0/\Gamma = 0.80(6)$. In the present work, the branching ratio of this state to the ground state yields $\Gamma_0/\Gamma = 0.71^{+0.08}_{-0.06}$ which agrees with Herzbergs findings within the uncertainties. However, it should be noted that this particular level exhibits a self absorption R_{exp} that is significantly larger than R_{max} and, hence, is difficult to interpret. Furthermore, no peak corresponding to the inelastic decay to the first excited 2^+ level at ~ 1596 keV at an energy of ~ 4940 keV has been observed in the present spectra. Eventually, no information on a branching ratio to the 2_1^+ level of this excited state is reported in the work of Löher [Löh14], although the $\gamma - \gamma$ coincidence measurement has been sensitive to branching ratios down to the 1% level.

For four out of the 29 excited states investigated in this work, namely those at 5573.5 keV, 5659.6 keV, 6440.4 keV, and 6617.4 keV, branching ratios to the 2_1^+ state have been reported in Ref. [Löh14]. They do not exceed 5% and, for the case that they do not exhibit any other strong decay to lower-lying states, decay predominantly directly back to the ground state. This is in good agreement with the findings of the present work. The branching ratio to the ground state of these states has been determined to 98% and 99% (Table 7.9), respectively. The excited states for which small branching ratios to the ground state have been found in the present work are not discussed in Ref. [Löh14].

As a general observation, the strongly excited states decay preferentially directly back to the ground state. They exhibit branching ratios to the ground state of one or close to one. In contrast, the weaker excited states with $\Gamma_0^2/\Gamma \lesssim 300$ meV also decay via lower-lying excited states. They have branching ratios to the ground state that are substantially smaller than one. In the following, calculations within the statistical model will be exploited to further

study and interpret the findings concerning the decay pattern of the observed excited states.

7.6 The Statistical Model

A statistical approach is often used to study average properties of complex systems such as atomic nuclei. In the present work, the nuclear statistical model is exploited to study the average decay pattern of excited states of ^{140}Ce . For this purpose, γ -ray cascades have been simulated in so-called *nuclear realisations* of ^{140}Ce . A nuclear realisation is a generic level scheme of a particular nucleus with given averaged properties. In general, two input parameters are needed to generate a nuclear realisation. These are, on the one hand, the level density $\rho(E)$, which describes the number of excited states per energy, and, on the other hand, the photon-strength function $S(E_\gamma)$ [Bar73], which describes the averaged radiative transition probabilities between excited states as a function of the corresponding transition energy E_γ .

In the following paragraph, the photon-strength functions will further be discussed. Afterwards, the DICEBOX code [Beč98] and its functionality will be introduced. It has been used to perform the calculations within the statistical model for the present work. Eventually, the results of the γ -ray cascade simulations will be compared to the experimental findings.

Photon-Strength Functions

Photon- or γ -ray strength functions (PSFs) [Bar73] provide a fundamental quantity to describe the averaged excitation and decay pattern of nuclei. Thus, they are also an essential input for calculations within the nuclear statistical model. They describe the distribution of averaged radiative transition widths as a function of the corresponding transition energy E_γ with respect to particular multipole types σL (where σ is either E for electric or M for magnetic radiation of multipolarity L). Two kinds of strength functions can be encountered, describing either photoabsorption or γ decay. For the absorption of a photon by a nucleus in its ground state and the corresponding excitation of levels i with spin J within an energy interval E_i , the strength function is expressed as

$$S_{\sigma L}^J(E_\gamma) \uparrow = \frac{\bar{\Gamma}_{0i\sigma L}^J}{E_\gamma^{2L+1}} \cdot \rho_J(E_i), \quad (7.35)$$

where $E_\gamma = E_i$. Furthermore, $\bar{\Gamma}_{0i\sigma L}^J$ denotes the ground-state transition width averaged over the excited states i in the vicinity of E_i with spin quantum number J . The function $\rho_J(E_i)$ describes the average level density for such states. The strength function for the decay of levels within an unit energy interval E_i to lower-lying ones at E_j can analogously be written as

$$S_{\sigma L}^J(E_\gamma) \downarrow = \frac{\bar{\Gamma}_{ij\sigma L}^J}{E_\gamma^{2L+1}} \cdot \rho_J(E_i). \quad (7.36)$$

Here, $E_\gamma = E_i - E_j$. For the concept of photon-strength functions to be valid, it is conjectured that $S_{\sigma L}^J(E_\gamma) \downarrow$ would be independent of the excitation energy E_i .

Obviously, photon-strength functions represent an averaged quantity. Therefore, its application becomes appropriate at sufficiently high excitation energies, where the level density is high enough to study average properties. At low energies and accordingly low level densities, individual radiation widths should be studied especially with regard to so-called *Porter-Thomas fluctuations* [Por56]. The Porter-Thomas distribution

$$p\left(\frac{\Gamma_\gamma}{\bar{\Gamma}_\gamma}\right) = \left(\frac{2\pi\Gamma_\gamma}{\bar{\Gamma}_\gamma}\right)^{-1/2} \cdot \exp\left(-\frac{\Gamma_\gamma}{2\bar{\Gamma}_\gamma}\right) \quad (7.37)$$

describes the distribution of individual radiative transition widths for a given mean $\bar{\Gamma}_\gamma$. It is illustrated in Fig. 7.26 which demonstrates that individual transition widths can substantially differ from the average value.

Photon-strength functions are often difficult to be accessed in experiments. In most cases, they allow only for the determination of particular contributions to the strength functions. NRF measurements, *e.g.*, probe the strength functions with respect to photoabsorption. However, in general, they provide only little information on the decay. Other methods, such as the recently developed proton- γ - γ correlation approach [Wie12] give insight to transitions between excited states. At the same time, it is challenging to distinguish between particular radiation types, such that PSFs often comprise contributions of various radiation types.

A relation between the PSFs $S \uparrow$ for excitation from the ground state and $S \downarrow$ for γ decay to any lower-lying state can be drawn via the *Axel-Brink hypothesis* [Bri55]. It states that, in analogy to the ground state, giant resonances are build on each excited state. They are just shifted by the excitation energy of the

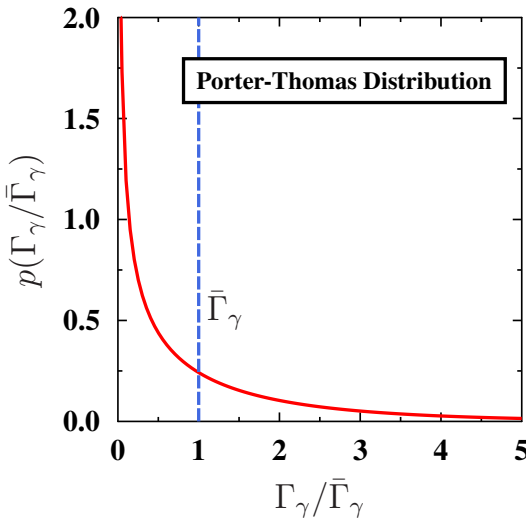


Figure 7.26.: The Porter-Thomas distribution (red, solid line) demonstrates how individual radiative transition widths Γ_γ are distributed with respect to the average value $\bar{\Gamma}_\gamma$ (blue, dotted line).

excited state they are build on. This means, that the energy dependence of photon interactions does not depend on the detailed structure of the initial state. In other words, would it be possible to prepare a target in an excited state, the energy dependence of the photoabsorption cross section would be the same as for an excitation from the ground state. However, this idea is still under debate. For instance, contradictory observations for the $E1$ -PSF have been made. While experimental investigations of the electric giant dipole resonance confirm the Axel-Brink hypothesis (see, e.g., Refs. [Sze83, Sno86]), investigations of the pygmy dipole resonance hint at a violation of the hypothesis (see, e.g., [Ang12, Isa13]). However, information on the PSFs below the particle separation threshold is scarce and often contradictory [Rus08]. One of the simplest approaches to describe the $E1$ -PSF at low energies is the extrapolation of the giant dipole resonance parametrised via a standard Lorentzian. However, this approach does not provide an appropriate description of the strength in the energy region the PDR is supposed to be located. Moreover, it cannot reproduce the low-energy enhancement in the PSFs which has recently been observed

in various nuclei (see, e.g., [Voi04, Gut05, Wie12]). Furthermore, the energy range below the separation threshold represents a region where the level density just starts to strongly increase and where nuclear structure effects still may play a crucial role. Therefore, the validity of a statistical approach can also be questioned.

In conclusion, a further investigation of photon-strength functions, especially below the particle separation threshold, is mandatory for a comprehensive understanding of the energy dependence of the strength functions.

DICEBOX Code

An adapted version of the DICEBOX code [Beč98] has been used to perform calculations within the nuclear statistical model in the present work. It was initially developed to study the γ decay following neutron capture processes. The adapted version allows to “simulate” NRF measurements, as well. The levels of a nuclear realisation are “populated” randomly according to a photon-flux distribution which is required as input for DICEBOX. As has already been mentioned at the beginning of this section, *nuclear realisations* of level sets are generated for a given nucleus. Additionally, a partial decay width is passed to each state within such a level scheme. The generation of a nuclear realisation and the subsequent simulation of γ -ray cascades is shortly introduced in the following. A detailed description of the functionality of the code can be found in Ref. [Beč98].

In DICEBOX, each nuclear realisation is divided into two parts (Fig.7.27). Up to a particular critical energy E_{crit} experimental data are exploited to generate the nuclear realisation. Below this energy, all nuclear levels and their spectroscopic properties are assumed to be known. For the remaining part of the level scheme above E_{crit} , excited levels are randomly created according to a discretised level-density function. Thus, the part below E_{crit} is identical for each nuclear realisation of a particular nucleus, whereas the part above E_{crit} varies. Afterwards, partial decay widths $\Gamma_{i \rightarrow j}$ from each state i above E_{crit} to each lower-lying state j are randomly distributed according to $E1$, $M1$, and $E2$ photon-strength functions that are discretised. At this, Porter-Thomas fluctuations [Por56] are taken into account to generate an appropriate distribution of the partial transition widths. Figure 7.27 illustrates a generic nuclear realisation.

After a nuclear realisation has been created, the levels are randomly “populated” according to a pre-defined photon-flux distribution and their ground-state transition widths. Hence, it is possible to imitate the photo-excitation of

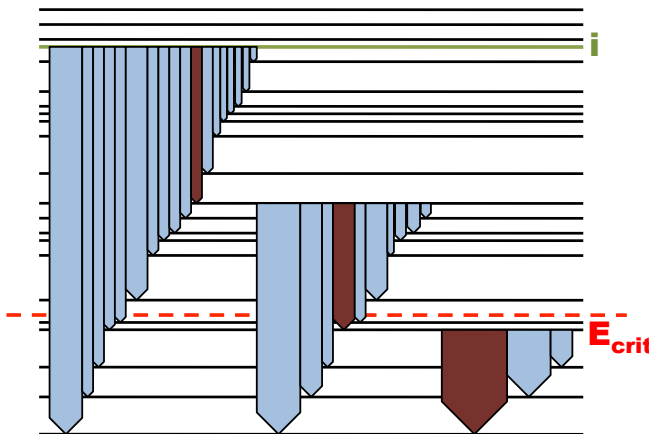


Figure 7.27.: Schematic nuclear realisation of a nucleus within DICEBOX. Below the critical energy E_{crit} experimental data are used to describe the level scheme. Partial decay widths are illustrated via the width of the arrows connecting different levels with each other. A typical γ cascade of the level i is visualised via the red decay path.

levels in an NRF measurement. With the population of a level in the nuclear realisation, the simulation of a γ -ray cascade is initialised and the excited state decays randomly back to the ground state according to the partial decay widths that have been passed to the individual states. A typical γ -ray cascade is shown in Fig. 7.27 with the red decay path. For each γ -ray cascade, the number of intermediate states and their excitation energies can be extracted from DICEBOX. The level energy, the spin and parity quantum numbers, and the partial decay widths can be extracted for each level of a nuclear realisation, as well. These data can be analysed in exactly the same definitions as in NRF experiments and, hence, allow for a direct comparison with the experimental data. For instance, it is possible to determine the excitation strengths of individual levels. Since the exact decay path is known for each γ -ray cascade, especially the decay pattern of the states can be accessed.

Typically, not only one but a large number of nuclear realisations are simulated, each, in turn, with a large number of γ -ray cascades. Eventually, the quantity of interest is extracted and averaged over all nuclear realisations. This provides access to the effect of the Porter-Thomas distribution and the discreti-

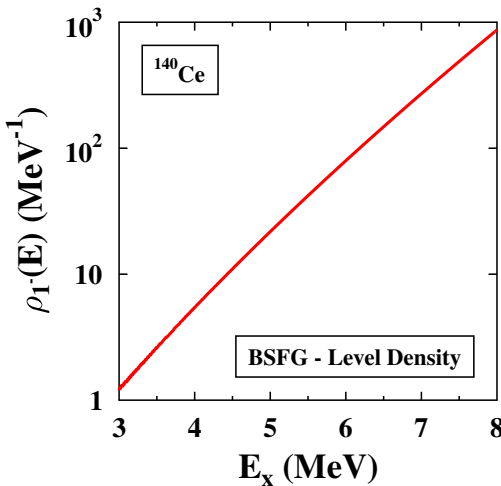


Figure 7.28.: The level density $\rho_{1^-}(E)$ of 1^- states used in the DICEBOX simulations has been parametrised with the energy-dependent back-shifted Fermi gas model according to Ref. [Egi05].

sation of averaged properties to the final results.

In the present case, measured data has been used to describe the level scheme of ^{140}Ce up to $E_{\text{crit}} = 3.1\text{ MeV}$. Above this energy, the level density was described according to the energy-dependent back-shifted Fermi gas model. The parametrisation of the level density has been taken from Ref. [Egi05]. The level density $\rho_{1^-}(E)$ for 1^- states, used here, is plotted as a function of the excitation energy in Fig. 7.28. The PSFs have been parametrised with standard Lorentzian functions. The according parameters for the $E1$ PSF stem from a fit to (γ, n) data [Lep76], whereas the parameters for the $M1$ strength have been extracted from a global parametrisation of spin-flip resonances which have been proposed in Ref. [Bel06]. Eventually, corresponding parameters of a global parametrisation of $E2$ PSFs have been taken from Ref. [Pre84].

The simulations have been performed in 200 keV wide bins of constant photon flux between 3.2 MeV and 7.8 MeV. It has not been necessary to match the actual photon flux from the experiment, since the simulations aimed in the investigation of the decay pattern of the excited states. For each energy setting,

30 nuclear realisations have been generated and, in turn, $2 \cdot 10^5$ γ -ray cascades have been simulated within each nuclear realisation. With the results of the simulations, the weighted, average branching ratio

$$b_0 = \frac{\sum_i \left(\frac{\Gamma_0^2}{\Gamma} \right)_i}{\sum_i \left(\sum_j \frac{\Gamma_0 \Gamma_j}{\Gamma} \right)_i} = \frac{\sum_i \left(\frac{\Gamma_0^2}{\Gamma} \right)_i}{\sum_i (\Gamma_0)_i} = \frac{\sum_i N_{i \rightarrow 0}}{\sum_i N_{i \rightarrow j}} \quad (7.38)$$

has been evaluated. In this expression, i runs over all excited levels, while j denotes all lower-lying levels with respect to level i including also the ground state. Therefore, $\sum_i N_{i \rightarrow 0}$ expresses the sum of the intensities corresponding to ground-state transitions from all levels i and $\sum_i N_{i \rightarrow j}$ denotes the total intensity of all transitions to lower-lying levels j which depopulate the i^{th} level. The b_0 value has been determined for bins of the excitation energy as well as of Γ_0^2/Γ . The results are discussed in the following paragraph and compared to the experimentally determined branching ratios b_0 .

Comparison with Experimental Data

The weighted average b_0 of branching ratios to the ground state has been extracted from the RSA measurement ($b_{0,\text{exp}}$) as well as from DICEBOX calculations within the nuclear statistical model ($b_{0,\text{sim}}$). For the experimental results, solely the 29 excited states, for which the self absorption R_{exp} accounted to a value between zero and R_{max} within its uncertainties, have been taken into account. In Fig. 7.29, b_0 is shown as function of the excitation energy. Furthermore, Fig. 7.30 presents the results as function of the NRF observable Γ_0^2/Γ . In both figures, the results of the γ -ray cascade simulations are represented via the red coloured area. It corresponds to 500 keV wide energy bins and to 100 meV wide bins of Γ_0^2/Γ , respectively. The blue and green boxes illustrate the confidence intervals of the $b_{0,\text{exp}}$ values which result from the RSA measurement. The centre line corresponds to the most probable value of the b_0 -probability distribution. Where no centre line is seen, the most probable value coincides with the upper limit of the confidence interval. Eventually, the numbers at the top of the figures quantify the number of excited states which have been exploited to determine $b_{0,\text{exp}}$ for a particular bin.

As depicted in Fig. 7.29, the results of the simulations within the nuclear statistical model are in a rather good agreement with the experimental findings up to an excitation energy of $E_x \sim 5.5$ MeV. At higher energies, the experimentally deduced $b_{0,\text{exp}}$ exhibits a steep increase from $b_0 \sim 70\%$ to $b_0 \sim 100\%$. In

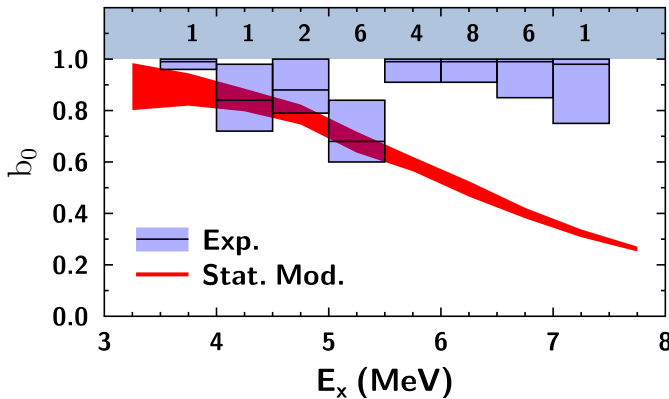


Figure 7.29.: The weighted average branching ratio to the ground state as a function of the excitation energy of the excited states has been extracted from calculations within the statistical model (red area) and from the RSA measurement (blue boxes). The numbers at the top denote how many states entered the determination of b_0 for each bin.

contrast, $b_{0,\text{sim}}$ smoothly decreases towards larger excitation energies. Thus, $b_{0,\text{exp}}$ and $b_{0,\text{sim}}$ deviate significantly above $E_x \sim 5.5$ MeV. However, it should be noted that the experimental data partly base on one or two excited states which, furthermore, are particularly strongly excited, only.

A deviation of the simulated and the experimentally determined results of b_0 has already been observed for the nucleus ^{94}Mo [Rom13]. The results for ^{94}Mo have been depicted in Fig. 2.3 in the motivation chapter (Ch. 2) of this thesis. In this case, the simulated data show a good agreement at ~ 5.5 MeV and at ~ 7 MeV with the experiment, whereas in-between the experimentally deduced values substantially exceed the simulation. In both cases, for ^{94}Mo and ^{140}Ce , an enhanced branching ratio to the ground state with respect to the simulation occurs in the energy range between about 6 MeV and 7 MeV. This is the energy range where the pygmy dipole resonance is supposed to be located in. Indeed, an accumulation of strong electric dipole states is observed in this energy range for ^{94}Mo [Rom13] as well as for ^{140}Ce (Fig. 7.4). For ^{140}Ce this observation is emphasised by the investigation of the directly determined ground-state transition widths. They also exhibit comparatively strong values

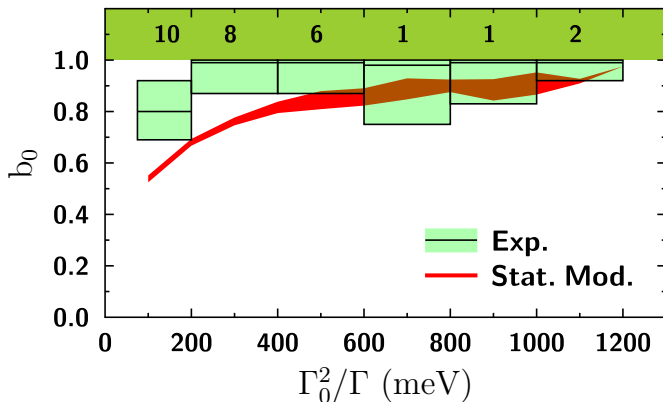


Figure 7.30.: Experimental results (green boxes) and results extracted from DICEBOX calculations (red area) for b_0 are shown as function of Γ_0^2/Γ . The numbers at the top of the figure quantify how many excited states have been available for each bin to deduce the experimental result.

in the energy range the PDR is supposed to be located in as has been shown before (Figs. 7.21 and 7.22).

For the γ -cascade simulations of ^{94}Mo and ^{140}Ce , respectively, standard Lorentzian parametrisations have been used for the $E1$ photon-strength function. This structureless strength function, which smoothly increases from low to high energies, is apparently not sufficient to reproduce the experimental observations as a function of the excitation energy. Hence, the observations in the case of ^{94}Mo and ^{140}Ce indicate a non-statistical, localised structure of $E1$ excitation in the vicinity of $E_x \sim 6.5$ MeV and, thus, in the energy regime of the PDR. Such a non-statistical structure may either occur because the statistical model does not correctly describe the decay behaviour of the strongly excited states in the energy domain of the PDR. Or the statistical model cannot reproduce the accumulation of strongly excited states in this energy region.

The present data allow for the first time also for a comparison of $b_{0,\text{exp}}$ and $b_{0,\text{sim}}$ as function of Γ_0^2/Γ as it is depicted in Fig. 7.30. During the evaluation of $b_{0,\text{sim}}$ only states with excitation energies between 4.2 and 7.2 MeV have been taken into account which matches the energy range of the experimental

findings. The result for the two-phonon state at $E_i = 3642.9$ keV has not been regarded in this case. Again, the low number of states available to deduce $b_{0,\text{exp}}$ for the three highest-lying bins should be noted. A trend of an increasing branching ratio to the ground state with increasing Γ_0^2/Γ becomes apparent from the experimental as well as the simulated data. However, the absolute values of $b_{0,\text{exp}}$ are not reproduced by the results extracted from the DICEBOX calculation below $\Gamma_0^2/\Gamma \lesssim 600$ meV. There, the $b_{0,\text{sim}}$ values underestimate the experimental findings. With this observation, it can be concluded that the non-statistical structure in the energy domain of the PDR does not only arise due to a problem of the statistical model with the description of the accumulation of strongly excited states in this energy region. The statistical model is not capable to completely describe the decay behaviour of those states at least not with a rather simple parametrisation of the $E1$ photon-strength function such as a Lorentzian function.

However, for a further investigation of these observations and conclusions further systematic measurements are highly required.

7.7 Conclusions

In this work, a self-absorption experiment has been applied pioneering to study the ground-state transition width Γ_0 , the level width Γ , and the branching ratio Γ_0/Γ to the ground state of excited states of ^{140}Ce in a direct and model-independent way. For this purpose, two measurements have been performed, an NRF measurement and the actual self-absorption measurement. The measurements and the according analysis have been presented in this chapter. In total, the NRF measurement has been analysed for 117 excited states of ^{140}Ce out of which four levels were already known as 2^+ states. Spin $J = 1$ has been assigned to the remaining ones. The results for the product $\Gamma_0 \cdot \Gamma_0/\Gamma$ of the ground-state transition width and the branching ratio to the ground state exhibited a substantial deviation to results of earlier measurements by Herzberg and co-workers [Her95b, Her95a, Her97] and by Volz and collaborators [Vol06].

The analysis of the RSA measurement yielded R_{exp} for 104 excited levels of ^{140}Ce . However, the measured self absorption often exhibited comparatively large uncertainties. The sensitivity also to weakly excited states may be increased by using a thicker absorption target, which would enhance the self-absorption effect. From the experimentally determined self absorption R_{exp} the

ground-state transition width, the level width, and the branching ratio to the ground state have been determined. To avoid problems with asymmetric uncertainties during the error propagation, a Bayesian approach for the analysis has been chosen and probability-density functions have been used to describe the regarded quantities. Applying the principle of maximal information entropy allowed for the exclusion of non-physical regions during the analysis such as branching ratios to the ground state being larger than one. A systematic investigation of the analysis procedure has shown that reliable results can be obtained in cases where R_{exp} has been measured to a sufficient precision $\Delta R_{\text{exp}}/R_{\text{exp}} \sim 1/3$. For less certain values of the self absorption, the analysis procedure tends to be prone to systematical artefacts, in particular, for the ground-state branching ratio Γ_0/Γ . Thus, the analysis has been constrained to 29 excited states for which R_{exp} has been found to be larger than zero and smaller than R_{max} within a 1σ uncertainty interval.

Eventually, simulations of γ -ray cascades in ^{140}Ce have been performed within the nuclear statistical model exploiting the DICEBOX code. The simulations allowed for the determination of quantities such as the weighted average branching ratio b_0 to the ground state in exactly the same definition as in the experiment. The results have been compared to the experimental findings. The calculations within the statistical model exploiting a rather simple, structureless photon-strength function are capable of completely reproducing the dependence of b_0 neither on Γ_0^2/Γ nor on the excitation energy. The made observations hint at a structural feature, an accumulation of strongly excited dipole states which preferentially decay directly back to the ground state at an excitation energy between 6 MeV and 7 MeV which cannot be described by means of statistical methods. However, more systematic studies are needed to study this phenomenon, which go beyond this pioneering experimental approach.

In conclusion, this work demonstrates that the approach of relative self absorption measurements is a powerful method which provides valuable insight in the ground-state transition width Γ_0 , the level width Γ , as well as the branching ratio to the ground state of individual states in a model-independent way.

8 High-Precision Self-Absorption Measurement on ${}^6\text{Li}$

The second experiment that has been performed in the framework of this thesis is a high-precision self-absorption measurement on ${}^6\text{Li}$. It aims at a detailed investigation of the $J^\pi = 0^+$, $T = 1$ level of ${}^6\text{Li}$ at an excitation energy of $E_i = 3563$ keV (compare the level scheme in Fig. 2.5). This excited state decays via a strong $M1$ transition to the $J^\pi = 1^+$ ground state. The corresponding transition width is known to a relative uncertainty of 2.3 %. The intention of this work is to improve the relative uncertainty to less than 1 % requiring an even smaller relative uncertainty of the self absorption of this level.

In the following section, the specifications of the experiment on ${}^6\text{Li}$ will be provided. Afterwards, the determination of the self absorption will be explained and the achieved result will be presented. A further section treats the subsequent determination of the level width Γ and problems that occurred during the analysis. Eventually, this chapter closes with a discussion of the measurement on ${}^6\text{Li}$, of resulting conclusions and of a follow-up measurement.

8.1 The Measurement

As well as for the measurement on ${}^{140}\text{Ce}$, three targets have been required for the self-absorption measurement on ${}^6\text{Li}$. Information on these targets are summarised in Table 8.1. Both, the absorption and the scattering target, consisted of lithium carbonate Li_2CO_3 , which has been enriched to 95 % in ${}^6\text{Li}$. The natural abundance of ${}^6\text{Li}$ amounts solely to 7.5 %. The target mass of the absorber yielded $m_a = 9.938$ g, the one of the scatterer amounted to $m_s = 5.033$ g. The Li_2CO_3 powder has been filled into small plastic tubes and closed such that the material is carefully compressed. It is crucial for the measurements that especially the material in the absorption target is homogeneously distributed ensuring a constant areal particle density. Only in this case, all photons passing the targets undergo the same attenuation and resonant absorption effects which is also assumed for the calculation of $R_{\Gamma_0, \Gamma}$. With the inner diameter of $d = 1.9$ cm

Table 8.1.: Information on the targets that have been exploited for the self-absorption experiment on ${}^6\text{Li}$. Besides the chemical composition, the mass and the enrichment also the areal particle density d_x is given.

target	chem. compound	mass (g)	enrichment	d_x (b^{-1})
absorber	Li_2CO_3	5.033	95 % in ${}^6\text{Li}$	0.0282
scatterer	Li_2CO_3	9.938	95 % in ${}^6\text{Li}$	0.0556
monitor I	B	2.118	99.52 % in ${}^{11}\text{B}$	0.0407
monitor II	B	2.119	99.52 % in ${}^{11}\text{B}$	0.0407

of the tubes, the areal particle density of ${}^6\text{Li}$ nuclei follows to $d_a = 0.0556 \text{ b}^{-1}$ for the absorber and to $d_s = 0.0282 \text{ b}^{-1}$ for the scatterer, respectively. According to these parameters and the current literature value $\Gamma_{\text{lit}} = 8.19(17) \text{ eV}$ of the level width, a self absorption amounting to $R_{\text{exp}} \approx 50\%$ is expected for the level at 3563 keV excitation energy.

The monitoring target being composed out of boron enriched to 99.52 % in ${}^{11}\text{B}$ has been split into two individual targets. The first one had a mass of $m_{m,I} = 2.118 \text{ g}$, the second one of $m_{m,II} = 2.119 \text{ g}$. During the measurements, the scattering target has been placed in-between the monitoring targets. In this way, the influence of the rather massive scattering target on the photon-flux intensity is accounted for and the average number of NRF reactions in the monitoring target can be interpreted to correspond to the photon flux in the centre of the scatterer.

For the experiment on ${}^6\text{Li}$, three measurements have been performed at the bremsstrahlung facility in Darmstadt (Sec. 6.2); a classical NRF and the RSA measurement as well as a measurement with monitoring target but without scatterer. The NRF measurement has been conducted with the scatterer being sandwiched between the monitoring targets at position S1 (see Fig. 6.2). In contrast to the RSA measurement on ${}^{140}\text{Ce}$, the absorption target has been placed in front of the collimator at position A1 during the RSA measurement on ${}^6\text{Li}$. The inner diameter of the absorber exceeded the one of the collimator entrance. With this, it has been ensured that exclusively photons which have passed the absorption target entered the collimator. Eventually, a second measurement with the absorber located at A1 has been performed. However, in this case, only the monitoring target has been put at position S1. Adopting the nomenclature of the measurements on ${}^{140}\text{Ce}$, this measurement is referred

Table 8.2.: Information on the measurements performed during the self-absorption experiment on ${}^6\text{Li}$. The positions of the targets correspond to the nomenclature introduced in Fig. 6.2.

	E_0 (MeV)	absorber pos.	scatterer pos.	monitor pos.	t_{meas}
ABS	7.1(2)	A1	X	S1	8 h
NRF	7.1(2)	X	S1	S1	122 h
RSA	7.1(2)	A1	S1	S1	189 h

to as absorption (ABS) measurement. For all measurements, the endpoint energy has been set to $E_0 = 7.1(2)$ MeV. At this energy, the NRF measurement lasted for 122 h while the RSA measurement took 189 h. The ABS measurement served to check whether photons are scattered from the absorber into the detectors and lasted 8 h. An overview of the individual measurements is provided via Table 8.2.

8.2 Self Absorption

Figure 8.1 shows the total γ -ray spectra observed. The combination of long measuring times, massive scattering targets and especially the large level widths of the investigated 0_1^+ state of ${}^6\text{Li}$ and of the ${}^{11}\text{B}$ levels results in large statistics. The relevant peaks for the determination of the self absorption in the recorded spectra contain in the order of 10^4 and 10^5 events. Before the self absorption can be deduced from the measured intensities according to Eq. (5.4), the correction factor for atomic attenuation has to be determined. Furthermore, it must be checked whether the position of the absorption target has any impact on the experiment. Both aspects are discussed in the following paragraphs.

Correction for Atomic Attenuation and Normalisation

The normalisation factor $f_{\text{RSA,NRF}}$ has been determined according to Eq. (5.5) at the ground-state transition energies of the ${}^{11}\text{B}$ monitoring target for each detector. Afterwards, the results have been averaged. They are tabulated in Table 8.3. Next to atomic attenuation effects, the normalisation factor takes also different measuring times and photon-flux intensities into account and, thus, can exceed one. As discussed in detail in the case of the ${}^{140}\text{Ce}$ measurement, $f_{\text{RSA,NRF}}(E)$ exhibits an energy dependence. Since the three observed

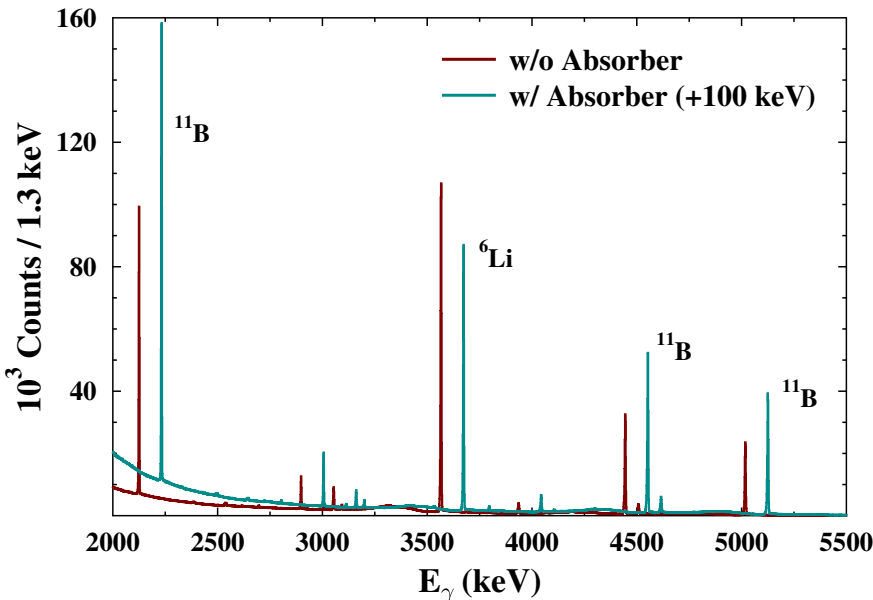


Figure 8.1.: Spectra recorded during the NRF (red) and RSA (turquoise, shifted by 100 keV) measurements in the energy range between 2000 keV and 5500 keV. Small unmarked peaks correspond to single escape events or to those from inelastic decays.

excited states of ^{11}B are not sufficient to describe this dependence, two other approaches have been combined to investigate the energy dependence. Firstly, a GEANT4 simulation of the γ -ray beam attenuation effects in the absorption target has been performed in the relevant energy region between 0.5 and 5.5 MeV in steps of 100 keV. Secondly, for a test of the simulated results, a measurement with a ^{56}Co source has been conducted. Photons emitted by the source have been measured with and without passing the Li_2CO_3 absorber. From a comparison of both measurements, the attenuation can be determined, as well.

Figure 8.2 depicts all results. The simulated atomic attenuation agrees well with the experimentally deduced results from the ^{56}Co measurement. Therefore, the results of the simulation have been interpolated for the description of the energy dependence of $f_{\text{RSA},\text{NRF}}$. Subsequently, the resulting curve has

Table 8.3.: The normalisation factors $f_{\text{RSA,NRF}}$ have been determined at the ^{11}B transition energies individually for each detector. For further analysing steps, the error-weighted average, given in the last column, will be taken.

E_γ (keV)	DET1	DET2	DET3	$\bar{f}_{\text{RSA,NRF}}$
2124.5	1.588(32)	1.540(21)	1.561(21)	1.561(14)
4443.9	1.623(10)	1.641(6)	1.658(8)	1.643(8)
5019.1	1.675(12)	1.677(7)	1.654(10)	1.670(7)

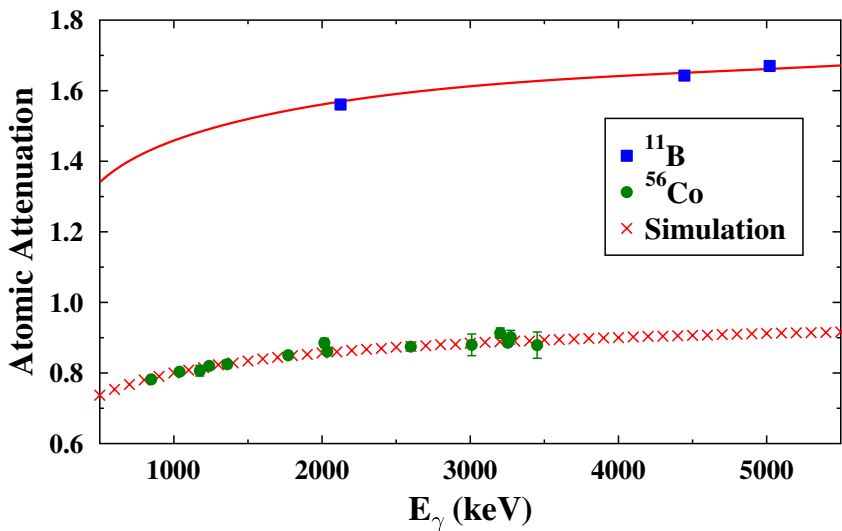


Figure 8.2.: The normalisation factor $f_{\text{RSA,NRF}}$ between the RSA and the NRF measurement in the case of the ^6Li experiment. The results have been obtained from a GEANT4 simulation (red crosses), from a measurement with a ^{56}Co source (green circles), and from the measurements exploiting the ^{11}B monitoring target (blue squares). The red curve is an interpolation of the simulated results that has been scaled to the results from the monitoring target.

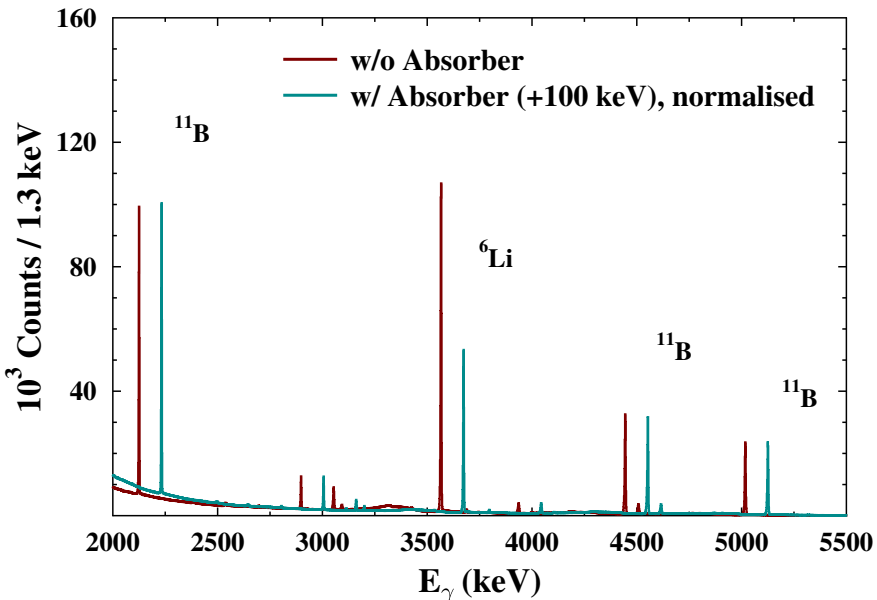


Figure 8.3.: The recorded NRF spectrum (left-hand spectrum, red) and the corresponding RSA spectrum (right-hand, turquoise, shifted by 100 keV). The RSA spectrum has been normalised to the NRF spectrum multiplying it with $f_{\text{RSA,NRF}}^{-1}(E)$. Small unmarked peaks correspond to single escape events or to those from inelastic decays.

been scaled to the experimentally determined results for $f_{\text{RSA,NRF}}$. This curve is depicted in Fig. 8.2, too.

Figure 8.3 again shows the recorded NRF and RSA spectra. However, in this case, they have been normalised to each other exploiting the correction factor $f_{\text{RSA,NRF}}(E)$. As is apparent, the peaks corresponding to transitions in the ^{11}B monitor are equally high, now. The intensity in the peak corresponding to the ground-state transition of the investigated 0_1^+ level of ^{6}Li is approximately halved in the RSA measurement with respect to the NRF measurement. Thus, the self absorption accounts as expected to $R_{\text{exp}} \approx 0.5$ (see also Sec. 8.1).

For the following detailed determination of R_{exp} , the interpolated curve describing $f_{\text{RSA,NRF}}(E)$ has been evaluated at the excitation energy $E_i = 3563\text{ keV}$ of the investigated ^{6}Li level. It yields $f_{\text{RSA,NRF}}(3563\text{ keV}) = 1.631(6)$.

Impact of the Absorber Position

During the measurements on ^{140}Ce , the absorption target has been placed at position A2 (see Fig. 6.2). It has been observed that a small part of photons scattered in the absorber passed through the shielding and has been registered in the detectors. To remedy this problem, the Li_2CO_3 absorber has been positioned in front of the collimator at position A1. The ABS measurement revealed that, indeed, photons scattered in the absorption target cannot reach the detectors anymore. However, positioning the absorber in front of the collimator may give rise to another issue. The collimator selects those photons which move in direction of the scatterer. Photons with other directions of movement are mainly absorbed. However, a small part of them may also be scattered at small angles within the absorber and, as a consequence, still irradiate the scatterer. Thereby, they loose energy via the Compton scattering process and are shifted to smaller energies. Consequently, they produce additional photon-flux intensity at smaller energies. This effect would not affect classical NRF measurements since the entire photon-flux distribution is just slightly shifted towards smaller energies. However, in self-absorption experiments, the number of NRF reactions at a particular excitation energy in the scatterer target and, thus, the total photon flux at this energy, is compared between two measurements. This comparison, *i.e.*, the self absorption, may be affected as the following example shows. At first, the absorption target shall be placed behind the collimator system. For a given state, the self absorption shall yield 50%. This means, the photon flux at the resonance energy of this level is halved within the absorber and, consequently, also the number N_{RSA}/f of NRF reactions in the scatterer is halved with respect to the measurement without absorber yielding N_{NRF} NRF reactions. Here, f abbreviates the above discussed normalisation factor $f_{\text{RSA,NRF}}$. As it is expected, the self absorption accounts to

$$R = 1 - \frac{N_{\text{RSA}}/f}{N_{\text{NRF}}} = 1 - \frac{0.5 \cdot N_{\text{NRF}}}{N_{\text{NRF}}} = 0.5. \quad (8.1)$$

Assuming now that the absorber is placed in front of the collimator, the photon flux is still halved. However, in the collimator system, a part of the photons is slightly shifted in energy resulting in an additional amount of photons also at the resonance energy of the regarded state. In the case that both measurements are normalised to each other, the number of additional photons is identical in

both measurements. The number of NRF reactions increases by N^+ and the self absorption accounts to

$$R = 1 - \frac{N_{\text{RSA}}/f + N^+}{N_{\text{NRF}} + N^+} = 1 - \frac{0.5 \cdot N_{\text{NRF}} + N^+}{N_{\text{NRF}} + N^+} < 0.5. \quad (8.2)$$

Apparently, the measured self absorption becomes smaller as the expected value. This consideration suggests that the impact of scattering reactions in the collimator must be further analysed. In particular, it must be quantified how many photons are shifted to a particular energy.

For this purpose, simulations of mono-energetic γ -ray beams have been performed with GEANT4 imitating the specifications of the DHIPS measuring site and, in particular, of the collimator system. The photons are emitted into a solid angle covering the collimator entrance. Behind the collimator, the photons are detected in an area matching the position and dimensions of the scattering target. A Li_2CO_3 absorption target can optionally be placed in front of the collimator system.

Figure 8.4 depicts typical results of such simulations. In this case, they have been performed with mono-energetic beams of 5000 keV and of 7000 keV with and without the absorption target being placed in front of the collimator, respectively. Indeed, photons experience scattering at small angles and are partly shifted to smaller energies. In total, $100 \cdot 10^6$ photons have been simulated for each setting out of which $\sim 2.6 \cdot 10^6$ reached the scatterer position and have been “detected”. The remaining part of the photons enters the collimator such that they are absorbed. Only a small part of the photons that reached the scatterer position had energies different from the original one. For the initial energy of 5000 keV, about $1 \cdot 10^4$ photons have been shifted to smaller energies. In the case of 7000 keV, this number slightly increases to $1.2 \cdot 10^4$ photons. The energy distributions of these photons are illustrated in Fig. 8.4. As is apparent, the absorption target influences neither the amount of photons with energies smaller as the initial one nor their distribution. This is not surprising taking into account that photons from a bremsstrahlung source are not aligned and, thus, enter the collimator at random angles anyway.

To quantify the impact of the scattering reactions in the collimator on the self absorption, the above mentioned number N^+ of additional NRF reactions in the scatterer has to be determined. However, this quantity cannot be accessed

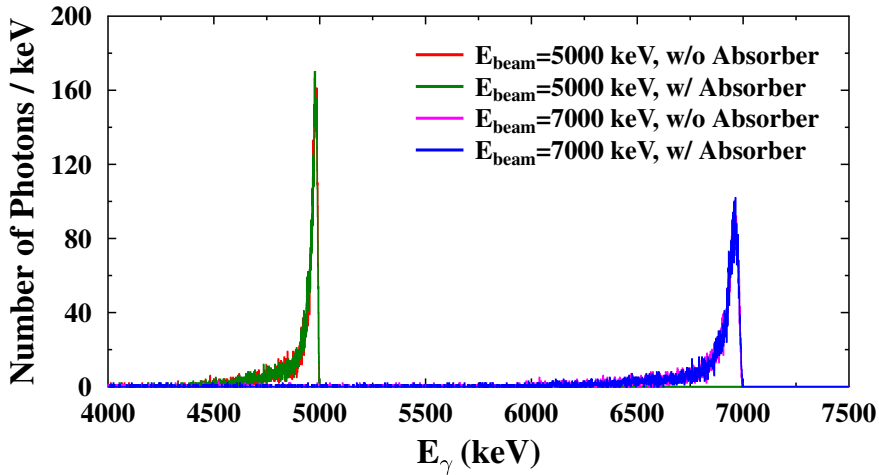


Figure 8.4.: With GEANT4 simulated energy distributions of initially mono-energetic photons after they have passed the collimator. Only photons with energies different from the original one (5000 keV and 7000 keV, respectively) are shown. The simulations have been performed with and without taking an absorber in front of the collimator into account. Apparently, the distributions are not affected by the absorption target.

directly via the simulations where only photon-flux intensities can be regarded. Therefore, the self absorption has to be rewritten as follows:

$$R = 1 - \frac{N_{RSA}/f + N^+}{N_{NRF} + N^+} \quad (8.3)$$

$$= 1 - \frac{N_{RSA}/f \cdot \left(1 + n \cdot \frac{N^+}{N_{NRF}}\right)}{N_{NRF} \cdot \left(1 + \frac{N^+}{N_{NRF}}\right)} \quad (8.4)$$

$$= 1 - \frac{N_{RSA}/f \cdot \left(1 + n \cdot \frac{N_\gamma^+}{N_{\gamma,NRF}}\right)}{N_{NRF} \cdot \left(1 + \frac{N_\gamma^+}{N_{\gamma,NRF}}\right)} \quad (8.5)$$

$$\equiv 1 - \frac{N_{RSA}/f}{N_{NRF}} \cdot f^+ \quad (8.6)$$

where

$$n = \frac{N_{\text{NRF}}}{N_{\text{RSA}}/f}. \quad (8.7)$$

In Eq. (8.5), the ratios of the NRF reactions in the scatterer have been replaced by the proportional ratios of the corresponding photon-flux intensities. The factor f^+ describes the influence of scattering reactions on the self absorption.

For the determination of the additional photon flux, simulations with mono-energetic photon beams of energies $E_{x,i}$ have been performed in steps of 400 keV from 2 MeV up to 7.2 MeV. The resulting distributions of photons that have been shifted to smaller energies E have been evaluated with respect to the total number $N_{\text{tot}}(E_{x,i})$ of photons reaching the scatterer position for each energy setting $E_{x,i}$ yielding the normalised distribution $r^+(E, E_{x,i})$. It describes the relative share of photons with an initial energy $E_{x,i}$ that are shifted to smaller energies E and, hence, appear as additional photon flux $N_\gamma^+(E, E_{x,i})$ at these energies. So far, $r^+(E, E_{x,i})$ has only been described at discrete anchor points $E_{x,i}$. For the determination of a general function $N_\gamma^+(E)$ which takes photons shifted from each energy $E_>$ to each lower energy $E_<$ into account, $r^+(E, E_{x,i})$ and the initial photon-flux distribution $N_{\gamma, \text{NRF}}(E)$ entering the collimator have to be convoluted via

$$N_\gamma^+(E) = \int_{2 \text{ MeV}}^{7.2 \text{ MeV}} r^+(E, E_x) \cdot N_{\gamma, \text{NRF}}(E_x) dE_x, \quad (8.8)$$

where E_x runs now over all possible initial beam energies. For practical reasons, the integral has been transferred into the corresponding sum

$$N_\gamma^+(E) = \sum_{2 \text{ MeV}}^{7.2 \text{ MeV}} r^+(E, E_x) \cdot N_{\gamma, \text{NRF}}(E_x). \quad (8.9)$$

The distribution $r^+(E, E_x)$ between two energy settings $E_{x,i}$ and $E_{x,i+1}$ with $E_{x,i+1} > E_{x,i}$ has been interpolated in steps of 1 keV via

$$r^+(E, E_x) = a \cdot r^+(E, E_{x,i}) + b \cdot r^+(E, E_{x,i+1}) \quad (8.10)$$

with

$$a = \frac{E_{x,i+1} - E_x}{400 \text{ keV}} \text{ and } b = 1 - a. \quad (8.11)$$

With the additional photon flux determined in this way, the factor f^+ can be determined for the 0_1^+ level of ${}^6\text{Li}$ investigated in this work. It accounts to $f^+ = 1.0033$. Apparently, scattering reactions at small angles affect the self absorption only little, namely on a sub-% level. However, in the present high-precision measurement aiming at an accuracy of better than 1 %, this effect cannot be neglected as will be shown in the following paragraph.

Experimentally Deduced Self Absorption R_{exp}

Eventually, the result for the self absorption of the $0_1^+, T = 1$ level of ${}^6\text{Li}$ at an excitation energy of 3563 keV can be determined with the so far made preparations. It has been deduced with and without correcting for scattering reactions in the collimator system of the DHIPS measuring site. The individual results for each detector as well as their error-weighted average are summarised in Table 8.4 for both cases. Taking the scattering reactions into account, the averaged self absorption yields $R_{\text{exp}} = 0.5193(15)$. If they are not accounted for, the self absorption results in a slightly smaller value $R_{\text{exp}} = 0.5178(15)$. Both results exhibit a relative uncertainty of only 0.3 % demonstrating that the self absorption can be and has been determined with highest precision. The impact of scattering reactions in the collimator system is rather small. It changes the result solely by 0.3 % and, hence, on the sub-% level. However, in the case of the present high-precision measurement, this effect is in the order of the uncertainty of the measured self absorption. Thus, it must be taken into account. Consequently, the following determination of the level width of the investigated excited state will rely on the corrected value $R_{\text{exp}} = 0.5193(15)$.

8.3 Determination of the Level Width

At last, the level width of the excited $J^\pi = 0_1^+, T = 1$ state of ${}^6\text{Li}$ with an excitation energy of 3563 keV can be determined. For this purpose, the self absorption $R_{\Gamma_0, \Gamma}$ has been determined according to Eq. (5.12). Thereby, a relation between Γ_0 and Γ as well as information on the Debye temperature of lithium is required. These points will be discussed in the following, before the results obtained for Γ will be presented and discussed.

Competitive Decay Channels

The regarded 0_1^+ level at 3563 keV excitation energy is the second excited state of ${}^6\text{Li}$ (compare the level scheme in Fig. 2.5). Consequently, an electro-

Table 8.4.: The self absorption R_{exp} has been determined for each detector individually with and without taking the correction for scattering reactions in the collimator into account. The error-weighted average over the three detectors is given in the last column.

Correction	DET1	DET2	DET3	\bar{R}_{exp}
✗	0.5145(29)	0.5199(22)	0.5175(25)	0.5178(15)
✓	0.5160(29)	0.5214(22)	0.5190(25)	0.5193(15)

magnetic decay of the 0_1^+ level can only occur to the first excited as well as to the ground state. The first excited state is located at $E_i = 2185$ keV and has a spin quantum number of $J^\pi = 3^+$. As a consequence, the 0_1^+ level could only decay via a magnetic octupole transition to the first excited state. However, this kind of radiation is strongly suppressed since photons carry only small angular momentum. In contrast, the ground state of ${}^6\text{Li}$ is a $J^\pi = 1^+$ level and can be reached via an $M1$ transition from the 0_1^+ state which is much more probable. Indeed, the 0^+ level exhibits a strong $M1$ decay width to the ground state. This electromagnetic decay competes with the decay via the α channel, *i.e.*, the decay of the ${}^6\text{Li}$ nucleus into an α particle and a deuteron. However, this decay channel is parity forbidden as has been discussed in the motivation chapter (Ch. 2). The corresponding decay width Γ_{ad} has been found to be smaller than $\Gamma_{ad} \leq 17$ meV on a confidence level of 90 % in 1975 [Bar75]. In 1984, this upper limit has been further reduced to $6.5 \cdot 10^{-7}$ eV [Rob84], emphasising that this decay channel can be neglected. Consequently, the level width has been determined with the condition $\Gamma_0 = \Gamma$.

Debye Temperature

Another crucial ingredient for the determination of $R_{\Gamma_0, \text{r}}$ is the Debye temperature of ${}^6\text{Li}$ in the Li_2CO_3 compound. It enters the Doppler width Δ [Eq. (4.23)] in form of the effective temperature [Eq. (4.27)] (see also Sec. 4.2) and accounts for vibrational degrees of freedom. At the Debye temperature, all possible phonon vibrations are occupied. However, the Debye temperature for this particular chemical compound is not yet measured.

In general, the Debye temperature is comparatively difficult to obtain for complex compounds. In principle, possible vibrational states of a chemical compound can be identified with the well-established method of *Raman spectroscopy*. The material of interest is irradiated with monochromatic light,

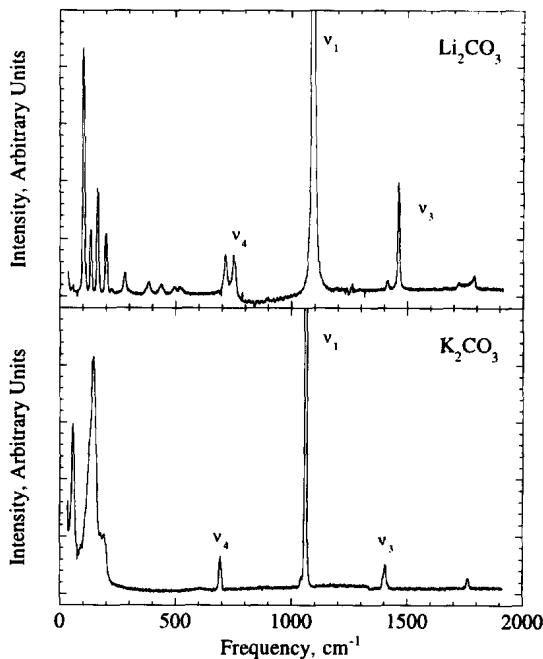


Figure 8.5.: Raman spectra of Li_2CO_3 and K_2CO_3 . The vibrational modes denoted as ν_1 , ν_3 , ν_4 occur in both spectra and, thus, are supposed to be related to the CO_3 complex.

Reprinted with permission from [Kou96]. Copyright 1996, AIP Publishing LLC.

usually generated via a laser, and the spectral distribution of the scattered photons is measured. Typically, the distribution is measured as a function of the wave number of the electromagnetic radiation. Besides the elastically scattered photons (Rayleigh scattering, [Str71]) also photons with wave numbers or frequencies deviating from the original one are observed. They have been inelastically scattered (Raman scattering, [Ram28]). The difference to the original frequency corresponds to the specific excitation energies of vibrational or rotational states of the investigated material. However, the actual assignment of the observed vibrations to the components of the investigated compound often is not feasible. For instance, the Raman spectrum of Li_2CO_3 has been

measured [Kou96]. It is depicted in Fig. 8.5 together with the Raman spectrum of K_2CO_3 . Both spectra exhibit vibrational states up to a frequency of $f \sim 1500 \text{ cm}^{-1}$. A reliable assignment of the observed lattice vibrations to either the Li or K atoms or the CO_3 complex is not possible so far. Since the vibrational modes denoted as ν_1 , ν_3 , ν_4 in Fig. 8.5 occur in both spectra, they are supposed to be related to the CO_3 complex. From this point of view, vibrations with frequencies exceeding $f \sim 600 \text{ cm}^{-1}$ can rather be ascribed to the CO_3 part of the molecule than to the Li or K atoms. This frequency corresponds to a Debye temperature of $T_D \sim 860 \text{ K}$. In turn, low frequent vibrations below $f \sim 200 \text{ cm}^{-1}$ are expected to be related to the Li and K atoms. This provides a lower constraint for the Debye temperature of $T_D \sim 300 \text{ K}$. For comparison, the Debye temperature of metal lithium accounts to $T_D = 344 \text{ K}$ [Mar65], the one of LiCl to $T_D = 429 \text{ K}$ [Lew67], and eventually the one of LiF to $T_D = 734 \text{ K}$ [Lew67]. It should be noted, that the given Debye temperatures correspond to the one of the compound, not to the one of Li within the compound. These numbers demonstrate that the Debye temperature is strongly related to the characteristics of specific compounds like the chemical bonding.

In conclusion, the Debye temperature of the Li atoms in the Li_2CO_3 compound is not known and, thus, missing for the calculation of the self absorption $R_{\Gamma_0, \Gamma}$. From the above made considerations only very rough constraints on the value of the Debye temperature between 300 K and 900 K can be made. However, it is supposed to take a rather small value in the region of 300 K to 400 K instead of higher temperatures. In the following paragraph, it will be discussed how the results for the level width Γ change with the chosen Debye temperature.

The Level Width Γ

The level width Γ has been determined in two ways. On the one hand, it has been deduced from the experimentally determined self absorption R_{\exp} exploiting the conventional and the Bayesian approach that have already been discussed in the case of the measurement on ^{140}Ce (see Sec. 7.4). However, the relation between Γ_0 and Γ which is required to calculate $R_{\Gamma_0, \Gamma}$ has not been taken from the NRF result but has been set to $\Gamma_0 = \Gamma$ as discussed above. As a consequence, $R_{\Gamma_0, \Gamma}$ does not exhibit a maximum and, hence, an unambiguous result for Γ and Γ_0 , respectively, can be obtained. The self absorption has been evaluated for different Debye temperatures from 300 K to 1000 K in steps of 100 K. Owed to the small uncertainty of the measured self absorption, the conventional and the Bayesian approach yielded identical results. Thus, only the

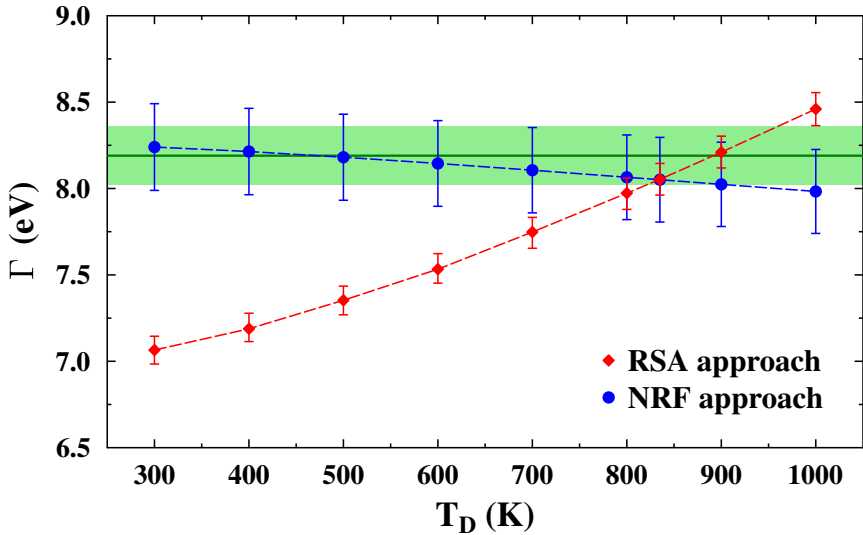


Figure 8.6.: Results for the level width Γ of the $J^\pi = 0^+$ level of ${}^6\text{Li}$ at 3563 keV excitation energy as a function of the Debye temperature. The data points represented via red diamonds have been extracted from R_{exp} . In contrast, the results shown with blue circles correspond to an independent analysis of the NRF measurement which is further explained in the text. The dotted lines shall guide the eyes. Eventually, the green coloured area represents the current literature value with the corresponding uncertainty [Til02].

results obtained with the Bayesian approach will be discussed in the following. The results for Γ are shown in Fig. 8.6 as a function of the Debye temperature. The level width increases with increasing Debye temperature. Within the region of $T_D = 300\text{ K}$ to $T_D = 900\text{ K}$, where the Debye temperature is supposed to be, it varies between $\Gamma = 7.065^{+(80)}_{-(81)}\text{ eV}$ and $\Gamma = 8.210^{+(93)}_{-(91)}\text{ eV}$. As a reference, the current literature value for the level width accounting to $\Gamma_{\text{lit}} = 8.19(17)\text{ eV}$ [Til02] is also shown. The results of the present work agree with the literature value for Debye temperatures between $\sim 800\text{ K}$ and 950 K . However, the Debye temperature is supposed to be considerably smaller as discussed above. The relative uncertainties of the level widths obtained in this work account to $\sim 1.1\%$ for a chosen Debye temperature demonstrating that a highly precise

determination of the level width is feasible if the relevant Debye temperature would be known to a sufficient accuracy of about 1-3 %. The intention of the present experiment has been the determination of the level width to a relative uncertainty of better than 1 %.

On the other hand, the level width has been determined with a second independent approach exploiting the NRF measurement. This measurement has been analysed analogously to the proceeding described in Sec. 7.2 for the measurement on ^{140}Ce . The naive analysis yielded $\Gamma_0^2/\Gamma = 6.38(19)\text{ eV}$ for the NRF result. In contrast to the RSA measurement, the integrated cross sections of the ^{11}B states enter the NRF analysis during the photon-flux calibration resulting in larger uncertainties of the NRF result compared to the above discussed results of the RSA measurement. With the assumption $\Gamma_0 = \Gamma$, also the level width and ground-state transition width account to $\Gamma = \Gamma_0 = 6.38(19)\text{ eV}$. This result is substantially smaller as the literature value Γ_{lit} . The deviation can be ascribed to the self-absorption effect which also occurs in the scattering target and which has to be accounted for. Due to resonant absorption, the photon-flux intensity at the resonance energy of the investigated level decreases in the scattering target with increasing penetration depth. However, during the NRF analysis, the photon flux has been assumed to stay constant. The resonance-absorption density $\alpha(E, z)$ [Eq. 5.7], which has been discussed in detail in Sec. 5.4.2, can be exploited to determine the correct photon-flux intensity. It describes the probability for the resonant absorption of a photon with energy E at a particular penetration depth z into the target. Consequently,

$$P_{\text{res}} = \int_{E_i-3\Delta}^{E_i+3\Delta} \int_0^{d_s} \alpha(E, z) dE dz. \quad (8.12)$$

describes the total probability for resonant absorption of photons in the scattering target with thickness d_s in an energy interval between $E_i - 3\Delta$ and $E_i + 3\Delta$, *i.e.*, in the vicinity of the resonance energy E_i . It is compared to the assumption used during the NRF analysis that the photon-flux intensity does not change with the penetration depth into the target, *i.e.*, the photon flux at each point of the scattering target equals the initial one, via

$$r_{\text{flux}} = \frac{\int_{E_i-3\Delta}^{E_i+3\Delta} \int_0^{d_s} \alpha(E, z) dE dz}{\int_{E_i-3\Delta}^{E_i+3\Delta} \int_0^{d_s} \alpha(E, 0) dE dz}. \quad (8.13)$$

In the denominator, the photon-flux intensity is kept constant at the value corresponding to a penetration depth $z = 0$ into the target. The ratio r_{flux} can be used to correct the photon-flux intensity. Alternatively, it can be applied directly to Γ_0^2/Γ since this quantity is proportional to the photon flux.

In practice, firstly the NRF analysis has been performed without applying any correction. This result, assuming again $\Gamma_0 = \Gamma$, is required to deduce $\alpha(E, z)$ and, thus, has been exploited to determine r_{flux} . Afterwards, r_{flux} has been used in turn to correct Γ_0^2/Γ . The corrected result has been used to determine r_{flux} again which has been applied to correct Γ_0^2/Γ anew. This procedure has iteratively been repeated until Γ_0^2/Γ reached a saturation value. The results for Γ obtained in this way are shown in Fig. 8.6, as well. They exhibit a weaker dependence on the Debye temperature as the results of the RSA approach and slightly decrease with increasing Debye temperature. Both approaches result in the same value of the level width at a Debye temperature of $T_D = 835$ K, suggesting that this is the Debye temperature of ${}^6\text{Li}$ in the Li_2CO_3 compound. However, this value contradicts the expectation of a much smaller Debye temperature. The RSA approach yields $\Gamma = 8.053_{-91}^{+92}$ eV at this temperature. The NRF approach gives $\Gamma = 8.05(25)$ eV. The uncertainty of the result obtained with the NRF approach is larger than the one from the RSA approach. It suffers from a lower limit for its uncertainty due to the uncertainties of the transition strengths of the ${}^{11}\text{B}$ calibration standard which is exploited to calibrate the photon flux in the NRF approach. In contrast, the RSA approach does not depend on these transition strengths. The results obtained at $T_D = 835$ K agree within the uncertainties with the current literature value of $\Gamma_{\text{lit}} = 8.19(17)$ eV [Til02] supporting the fact that the Debye temperature may indeed be unexpectedly high.

All previously measured values as well as the results of the present work are summarised in Fig. 8.7.

8.4 Conclusions

A high-precision self-absorption experiment has been performed on ${}^6\text{Li}$ to study the level width of its 0_1^+ state at an excitation energy of $E_i = 3563$ keV. The self absorption $R_{\text{exp}} = 0.5193(15)$ of this state has been successfully measured to a relative uncertainty of only 0.3 %. On this level of accuracy, even small effects on the sub-% level such as scattering reactions in the collimator have to be accounted for. For the subsequent determination of the level width, two

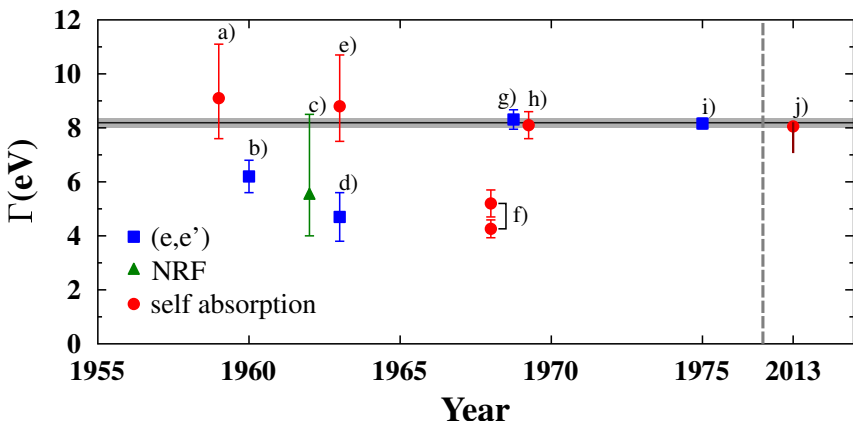


Figure 8.7.: Overview of the results for the level width of the 0_1^+ level of ${}^6\text{Li}$. The literature values are taken from a) Ref. [Coh59], b) Ref. [Bar60], c) Ref. [Boo62], d) Ref. [Bar63], e) Ref. [Sko63], f) Ref. [Cre68], g) Ref. [Eig69], h) Ref. [Ras69], and i) Ref. [Ber75]. In Ref. [Cre68] (f) two self-absorption measurements with different targets are reported. Therefore, two results are shown. The grey bar represents the current literature value [Til02], the average of the three most recent measurements which are g, h, and i. Eventually, the results of j) the present work are shown. The red point corresponds to the result obtained with a Debye temperature of $T_D = 835\text{ K}$. The red line illustrates the range of Γ which is covered with Debye temperatures ranging from 300 K to 900 K.

approaches have been chosen which based on the NRF and the RSA measurement, respectively, since the Debye temperature of Li in the chemical compound of Li_2CO_3 is not known. It is difficult to obtain for rather complex compounds and only rough estimates for the actual value of the Debye temperature can be made. From an empirical point of view, it is supposed to be smaller than $\sim 400\text{ K}$ for the present case. However, the results of the present analysis agree with each other at a Debye temperature of $T_D = 835\text{ K}$. They account to $\Gamma = 8.053^{+(92)}_{-(91)}\text{ eV}$ (RSA approach) and to $\Gamma = 8.05(25)\text{ eV}$ (NRF approach) which is in good agreement with the current literature value $\Gamma_{\text{lit}} = 8.19(17)\text{ eV}$

[Til02]. In contrast, a substantially smaller Debye temperature $T_D = 300\text{ K}$ would yield a considerably smaller level width $\Gamma = 7.065^{+(80)}_{-(81)}\text{ eV}$ (RSA approach) which clearly deviates from Γ_{lit} . Furthermore, this result is inconsistent with $\Gamma = 8.24(25)\text{ eV}$ obtained with the NRF approach. Besides these issues, the level widths obtained with the RSA approach exhibit relative uncertainties of $\sim 1.1\%$. This demonstrates the feasibility of high-precision measurements not only of the self absorption but also of the corresponding level width. Therefore, a follow-up measurement should be performed to clarify the unsolved problem with the unknown Debye temperature. For such a measurement, it is recommended to choose metal lithium as target material. Metal lithium is highly hygroscopic and, thus, difficult to handle. However, its Debye temperature $T_D = 344\text{ K}$ [Mar65], which has been shown to be a crucial ingredient of the analysis of self-absorption measurements, is well known. Furthermore, the absorption target should be positioned behind the collimator system to avoid influences from scattering reactions at small scattering angles. In turn, it must be carefully shielded against the detectors such that photons scattered in the absorber are not detected either. It has been shown with the present work that, with these necessary precautions, a high-precision measurement of the level width of the 0_1^+ level of ${}^6\text{Li}$ is feasible.



9 Aspects of Relative Self-Absorption Measurements - A Conclusion

In the framework of this thesis, the technique of self absorption has been exploited to study aspects of nuclear structure. The method of self-absorption measurements is already known for many years. However, in the recent past, it has seldom been used and almost fell into oblivion. In this work, self absorption has been advanced and an improved, simple normalisation procedure has been established requiring measurements relative to a monitoring target. This approach of relative self absorption has been used to investigate low-lying dipole strength. In particular, the decay pattern of dipole excited states that are attributed to the pygmy dipole resonance has been addressed for the first time with a RSA experiment on the nucleus ^{140}Ce . Furthermore, the $M1$ transition width of the strongly excited $J^\pi = 0_1^+$ level of ^6Li with $T = 1$ at an excitation energy of $E_i = 3563\text{ keV}$ has been investigated via a high-precision measurement of its self absorption. The corresponding results have been discussed in extenso in the Chapters 7 and 8. In this concluding chapter of the present work, the focus will be placed on the relative self-absorption technique itself, discussing the crucial key aspects of RSA experiments.

The first important step of a relative self-absorption measurement and of experiments in general, is the planning and preparation of the experiment. Here, the absorption target is of particular importance. The choice of the target material, especially, with respect to its Debye temperature is a crucial preparatory aspect as has been demonstrated by the measurement on ^6Li . The Debye temperature describes the threshold where all possible phonon states of the investigated material are occupied. During the analysis of RSA measurements, it is required to deduce the Doppler broadening of the width of excited states. It enters the analytical calculation of the self absorption as a function of Γ_0 and Γ and is required to eventually extract these quantities from the measurement. However, the Debye temperature is difficult to obtain. In

particular, this is the case for rather complex chemical compounds where the various vibrational states have to be assigned to specific parts of the compound molecules. It is therefore appropriate to exploit targets consisting out of elemental material and to keep the Debye temperature in mind during the search for appropriate target material.

The mass of the absorption target or rather the areal particle density of the target nuclei affect the sensitivity of the RSA measurement. In general, it is difficult to investigate rather weakly and rather strongly excited states with the same absorption target. Strongly excited states exhibit clear self-absorption effects in thin absorption targets, whereas weakly excited states require more massive absorbers to measure their self absorption. In turn, the self absorption of strongly excited states in a thick absorber may become such strong that the photon flux is reduced to zero and, thus, no signal would be measured in the RSA experiment. Therefore, the absorber has to be chosen with regard to the aim of the planned measurement.

For the actual measurement, it is of importance to care for a homogenous distribution of the target material within the target since not the target mass but the areal particle density enters the analysis of RSA measurements. Furthermore, it has to be ensured that all photons that reach the scattering target passed through the absorption target before. If also a part of the original γ -ray beam reaches the scatterer, the self-absorption effect will be distorted. In general, the position of the absorption target is a fundamental aspect of self-absorption experiments. In the present work, two absorber positions have been tested at the DHIPS facility. For the measurement on ^{140}Ce , it has been placed inside the end of the collimator system. At this position, it has been shielded by the copper collimator and additional lead bricks. Nevertheless, a small part of the photons scattered in the absorber still passed through the shielding and reached the detectors. The actual RSA measurement can be corrected for those events. However, this requires a third measurement to determine the contribution of photons scattered from the absorber into the detectors. When the absorption target has been placed in front of the collimator as during the measurement on ^6Li , the detectors were completely shielded against radiation scattered in the absorber. However, in this case another issue occurred. The photons passing the collimator are partly scattered at small scattering angles. Thereby, they are slightly shifted in energy which affects the self absorption. As has been discussed in the case of ^6Li , this effect is very small. Nevertheless, particularly for high-precision measurements of the self absorption, it can be in the order of the desired uncertainty of the measurement. It can be corrected

for exploiting simulations with **GEANT4**. Nevertheless, in the case of highly precise measurements, the absorber should be placed behind the collimator if an appropriate shielding is feasible.

With these preparations, the actual self-absorption experiment can be performed. Usually, self-absorption experiments consist out of two individual measurements, the actual self-absorption measurement and a second one which is needed as a standard. It is exploited to correct for atomic attenuation effects that occur in the absorption target and works as a reference to determine the decrease of NRF reactions in the scatterer target due to resonant absorption in the absorber. In earlier measurements, the normalisation of these measurements often turned out to be laborious and imprecise. For instance, the total photon flux of both measurements has been determined by measuring the current of electrons which generated the bremsstrahlung beam used for the experiments. In this work, a new, improved normalisation approach has been chosen. The measurements have been conducted relative to a monitoring target which allows for an comparatively easy and precise determination of the normalisation factor as a function of the energy. The new approach requires only to compare measured intensities which correspond to transitions in the monitoring target. For this purpose, it is not necessary to know the corresponding transition widths since only ratios of intensities are investigated. The change of these intensities between both measurements accounts for atomic-attenuation effects as well as for different photon-flux intensities or measuring times and any other global normalisation factor. Therefore, systematic uncertainties are reduced to a minimum, as well. This approach works very well as has been demonstrated with the measurements of the present work. It is even sensitive to small changes of the endpoint energy of the used bremsstrahlung as has been shown with the measurement on ^{140}Ce . In contrast, energy depending effects like this are not taken into account when only integrated quantities such as the electron current are investigated.

Eventually, as the final aspect of self-absorption measurements, their analysis shall be discussed. Two issues occurred during the analysis of the present experiments. On the one hand, without knowledge of the level width Γ , the ground-state transition width Γ_0 can only be extracted from the RSA measurement in the limiting case of the level width being significantly smaller than the Doppler width of an excited state ($\Gamma \ll \Delta$). In general, a relation between the ground-state transition width Γ_0 and the level width Γ is required

to extract these quantities from self-absorption measurements. Such a relation can be provided by Γ_0^2/Γ from the NRF measurement, which is always part of RSA experiments. However, the self-absorption curve determined with Γ_0^2/Γ fixed by the NRF result exhibits a maximum. As a consequence, the experimentally deduced self absorption R_{exp} either corresponds to two solutions for the ground-state transition width or it is not related to any solution at all. Although, the second of the two solutions is often related to non-physically large level widths, it cannot completely be neglected. In particular, for cases where R_{exp} is close to the maximum of this curve, it may become difficult to rule out one of the solutions.

On the other hand, asymmetric uncertainties occur for the ground-state transition width. Those cannot be treated with classical Gaussian error propagation making it difficult to determine further, related quantities. Therefore, in this work, an analysis approach based on the Bayesian concept of probability has been chosen which is well established for the analysis of radiation measurements. For this purpose, probability density functions of the relevant quantities have been regarded instead of discrete values. This approach allowed for a proper treatment of asymmetric uncertainties. For a visualisation of the obtained results, characteristic properties of the distributions have to be extracted. In this work, the most probable value as well as the 68.3 % confidence interval surrounding the most probable value has been chosen. This approach allows also for the application of the principle of maximal information entropy. It suggests to exclude physically forbidden parts of the probability density functions. As a consequence, it is possible to determine the ground-state transition width and further quantities even if the experimentally deduced self absorption yielded a non-physical value. However, the results obtained with this approach have to be assessed with care. A detailed investigation of the results revealed that especially the uncertainties of the branching ratio to the ground state do not reflect the original ones of the self absorption. Furthermore, artificial deviations from the true value can be induced by this analysis procedure if the primary data are not accurate enough. Nevertheless, when applied with care and responsibly assessed, the approach is powerful in handling asymmetric uncertainties and also in taking additional information into account that go beyond the actual measurement and therefore improve the results.

In conclusion, with this work, it has been demonstrated that the technique of relative self absorption is a powerful method to address different topics such as the decay pattern of individual states or high-precision measurements if

some tripping hazards are taken into account. It can provide valuable insight to nuclear structure effects that are difficult to achieve with other approaches. Therefore, further measurements exploiting the RSA technique are highly recommended.



A Spectra

The spectra recorded during the ABS, NRF and RSA measurements on ^{140}Ce have been summed over the three detectors used for the measurements. The resulting spectra are shown in Figs. A.1 to A.6. Peaks emphasised with arrows have been assigned to transitions of ^{140}Ce if not marked differently. Peaks marked as “SE” correspond to pure single escape peaks of transitions in ^{140}Ce . Furthermore, peaks stemming from transitions in the monitoring target ^{11}B and corresponding single escape peaks have been marked as such. Eventually, also peaks stemming from natural background as well as from neutron capture reactions in material surrounding the detectors at DHIPS are pointed out and assigned to the corresponding source.

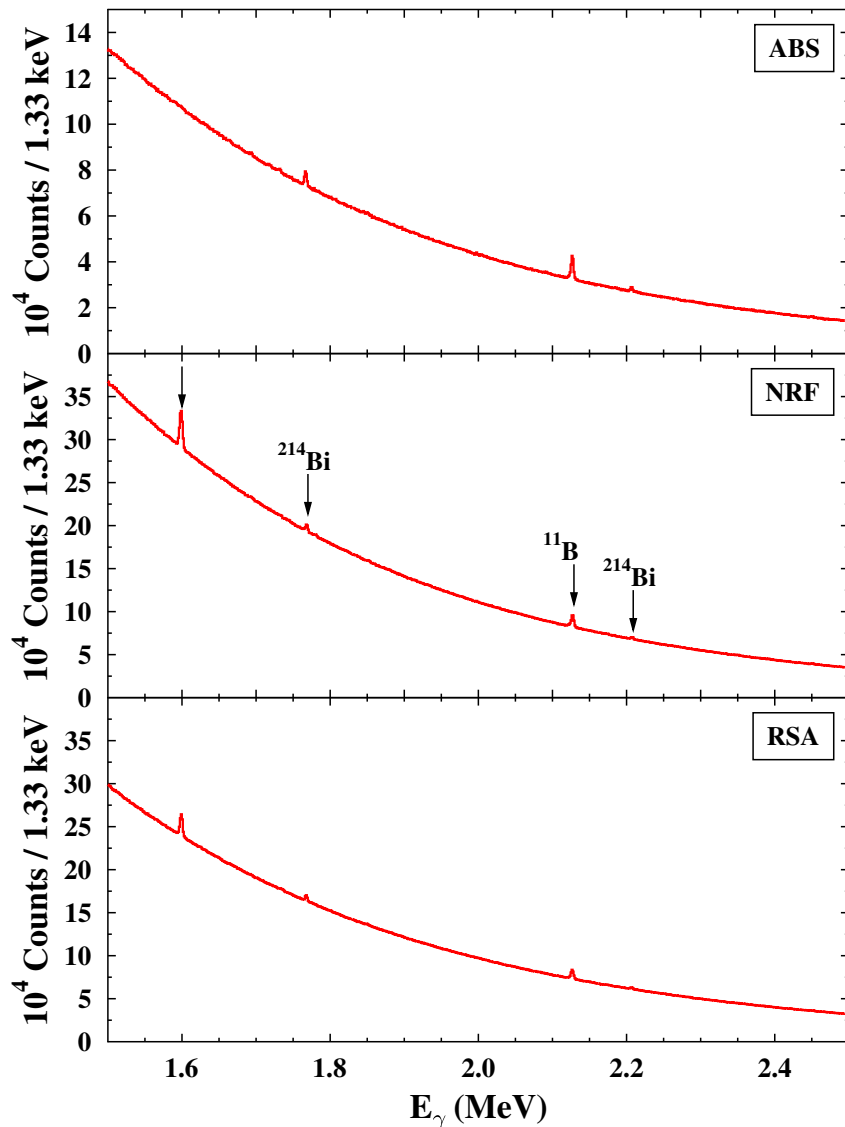


Figure A.1.: Summed spectra of all three detectors recorded during the ABS, NRF, and RSA measurements on the nucleus ^{140}Ce . The energy range between 1.5 MeV and 2.5 MeV is shown. See text for details.

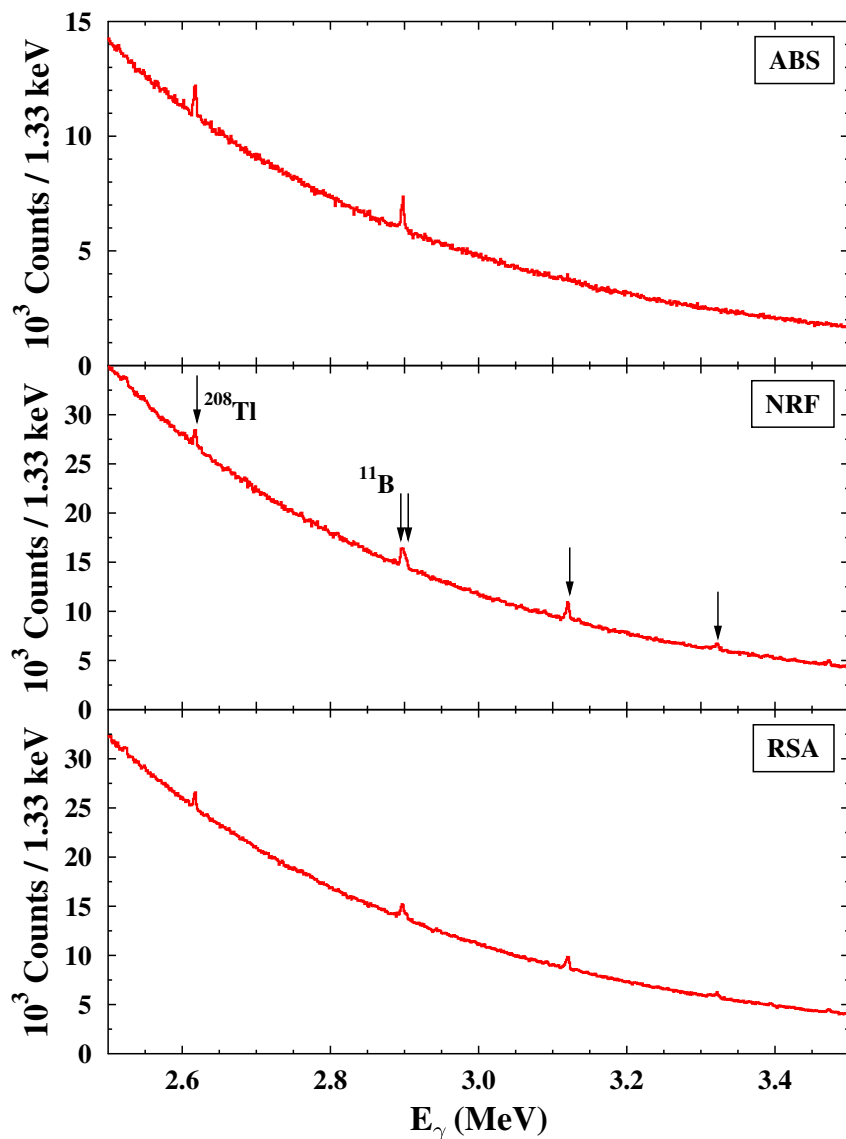


Figure A.2.: Summed spectra of all three detectors recorded during the ABS, NRF, and RSA measurements on the nucleus ^{140}Ce . The energy range between 2.5 MeV and 3.5 MeV is shown. See text for details.

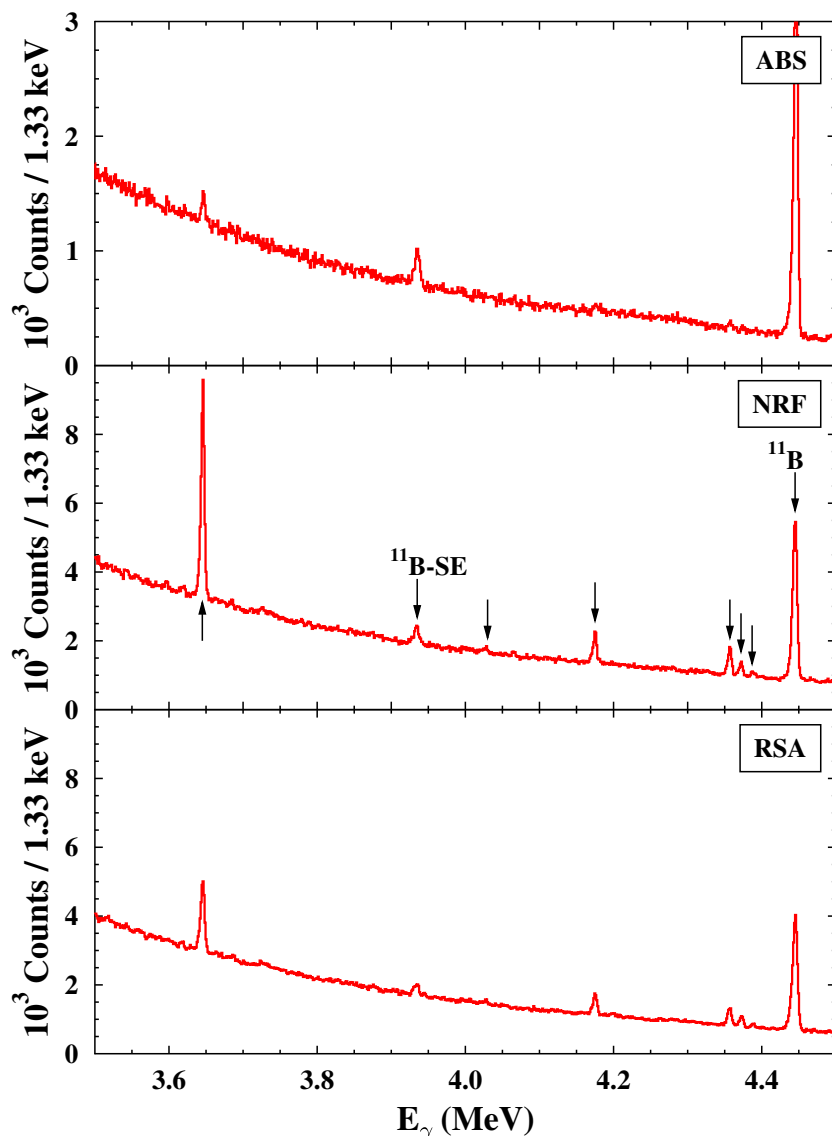


Figure A.3.: Summed spectra of all three detectors recorded during the ABS, NRF, and RSA measurements on the nucleus ^{140}Ce . The energy range between 3.5 MeV and 4.5 MeV is shown. See text for details.

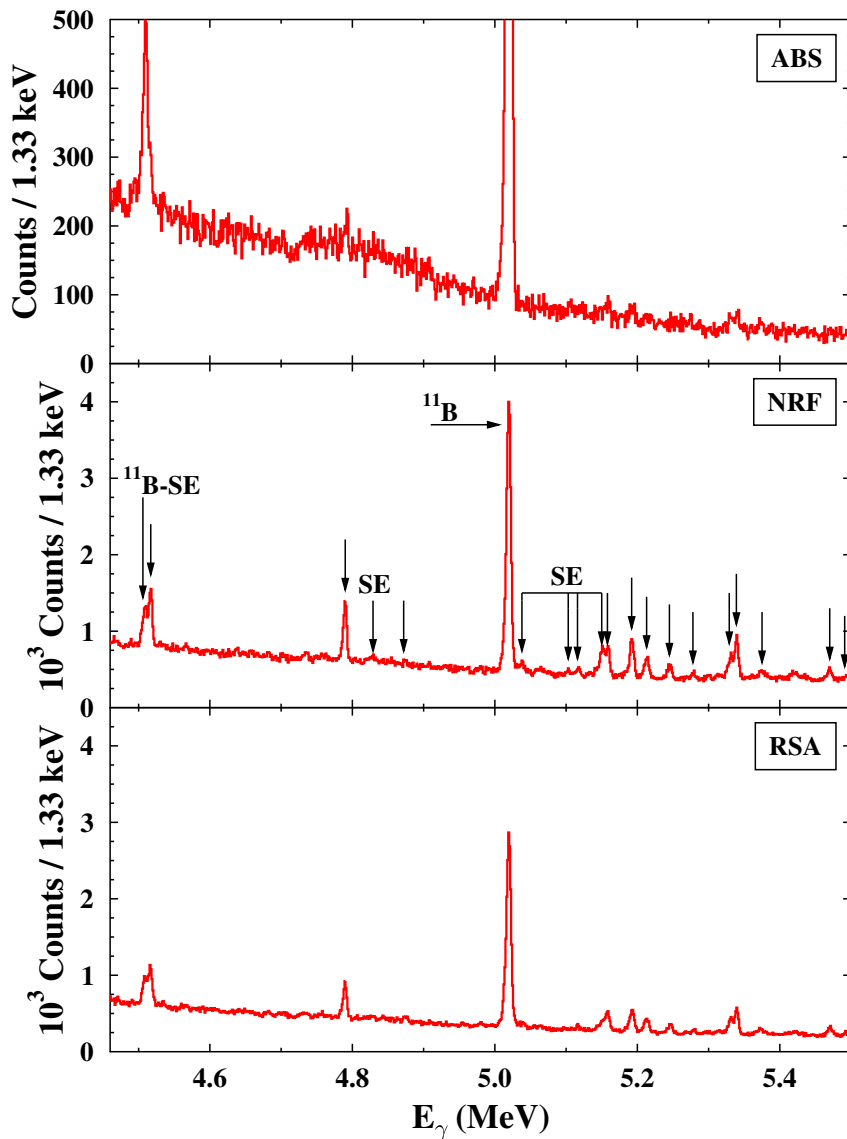


Figure A.4.: Summed spectra of all three detectors recorded during the ABS, NRF, and RSA measurements on the nucleus ^{140}Ce . The energy range between 4.5 MeV and 5.5 MeV is shown. See text for details.

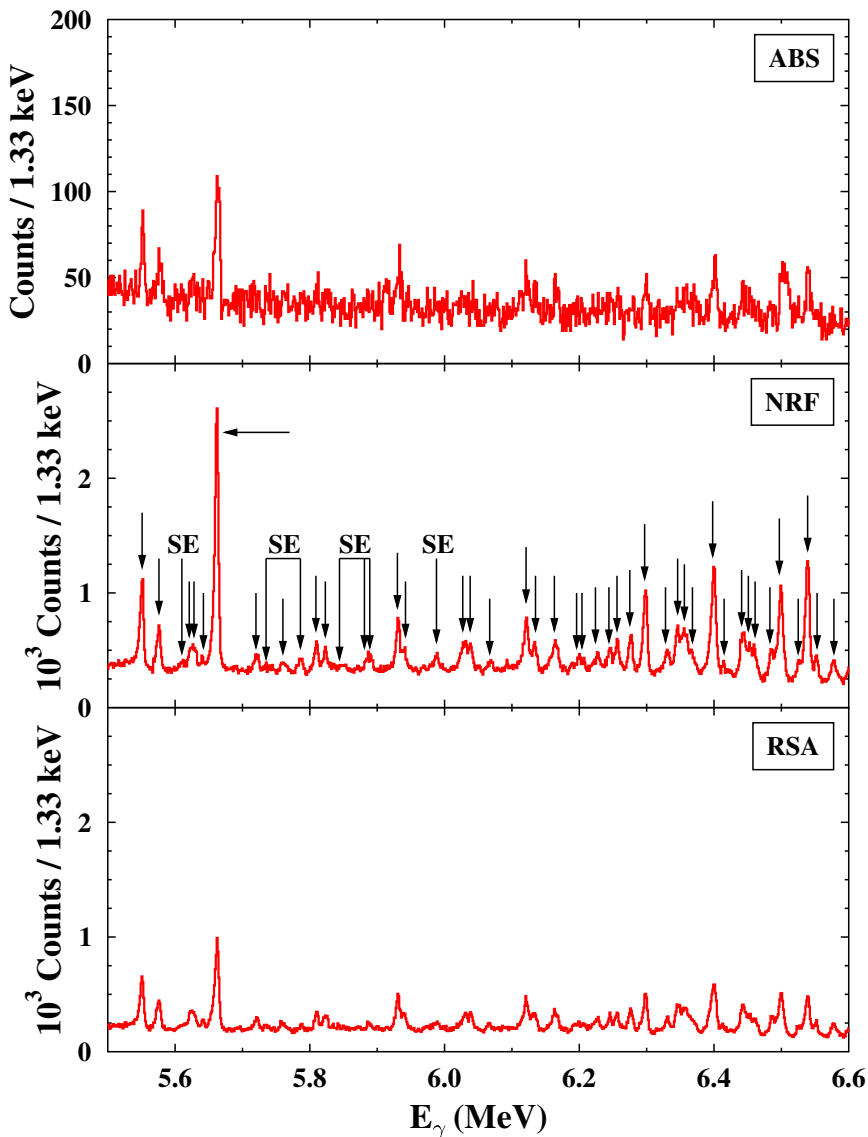


Figure A.5.: Summed spectra of all three detectors recorded during the ABS, NRF, and RSA measurements on the nucleus ^{140}Ce . The energy range between 5.5 MeV and 6.6 MeV is shown. See text for details.

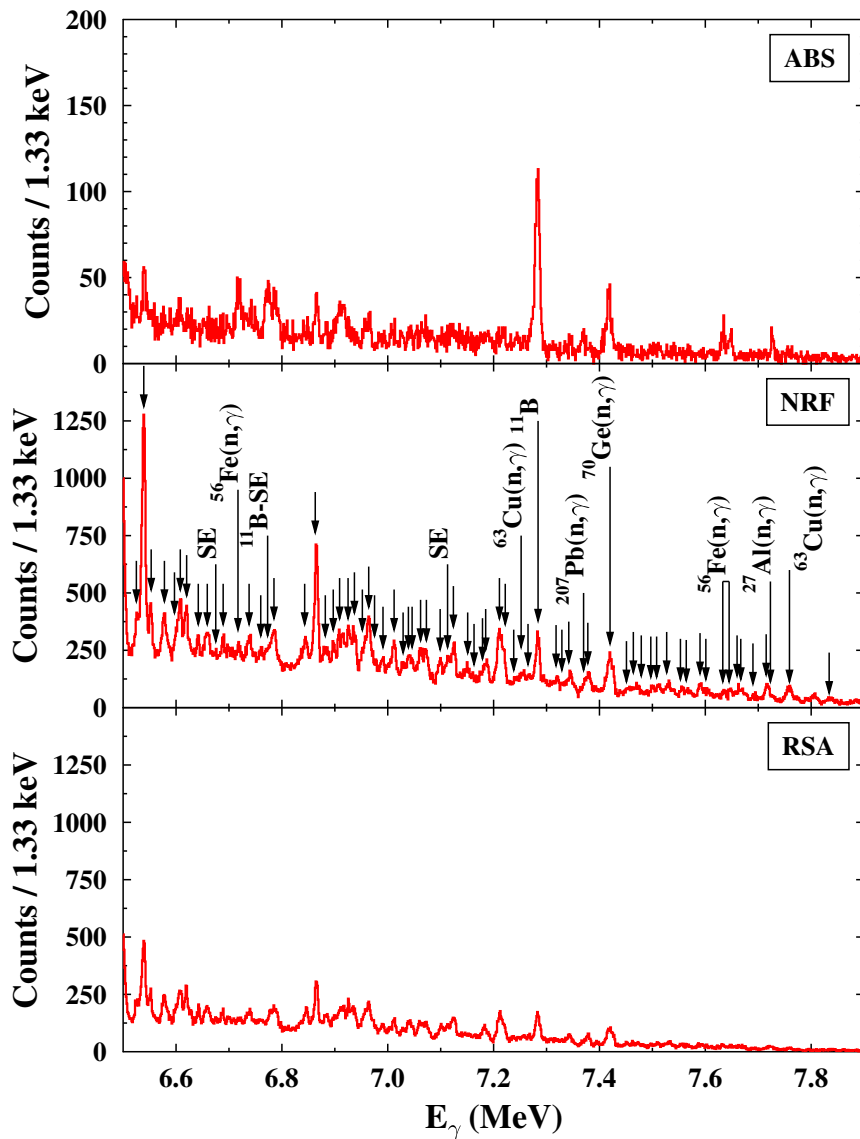


Figure A.6.: Summed spectra of all three detectors recorded during the ABS, NRF, and RSA measurements on the nucleus ^{140}Ce . The energy range between 6.5 MeV and 7.9 MeV is shown. See text for details.



B Results of the NRF Measurement on ^{140}Ce

NRF Intensities and Spin Quantum Numbers

The following tables list the intensities that have been collected during the NRF measurement. The given numbers are corrected for possible contributions of single-escape events and for inelastic decays, *i.e.*, feeding from higher-lying levels. Furthermore, the intensity ratio w is given. It is the averaged result of the detector combinations DET3 with DET1 and DET3 with DET2, respectively, where both values are available. The last two columns give the corresponding spin assignment from the present work and literature values for comparison. The first table treats the four lowest-lying levels observed in this work which are known as 2^+ levels in the literature (Table B.1). The second one (Table B.2) summarises the results for 113 remaining states.

Table B.1.: NRF intensities and the corresponding intensity ratio w for the lowest-lying states that have been observed in this work. They are already known as $J^\pi = 2^+$ levels. The literature values for the spin quantum numbers are taken from Ref. [Nic07].

E_i (keV)	$A(\text{DET1})$	$A(\text{DET2})$	$A(\text{DET3})$	w	J	$J^\pi_{\text{lit.}}$
1596.5(4)	40612(1203)	60996(692)	58651(809)	1.08(06)	(1,2)	2^+
2899.2(3)	941(237)	1271(152)	2723(354)	2.47(40)	2	2^+
3117.9(1)	1772(196)	2506(146)	3204(214)	1.49(14)	(1,2)	2^+
3319.0(2)	234(104)	1207(118)	1015(166)	1.05(30)	(1,2)	2^+

Table B.2.: NRF intensities and the corresponding intensity ratio w for excited states that have been identified as $J = 1$ levels or where no spin assignment was possible. The literature values for the spin and parity quantum numbers are taken from Ref. [Löh14] if not marked differently.

E_i (keV)	$A(\text{DET1})$	$A(\text{DET2})$	$A(\text{DET3})$	w	J	$J^\pi_{\text{lit.}}$
3642.9(1)	8175 (163)	12878 (144)	7724 (159)	0.74 (4)	1	1^{-a}
4025.2(4)	216 (74)	294 (52)	263 (76)	1.04 (29)	(1,2)	1^c
4172.7(2)	1153 (90)	2004 (76)	1242 (89)	0.79 (7)	1	1^b
4354.3(2)	1153 (82)	1852 (63)	1105 (72)	0.74 (6)	1	1^b
4369.8(2)	538 (88)	892 (53)	506 (65)	0.71 (9)	1	1^b
4385.6(5)	251 (60)	337 (46)	163 (61)	0.55 (17)	1	1^b
4514.1(2)	1193 (176)	1702 (61)	1182 (73)	0.83 (8)	1	1^b
4787.0(2)	1233 (71)	1905 (59)	1132 (69)	0.73 (6)	1	1^b
4872.0(4)	0 (0)	211 (36)	157 (50)	0.91 (34)	1	1^b
5156.2(2)	590 (54)	992 (49)	588 (50)	0.75 (7)	1	1^-
5190.0(1)	772 (48)	1313 (50)	855 (47)	0.83 (6)	1	1^-
5210.8(3)	424 (43)	754 (43)	480 (42)	0.82 (8)	1	1^-
5243.5(3)	294 (40)	440 (38)	380 (40)	1.04 (12)	1	1
5276.8(4)	116 (41)	217 (37)	174 (40)	1.03 (25)	1	1
5327.9(3)	392 (54)	689 (49)	410 (54)	0.76 (10)	1	1^-

continued on next page

continued from previous page

E_i (keV)	$A(\text{DET1})$	$A(\text{DET2})$	$A(\text{DET3})$	w	J	$J_{\text{lit.}}^\pi$
5337.1(2)	982 (63)	1475 (59)	972 (63)	0.80 (6)	1	1 ⁻
5370.9(10)	225 (43)	313 (44)	196 (45)	0.73 (15)	1	1 ⁻
5468.0(3)	295 (42)	471 (41)	324 (41)	0.85 (11)	1	1
5491.3(6)	205 (40)	225 (37)	131 (37)	0.58 (14)	1	1 ⁻
5548.3(1)	1402 (60)	2265 (64)	1258 (59)	0.70 (5)	1	1 ⁻
5573.5(2)	680 (48)	1039 (50)	491 (44)	0.58 (5)	1	1 ⁻
5620.4(4)	150 (84)	359 (74)	167 (78)	0.62 (27)	1	1
5626.5(3)	325 (84)	510 (73)	366 (78)	0.89 (19)	1	1
5638.5(4)	204 (57)	258 (51)	143 (51)	0.61 (19)	1	1
5659.6(1)	4076 (114)	6195 (127)	3816 (109)	0.75 (4)	1	1 ⁻
5719.1(3)	279 (54)	442 (54)	190 (51)	0.53 (12)	1	1 ⁻
5757.7(5)	143 (51)	242 (49)	118 (49)	0.62 (22)	1	1
5807.7(2)	394 (58)	592 (58)	412 (56)	0.84 (12)	1	1
5821.0(3)	427 (59)	563 (57)	308 (54)	0.62 (10)	1	1
5928.5(2)	618 (77)	1150 (84)	678 (78)	0.77 (9)	1	1
5938.2(3)	258 (67)	349 (69)	337 (72)	1.11 (25)	1	1 ⁻
6026.5(4)	232 (73)	215 (76)	162 (70)	0.65 (26)	1	1 ⁻
6036.2(3)	419 (66)	666 (75)	311 (68)	0.58 (11)	1	1 ⁻
6065.3(6)	166 (54)	168 (56)	0 (0)	0.00 (0)	(1)	1 ⁻
6118.9(1)	821 (68)	1349 (74)	893 (70)	0.83 (8)	1	1 ⁻
6131.0(2)	518 (64)	657 (62)	466 (62)	0.78 (10)	1	1 ⁺
6162.6(4)	352 (77)	720 (75)	563 (68)	1.03 (15)	1	1 ⁻
6196.1(9)	166 (55)	299 (63)	238 (62)	1.03 (28)	1	1 ⁻
6204.9(9)	72 (51)	244 (60)	138 (59)	0.75 (34)	1	1 ⁻
6224.7(3)	233 (56)	387 (57)	256 (56)	0.83 (18)	1	1 ⁻
6242.8(3)	284 (57)	462 (60)	381 (60)	1.03 (17)	1	1 ⁻
6253.8(4)	418 (60)	740 (65)	468 (62)	0.82 (11)	1	1 ⁻
6274.0(2)	422 (59)	838 (67)	526 (63)	0.84 (11)	1	1 ⁻
6295.8(2)	1199 (77)	1970 (85)	1207 (76)	0.77 (6)	1	1
6328.2(4)	294 (60)	585 (64)	338 (59)	0.77 (13)	1	1 ⁻
6344.2(2)	670 (79)	1138 (82)	697 (75)	0.78 (9)	1	1 ⁻
6354.5(2)	658 (79)	1388 (87)	770 (81)	0.75 (11)	1	1
6365.2(3)	404 (64)	693 (70)	393 (74)	0.73 (12)	1	1 ⁻

continued on next page

continued from previous page

E_i (keV)	$A(\text{DET1})$	$A(\text{DET2})$	$A(\text{DET3})$	w	J	$J_{\text{lit.}}^\pi$
6397.3(1)	1720 (90)	3076 (103)	1786 (89)	0.76 (5)	1	1
6411.9(6)	0 (0)	196 (57)	121 (57)	0.76 (42)	1	1 ⁻
6440.4(2)	631 (51)	1098 (59)	690 (62)	0.81 (8)	1	1 ⁻
6449.7(3)	213 (88)	637 (56)	271 (67)	0.56 (14)	1	1 ⁻
6458.3(3)	301 (96)	658 (52)	436 (72)	0.86 (15)	1	1 ⁻
6484.4(3)	466 (39)	738 (42)	467 (41)	0.79 (8)	1	1 ⁻
6497.2(2)	1277 (52)	2447 (63)	1387 (55)	0.76 (8)	1	1 ⁻
6524.5(4)	383 (37)	296 (38)	310 (37)	0.74 (24)	1	1
6536.4(2)	1665 (54)	3045 (68)	1726 (56)	0.75 (6)	1	1 ⁻
6549.4(2)	290 (35)	491 (39)	273 (36)	0.71 (9)	1	1 ⁻
6574.9(3)	292 (39)	483 (46)	303 (34)	0.79 (10)	1	1 ⁻
6581.8(7)	57 (35)	220 (42)	0 (0)	0.00 (0)	(1)	1 ⁻
6597.8(5)	186 (43)	233 (44)	118 (55)	0.55 (20)	1	1
6605.6(2)	366 (44)	700 (49)	429 (56)	0.81 (10)	1	1
6617.4(2)	344 (34)	619 (38)	387 (36)	0.81 (8)	1	1
6639.8(4)	133 (29)	190 (30)	181 (31)	1.13 (21)	1	1
6656.6(3)	212 (30)	376 (33)	258 (33)	0.89 (12)	1	1 ⁻
6736.0(8)	197 (29)	339 (33)	264 (31)	1.00 (13)	1	1
6758.4(6)	106 (26)	203 (29)	122 (29)	0.79 (18)	1	1 ⁻
6779.4(7)	0 (0)	309 (50)	161 (38)	0.64 (19)	1	1 ⁻
6843.0(3)	317 (37)	423 (37)	174 (33)	0.47 (8)	1	1
6863.1(1)	1126 (50)	1616 (49)	944 (45)	0.69 (5)	1	1
6880.9(3)	203 (34)	339 (31)	198 (30)	0.74 (11)	1	1 ⁻
6895.3(4)	224 (38)	282 (33)	186 (33)	0.73 (12)	1	1 ⁻
6906.8(8)	349 (38)	387 (57)	179 (49)	0.46 (10)	1	1 ⁻
6923.8(3)	352 (40)	569 (38)	354 (36)	0.78 (8)	1	1 ⁻
6934.2(3)	417 (41)	655 (39)	306 (35)	0.58 (6)	1	1
6952.4(6)	178 (62)	356 (35)	183 (35)	0.66 (13)	1	1
6962.0(3)	445 (65)	781 (43)	484 (40)	0.79 (8)	1	1 ⁻
6971.5(5)	129 (37)	175 (31)	115 (29)	0.76 (19)	1	1 ⁻
6987.6(4)	107 (31)	166 (28)	64 (28)	0.47 (17)	1	1
7009.4(3)	332 (34)	450 (36)	204 (29)	0.52 (7)	1	1 ⁻
7026.4(6)	57 (68)	183 (28)	95 (26)	0.65 (20)	1	1 ⁻

continued on next page

continued from previous page

E_i (keV)	$A(\text{DET1})$	$A(\text{DET2})$	$A(\text{DET3})$	w	J	$J_{\text{lit.}}^\pi$
7038.2(5)	98 (144)	261 (45)	120 (31)	0.57 (18)	1	1 ⁻
7045.3(8)	145 (186)	194 (44)	100 (31)	0.63 (24)	1	1 ⁻
7059.4(3)	207 (30)	393 (33)	231 (28)	0.77 (10)	1	1
7070.1(3)	209 (30)	421 (33)	210 (27)	0.67 (9)	1	1 ⁻
7097.4(4)	164 (26)	282 (28)	107 (24)	0.49 (9)	1	1 ⁻
7122.5(3)	269 (31)	539 (34)	302 (30)	0.75 (9)	1	- ^c
7146.9(5)	104 (26)	130 (25)	110 (38)	0.92 (27)	1	1 ⁻
7159.5(12)	53 (23)	71 (23)	0 (0)	0.00 (0)	(1)	1 ⁻
7178.4(11)	113 (37)	132 (63)	109 (59)	0.83 (40)	1	1 ⁻
7184.1(7)	175 (38)	280 (65)	198 (61)	0.88 (24)	1	1 ⁻
7208.5(5)	412 (57)	693 (74)	426 (57)	0.78 (11)	1	1 ^b
7216.3(5)	245 (55)	581 (74)	337 (56)	0.79 (15)	1	1 ⁻
7238.0(8)	61 (32)	107 (33)	78 (31)	0.93 (38)	1	1 ⁻
7265.3(7)	107 (34)	162 (36)	95 (37)	0.71 (24)	1	1 ⁻
7317.5(8)	98 (30)	128 (32)	101 (36)	0.88 (29)	1	1 ⁻
7329.3(15)	64 (29)	77 (35)	38 (29)	0.52 (33)	1	1 ⁻
7342.0(9)	91 (30)	292 (42)	181 (34)	0.84 (23)	1	1 ⁻
7376.7(6)	158 (37)	229 (50)	170 (53)	0.88 (24)	1	1 ⁻
7451.6(9)	79 (30)	91 (32)	56 (23)	0.63 (25)	1	1 ⁻
7464.9(11)	92 (31)	133 (42)	53 (27)	0.47 (20)	1	- ^c
7473.5(11)	0 (0)	144 (43)	55 (28)	0.47 (28)	1	- ^c
7497.3(9)	88 (30)	90 (38)	88 (24)	0.88 (30)	1	1 ⁻
7509.9(8)	96 (30)	189 (40)	76 (23)	0.54 (16)	1	1 ⁻
7527.9(11)	123 (29)	278 (35)	88 (23)	0.43 (10)	1	- ^c
7553.2(8)	54 (25)	135 (34)	72 (23)	0.73 (25)	1	1 ⁻
7565.7(10)	42 (25)	138 (34)	57 (22)	0.56 (23)	1	1 ⁻
7589.0(6)	99 (24)	202 (30)	116 (25)	0.77 (16)	1	1 ⁻
7601.2(8)	56 (21)	137 (27)	34 (20)	0.35 (17)	1	1 ⁻
7659.5(9)	90 (26)	129 (26)	0 (0)	0.00 (0)	(1)	- ^c
7667.8(18)	70 (26)	142 (26)	114 (24)	1.05 (26)	1	1 ⁻
7714.7(6)	138 (24)	236 (30)	133 (25)	0.72 (13)	1	1 ⁻
7834.2(9)	47 (16)	60 (17)	32 (15)	0.58 (24)	1	1 ⁻

^a from Ref. [Nic07], ^b from Ref. [Vol06]

^c not observed in Refs. [Her95a, Vol06, Löh14]

Integrated Cross Section and Related Quantities

The integrated cross section, Γ_0^2/Γ and the resulting $B(E1)\uparrow$ and $B(M1)\uparrow$ -transition strengths, respectively, that have been determined from the NRF measurement in this work are shown in Table B.3. For the case that the corresponding values were available, error-weighted averages are given for each quantity. The information on the spin and parity quantum numbers is a combination of the results of the present work and of previous measurements [Vol06, Löh14]. Where no parity quantum number is measured yet, both, the $B(E1)\uparrow$ and $B(M1)\uparrow$ values are given. The transition strengths are determined with the condition $\Gamma_0/\Gamma = 1$.

The subsequent table (Table B.4) provides a comparison to previous measurements of Herzberg and collaborators [Her95a, Her97] and Volz and co-workers [Vol06]. For this comparison, the $B(E1)\uparrow$ -transition strength has been chosen since most of the investigated states are $J^\pi = 1^-$ levels. Excited states for which no parity is known yet are treated as 1^- states, too. The only identified 1^+ level is not listed in Table B.4. The present result for this state accounts to $B(M1)\uparrow = 24(2) \cdot 10^{-2} \mu_N^2$. The transition strengths of Herzberg and Volz are deduced from the $B(E1)\uparrow$ -transition strengths reported in Ref. [Her95a] and Ref. [Vol06] since this state has been assumed to be excited by an electric dipole transition before. The corresponding results yield $B(M1)\uparrow = 28_{-10}^{+6} \cdot 10^{-2} \mu_N^2$ [Her95a] and $B(M1)\uparrow = 34(7) \cdot 10^{-2} \mu_N^2$ [Vol06].

Eventually, Fig. B.1 illustrates the experimental sensitivity limit of the NRF measurement on ^{140}Ce for $E1$ transitions (upper panel) as well as $E2$ transitions (lower panel). Transitions corresponding to transition strengths weaker as the experimental sensitivity can not be resolved from the background.

Table B.3.: This table lists the integrated cross section, Γ_0^2/Γ , and the reduced ground-state transition strengths for the $J = 1$ levels observed in the present work. If the parity quantum number is already known either the $B(E1)\uparrow$ or the $B(M1)\uparrow$ strength is given. For those cases where the parity quantum number is not yet measured both quantities are listed. The transition strengths have been deduced with $\Gamma_0/\Gamma = 1$.

E_i (keV)	J^π	$I_{0 \rightarrow i \rightarrow 0}$ (keV fm 2)	Γ_0^2/Γ (meV)	$B(E1)\uparrow$ (10^{-3} e 2 fm 2)	$B(M1)\uparrow$ $10^{-2} \mu_N^2$
3642.9(1)	1^-	23.0 (7)	265 (9)	15.7 (5)	
4025.2(4) ^a	(1,2)	0.7 (1)	11 (2)	0.5 (1)	4 (1)
4172.7(2)	1	5.0 (3)	76 (4)	3.0 (2)	27 (1)
4354.3(2)	1	5.3 (2)	88 (4)	3.1 (1)	28 (1)
4369.8(2)	1	2.6 (2)	42 (3)	1.5 (1)	13 (1)
4385.6(5)	1	1.0 (1)	17 (2)	0.6 (1)	5 (1)
4514.1(2)	1	5.9 (3)	104 (6)	3.2 (2)	29 (2)
4787.0(2)	1	7.3 (3)	146 (6)	3.8 (2)	34 (1)
4872.0(4)	1	0.9 (1)	19 (3)	0.4 (1)	4 (1)
5156.2(2)	1^-	4.7 (3)	109 (6)	2.3 (1)	
5190.0(1)	1^-	6.5 (4)	152 (10)	3.1 (2)	
5210.8(3)	1^-	3.7 (2)	88 (5)	1.8 (1)	
5243.5(3)	1	2.5 (3)	60 (8)	1.2 (1)	11 (1)
5276.8(4)	1	1.2 (2)	28 (4)	0.5 (1)	5 (1)
5327.9(3)	1^-	3.6 (2)	89 (6)	1.7 (1)	
5337.1(2)	1^-	8.4 (4)	207 (9)	3.9 (2)	
5370.9(10)	1^-	1.8 (2)	45 (5)	0.8 (1)	
5468.0(3)	1	2.9 (2)	75 (6)	1.3 (1)	12 (1)
5491.3(6)	1^-	1.5 (2)	38 (5)	0.6 (1)	
5548.3(1)	1^-	13.6 (5)	365 (14)	6.1 (2)	
5573.5(2)	1^-	6.2 (4)	166 (11)	2.7 (2)	
5620.4(4)	1	2.1 (4)	56 (11)	0.9 (2)	8 (2)
5626.5(3)	1	3.5 (4)	95 (11)	1.5 (2)	14 (2)
5638.5(4)	1	1.8 (3)	49 (7)	0.8 (1)	7 (1)
5659.6(1)	1^-	42.5 (15)	1181 (40)	18.7 (6)	

continued on next page

continued from previous page

E_i (keV)	J^π	$I_{0 \rightarrow i \rightarrow 0}$ (keV fm ²)	Γ_0^2/Γ (meV)	$B(E1)\uparrow$ (10^{-3} e ² fm ²)	$B(M1)\uparrow$ $10^{-2} \mu_N^2$
5719.1(3)	1^-	2.9 (3)	81 (9)	1.2 (1)	
5757.7(5)	1	1.6 (3)	47 (8)	0.7 (1)	6 (1)
5807.7(2)	1	4.6 (4)	134 (11)	2.0 (1)	18 (1)
5821.0(3)	1	4.3 (4)	126 (10)	1.8 (1)	17 (1)
5928.5(2)	1	8.7 (6)	264 (17)	3.6 (2)	33 (2)
5938.2(3)	1^-	3.2 (5)	99 (15)	1.3 (2)	
6026.5(4)	1^-	2.2 (5)	70 (15)	0.9 (2)	
6036.2(3)	1^-	5.4 (5)	169 (16)	2.2 (2)	
6065.3(6)	1^-	1.7 (4)	54 (13)	0.7 (2)	
6118.9(1)	1^-	12.3 (7)	401 (22)	5.0 (3)	
6131.0(2)	1^+	6.6 (5)	214 (16)		24 (2)
6162.6(4)	1^-	6.8 (10)	224 (33)	2.7 (4)	
6196.1(9)	1^-	2.9 (4)	97 (15)	1.2 (2)	
6204.9(9)	1^-	1.9 (4)	63 (14)	0.8 (2)	
6224.7(3)	1^-	3.8 (4)	127 (15)	1.5 (2)	
6242.8(3)	1^-	4.8 (6)	163 (19)	2.0 (3)	
6253.8(4)	1^-	7.2 (5)	243 (18)	2.9 (2)	
6274.0(2)	1^-	7.9 (7)	270 (25)	3.2 (3)	
6295.8(2)	1	19.9 (9)	685 (31)	7.9 (4)	71 (3)
6328.2(4)	1^-	5.7 (5)	198 (18)	2.3 (2)	
6344.2(2)	1^-	11.8 (8)	412 (26)	4.7 (3)	
6354.5(2)	1	13.2 (12)	462 (42)	5.2 (5)	47 (4)
6365.2(3)	1^-	7.1 (6)	250 (21)	2.8 (2)	
6397.3(1)	1	31.9 (15)	1134 (54)	12.5 (6)	112 (5)
6411.9(6)	1^-	2.2 (6)	78 (20)	0.8 (2)	
6440.4(2)	1^-	12.1 (6)	434 (23)	4.6 (3)	
6449.7(3)	1^-	6.2 (9)	225 (33)	2.4 (4)	
6458.3(3)	1^-	7.4 (6)	266 (23)	2.9 (3)	
6484.4(3)	1^-	8.7 (5)	317 (17)	3.3 (2)	
6497.2(2)	1^-	26.3 (18)	963 (64)	10.1 (7)	
6524.5(4)	1^-	4.9 (12)	181 (42)	1.9 (4)	
6536.4(2)	1^-	34.3 (17)	1271 (64)	13.0 (7)	
6549.4(2)	1^-	5.8 (4)	214 (15)	2.2 (1)	

continued on next page

continued from previous page

E_i (keV)	J^π	$I_{0 \rightarrow i \rightarrow 0}$ (keV fm 2)	Γ_0^2/Γ (meV)	$B(E1)\uparrow$ (10^{-3} e 2 fm 2)	$B(M1)\uparrow$ $10^{-2} \mu_N^2$
6574.9(3)	1^-	6.0 (4)	226 (16)	2.3 (2)	
6581.8(7)	1^-	2.1 (8)	78 (29)	0.8 (3)	
6597.8(5)	1	3.1 (4)	116 (17)	1.2 (2)	10 (2)
6605.6(2)	1	8.4 (6)	317 (23)	3.2 (2)	29 (2)
6617.4(2)	1	7.7 (5)	292 (18)	2.9 (2)	26 (2)
6639.8(4)	1	2.8 (4)	108 (16)	1.1 (2)	10 (1)
6656.6(3)	1^-	5.0 (4)	190 (15)	1.8 (2)	
6736.0(8)	1^-	5.0 (6)	195 (22)	1.8 (2)	
6758.4(6)	1^-	2.8 (3)	109 (13)	1.0 (1)	
6779.4(7)	1^-	4.3 (6)	172 (24)	1.6 (2)	
6843.0(3)	1	6.2 (8)	252 (31)	2.2 (3)	20 (3)
6863.1(1)	1	25.9 (10)	1059 (42)	9.4 (4)	85 (3)
6880.9(3)	1^-	5.3 (4)	217 (17)	1.9 (1)	
6895.3(4)	1^-	4.9 (4)	201 (18)	1.7 (2)	
6906.8(8)	1^-	6.9 (11)	287 (45)	2.5 (4)	
6923.8(3)	1^-	9.5 (6)	393 (24)	3.4 (2)	
6934.2(3)	1	10.2 (7)	425 (28)	3.7 (2)	33 (2)
6952.4(6)	1	5.7 (5)	237 (23)	2.0 (2)	18 (2)
6962.0(3)	1^-	13.3 (8)	561 (33)	4.7 (3)	
6971.5(5)	1^-	3.2 (4)	134 (18)	1.1 (2)	
6987.6(4)	1	2.7 (4)	114 (17)	0.9 (1)	9 (1)
7009.4(3)	1^-	7.8 (8)	330 (33)	2.7 (3)	
7026.4(6)	1^-	3.1 (4)	134 (19)	1.1 (2)	
7038.2(5)	1^-	4.3 (6)	185 (28)	1.5 (2)	
7045.3(8)	1^-	3.4 (6)	147 (27)	1.2 (2)	
7059.4(3)	1	7.0 (5)	302 (22)	2.4 (2)	22 (2)
7070.1(3)	1^-	7.1 (5)	308 (22)	2.5 (2)	
7097.4(4)	1^-	4.8 (5)	211 (24)	1.7 (2)	
7122.5(3)	1	9.9 (7)	436 (31)	3.5 (2)	31 (2)
7146.9(5)	1^-	2.9 (4)	131 (19)	1.0 (2)	
7159.5(12)	1^-	1.5 (4)	68 (18)	0.5 (2)	
7178.4(11)	1^-	3.4 (8)	152 (38)	1.2 (3)	
7184.1(7)	1^-	6.1 (9)	273 (40)	2.1 (3)	

continued on next page

continued from previous page

E_i (keV)	J^π	$I_{0 \rightarrow i \rightarrow 0}$ (keV fm 2)	Γ_0^2/Γ (meV)	$B(E1)\uparrow$ (10 $^{-3}$ e 2 fm 2)	$B(M1)\uparrow$ 10 $^{-2}$ μ_N^2
7208.5(5)	1	15.1 (12)	680 (54)	5.2 (4)	47 (4)
7216.3(5)	1 $^-$	11.4 (14)	513 (65)	3.9 (5)	
7238.0(8)	1 $^-$	2.5 (6)	113 (25)	0.9 (2)	
7265.3(7)	1 $^-$	3.8 (6)	175 (30)	1.3 (2)	
7317.5(8)	1 $^-$	3.5 (6)	165 (29)	1.2 (2)	
7329.3(15)	1 $^-$	2.1 (6)	95 (29)	0.7 (2)	
7342.0(9)	1 $^-$	6.2 (14)	292 (64)	2.1 (5)	
7376.7(6)	1 $^-$	6.6 (10)	314 (46)	2.3 (3)	
7451.6(9)	1 $^-$	3.0 (7)	146 (33)	1.0 (2)	
7464.9(11)	1	3.8 (8)	185 (40)	1.3 (3)	11 (2)
7473.5(11)	1	3.8 (10)	186 (49)	1.2 (4)	12 (3)
7497.3(9)	1 $^-$	4.0 (8)	197 (39)	1.3 (3)	
7509.9(8)	1 $^-$	5.3 (8)	257 (41)	1.7 (3)	
7527.9(11)	1	7.3 (13)	360 (65)	2.5 (5)	22 (4)
7553.2(8)	1 $^-$	4.2 (8)	209 (40)	1.4 (3)	
7565.7(10)	1 $^-$	3.9 (8)	193 (40)	1.3 (3)	
7589.0(6)	1 $^-$	7.3 (8)	366 (42)	2.4 (3)	
7601.2(8)	1 $^-$	4.1 (9)	202 (46)	1.3 (3)	
7659.5(9)	(1)	6.1 (11)	313 (54)	2.0 (3)	18 (3)
7667.8(18)	1 $^-$	7.0 (10)	355 (52)	2.2 (3)	
7714.7(6)	1 $^-$	12.5 (12)	645 (62)	4.0 (4)	
7834.2(9)	1 $^-$	5.8 (12)	308 (62)	1.8 (4)	

^a $B(E2)\uparrow = 35(5)$ e 2 fm 4

Table B.4.: Comparison of the $B(E1)\uparrow$ -transition strengths determined in the framework of this thesis with results of Volz [Vol06] and Herzberg [Her95a, Her97]. In this table, electric dipole character is also assumed for states where no parity assignment has been done so far.

E_i (keV)	$B(E1)\uparrow$ ($10^{-3} e^2 fm^2$)	Volz <i>et al.</i> $B(E1)\uparrow$ ($10^{-3} e^2 fm^2$)	Herzberg <i>et al.</i> $B(E1)\uparrow$ ($10^{-3} e^2 fm^2$)
3642.9(1)	15.7 (5)	21.7 (33)	18.2 (23)
4025.2(4)	0.5 (1)		
4172.7(2)	3.0 (2)	5.1 (10)	3.2 (4)
4354.3(2)	3.1 (1)	4.3 (9)	3.8 (5)
4369.8(2)	1.5 (1)		1.9 (3)
4385.6(5)	0.6 (1)		0.6 (1)
4514.1(2)	3.2 (2)	5.3 (10)	3.7 (5)
4787.0(2)	3.8 (2)	5.2 (10)	4.3 (6)
4872.0(4)	0.4 (1)		0.5 (1)
5156.2(2)	2.3 (1)	3.7 (7)	3.5 (6)
5190.0(1)	3.1 (2)	4.6 (9)	4.6 (7)
5210.8(3)	1.8 (1)	2.7 (7)	3.7 (6)
5243.5(3)	1.2 (2)		1.9 (3)
5276.8(4)	0.5 (1)		
5327.9(3)	1.7 (1)		2.5 (4)
5337.1(2)	3.9 (2)	4.8 (10)	4.2 (7)
5370.9(10)	0.8 (1)		
5468.0(3)	1.3 (1)		1.1 (2)
5491.3(6)	0.6 (1)		1.0 (2)
5548.3(1)	6.1 (2)	7.9 (14)	7.5 (14)
5573.5(2)	2.7 (2)	4.5 (10)	3.9 (7)
5620.4(4)	0.9 (2)		
5626.5(3)	1.5 (2)		2.5 (5)
5638.5(4)	0.8 (1)		
5659.6(1)	18.7 (6)	26.0 (40)	23.5 (46)
5719.1(3)	1.2 (1)		1.5 (3)

continued on next page

continued from previous page

E_i (keV)	$B(E1)\uparrow$ ($10^{-3} e^2 fm^2$)	$B(E1)\uparrow$ ($10^{-3} e^2 fm^2$)	$B(E1)\uparrow$ ($10^{-3} e^2 fm^2$)
5757.7(5)	0.7 (1)		1.2 (3)
5807.7(2)	2.0 (1)		2.9 (6)
5821.0(3)	1.8 (1)		2.1 (5)
5928.5(2)	3.6 (2)	5.4 (11)	5.1 (11)
5938.2(3)	1.3 (2)		2.1 (5)
6026.5(4)	0.9 (2)		$2.7^{+0.7}_{-0.8}$
6036.2(3)	2.2 (2)		
6065.3(6)	0.7 (2)		
6118.9(1)	5.0 (3)	8.2 (14)	$6.1^{+1.5}_{-2.0}$
6131.0(2)	2.7 (2)	3.8 (8)	$3.1^{+0.7}_{-1.1}$
6162.6(4)	2.7 (4)	5.2 (12)	$4.3^{+1.1}_{-1.6}$
6196.1(9)	1.2 (2)		
6204.9(9)	0.8 (2)		
6224.7(3)	1.5 (2)		$2.1^{+0.6}_{-0.9}$
6242.8(3)	2.0 (3)		$2.7^{+0.7}_{-0.8}$
6253.8(4)	2.9 (2)		$3.9^{+0.9}_{-1.6}$
6274.0(2)	3.2 (3)	5.0 (9)	$4.4^{+1.2}_{-2.0}$
6295.8(2)	7.9 (4)	11.4 (20)	$10.5^{+2.6}_{-4.9}$
6328.2(4)	2.3 (2)	4.0 (15)	$1.9^{+0.5}_{-1.0}$
6344.2(2)	4.7 (3)	6.6 (13)	$7.3^{+1.9}_{-3.9}$
6354.5(2)	5.2 (5)	7.4 (14)	
6365.2(3)	2.8 (2)		
6397.3(1)	12.5 (6)	17.4 (28)	$19.1^{+4.9}_{-11.2}$
6411.9(6)	0.8 (2)		
6440.4(2)	4.6 (2)	9.1 (16)	$10.4^{+2.8}_{-6.6}$
6449.7(3)	2.4 (4)	5.4 (11)	
6458.3(3)	2.9 (3)	4.8 (10)	
6484.4(3)	3.3 (2)	4.7 (10)	$7.8^{+2.1}_{-5.5}$
6497.2(2)	10.1 (7)	14.3 (24)	$21.9^{+6.1}_{-15.7}$
6524.5(4)	1.9 (4)		
6536.4(2)	13.0 (7)	21.1 (33)	$28.7^{+8.2}_{-22.6}$
6549.4(2)	2.2 (1)	3.7 (8)	$5.9^{+1.7}_{-4.7}$
6574.9(3)	2.3 (2)	4.0 (8)	$6.2^{+1.9}_{-5.2}$

continued on next page

continued from previous page

E_i (keV)	$B(E1)\uparrow$ (10^{-3} e ² fm ²)	Volz <i>et al.</i> $B(E1)\uparrow$ (10^{-3} e ² fm ²)	Herzberg <i>et al.</i> $B(E1)\uparrow$ (10^{-3} e ² fm ²)
6581.8(7)	0.8 (3)		
6597.8(5)	1.2 (2)		
6605.6(2)	3.2 (2)	6.5 (11)	$10.4^{+3.1}_{-9.1}$
6617.4(2)	2.9 (2)	6.0 (11)	
6639.8(4)	1.1 (2)		
6656.6(3)	1.8 (2)		
6736.0(8)	1.8 (2)		
6758.4(6)	1.0 (1)		
6779.4(7)	1.6 (2)	4.9 (11)	
6843.0(3)	2.2 (3)	5.2 (14)	
6863.1(1)	9.4 (4)	16.5 (29)	
6880.9(3)	1.9 (1)		
6895.3(4)	1.7 (2)		
6906.8(8)	2.5 (4)	8.8 (19)	
6923.8(3)	3.4 (2)		
6934.2(3)	3.7 (2)	7.5 (16)	
6952.4(6)	2.0 (2)		
6962.0(3)	4.7 (3)	8.2 (17)	
6971.5(5)	1.1 (2)		
6987.6(4)	0.9 (1)		
7009.4(3)	2.7 (3)		
7026.4(6)	1.1 (2)		
7038.2(5)	1.5 (2)		
7045.3(8)	1.2 (2)		
7059.4(3)	2.4 (2)		
7070.1(3)	2.5 (2)		
7097.4(4)	1.7 (2)		
7122.5(3)	3.5 (2)		
7146.9(5)	1.0 (2)		
7159.5(12)	0.5 (2)		
7178.4(11)	1.2 (3)		
7184.1(7)	2.1 (3)		
7208.5(5)	5.2 (4)	11.0 (19)	

continued on next page

continued from previous page

E_i (keV)	$B(E1)\uparrow$ (10^{-3} e 2 fm 2)	$B(E1)\uparrow$ (10^{-3} e 2 fm 2)	$B(E1)\uparrow$ (10^{-3} e 2 fm 2)
7216.3(5)	3.9 (5)	10.2 (17)	
7238.0(8)	0.9 (2)		
7265.3(7)	1.3 (2)		
7317.5(8)	1.2 (2)		
7329.3(15)	0.7 (2)		
7342.0(9)	2.1 (5)	3.7 (14)	
7376.7(6)	2.3 (3)		
7451.6(9)	1.0 (2)		
7464.9(11)	1.3 (3)		
7473.5(11)	1.2 (4)		
7497.3(9)	1.3 (3)		
7509.9(8)	1.7 (3)		
7527.9(11)	2.5 (5)		
7553.2(8)	1.4 (3)		
7565.7(10)	1.3 (3)		
7589.0(6)	2.4 (3)		
7601.2(8)	1.3 (3)		
7659.5(9)	2.0 (3)		
7667.8(18)	2.2 (3)		
7714.7(6)	4.0 (4)		
7834.2(9)	1.8 (4)		

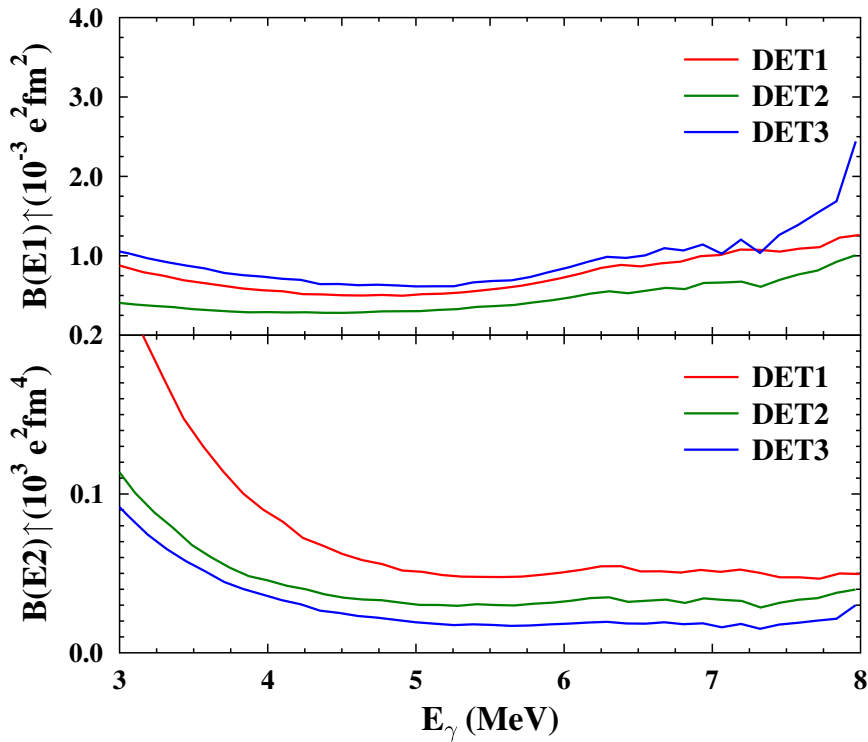


Figure B.1.: Experimental sensitivity limits for $E1$ (upper panel) and $E2$ (lower panel) transitions for each detector. DET3 has been positioned at 90° with respect to the incoming beam. The angular distribution of photons emitted in a $0 \rightarrow 1 \rightarrow 0$ spin sequence has a minimum there, whereas the distribution of photons emitted after a $0 \rightarrow 2 \rightarrow 0$ spin sequence exhibits a maximum at 90° . Therefore, DET3 has a rather low limit to detect $E2$ radiation and a comparatively high sensitivity limit for $E1$ radiation.



C Results of the RSA Measurement on ^{140}Ce

Examples for the Determination of Γ_0

In addition to the example shown in Fig. 7.13 in Sec. 7.4.2, two further examples for the determination of Γ_0 exploiting probability density functions are presented in the following. Figure C.1 demonstrates the case, that the Gaussian distribution, which describes the experimentally deduced value R_{exp} of the self absorption, is not influenced by the a-priori constraints. In this case, the self absorption $R_{\text{exp}} = 0.57(1)$ of the level at 3643 keV has a comparatively small uncertainty. Within this uncertainty R_{exp} is located neither close to $R = 0$ nor to $R_{\text{max}} = 0.696$. In contrast, the second example illustrated via Fig. C.2 shows a case where the distribution of R_{exp} is cut off at $R = 0$. The self absorption $R_{\text{exp}} = 0.8(7)$ is located close to $R = 0$ and has a comparatively large uncertainty. In this case, the upper limit $R_{\text{max}} = 0.3$ must not be taken into account, too, since the probability of the distribution of R_{exp} already reaches zero at this point.

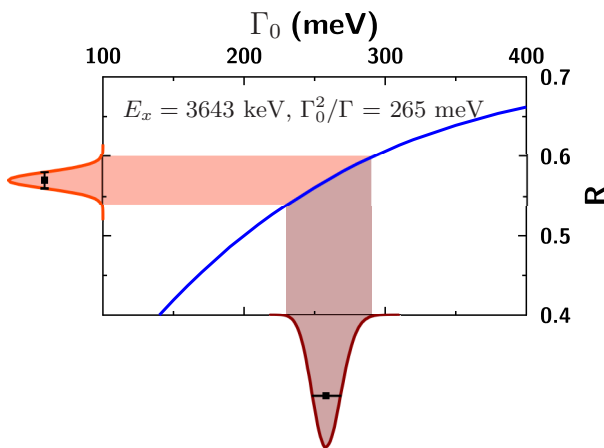


Figure C.1.: Determination of Γ_0 of the two-phonon state at 3643 keV excitation energy exploiting probability density functions. The Gaussian distribution of R_{exp} is not affected by the a-priori constraints given as $R = 0$ and $R_{\text{max}} = 0.696$.

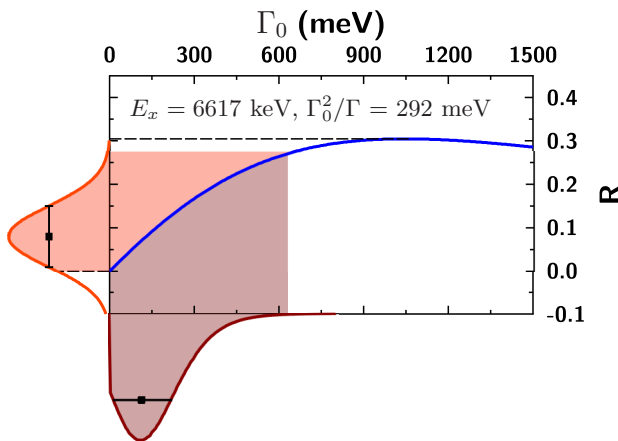


Figure C.2.: Determination of Γ_0 of the $E_i = 6617$ keV level exploiting probability density functions. The Gaussian distribution of R_{exp} is cut off at $R = 0$.

Self Absorption and Related Quantities

Tables C.1 and C.2 summarise the results of the RSA measurement. In Table C.1, an overview of the experimentally deduced self absorption R_{exp} is given. Furthermore, the maximum R_{max} , that the self absorption curve $R_{\Gamma_0, \Gamma}$ exhibits when determined with Γ_0^2/Γ being fixed by the result of the NRF measurement, is given, as well.

Eventually, Table C.2 shows all results for the self absorption R_{exp} , for Γ_0^2/Γ , for the ground-state transition width Γ_0 , for the level width Γ , and for the branching ratio Γ_0/Γ to the ground state that have been extracted from the RSA experiment exploiting the Bayesian analysis approach. In the cases of Γ_0 , Γ , and Γ_0/Γ the most probable value and the 68.3 % confidence interval around this value of the corresponding probability density function are given. They should not be misinterpreted as classical Gaussian uncertainties.

Table C.1.: This table gives an overview of the experimentally deduced self absorption R_{exp} as well as on the maximum R_{max} of the self absorption curve $R_{\Gamma_0, \Gamma}$, that has been determined with Γ_0^2/Γ being fixed by the NRF result. Those numbers are also listed.

E_i (keV)	Γ_0^2/Γ (meV)	R_{exp}	R_{max}
3642.9(1)	265 (9)	0.57 (1)	0.70
4025.2(4)	10 (2)	0.10 (33)	0.22
4172.7(2)	76 (4)	0.08 (8)	0.43
4354.3(2)	88 (4)	0.19 (4)	0.42
4369.8(2)	42 (3)	0.02 (12)	0.32
4385.6(5)	17 (2)	0.17 (18)	0.22
4514.1(2)	104 (6)	0.19 (5)	0.42
4787.0(2)	146 (6)	0.22 (5)	0.42
4872.0(4)	18 (3)	-0.38 (29)	0.19
5156.2(2)	109 (6)	0.14 (6)	0.34
5190.0(1)	152 (9)	0.22 (4)	0.38
5210.8(3)	88 (6)	0.11 (6)	0.30
5243.5(3)	59 (7)	0.15 (12)	0.26
5276.8(4)	28 (4)	0.14 (18)	0.18
5327.9(3)	89 (6)	0.19 (9)	0.29
5337.1(2)	207 (9)	0.24 (4)	0.40
5370.9(10)	45 (5)	0.14 (14)	0.22
5468.0(3)	74 (5)	0.13 (9)	0.26
5491.3(6)	38 (5)	0.30 (14)	0.19
5548.3(1)	364 (14)	0.30 (3)	0.45
5573.5(2)	166 (11)	0.12 (5)	0.34
5620.4(4)	57 (11)	-0.19 (34)	0.22
5626.5(3)	95 (11)	0.19 (18)	0.27
5638.5(4)	48 (7)	-0.06 (23)	0.20
5659.6(1)	1180 (41)	0.56 (2)	0.60
5719.1(3)	81 (9)	0.02 (15)	0.24
5757.7(5)	47 (8)	-0.06 (26)	0.19
5807.7(2)	134 (10)	0.13 (10)	0.29

continued on next page

continued from previous page

E_i (keV)	Γ_0^2/Γ (meV)	R_{exp}	R_{max}
5821.0(3)	126 (10)	0.10 (12)	0.28
5928.5(2)	264 (18)	0.29 (7)	0.36
5938.2(3)	98 (15)	-0.01 (19)	0.24
6026.5(4)	70 (15)	-0.07 (29)	0.21
6036.2(3)	169 (16)	0.24 (11)	0.29
6065.3(6)	54 (13)	0.50 (26)	0.18
6118.9(1)	401 (22)	0.28 (5)	0.39
6131.0(2)	214 (16)	0.24 (14)	0.31
6162.6(4)	224 (33)	0.11 (14)	0.32
6196.1(9)	97 (15)	0.10 (20)	0.22
6204.9(9)	64 (14)	0.12 (32)	0.18
6224.7(3)	127 (15)	-0.01 (16)	0.25
6242.8(3)	163 (19)	0.07 (13)	0.27
6253.8(4)	243 (18)	0.26 (9)	0.32
6274.0(2)	270 (24)	0.13 (8)	0.33
6295.8(2)	686 (31)	0.42 (4)	0.45
6328.2(4)	197 (18)	0.20 (11)	0.28
6344.2(2)	412 (26)	0.20 (10)	0.37
6354.5(2)	462 (42)	0.26 (7)	0.39
6365.2(3)	250 (22)	0.24 (11)	0.31
6397.3(1)	1133 (54)	0.38 (6)	0.51
6411.9(6)	78 (20)	0.11 (35)	0.19
6440.4(2)	434 (23)	0.17 (6)	0.37
6449.7(3)	225 (33)	0.27 (15)	0.29
6458.3(3)	267 (23)	0.34 (10)	0.31
6484.4(3)	317 (17)	0.21 (6)	0.33
6497.2(2)	962 (64)	0.39 (4)	0.47
6524.5(4)	182 (43)	0.33 (16)	0.26
6536.4(2)	1270 (64)	0.56 (2)	0.51
6549.4(2)	214 (15)	0.14 (8)	0.28
6574.9(3)	226 (16)	0.07 (11)	0.28
6581.8(7)	79 (30)	0.43 (23)	0.18
6597.8(5)	116 (17)	0.12 (20)	0.21

continued on next page

continued from previous page

E_i (keV)	Γ_0^2/Γ (meV)	R_{exp}	R_{max}
6605.6(2)	317 (23)	0.22 (8)	0.32
6617.4(2)	293 (18)	0.08 (7)	0.30
6639.8(4)	108 (16)	0.08 (15)	0.20
6656.6(3)	190 (15)	0.07 (9)	0.25
6736.0(8)	195 (22)	0.20 (10)	0.25
6758.4(6)	109 (13)	0.05 (16)	0.20
6779.4(7)	172 (24)	-0.21 (49)	0.23
6843.0(3)	252 (31)	-0.02 (18)	0.27
6863.1(1)	1059 (42)	0.43 (3)	0.45
6880.9(3)	217 (17)	-0.14 (12)	0.25
6895.3(4)	201 (19)	0.25 (26)	0.24
6906.8(8)	286 (44)	0.18 (22)	0.28
6923.8(3)	393 (24)	0.09 (8)	0.31
6934.2(3)	425 (27)	0.19 (7)	0.32
6952.4(6)	238 (23)	0.26 (15)	0.26
6962.0(3)	561 (32)	0.23 (7)	0.35
6971.5(5)	134 (18)	-0.44 (30)	0.20
6987.6(4)	114 (17)	-0.31 (25)	0.18
7009.4(3)	330 (33)	0.27 (8)	0.29
7026.4(6)	133 (19)	0.35 (18)	0.20
7038.2(5)	185 (28)	-0.18 (26)	0.22
7045.3(8)	147 (27)	0.23 (31)	0.20
7059.4(3)	302 (22)	0.29 (9)	0.27
7070.1(3)	308 (22)	0.23 (9)	0.27
7097.4(4)	211 (24)	0.12 (12)	0.23
7122.5(3)	435 (32)	0.01 (9)	0.31
7146.9(5)	130 (19)	0.23 (22)	0.19
7159.5(12)	68 (18)	0.17 (44)	0.14
7178.4(11)	152 (38)	-0.74 (73)	0.20
7184.1(7)	273 (40)	0.06 (24)	0.25
7208.5(5)	679 (54)	0.11 (10)	0.36
7216.3(5)	513 (65)	0.54 (11)	0.32
7238.0(8)	113 (26)	0.06 (30)	0.17

continued on next page

continued from previous page

E_i (keV)	Γ_0^2/Γ (meV)	R_{exp}	R_{max}
7265.3(7)	175 (30)	0.11 (23)	0.20
7317.5(8)	165 (29)	0.04 (28)	0.20
7329.3(15)	96 (29)	0.03 (48)	0.15
7342.0(9)	292 (64)	0.14 (14)	0.25
7376.7(6)	314 (46)	-0.12 (21)	0.25
7451.6(9)	146 (33)	0.25 (30)	0.18
7464.9(11)	184 (40)	0.34 (27)	0.20
7473.5(11)	186 (50)	0.43 (32)	0.20
7497.3(9)	197 (39)	0.34 (30)	0.20
7509.9(8)	258 (41)	0.10 (28)	0.23

Table C.2.: Results for R_{exp} , Γ_0^2/Γ , Γ_0 , Γ , and Γ_0/Γ as extracted from the RSA measurement.

E_i (keV)	R_{exp}	Γ_0^2/Γ (meV)	Γ_0 (eV)	Γ (eV)	Γ_0/Γ
3642.9(1)	0.57 (1)	265 (9)	$0.26^{+0.01}_{-0.01}$	$0.25^{+0.02}_{-0.02}$	$0.99^{+0.01}_{-0.03}$
4025.2(4)	0.10 (33)	10 (2)	$0^{+0.06}_{-0}$	$0^{+0.36}_{-0}$	$0.12^{+0.22}_{-0.05}$
4172.7(2)	0.08 (8)	76 (4)	$0.03^{+0.03}_{-0.03}$	$0^{+0.04}_{-0}$	$0.99^{+0.01}_{-0.25}$
4354.3(2)	0.19 (4)	88 (4)	$0.09^{+0.03}_{-0.02}$	$0.09^{+0.06}_{-0.04}$	$0.84^{+0.14}_{-0.12}$
4369.8(2)	0.02 (12)	42 (3)	$0.01^{+0.06}_{-0.01}$	$0^{+0.09}_{-0}$	$0.48^{+0.31}_{-0.18}$
4385.6(5)	0.17 (18)	17 (2)	$0.04^{+0.05}_{-0.04}$	$0^{+0.46}_{-0}$	$0.13^{+0.23}_{-0.04}$
4514.1(2)	0.19 (5)	104 (6)	$0.10^{+0.04}_{-0.03}$	$0.08^{+0.08}_{-0.05}$	$0.87^{+0.13}_{-0.15}$
4787.0(2)	0.22 (5)	146 (6)	$0.14^{+0.05}_{-0.04}$	$0.12^{+0.11}_{-0.07}$	$0.85^{+0.15}_{-0.11}$
4872.0(4)	-0.38 (29)	18 (3)	$0^{+0.07}_{-0}$	$0^{+0.28}_{-0}$	$0.16^{+0.29}_{-0.07}$
5156.2(2)	0.14 (6)	109 (6)	$0.11^{+0.06}_{-0.06}$	$0.04^{+0.15}_{-0.04}$	$0.74^{+0.20}_{-0.17}$
5190.0(1)	0.22 (4)	152 (9)	$0.19^{+0.05}_{-0.05}$	$0.21^{+0.14}_{-0.10}$	$0.70^{+0.18}_{-0.12}$
5210.8(3)	0.11 (6)	88 (6)	$0.08^{+0.06}_{-0.04}$	$0^{+0.16}_{-0}$	$0.69^{+0.21}_{-0.19}$
5243.5(3)	0.15 (12)	59 (7)	$0.10^{+0.08}_{-0.09}$	$0^{+0.47}_{-0}$	$0.28^{+0.28}_{-0.11}$
5276.8(4)	0.14 (18)	28 (4)	$0.04^{+0.08}_{-0.04}$	$0^{+0.55}_{-0}$	$0.16^{+0.23}_{-0.06}$
5327.9(3)	0.19 (9)	89 (6)	$0.14^{+0.11}_{-0.08}$	$0^{+0.55}_{-0}$	$0.36^{+0.25}_{-0.13}$
5337.1(2)	0.24 (4)	207 (9)	$0.23^{+0.06}_{-0.05}$	$0.22^{+0.16}_{-0.08}$	$0.80^{+0.16}_{-0.13}$
5370.9(10)	0.14 (14)	45 (5)	$0.06^{+0.09}_{-0.06}$	$0^{+0.09}_{-0}$	$0.22^{+0.25}_{-0.09}$
5468.0(3)	0.13 (9)	74 (5)	$0.10^{+0.09}_{-0.07}$	$0^{+0.40}_{-0}$	$0.35^{+0.28}_{-0.14}$
5491.3(6)	0.30 (14)	38 (5)	$0.14^{+0.08}_{-0.09}$	$0^{+0.93}_{-0}$	$0.16^{+0.18}_{-0.05}$
5548.3(1)	0.30 (3)	364 (14)	$0.35^{+0.05}_{-0.05}$	$0.34^{+0.10}_{-0.10}$	$0.97^{+0.03}_{-0.11}$
5573.5(2)	0.12 (5)	166 (11)	$0.11^{+0.06}_{-0.06}$	$0.04^{+0.09}_{-0.04}$	$0.99^{+0.01}_{-0.22}$
5620.4(4)	-0.19 (34)	57 (11)	$0.01^{+0.14}_{-0.01}$	$0^{+0.40}_{-0}$	$0.22^{+0.34}_{-0.08}$
5626.5(3)	0.19 (18)	95 (11)	$0.08^{+0.14}_{-0.08}$	$0^{+0.55}_{-0}$	$0.28^{+0.32}_{-0.08}$

continued on next page

continued from previous page

E_i (keV)	R_{exp}	Γ_0^2/Γ (meV)	Γ_0 (eV)	Γ (eV)	Γ_0/Γ
5638.5(4)	-0.06 (23)	48 (7)	$0.01^{+0.12}_{-0.01}$	$0^{+0.39}_{-0}$	$0.21^{+0.33}_{-0.07}$
5659.6(1)	0.56 (2)	1180 (41)	$1.05^{+0.14}_{-0.11}$	$0.90^{+0.28}_{-0.17}$	$0.99^{+0.01}_{-0.10}$
5719.1(3)	0.02 (15)	81 (9)	$0.01^{+0.14}_{-0.01}$	$0^{+0.29}_{-0}$	$0.31^{+0.37}_{-0.10}$
5757.7(5)	-0.06 (26)	47 (8)	$0^{+0.14}_{-0}$	$0^{+0.44}_{-0}$	$0.21^{+0.31}_{-0.08}$
5807.7(2)	0.13 (10)	134 (10)	$0.11^{+0.12}_{-0.10}$	$0^{+0.36}_{-0}$	$0.54^{+0.23}_{-0.22}$
5821.0(3)	0.10 (12)	126 (10)	$0.06^{+0.14}_{-0.06}$	$0^{+0.32}_{-0}$	$0.47^{+0.29}_{-0.17}$
5928.5(2)	0.29 (7)	264 (18)	$0.38^{+0.17}_{-0.13}$	$0.42^{+0.58}_{-0.28}$	$0.52^{+0.23}_{-0.14}$
5938.2(3)	-0.01 (19)	98 (15)	$0.01^{+0.18}_{-0.01}$	$0^{+0.34}_{-0}$	$0.35^{+0.32}_{-0.14}$
6026.5(4)	-0.07 (29)	70 (15)	$0^{+0.18}_{-0}$	$0^{+0.46}_{-0}$	$0.23^{+0.35}_{-0.08}$
6036.2(3)	0.24 (11)	169 (16)	$0.26^{+0.17}_{-0.15}$	$0^{+0.81}_{-0}$	$0.39^{+0.27}_{-0.12}$
6065.3(6)	0.50 (26)	54 (13)	$0.13^{+0.11}_{-0.11}$	$0^{+0.88}_{-0}$	$0.19^{+0.24}_{-0.07}$
6118.9(1)	0.28 (5)	401 (22)	$0.43^{+0.12}_{-0.12}$	$0.40^{+0.31}_{-0.20}$	$0.81^{+0.17}_{-0.12}$
6131.0(2)	0.24 (14)	214 (16)	$0.26^{+0.18}_{-0.19}$	$0^{+0.69}_{-0}$	$0.45^{+0.27}_{-0.14}$
6162.6(4)	0.11 (14)	224 (33)	$0.09^{+0.19}_{-0.09}$	$0^{+0.34}_{-0}$	$0.57^{+0.30}_{-0.15}$
6196.1(9)	0.10 (20)	97 (15)	$0.02^{+0.20}_{-0.02}$	$0^{+0.54}_{-0}$	$0.31^{+0.30}_{-0.12}$
6204.9(9)	0.12 (32)	64 (14)	$0^{+0.19}_{-0}$	$0^{+0.61}_{-0}$	$0.22^{+0.29}_{-0.09}$
6224.7(3)	-0.01 (16)	127 (15)	$0^{+0.19}_{-0}$	$0^{+0.29}_{-0}$	$0.41^{+0.35}_{-0.14}$
6242.8(3)	0.07 (13)	163 (19)	$0.06^{+0.16}_{-0.06}$	$0^{+0.32}_{-0}$	$0.47^{+0.35}_{-0.14}$
6253.8(4)	0.26 (9)	243 (18)	$0.34^{+0.21}_{-0.15}$	$0.26^{+0.68}_{-0}$	$0.47^{+0.24}_{-0.14}$
6274.0(2)	0.13 (8)	270 (24)	$0.16^{+0.14}_{-0.11}$	$0^{+0.25}_{-0}$	$0.91^{+0.09}_{-0.25}$
6295.8(2)	0.42 (4)	686 (31)	$0.89^{+0.20}_{-0.18}$	$1.04^{+0.62}_{-0.36}$	$0.71^{+0.15}_{-0.13}$
6328.2(4)	0.20 (11)	197 (18)	$0.27^{+0.16}_{-0.19}$	$0^{+0.70}_{-0}$	$0.45^{+0.27}_{-0.15}$
6344.2(2)	0.20 (10)	412 (26)	$0.27^{+0.20}_{-0.17}$	$0^{+0.42}_{-0}$	$0.94^{+0.06}_{-0.28}$
6354.5(2)	0.26 (7)	462 (42)	$0.42^{+0.17}_{-0.17}$	$0.30^{+0.35}_{-0.23}$	$0.89^{+0.11}_{-0.20}$
6365.2(3)	0.24 (11)	250 (22)	$0.29^{+0.23}_{-0.17}$	$0^{+0.81}_{-0}$	$0.47^{+0.27}_{-0.14}$
6397.3(1)	0.38 (6)	1133 (54)	$0.70^{+0.23}_{-0.17}$	$0.39^{+0.32}_{-0.18}$	$0.99^{+0.01}_{-0.15}$

continued on next page

continued from previous page

E_i (keV)	R_{exp}	Γ_0^2/Γ (meV)	Γ_0 (eV)	Γ (eV)	Γ_0/Γ
6411.9(6)	0.11 (35)	78 (20)	$0^{+0.22}_{-0}$	$0^{+0.62}_{-0}$	$0.27^{+0.29}_{-0.13}$
6440.4(2)	0.17 (6)	434 (23)	$0.25^{+0.13}_{-0.11}$	$0.10^{+0.17}_{-0.09}$	$0.98^{+0.02}_{-0.17}$
6449.7(3)	0.27 (15)	225 (33)	$0.30^{+0.20}_{-0.21}$	$0^{+0.85}_{-0}$	$0.45^{+0.25}_{-0.16}$
6458.3(3)	0.34 (10)	267 (23)	$0.47^{+0.21}_{-0.18}$	$0.50^{+0.94}_{-0.38}$	$0.42^{+0.21}_{-0.11}$
6484.4(3)	0.21 (6)	317 (17)	$0.34^{+0.16}_{-0.13}$	$0.24^{+0.42}_{-0.18}$	$0.73^{+0.20}_{-0.17}$
6497.2(2)	0.39 (4)	962 (64)	$0.81^{+0.20}_{-0.14}$	$0.66^{+0.38}_{-0.23}$	$0.99^{+0.01}_{-0.16}$
6524.5(4)	0.33 (16)	182 (43)	$0.30^{+0.20}_{-0.18}$	$0^{+1.04}_{-0}$	$0.37^{+0.26}_{-0.14}$
6536.4(2)	0.56 (2)	1270 (64)	$1.75^{+0.15}_{-0.15}$	$2.37^{+0.46}_{-0.38}$	$0.71^{+0.08}_{-0.06}$
6549.4(2)	0.14 (8)	214 (15)	$0.19^{+0.17}_{-0.12}$	$0^{+0.46}_{-0}$	$0.58^{+0.27}_{-0.16}$
6574.9(3)	0.07 (11)	226 (16)	$0.10^{+0.14}_{-0.10}$	$0^{+0.27}_{-0}$	$0.71^{+0.23}_{-0.22}$
6581.8(7)	0.43 (23)	79 (30)	$0.17^{+0.13}_{-0.14}$	$0^{+1.77}_{-0}$	$0.21^{+0.28}_{-0.10}$
6597.8(5)	0.12 (20)	116 (17)	$0.06^{+0.21}_{-0.06}$	$0^{+0.62}_{-0}$	$0.30^{+0.31}_{-0.10}$
6605.6(2)	0.22 (8)	317 (23)	$0.36^{+0.20}_{-0.17}$	$0.23^{+0.55}_{-0}$	$0.59^{+0.25}_{-0.15}$
6617.4(2)	0.08 (7)	293 (18)	$0.13^{+0.10}_{-0.11}$	$0^{+0.14}_{-0}$	$0.98^{+0.02}_{-0.24}$
6639.8(4)	0.08 (15)	108 (16)	$0.03^{+0.27}_{-0.03}$	$0^{+0.55}_{-0}$	$0.29^{+0.32}_{-0.10}$
6656.6(3)	0.07 (9)	190 (15)	$0.10^{+0.24}_{-0.10}$	$0^{+0.27}_{-0}$	$0.67^{+0.24}_{-0.20}$
6736.0(8)	0.20 (10)	195 (22)	$0.28^{+0.21}_{-0.16}$	$0^{+0.90}_{-0}$	$0.37^{+0.29}_{-0.10}$
6758.4(6)	0.05 (16)	109 (13)	$0.02^{+0.22}_{-0.02}$	$0^{+0.53}_{-0}$	$0.29^{+0.34}_{-0.09}$
6779.4(7)	-0.21 (49)	172 (24)	$0^{+0.30}_{-0}$	$0^{+0.53}_{-0}$	$0.35^{+0.34}_{-0.10}$
6843.0(3)	-0.02 (18)	252 (31)	$0.01^{+0.28}_{-0.01}$	$0^{+0.32}_{-0}$	$0.51^{+0.35}_{-0.11}$
6863.1(1)	0.43 (3)	1059 (42)	$1.23^{+0.27}_{-0.17}$	$1.34^{+0.70}_{-0.36}$	$0.79^{+0.13}_{-0.12}$
6880.9(3)	-0.14 (12)	217 (17)	$0^{+0.13}_{-0}$	$0^{+0.08}_{-0}$	$0.93^{+0.07}_{-0.30}$
6895.3(4)	0.25 (26)	201 (19)	$0.13^{+0.26}_{-0.13}$	$0^{+0.73}_{-0}$	$0.37^{+0.30}_{-0.11}$
6906.8(8)	0.18 (22)	286 (44)	$0.09^{+0.33}_{-0.09}$	$0^{+0.64}_{-0}$	$0.46^{+0.32}_{-0.12}$
6923.8(3)	0.09 (8)	393 (24)	$0.14^{+0.15}_{-0.13}$	$0^{+0.18}_{-0}$	$0.99^{+0.01}_{-0.26}$
6934.2(3)	0.19 (7)	425 (27)	$0.38^{+0.17}_{-0.20}$	$0.17^{+0.39}_{-0.17}$	$0.87^{+0.13}_{-0.21}$

continued on next page

continued from previous page

E_i (keV)	R_{exp}	Γ_0^2/Γ (meV)	Γ_0 (eV)	Γ (eV)	Γ_0/Γ
6952.4(6)	0.26 (15)	238 (23)	$0.27^{+0.27}_{-0.18}$	$0^{+0.95}_{-0}$	$0.40^{+0.28}_{-0.11}$
6962.0(3)	0.23 (7)	561 (32)	$0.44^{+0.25}_{-0.17}$	$0.24^{+0.46}_{-0.20}$	$0.88^{+0.12}_{-0.18}$
6971.5(5)	-0.44 (30)	134 (18)	$0.01^{+0.21}_{-0.01}$	$0^{+0.36}_{-0}$	$0.34^{+0.36}_{-0.11}$
6987.6(4)	-0.31 (25)	114 (17)	$0^{+0.20}_{-0}$	$0^{+0.36}_{-0}$	$0.31^{+0.37}_{-0.10}$
7009.4(3)	0.27 (8)	330 (33)	$0.51^{+0.25}_{-0.19}$	$0.54^{+0.90}_{-0.44}$	$0.45^{+0.25}_{-0.11}$
7026.4(6)	0.35 (18)	133 (19)	$0.27^{+0.17}_{-0.19}$	$0^{+1.08}_{-0}$	$0.29^{+0.24}_{-0.10}$
7038.2(5)	-0.18 (26)	185 (28)	$0.01^{+0.27}_{-0.01}$	$0^{+0.40}_{-0}$	$0.41^{+0.33}_{-0.14}$
7045.3(8)	0.23 (31)	147 (27)	$0.09^{+0.24}_{-0.09}$	$0^{+0.73}_{-0}$	$0.32^{+0.31}_{-0.11}$
7059.4(3)	0.29 (9)	302 (22)	$0.50^{+0.27}_{-0.18}$	$0.44^{+1.08}_{-0.36}$	$0.43^{+0.21}_{-0.12}$
7070.1(3)	0.23 (9)	308 (22)	$0.43^{+0.23}_{-0.22}$	$0.24^{+0.84}_{-0.24}$	$0.48^{+0.26}_{-0.13}$
7097.4(4)	0.12 (12)	211 (24)	$0.13^{+0.23}_{-0.13}$	$0^{+0.60}_{-0}$	$0.43^{+0.30}_{-0.14}$
7122.5(3)	0.01 (9)	435 (32)	$0.01^{+0.18}_{-0.01}$	$0^{+0.09}_{-0}$	$0.99^{+0.01}_{-0.24}$
7146.9(5)	0.23 (22)	130 (19)	$0.13^{+0.19}_{-0.13}$	$0^{+0.82}_{-0}$	$0.29^{+0.29}_{-0.10}$
7159.5(12)	0.17 (44)	68 (18)	$0.02^{+0.21}_{-0.02}$	$0^{+0.75}_{-0}$	$0.21^{+0.29}_{-0.09}$
7178.4(11)	-0.74 (73)	152 (38)	$0^{+0.30}_{-0}$	$0^{+0.60}_{-0}$	$0.32^{+0.34}_{-0.11}$
7184.1(7)	0.06 (24)	273 (40)	$0^{+0.39}_{-0}$	$0^{+0.55}_{-0}$	$0.47^{+0.32}_{-0.14}$
7208.5(5)	0.11 (10)	679 (54)	$0.17^{+0.23}_{-0.17}$	$0^{+0.22}_{-0}$	$0.98^{+0.02}_{-0.23}$
7216.3(5)	0.54 (11)	513 (65)	$0.90^{+0.27}_{-0.24}$	$1.22^{+1.10}_{-0.64}$	$0.48^{+0.20}_{-0.10}$
7238.0(8)	0.06 (30)	113 (26)	$0^{+0.27}_{-0}$	$0^{+0.69}_{-0}$	$0.29^{+0.30}_{-0.12}$
7265.3(7)	0.11 (23)	175 (30)	$0^{+0.34}_{-0}$	$0^{+0.68}_{-0}$	$0.35^{+0.32}_{-0.12}$
7317.5(8)	0.04 (28)	165 (29)	$0.01^{+0.31}_{-0.01}$	$0^{+0.64}_{-0}$	$0.33^{+0.35}_{-0.10}$
7329.3(15)	0.03 (48)	96 (29)	$0^{+0.26}_{-0}$	$0^{+0.74}_{-0}$	$0.25^{+0.29}_{-0.11}$
7342.0(9)	0.14 (14)	292 (64)	$0.16^{+0.28}_{-0.16}$	$0^{+0.67}_{-0}$	$0.46^{+0.34}_{-0.13}$
7376.7(6)	-0.12 (21)	314 (46)	$0^{+0.32}_{-0}$	$0^{+0.32}_{-0}$	$0.58^{+0.31}_{-0.15}$
7451.6(9)	0.25 (30)	146 (33)	$0.09^{+0.26}_{-0.09}$	$0^{+0.82}_{-0}$	$0.31^{+0.30}_{-0.12}$
7464.9(11)	0.34 (27)	184 (40)	$0.21^{+0.20}_{-0.21}$	$0^{+0.91}_{-0}$	$0.33^{+0.31}_{-0.11}$

continued on next page

continued from previous page

E_i (keV)	R_{exp}	Γ_0^2/Γ (meV)	Γ_0 (eV)	Γ (eV)	Γ_0/Γ
7473.5(11)	0.43 (32)	186 (50)	$0.12^{+0.29}_{-0.12}$	$0^{+0.92}_{-0}$	$0.33^{+0.32}_{-0.12}$
7497.3(9)	0.34 (30)	197 (39)	$0.12^{+0.29}_{-0.12}$	$0^{+0.87}_{-0}$	$0.34^{+0.31}_{-0.11}$
7509.9(8)	0.10 (28)	258 (41)	$0.06^{+0.35}_{-0.06}$	$0^{+0.67}_{-0}$	$0.43^{+0.30}_{-0.14}$

Bibliography

[Adr05] P. Adrich, A. Klimkiewicz, M. Fallot, *et al.*, Phys. Rev. Lett. **95** (2005) 132501.

[Ago03] S. Agostinelli, J. Allison, K. Amako, *et al.*, Nucl. Instr. and Meth. A **506** (2003) 250.

[Ajz90] F. Ajzenberg-Selove, Nucl. Phys. A **506** (1990) 1.

[Ali12] B. Alikhani, A. Givechyan, A. Heinz, *et al.*, Nucl. Instr. and Meth. A **675** (2012) 144.

[And01] W. Andrejtscheff, C. Kohstall, P. von Brentano, *et al.*, Phys. Lett. B **506** (2001) 239.

[Ang12] C. T. Angell, S. L. Hammond, H. J. Karwowski, *et al.*, Phys. Rev. C **86** (2012) 051302.

[Bar11] C. G. Barkla, Phil. Mag. Ser. 6 **21** (1911) 648.

[Bar60] W. C. Barber, F. Berthold, G. Fricke, F. E. Gudden, Phys. Rev. **120** (1960) 2081.

[Bar61] G. A. Bartholomew, Annu. Rev. Nucl. Sci. **11** (1961) 259.

[Bar63] W. Barber, J. Goldemberg, G. Peterson, Y. Torizuka, Nucl. Phys. **41** (1963) 461.

[Bar73] G. A. Bartholomew, E. D. Earle, A. J. Ferguson, J. W. Knowles, M. A. Lone, Adv. Nucl. Phys. **7** (1973) 229.

[Bar75] J. Barrette, W. D. Bianco, P. Depommier, *et al.*, Nucl. Phys. A **238** (1975) 176.

[Bau00] F. Bauwens, J. Bryssinck, D. De Frenne, *et al.*, Phys. Rev. C **62** (2000) 024302.

[Bec96] H. Becquerel, C. R. Acad. Sci. Paris **122** (1896) 501.

[Beč98] F. Bečvář, Nucl. Instr. and Meth. A **417** (1998) 434.

[Bel06] T. Belgia, O. Bersillon, R. Capote, *et al.*, *Handbook for Calculations of Nuclear Reaction Data, RIPL-2*, IAEA-TECDOC-1506, IAEA, Vienna (2006), <http://www-nds.iaea.org/RIPL-2/>.

[Ben09] N. Benouaret, R. Schwengner, G. Rusev, *et al.*, Phys. Rev. C **79** (2009) 014303.

[Ber75] J. Bergstrom, I. Auer, R. Hicks, Nucl. Phys. A **251** (1975) 401.

[Ber98] M. Berger, J. Hubbell, S. Seltzer, *et al.*, *XCOM: Photon Cross Sections Database*, National Institute for Standards and Technology, Standard Reference Database 8 (XGAM) (1998).

[Ber05] W. Bertozi, R. J. Ledoux, Nucl. Instr. and Meth. B **241** (2005) 820.

[Boh84] D. Bohle, A. Richter, W. Steffen, *et al.*, Phys. Lett. B **137** (1984) 27.

[Boo62] E. Booth, K. A. Wright, Nucl. Phys. **35** (1962) 472.

[Bot30] W. Bothe, H. Becker, Z. Phys. **66** (1930) 289.

[Bot37] W. Bothe, W. Gentner, Z. Phys. **71** (1937) 236.

[Bre36] G. Breit, E. Wigner, Phys. Rev. **49** (1936) 519.

[Bri55] D. Brink, Dissertation, Oxford University (1955).

[Bro00] B. Brown, Phys. Rev. Lett. **85** (2000) 5296.

[Bru00] M. Brunken, H. Genz, M. Gopych, *et al.*, in A. Chao, S. Yu, R. Ruth, ed., *Proc. of the 2000 Lin. Acc. Conf.*, SLAC-R-561 (2000), p. 152.

[Brz69] J. S. Brzosko, E. Gierlik, A. Soltan Jr., Z. Wilhelmi, Can. J. Phys. **47** (1969) 2849.

[Büs08] M. A. Büsing, M. Elvers, J. Endres, *et al.*, Phys. Rev. C **78** (2008) 044309.

[Cha32] J. Chadwick, Proc. R. Soc. Lond. A **136** (1932) 692.

- [CHU02] Z. CHUNMEI, Nucl. Data Sheets **95** (2002) 59.
- [Coh59] L. Cohen, R. A. Tobin, Nucl. Phys. **14** (1959) 243.
- [Com23] A. H. Compton, Phys. Rev. **21** (1923) 483.
- [Cre68] W. Creten, R. Jacobs, H. Ferdinand, Nucl. Phys. A **120** (1968) 126.
- [Cur98] P. Curie, M. Curie, G. Bémont, C. R. Acad. Sci. Paris **127** (1898) 1215.
- [Der13] V. Derya, J. Endres, M. Elvers, *et al.*, Nucl. Phys. A **906** (2013) 94.
- [Egi05] T. v. Egidy, D. Bucurescu, Phys. Rev. C **72** (2005) 044311.
- [Eig69] F. Eigenbrod, Z. Phys. A **228** (1969) 337.
- [Ein05a] A. Einstein, Ann. Phys. **322** (1905) 549.
- [Ein05b] A. Einstein, Ann. Phys. **322** (1905) 132.
- [End03] J. Enders, P. von Brentano, J. Eberth, *et al.*, Nucl. Phys. A **724** (2003) 243.
- [End09] J. Endres, D. Savran, A. M. v. d. Berg, *et al.*, Phys. Rev. C **80** (2009) 034302.
- [End10] J. Endres, E. Litvinova, D. Savran, *et al.*, Phys. Rev. Lett. **105** (2010) 212503.
- [Erh10] M. Erhard, A. R. Junghans, C. Nair, *et al.*, Phys. Rev. C **81** (2010) 034319.
- [Fag59] L. W. Fagg, S. S. Hanna, Rev. Mod. Phys. **31** (1959) 711.
- [Fra65] H. Frauenfelder, R. M. Steffen, in K. Siegbahn, ed., *Alpha-, Beta-, and Gamma-Ray Spectroscopy*, North-Holland Publishing Company, Amsterdam, The Netherlands (1965), 997.
- [Fri11] Y. Fritzsche, *Aufbau und Inbetriebnahme einer Quelle polarisierter Elektronen am supraleitenden Darmstädter Elektronenlinearbeschleuniger S-DALINAC*, Dissertation, TU Darmstadt (2011).

- [Fur02] R. Furnstahl, Nucl. Phys. A **706** (2002) 85.
- [Gei09] H. Geiger, E. Marsden, Proc. R. Soc. Lond. A **82** (1909) 495.
- [Gol48] M. Goldhaber, E. Teller, Phys. Rev. **74** (1948) 1046.
- [Gor98] S. Goriely, Phys. Lett. B **436** (1998) 10.
- [Gor04] S. Goriely, E. Khan, M. Samyn, Nucl. Phys. A **739** (2004) 331.
- [Gov98] K. Govaert, F. Bauwens, J. Bryssinck, *et al.*, Phys. Rev. C **57** (1998) 2229.
- [Gre96] W. Greiner, J. A. Maruhn, *Nuclear Models*, Springer, Berlin (1996).
- [Gut05] M. Guttormsen, R. Chankova, U. Agvaanluvsan, *et al.*, Phys. Rev. C **71** (2005) 044307.
- [Har01] M. N. Harakeh, A. van der Woude, *Giant Resonances*, Oxford University Press (2001).
- [Har04] T. Hartmann, M. Babilon, S. Kamerdzhiev, *et al.*, Phys. Rev. Lett. **93** (2004) 192501.
- [Hay57] E. Hayward, E. G. Fuller, Phys. Rev. **106** (1957) 991.
- [Her87] H. Hertz, Ann. Phys. **267** (1887) 983.
- [Her95a] R.-D. Herzberg, *Untersuchung von gekoppelten Phononenanregungen in Kernen um $A = 140$* , Dissertation, Universität zu Köln (1995).
- [Her95b] R.-D. Herzberg, I. Bauske, P. von Brentano, *et al.*, Nucl. Phys. A **592** (1995) 211.
- [Her97] R.-D. Herzberg, P. von Brentano, J. Eberth, *et al.*, Phys. Lett. B **390** (1997) 49.
- [His06] T. Hisashige, Y. Yamamura, T. Tsuji, J. All. Comp. **408** (2006) 1153.
- [Hor01a] C. J. Horowitz, J. Piekarewicz, Phys. Rev. C **64** (2001) 062802.
- [Hor01b] C. J. Horowitz, J. Piekarewicz, Phys. Rev. Lett. **86** (2001) 5647.

- [Hor02] C. J. Horowitz, J. Piekarewicz, Phys. Rev. C **66** (2002) 055803.
- [Hug11] F. Hug, C. Burandt, J. Conrad, *et al.*, in *Proc. of the 2011 Part. Acc. Conf.*, New York, NY, USA (2011), p. 1999.
- [Hut02] C. Hutter, M. Babilon, W. Bayer, *et al.*, Nucl. Instr. and Meth. A **489** (2002) 247.
- [Isa11] J. Isaak, D. Savran, M. Fritzsche, *et al.*, Phys. Rev. C **83** (2011) 034304.
- [Isa13] J. Isaak, D. Savran, M. Krčka, *et al.*, Phys. Lett. B **727** (2013) 361.
- [Jay57] E. T. Jaynes, Phys. Rev. **106** (1957) 620.
- [Jay89] E. T. Jaynes, R. D. Rosenkrantz (ed.), *Papers on Probability, Statistics and Statistical Physics*, Kluwer Academic Publishers, Dordrecht, The Netherlands (1989).
- [Jun95] A. Jung, S. Lindenstruth, H. Schacht, *et al.*, Nucl. Phys. A **584** (1995) 103.
- [Kli07] A. Klimkiewicz, N. Paar, P. Adrich, *et al.*, Phys. Rev. C **76** (2007) 051603.
- [Kne96] U. Kneissl, H. Pitz, A. Zilges, Prog. Part. Nucl. Phys. **37** (1996) 349.
- [Kne06] U. Kneissl, N. Pietralla, A. Zilges, J. Phys. G: Nucl. Part. Phys. **32** (2006) R217.
- [Kni91] M. Knirsch, *Konzeption, Aufbau und Erprobung eines hochauflösenden QCLAM-Elektronenspektrometers mit großem Raumwinkel und hoher Impulsakzeptanz am Elektronenbeschleuniger S-DALINAC*, Dissertation, TU Darmstadt (1991).
- [Kno10] G. Knoll, *Radiation Detection and Measurement*, John Wiley & Sons (2010).
- [Kou96] N. Koura, S. Kohara, K. Takeuchi, *et al.*, J. Mol. Struct. **382** (1996) 163.
- [Kra70] K. S. Krane, R. M. Steffen, Phys. Rev. C **2** (1970) 724.

[Kuh29] W. Kuhn, Phil. Mag. Ser. 7 **8** (1929) 625.

[Lan14] E. G. Lanza, A. Vitturi, E. Litvinova, D. Savran, Phys. Rev. C **89** (2014) 041601.

[Lep76] A. Leprêtre, H. Beil, R. Bergère, *et al.*, Nucl. Phys. A **258** (1976) 350.

[Lew67] J. T. Lewis, A. Lehoczky, C. V. Briscoe, Phys. Rev. **161** (1967) 877.

[Lip66] P. Lipas, Nucl. Phys. **82** (1966) 91.

[Löh13] B. Löher, V. Derya, T. Aumann, *et al.*, Nucl. Instr. and Meth. A **723** (2013) 136.

[Löh14] B. Löher, *Probing the Decay Characteristics of the Pygmy Dipole Resonance in the Semi-Magic Nucleus ^{140}Ce with $\gamma-\gamma$ Coincidence Measurements*, Dissertation, Johannes Gutenberg-Universität Mainz (2014).

[Mar65] D. L. Martin, Phys. Rev. **139** (1965) A150.

[Mar08] L. E. Marcucci, M. Pervin, S. C. Pieper, R. Schiavilla, R. B. Wiringa, Phys. Rev. C **78** (2008) 065501.

[Mas12] R. Massarczyk, R. Schwengner, F. Dönau, *et al.*, Phys. Rev. C **86** (2012) 014319.

[Men69] D. Mendelejeff, Z. Chem. **12** (1869) 405.

[Met56] F. R. Metzger, Phys. Rev. **103** (1956) 983.

[Met59] F. R. Metzger, Prog. in Nucl. Phys. **7** (1959) 53.

[Mig44] A. B. Migdal, J. Phys. (USSR) **8** (1944) 331.

[Moo51] P. B. Moon, Proc. Phys. Soc. London A **64** (1951) 76.

[Mot69] J. W. Motz, H. A. Olsen, H. W. Koch, Rev. Mod. Phys. **41** (1969) 581.

[Nic07] N. Nica, Nucl. Data Sheets **108** (2007) 1287.

[Nol79] P. J. Nolan, J. F. Sharpey-Schafer, Rep. Progr. Phys. **42** (1979) 1.

[Öze07] B. Özal, J. Enders, P. von Neuman Cosel, *et al.*, Nucl. Phys. A **788** (2007) 385.

- [Paa07] N. Paar, D. Vretenar, E. Khan, G. Colò, Rep. Progr. Phys. **70** (2007) 691.
- [Pai13] H. Pai, J. Beller, N. Benouaret, *et al.*, Phys. Rev. C **88** (2013) 054316.
- [Pas13] S. Pastore, S. C. Pieper, R. Schiavilla, R. B. Wiringa, Phys. Rev. C **87** (2013) 035503.
- [Per07] M. Pervin, S. C. Pieper, R. B. Wiringa, Phys. Rev. C **76** (2007) 064319.
- [Pie93] N. Pietralla, *Lebensdauerbestimmung im Kern ^{27}Al durch Selbstabsorptions-Experimente*, Diplomarbeit, Universität zu Köln (1993).
- [Pie95] N. Pietralla, I. Bauske, O. Beck, *et al.*, Phys. Rev. C **51** (1995) 1021.
- [Pie01] N. Pietralla, Z. Berant, V. N. Litvinenko, *et al.*, Phys. Rev. Lett. **88** (2001) 012502.
- [Pie04] S. C. Pieper, R. B. Wiringa, J. Carlson, Phys. Rev. C **70** (2004) 054325.
- [Pie06] J. Piekarewicz, Phys. Rev. C **73** (2006) 044325.
- [Pol11] I. Poltoratska, *Complete dipole response in ^{208}Pb from high-resolution proton scattering at 0°* , Dissertation, TU Darmstadt (2011).
- [Por56] C. E. Porter, R. G. Thomas, Phys. Rev. **104** (1956) 483.
- [Pre84] W. Prestwich, M. Islam, T. Kennett, Z. Phys. A **315** (1984) 103.
- [Pru06] J. Puet, D. P. McNabb, C. A. Hagmann, F. V. Hartemann, C. P. J. Barty, J. Appl. Phys. **99** (2006) 123102.
- [Pud95] B. S. Pudliner, V. R. Pandharipande, J. Carlson, R. B. Wiringa, Phys. Rev. Lett. **74** (1995) 4396.
- [Ram28] C. V. Raman, Indian J. Phys. **2** (1928) 387.
- [Ras69] V. K. Rasmussen, C. P. Swann, Phys. Rev. **183** (1969) 918.
- [Ric83] A. Richter, in P. Blasi, R. A. Ricci, ed., *Proc. of the Int. Conf. on Nuclear Physics*, Tipografica Compositori Bologna (1983), Vol. 2, p. 189.

- [Ric96] A. Richter, in S. Meyers, *et al.*, ed., *Proc. of the 5th EPAC*, IOP Publishing, Bristol (1996), p. 110.
- [Rob84] R. G. H. Robertson, P. Dyer, R. C. Melin, *et al.*, Phys. Rev. C **29** (1984) 755.
- [Rom13] C. Romig, J. Beller, J. Glorius, *et al.*, Phys. Rev. C **88** (2013) 044331.
- [Ros13] D. M. Rossi, P. Adrich, F. Aksouh, *et al.*, Phys. Rev. Lett. **111** (2013) 242503.
- [Rus08] G. Rusev, R. Schwengner, F. Dönau, *et al.*, Phys. Rev. C **77** (2008) 064321.
- [Rus09] G. Rusev, R. Schwengner, R. Beyer, *et al.*, Phys. Rev. C **79** (2009) 061302(R).
- [Rut11] E. Rutherford, Phil. Mag. Ser. 6 **21** (1911) 669.
- [Rut19] E. Rutherford, Phil. Mag. Ser. 6 **37** (1919) 537.
- [Rut20] E. Rutherford, Proc. R. Soc. London A **97** (1920) 374.
- [Rye02] N. Ryezayeva, T. Hartmann, Y. Kalmykov, *et al.*, Phys. Rev. Lett. **89** (2002) 272502.
- [Sav06a] D. Savran, M. Babilon, A. M. van den Berg, *et al.*, Phys. Rev. Lett. **97** (2006) 172502.
- [Sav06b] D. Savran, A. van den Berg, M. Harakeh, *et al.*, Nucl. Instr. and Meth. A **564** (2006) 267.
- [Sav08] D. Savran, M. Fritzsch, J. Hasper, *et al.*, Phys. Rev. Lett. **100** (2008) 232501.
- [Sav10] D. Savran, K. Lindenberg, J. Glorius, *et al.*, Nucl. Instr. and Meth. A **613** (2010) 232.
- [Sav11] D. Savran, M. Elvers, J. Endres, *et al.*, Phys. Rev. C **84** (2011) 024326.
- [Sav13] D. Savran, T. Aumann, A. Zilges, Prog. Part. Nucl. Phys. **70** (2013) 210.

- [Sch46] L. I. Schiff, Phys. Rev. **70** (1946) 761.
- [Sch51] L. I. Schiff, Phys. Rev. **83** (1951) 252.
- [Sch78] D. Schüll, J. Foh, H.-D. Gräf, *et al.*, Nucl. Instr. and Meth. **153** (1978) 29.
- [Sch07] R. Schwengner, G. Rusev, N. Benouaret, *et al.*, Phys. Rev. C **76** (2007) 034321.
- [Sch08] R. Schwengner, G. Rusev, N. Tsoneva, *et al.*, Phys. Rev. C **78** (2008) 064314.
- [Sch13a] M. Scheck, V. Yu. Ponomarev, T. Aumann, *et al.*, Phys. Rev. C **87** (2013) 051304(R).
- [Sch13b] M. Scheck, V. Yu. Ponomarev, M. Fritzsche, *et al.*, Phys. Rev. C **88** (2013) 044304.
- [Sch13c] R. Schwengner, R. Massarczyk, G. Rusev, *et al.*, Phys. Rev. C **87** (2013) 024306.
- [Sko63] S. Skorka, R. Hübner, T. Retz-Schmidt, H. Wahl, Nucl. Phys. **47** (1963) 417.
- [Sno86] K. A. Snover, Ann. Rev. Nucl. Part. Sci. **36** (1986) 545.
- [Sol92] V. G. Soloviev, *Theory of Atomic Nuclei, Quasi-particle and Phonons*, Taylor & Francis (1992).
- [Son11] K. Sonnabend, D. Savran, J. Beller, *et al.*, Nucl. Instr. and Meth. A **640** (2011) 6.
- [Ste50] H. Steinwedel, J. H. D. Jensen, P. Jensen, Phys. Rev. **79** (1950) 1019.
- [Str71] J. Strutt, Phil. Mag. Ser. 4 **41** (1871) 107.
- [Sze83] Z. Szeftliński, G. Szeftlińska, Z. Wilhelmi, *et al.*, Phys. Lett. B **126** (1983) 159.
- [Tam09] A. Tamii, Y. Fujita, H. Matsubara, *et al.*, Nucl. Instr. and Meth. A **605** (2009) 326.

- [Tam11] A. Tamii, I. Poltoratska, P. von Neumann-Cosel, *et al.*, Phys. Rev. Lett. **107** (2011) 062502.
- [The92] J. Theuerkauf, S. Esser, S. Krink, *et al.*, Programme Tv, Institut für Kernphysik, Universität zu Köln (1992).
- [Tho97] J. J. Thomson, Phil. Mag. Ser. 5 **44** (1897) 293.
- [Tho04] J. J. Thomson, Phil. Mag. Ser. 6 **7** (1904) 237.
- [Til02] D. Tilley, C. Cheves, J. Godwin, *et al.*, Nucl. Phys. A **708** (2002) 3.
- [Til04] D. Tilley, J. Kelley, J. Godwin, *et al.*, Nucl. Phys. A **745** (2004) 155.
- [Ton10] A. P. Tonchev, S. L. Hammond, J. H. Kelley, *et al.*, Phys. Rev. Lett. **104** (2010) 072501.
- [Vod84] R. Vodhanel, M. K. Brussel, R. Moreh, W. C. Sellyey, T. E. Chapuran, Phys. Rev. C **29** (1984) 409.
- [Vog71] P. Vogel, L. Kocbach, Nucl. Phys. A **176** (1971) 33.
- [Voi04] A. Voinov, E. Algin, U. Agvaanluvsan, *et al.*, Phys. Rev. Lett. **93** (2004) 142504.
- [Vol06] S. Volz, N. Tsoneva, M. Babilon, *et al.*, Nucl. Phys. A **779** (2006) 1.
- [Wei99] K. Weise, W. Wöger, *Meßunsicherheit und Meßdatenauswertung*, Wiley-VCH (1999).
- [Wei06] K. Weise, K. Hübel, E. Rose, *et al.*, Rad. Prot. Dos. **121** (2006) 52.
- [Wel09] H. R. Weller, M. W. Ahmed, H. Gao, *et al.*, Prog. Part. Nucl. Phys. **62** (2009) 257.
- [Wie09] O. Wieland, A. Bracco, F. Camera, *et al.*, Phys. Rev. Lett. **102** (2009) 092502.
- [Wie12] M. Wiedeking, L. A. Bernstein, M. Krtschka, *et al.*, Phys. Rev. Lett. **108** (2012) 162503.
- [Zil02] A. Zilges, S. Volz, M. Babilon, *et al.*, Phys. Lett. B **542** (2002) 43.

List of Publications

[Bel12] J. Beller, J. Wagner, M. Ahmed, *et al.*, J. Phys.: Conf. Ser. **366** (2012) 012003.

[Bel13] J. Beller, N. Pietralla, J. Barea, *et al.*, Phys. Rev. Lett. **111** (2013) 172501.

[Bel15] J. Beller, C. Stumpf, M. Scheck, *et al.*, Phys. Lett. B **741** (2015) 128.

[Ben14] N. Benouaret, J. Beller, J. Isaak, *et al.*, Act. Phys. Pol. B **45** (2014) 193.

[Coo12] N. Cooper, F. Reichel, V. Werner, *et al.*, Phys. Rev. C **86** (2012) 034313.

[Der13] V. Derya, J. Endres, M. Elvers, *et al.*, Nucl. Phys. A **906** (2013) 94.

[God13] P. M. Goddard, N. Cooper, V. Werner, *et al.*, Phys. Rev. C **88** (2013) 064308.

[Hum12] P. Humby, N. Cooper, V. Werner, *et al.*, in *APS Division of Nuclear Physics Meeting Abstracts* (2012), p. H9.

[Isa11] J. Isaak, D. Savran, M. Fritzsch, *et al.*, Phys. Rev. C **83** (2011) 034304.

[Isa13] J. Isaak, D. Savran, M. Krčka, *et al.*, Phys. Lett. B **727** (2013) 361.

[Isa14] J. Isaak, J. Beller, E. Fiori, *et al.*, EPJ Web of Conferences **66** (2014) 02055.

[Löh13] B. Löher, V. Derya, T. Aumann, *et al.*, Nucl. Instr. and Meth. A **723** (2013) 136.

[Pai13] H. Pai, J. Beller, N. Benouaret, *et al.*, Phys. Rev. C **88** (2013) 054316.

- [Pie14] N. Pietralla, J. Beller, T. Beck, *et al.*, J. Phys.: Conf. Ser. **533** (2014) 012008.
- [Rom13] C. Romig, J. Beller, J. Glorius, *et al.*, Phys. Rev. C **88** (2013) 044331.
- [Rom14a] C. Romig, T. Beck, J. Beller, *et al.*, submitted to proceedings of CGS15 conference (2014).
- [Rom14b] C. Romig, D. Savran, J. Birkhan, *et al.*, submitted to Phys. Lett. B (2014).
- [Sau14] A. Sauerwein, K. Sonnabend, M. Fritzsche, *et al.*, Phys. Rev. C **89** (2014) 035803.
- [Sav11] D. Savran, M. Elvers, J. Endres, *et al.*, Phys. Rev. C **84** (2011) 024326.
- [Sch12] F. Schlüter, J. Enders, A. Zilges, *et al.*, Act. Phys. Pol. B **43** (2012) 333.
- [Sch13a] M. Scheck, V. Yu. Ponomarev, T. Aumann, *et al.*, Phys. Rev. C **87** (2013) 051304(R).
- [Sch13b] M. Scheck, V. Yu. Ponomarev, M. Fritzsche, *et al.*, Phys. Rev. C **88** (2013) 044304.
- [Son11] K. Sonnabend, D. Savran, J. Beller, *et al.*, Nucl. Instr. and Meth. A **640** (2011) 6.
- [Yev10] O. Yevetska, J. Enders, M. Fritzsche, *et al.*, Phys. Rev. C **81** (2010) 044309.
- [Zwe12] M. Zweidinger, J. Beller, J. Isaak, *et al.*, J. Phys.: Conf. Ser. **366** (2012) 012054.

List of Figures

1.1. Alchemical symbols of the classical elements	2
1.2. The periodic system of elements	3
1.3. Thomsons and Rutherfords model of the atom	3
1.4. Nuclear chart	5
2.1. Schematic diagram of a detection setup to scan for hazardous materials	10
2.2. Total, elastic and inelastic cross sections of ^{94}Mo	12
2.3. Average branching ratio $\langle b_0 \rangle$ to the ground state of ^{94}Mo	13
2.4. Lowest-lying $M1$ transition widths of the lithium isotopes ^{6-9}Li	15
2.5. Decay scheme of the first excited 0^+ level of ^6Li	16
2.6. Previous results for the $M1$ transition width of the 0_1^+ level of ^6Li	18
3.1. Generic $E1$ -strength distribution of spherical even-even nuclei	20
4.1. Principle of nuclear resonance fluorescence	26
4.2. Angular distributions for two spin sequences	29
4.3. Definition of azimuthal and polar angles and of the polarisation plane	31
4.4. Azimuthal angular distribution for NRF with polarised photons	32
4.5. Comparison of absorption cross sections	38
5.1. Basic principle of self-absorption measurements	42
5.2. Schematic photon-flux distribution in front of and behind an absorber	43
5.3. Doppler broadened cross section for different values of Γ_0 and Γ	44
5.4. Illustration of the photo effect, Compton scattering and pair production	45
5.5. Total atomic attenuation cross section of ^{140}Ce	46
5.6. Photon-flux densities for two generic states of ^{140}Ce	47
5.7. Schematic NRF spectra obtained with and without absorption target	51

5.8. Resonance-absorption densities for two generic states of ^{140}Ce	53
5.9. Self absorption as function of Γ_0 and Γ	55
5.10. Self absorption as function of Γ_0 with Γ_0^2/Γ fixed to 100 meV	56
6.1. Schematic overview of the S-DALINAC	60
6.2. Schematic overview of DHIPS	62
7.1. Absorption, self-absorption and NRF spectrum of ^{140}Ce	67
7.2. Parametrisations of the photon flux, the efficiency and their product	73
7.3. Intensity ratio w and the corresponding spin assignments	78
7.4. $B(E1)\uparrow$ -strength distribution of ^{140}Ce	83
7.5. Comparison of $B(E1)\uparrow$ values to results of Herzberg and Volz	84
7.6. $B(E1)\uparrow$ ratios from the present work compared to Herzberg and Volz	85
7.7. Γ_0^2/Γ compared for the two-phonon state and 9 strongly excited states	87
7.8. Normalisation between the RSA and ABS measurement for ^{140}Ce	90
7.9. Normalisation between the RSA and NRF measurement for ^{140}Ce	92
7.10. RSA spectrum before and after applying the normalisation via $f_{\text{RSA,NRF}}$	94
7.11. Conventional approach to determine the ground-state transition width Γ_0	97
7.12. Illustration of the principle of maximum information entropy	99
7.13. Determination of Γ_0 exploiting probability distributions	101
7.14. Investigation of the analysing approach: results for Γ_0 , Γ , as well as Γ_0/Γ	105
7.15. Investigation of the analysing approach: probability distributions	107
7.16. Saturation value of the branching ratio to the ground state	108
7.17. Overview of R_{exp} as a function of the energy	109
7.18. Experimentally deduced self absorption as a function of Γ_0^2/Γ	110
7.19. Investigation of R_{max} for generic states as a function of Γ_0^2/Γ	112
7.20. First and second solution for Γ_0 from the conventional approach	115
7.21. Results for the ground-state transition width Γ_0	116
7.22. $B(E1)\uparrow$ -strength distributions from the RSA and NRF measurements	120
7.23. Results for the total transition width Γ	121
7.24. Results for the branching ratio Γ_0/Γ to the ground state	123

7.25. Γ_0/Γ obtained with the Bayesian and the conventional approach	124
7.26. Illustration of the Porter-Thomas distribution	128
7.27. Schematic nuclear realisation of a nucleus in DICEBOX	130
7.28. Level density $\rho_{1-}(E)$ for 1^- states of ^{140}Ce used with DICEBOX	131
7.29. Branching ratio b_0 to the ground state as a function of E_x	133
7.30. Branching ratio b_0 to the ground state as a function of Γ_0^2/Γ	134
8.1. Spectra taken during the NRF and RSA measurements on ^6Li	140
8.2. Normalisation between the RSA and NRF measurement for ^6Li	141
8.3. NRF spectrum and normalised RSA spectrum of ^6Li	142
8.4. Simulated energy distributions of photons behind the collimator	145
8.5. Raman spectra of Li_2CO_3 and K_2CO_3	149
8.6. Results for the level width Γ of the 0_1^+ level of ^6Li	151
8.7. Previous and current results for the level width of the 0_1^+ level of ^6Li	154
A.1. Summed spectra of ^{140}Ce between 1.5 MeV and 2.5 MeV	164
A.2. Summed spectra of ^{140}Ce between 2.5 MeV and 3.5 MeV	165
A.3. Summed spectra of ^{140}Ce between 3.5 MeV and 4.5 MeV	166
A.4. Summed spectra of ^{140}Ce between 4.5 MeV and 5.5 MeV	167
A.5. Summed spectra of ^{140}Ce between 5.5 MeV and 6.6 MeV	168
A.6. Summed spectra of ^{140}Ce between 6.5 MeV and 7.9 MeV	169
B.1. $B(E1)\uparrow$ and $B(E2)\uparrow$ sensitivity limits of the NRF measurement	185
C.1. Example for determination of Γ_0 : the excited state of ^{140}Ce at 3643 keV	188
C.2. Example for determination of Γ_0 : the excited state of ^{140}Ce at 6617 keV	188



List of Tables

7.1. Information on the targets used during the RSA experiment on ^{140}Ce	66
7.2. The measurements during the RSA experiment on ^{140}Ce	66
7.3. Information on the first four excited states of ^{11}B	71
7.4. Candidates for inelastic transitions to the 2_1^+ level of ^{140}Ce	76
7.5. Half-lives of four 2^+ levels of ^{140}Ce compared to previous measurements	80
7.6. Normalisation factors $f_{\text{RSA,ABS}}$ for the measurement on ^{140}Ce	90
7.7. Normalisation factors $f_{\text{RSA,NRF}}$ for the measurement on ^{140}Ce	93
7.8. Four excited states of ^{140}Ce with R_{exp} being larger than R_{max}	111
7.9. Overview of the results extracted from the RSA measurement on ^{140}Ce	113
7.10. Candidates for double peaks in the recorded spectra of ^{140}Ce	118
 8.1. Information on the targets used during the RSA measurements on ^6Li	138
8.2. The measurements during the RSA experiment on ^6Li	139
8.3. Normalisation factors $f_{\text{RSA,NRF}}$ for the measurement on ^6Li	141
8.4. Experimentally deduced self absorption of the 0_1^+ level of ^6Li	148
 B.1. NRF intensities and ratio w for the observed 2^+ states of ^{140}Ce .	172
B.2. NRF intensities and ratio w for the observed states with $J = 1$ of ^{140}Ce	172
B.3. Integrated cross sections and related quantities of ^{140}Ce	177
B.4. Comparison of the $B(E1)\uparrow$ -transition strengths of ^{140}Ce	181
 C.1. Experimentally determined self absorption R_{exp} and R_{max}	190
C.2. Results for R_{exp} , Γ_0^2/Γ , Γ_0 , Γ , and Γ_0/Γ from the RSA measurement	194



Danksagung

Dankbar zu sein, ist etwas sehr Schönes, heißt es doch, dass da Leute sind, die Vertrauen in mich gesetzt und mich unterstützt haben, sei es auf praktische oder moralische Art und Weise und die auch in nervenaufreibenden Zeiten geduldig mit Rat und Tat zur Stelle waren. Daher möchte ich zum Schluss dieser Arbeit meiner Dankbarkeit all jenen gegenüber Ausdruck verleihen, die auf die eine oder andere Art zum Entstehen dieser Arbeit beigetragen und mich durch die letzten Jahre begleitet haben.

Zunächst möchte ich Herrn Prof. Dr. Dr. h.c. Norbert Pietralla herzlich für die Gelegenheit danken, diese Doktorarbeit in seiner Arbeitsgruppe durchführen zu können. Auch in stressigen Zeiten steht seine Tür immer für Fragen und Diskussionen offen, wobei er immer mit seiner Begeisterung anzustecken weiß. Darüber hinaus ermöglichte er es mir, an verschiedenen Konferenzen teilzunehmen, um dort meine Arbeit vorzustellen, aber auch um mein Wissen über den Tellerrand der Selbstabsorptionstechnik hinaus zu vertiefen. Im Laufe der Jahre vertraute er mir immer mehr Verantwortung an, eine nicht immer leichte Aufgabe, die ich aber sehr gerne erfüllt habe. Dabei gab es auch ausreichend Spielraum, selbstständig zu arbeiten, eigene Ideen zu entwickeln und zu verfolgen. Auch für dieses in mich gesetzte Vertrauen möchte ich mich bedanken.

Weiterhin möchte ich mich bei meinen Betreuern während der Jahre der Promotion bedanken.

Hier sei zunächst Dr. Deniz Savran genannt, der das Institut für Kernphysik zwar relativ früh während meiner Promotion verließ, aber auch von der GSI aus für Fragen und sehr lehrreiche Diskussionen bezüglich der Auswertung und Interpretation der Messungen dieser Arbeit zur Verfügung stand. Für die hervorragende Betreuung auch über die “Pflicht” hinaus gilt ihm ein großer Dank.

Herrn Dr. Marcus Scheck möchte ich einen ganz besonderen Dank aussprechen. Unabhängig von seiner eigenen Arbeit oder stressigen Zeiten stand er mir stets mit Rat und Tat zur Seite und das auch weit über rein wissenschaftliche Themen hinaus. Mit seiner positiven Art verstand er es, mich immer wieder

zu motivieren. Für die tolle Zusammenarbeit bin ich ihm zu großem Dank verpflichtet.

Zuletzt hat Dr. Volker Werner die Teilprojektleitung übernommen. Auch ihm möchte ich für die Betreuung und Unterstützung während der finalen Phase meiner Promotion danken.

Mein Dank gilt außerdem allen administrativen Mitarbeitern am IKP. Ohne die hervorragende Unterstützung durch die Sekretariate wäre ein angenehmes und erfolgreiches Arbeiten am IKP kaum möglich. Auch den hausinternen Werkstätten und vor allem der Mannschaft rund um den Beschleuniger möchte ich danken. Wir erhalten für jede unserer Strahlzeiten immer wieder beste Strahlkonditionen, was erfolgreiches Experimentieren überhaupt erst möglich macht. Im selben Zuge sollen auch alle Experimentierschichten während der zahlreichen KRF Strahlzeiten erwähnt sein. Auch wenn die KRF-Gruppe zuletzt immer weiter gewachsen ist, können Strahlzeiten, die oft viele Wochen lang sind, nicht ohne ihre Hilfe gelingen. Auch dafür möchte ich mich bedanken.

Ein ganz besonderer Dank richtet sich natürlich auch an das ganze Haus und insbesondere die AG Pietralla für die tolle Arbeitsatmosphäre, die ich Tag für Tag genieße und die sicherlich maßgeblich zum Spaß an der Arbeit beiträgt. Insbesondere möchte ich mich für die tolle Zusammenarbeit mit Simela Aslanidou, Jonny Birkhan, Andreas Krugmann, Oliver Möller, Christian Stahl, Robert Stegmann und Michael Thürauf bedanken, mit denen es sich nicht nur hervorragend fachsimpeln lässt.

Ein ganz großer Dank richtet sich an die KRF-Gruppe. Das sind Tobias Beck, Jacob Beller, Udo Gayer, Laura Mertes, Haridas Pai, Philipp Ries und Markus Zweidinger. Zusammen haben wir so manche Strahlzeit gestemmt und viele Projekte bewältigt. Ihr seid eine tolle Truppe und es ist mir stets eine Freude mit euch zusammenzuarbeiten.

Weiterhin geht ein ganz besonderer Dank an Christopher Bauer, Timo Bloch, Matthias und Yuliya Fritzsche, Johann Isaak, Thomas Möller, Cathrin Wälzlein sowie Irina und Markus Zweidinger. Ihr seid mir in den letzten Jahren wirklich ans Herz gewachsen und so sehe ich es mit einem lachenden, aber auch einem weinenden Auge, dass wir uns so langsam aber sicher in alle vier Windrichtungen verteilen. Ohne euch, die ihr für die notwendige Zerstreuung und den Riesenspaß während und neben der Arbeit gesorgt habt, wären die letzten

Jahre um einiges trister gewesen. Danke für viele blöde Sprüche, lustige Unternehmungen aber auch viele ernsthafte Diskussionen.

Auch meiner Familie, das sind meine Eltern Ria und Uwe sowie mein Bruder Benjamin, möchte ich für die Unterstützung während der letzten Jahre danken. Ihr hattet immer einen offenen Ohr und auf eure moralische und tatkräftige Unterstützung war stets Verlass.

Nicht zuletzt möchte ich Dir, liebe Sabine, ganz herzlich für die letzten Jahre und vor allem für Deine Unterstützung in den letzten Wochen danken. Du warst und bist mein Ansporn und mein schöner Gedanke, wenn es mal nicht so gut läuft. Es ist wunderbar, dass es Dich gibt. Danke, dass Du so bist wie Du bist!

Diese Arbeit wurde von der *Deutschen Forschungsgemeinschaft* im Rahmen des *Sonderforschungsbereichs 634 - “Kernstruktur, nukleare Astrophysik und fundamentale Experimente bei kleinen Impulsüberträgen am supraleitenden Darmstädter Elektronenbeschleuniger S-DALINAC”* gefördert.



Lebenslauf

Persönliche Daten

Name	Christopher Romig
Geburtsdatum	02.06.1984
Geburtsort	Darmstadt
Staatsangehörigkeit	deutsch
Familienstand	ledig

Schulausbildung

1990 - 1994	Diesterwegschule Darmstadt
1994 - 2003	Justus-Liebig Gymnasium Darmstadt
Juni 2003	Abitur (Note 1,4)

Zivildienst

2003 - 2004	Caritasverband Darmstadt e.V.
-------------	-------------------------------

Hochschulausbildung

2004 - 2007	TU Darmstadt B.Sc. Physik (Note “sehr gut”) <i>Photoresponse von ^{94}Mo bei Energien bis 7 MeV</i>
2007 - 2009	TU Darmstadt M.Sc. Physik (Note “sehr gut”) <i>Kernstrukturuntersuchungen an den Kernen ^{94}Mo und ^{140}Ce mit der Methode der Kernresonanzfluoreszenz</i>
seit 2009	Promotionsstudium, TU Darmstadt



Erklärung zur Dissertation

Hiermit versichere ich, die vorliegende Dissertation ohne Hilfe Dritter nur mit den angegebenen Quellen und Hilfsmitteln angefertigt zu haben. Alle Stellen, die aus Quellen entnommen wurden, sind als solche kenntlich gemacht. Diese Arbeit hat in gleicher oder ähnlicher Form noch keiner Prüfungsbehörde vorgelegen.

Darmstadt, den 14.10.2014

(C. Romig)